The University Of Sheffield.

Understanding the Reaction, Structural Evolution, and Physical Property Development of Low-carbon Alkali-activated Slag Cements

Ella Cliff

Supervised by *Dr Brant Walkley*

A thesis submitted in fulfilment of the requirements for the degree of

Doctor of Philosophy

School of Chemical, Biological, and Materials Engineering
University of Sheffield
September 2025

Abstract

This study explores the use of the less commonly used low-carbon activators, sodium carbonate and sulphate, for the activation of blast furnace slag with the aim of furthering the use of alkali-activated binders as a sustainable alternative to Portland cement. It was found that there is delay in the onset of the main reaction by >48 hours for the sodium carbonate-activated slag binder due to an initial preferential reaction occurring in the first 2 hours after mixing, as observed *in situ*, preventing the calcium availability and alkalinity evolution of the system. However, once the main reaction does take place, a C-(N)-A-S-H structure forms as well as small amounts of N-A-S-H, not too dissimilar to a sodium silicate-activated binder. The inclusion of CaO in 1 and 3 wt.% replacements of slag in the system improved the initial rate of reaction, however, the specific mechanism is unchanged. Conversely, the sulphate-activated slag had a >100 hour delay in the onset of reaction, which itself saw limited development of key binding phases, due to the near-neutral nature of the activator. Overall, this study determined that the performance of an alkali-activate slag binder is a direct outcome of reaction pathway, controlled by activator chemistry.

Acknowledgements

First and foremost, I would like to express my sincerest gratitude to my supervisor, Brant Walkley, for introducing me to the world of sustainable cements during my MEng Research Project, inspiring me to tackle a PhD in it, and for supporting me throughout said PhD. Your continual feedback and mentoring has been inspiring, and your reassurance invaluable for allowing me to grow both professionally and personally. You foster a comfortable and collaborative research environment, enabling the freedom for me to explore my research interests. I would also like to thank John Provis for your supervision during the initial stage of my PhD project, and for writing the very handy state-of-the-art reports that have formed the backbone of my literature review!

Thank you to my friends and family for keeping me mostly sane and helping me sustain a healthy(ish) work-life balance. I would also like to extend my gratitude to my colleagues at the university, especially those in the SMASH and ISL research groups, for your continued support, feedback, and collaboration.

Finally, I want to acknowledge UKRI EPSRC for funding my PhD research, as well as the Grantham Centre for Sustainable Futures for their additional funding and professional development opportunities, including the amazing opportunity of attending COP28.

Thank you all – I wouldn't have been able to do this all without every single one of you!

Table of Contents

List of Figures

List of Tables

Thesis Overview

In response to the significant CO_2 emissions from the manufacture of Portland cement, it is vital that environmentally friendly strategies are implemented to mitigate the effect that the construction sector, specifically the cement industry, has on climate change. Alkali-activated slag binders have been proposed as a sustainable alternative to traditional Portland cement, as they often utilise industrial waste and by-products, as well as naturally occurring minerals, for their production, which in turn, maintains a low embodied carbon. These binders are formed from a reaction between an aluminosilicate precursor and an alkaline solution (often referred to as an activator), whose purpose is to induce dissolution of ions from the precursor and promote the subsequent precipitation of reaction products, including the key binding phases, C-A-S-H, C-(N)-A-S-H, and N-A-S-H.

Despite their potential for reduced cement-associated CO_2 emissions, it has been noted that the alkaline solution is the least sustainable component of these AACs in terms of carbon footprint. More so, the less commonly used alkali carbonates and sulphates can contribute a significantly reduced carbon footprint than the typical chemicals used for alkali activation – hydroxides and silicates. The use of the low-carbon activators, however, has seen delayed reaction and poor early strength development in the resultant binders, limiting their use.

Optimisation of the formulation of alkali-activated binders to maximise performance while minimising environmental impact is imperative for the adoption of such materials in industry and tackle cement-associated carbon emissions. As such, the aim of this study is to understand how the fundamental chemistry of slag binders activated by the low-carbon sodium carbonate and sodium sulphate influences their reaction, phase evolution, and physical properties, through the use of *in-situ* characterisation immediately after mixing, solid-state analysis at

various curing ages, fresh-state testing for workability, and mechanical testing measurements. The inclusion CaO and MgO, in small quantity replacements of slag in the sodium carbonate- and sulphate-activated binders was investigated, as was the blending of the low-carbon activators with more commonly used sodium silicate, all with the aim of improving the binder performance. The enhancement of early-age properties of the slag binders utilising low-carbon activators is paramount to forming effective binders while improving the sustainability of alkali-activated cements.

Determined using novel lab-scale *in-situ* IR and XRD techniques, an initial reaction was observed when sodium carbonate was utilised for activation of slag, where calcium ions from the precursor preferentially reacted with carbonates from the activator to form calcium carbonate polymorphs, which hindered the increase in alkalinity for the subsequent formation of C-A-S-H. The inclusion of CaO in small quantities greatly improved the reaction kinetics via the simultaneous formation of calcium carbonates and C-A-S-H at early age, however, this improved reaction came at the cost of the physical property performance – both compressive strength and workability reduced. Moreover, for the slag binder system activated with sodium sulphate, the time for the onset of reaction was significantly high, and when the reaction did eventually proceed, its extent is limited and thus is the physical property development. The incorporation of both CaO and MgO improved the rate of reaction; however, the reaction mechanism and phase evolution remain unchanged, thus hindering the performance of sodium sulphate-activated binders. Additionally, the use of sodium silicate blended with either of the low-carbon activators greatly improved their performance, with a clear tendency towards the nature of sodium silicate-activated binders.

Overall, the findings from this study will allow formulation optimisation of alkali-activated binders for tailored properties and improved sustainability, with the overarching aim of driving

implementation of such materials in industry and reducing cement-associated carbon emissions. Additionally, a lab-scale methodology for the *in-situ* investigation of cement reaction kinetics and mechanisms via IR and XRD measurements has been developed, which can be applied to other cement systems as well.

Chapter 1: Introduction

1.1 Research Background

With global climate change highlighting the limitations of many resources and industries around the world, the need for sustainability is at the forefront of current and future research.

Concrete and cementitious materials are quite literally the foundation of the urban world, with concrete production estimated at ~30 billion tonnes annually making it one of the most used materials globally, second only to water [1]. Cement is the 'glue' within concrete, where Portland cement is traditionally utilised as the binder, due to its extensive study proving its versatile nature: it is strong, durable, can be cast into many shapes, and is resistant to various physical and chemical stresses [2], [3]. Due to the vast quantities of concrete used, significant volumes of cement are also produced, however, the CO_2 emissions from its production are colossal, with an estimated 8 % of global man-made emissions attributed to it [4]–[6].

As the global population is forecast to increase by more than 20 % by 2050, the demand for construction, and thus cement production, is expected to mirror this growth to support rapid urbanisation and infrastructure development [7], [8]. This will result in an estimated increase in cement-associated carbon emissions from 8 to 24 % [9]. Therefore, it is vital that sustainable alternatives to Portland cement are implemented to mitigate the environmental effects of the built environment and construction sector.

Various industrial processes, including iron and steel production and coal combustion, produce large amounts of waste and by-products, some of which – blast furnace slags, fly ash, etc. – can be used as supplementary cementitious materials, through partial replacement of Portland cement-based clinkers, or as raw materials for the production of alternative cementitious materials through alkali activation, eradicating significant quantities of embodied carbon

associated with traditional cement production. Alkali-activated cements have gained interest as a sustainable alternative to traditional Portland cement and are produced from a reaction between an aluminosilicate powder, referred to as the 'precursor', and an alkaline solution – the 'activator'. Life cycle assessments of alkali-activated cements have reported reductions of CO_2 emissions compared to PC production of up to ~80 % [10]–[14], however, in order to maximise their carbon savings, AACs must be designed on a case-by-case basis, using components that are readily available, which will vary depending on region.

The most common precursors for alkali activation are ground granulated blast furnace slag (GGBFS/BFS) and fly ash. Where these high-calcium precursors are used, the resultant alkali-activated binder systems form an aluminium-substituted calcium silicate hydrate (C-A-S-H) as their primary binding phase, which is not too dissimilar to the key reaction product of Portland cement – C-S-H – but with increased crosslinking, suggesting a potential to reach superior performances than PC-based systems under certain conditions [15]. Secondary reaction products include hydrotalcite and AFm-type phases, similar to PC systems [2], [16].

Early studies into alkali-activated cements have focused predominantly on precursors, and where activation was investigated, alkali silicates and hydroxides were settled on. However, less commonly used activators, such as alkali carbonates and sulphates have the potential to further reduce the carbon footprint of AACs due to their availability and production, be it their natural occurrence or production via industrial chemical manufacture. They are also less alkaline in nature and thus pose less harm when handling compared to their common counterparts, silicates and hydroxides. The dismissal and limited use of carbonates and sulphates for alkali activation of aluminosilicate precursors is credited to their slow reaction and setting, and subsequent poor early strength development, which is ascribed to their near-neutral pH.

In this study, the use of the low-carbon activators – alkali carbonates and sulphates – will be investigated with the overarching aim of understanding the fundamental chemistry that governs the reaction kinetics and mechanisms, phase assemblage, and physical properties of these alkali-activated binder systems. This knowledge will enable optimisation of formulations for enhanced performance and sustainability, and thus, drive rapid industrial implementation of AACs.

1.2 Overall Aims

The aim of this study is to evaluate the effectiveness of the near-neutral salts, sodium carbonate and sodium sulphate, for use in the alkali activation of blast furnace slag, in order to mitigate cement-associated CO_2 emissions. As such, a literature review is undertaken to understand the gravity of the environmental effects associated with the construction industry, and more specifically, Portland cement, as well as possible strategies for reducing its carbon footprint. Moreover, the alternative cementitious binder type, alkali-activated cements, is explored with particular focus on activators, both the common and the less-used low-carbon alkali salts. Current understanding of how the activator influences the reaction mechanisms and kinetics is discussed, and the subsequent phase evolution and physical properties are explored.

This is followed by the design and development of AACs for testing and validation. With the aim of the study being to assess the use of more sustainable activators for use in alkali-activated slag cements, an alkali activator known to be feasible for use in AACs must be tested and understood – in this case, sodium silicate is used. Keeping all but the activator anion constant, alkali-activated slags utilising sodium carbonate and sodium sulphate for activation will be tested and validated against sodium silicate-activated slag. Where necessary, combinations of activators or replacement of precursor with CaO and MgO will also be investigated with the aim of improving performance. These AAC formulations are investigated to better understand

how the formulation chemistry impacts the early reaction, and their resulting phase assemblage and mechanical properties. Reaction mechanisms and kinetics are explored *in situ* via isothermal calorimetry, diffuse reflectance infrared Fourier transform spectroscopy (DRIFTS), and X-ray diffraction (XRD) measurements. Microstructure is characterised using solid state analysis techniques: Fourier transform infrared (FTIR) spectroscopy, thermogravimetric analysis (TGA), XRD, scanning electron microscopy (SEM) coupled with energy-dispersive X-ray (EDX) spectroscopy, and ^{27}Al and ^{29}Si magic angle spinning nuclear magnetic resonance (MAS NMR) spectroscopy. Furthermore, setting time, mini slump testing, and viscometry are evaluated to study the fresh properties of AACs, while compressive strength testing is utilised to assess the mechanical performance. Formulations are compared to previously reported AACs in this study as well as those in literature to assess their performance and feasibility. The experimental methodology used in this study is illustrated in **Figure 1-1**.

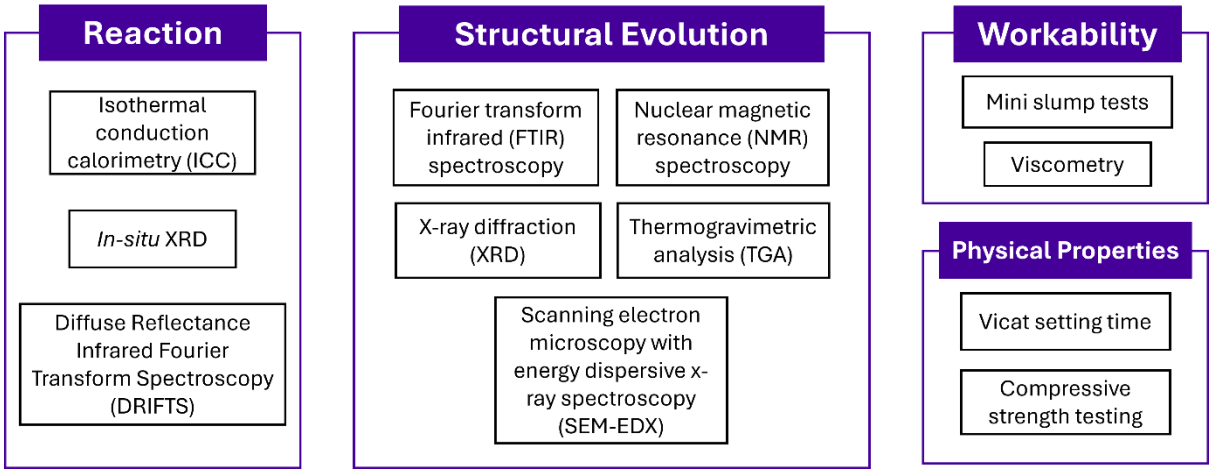

Figure 1-1 *Visualisation of the experimental methodology for the four performance criteria measured in this study.*

Overall, the work described here facilitates the understanding of binder chemistry to determine the suitability of the low-carbon alkali carbonates and sulphates, for use in the alkali activation of blast furnace slag. This insight will allow for the optimisation of alkali-activated binder formulations for performance and sustainability, aiding in their industrial implementation and

confronting the overarching goal of minimising the carbon footprint associated with the cement sector.

1.3 Thesis Synopsis

Chapter 2 reviews the existing literature in the field, outlining the shortcomings of the construction industry with regards to sustainability and how the sector is approaching reducing the CO_2 emissions of concrete. This narrows into alternative cementitious binders with particular focus on alkali-activated slags and how the use of less commonly used activating solutions could have the potential to reduce the carbon footprint.

Chapter 3 details the materials used herein to produce alkali-activated slag samples, their corresponding formulations, and the analytical techniques utilised to characterise said samples, including a novel lab-scale *in-situ* methodology for establishing reaction kinetics and mechanisms immediately after mixing. Each technique is described in terms of the information obtained, how this is applied to cementitious materials, and the specific parameters used for characterisation of binders in this study.

Chapter 4 assesses a sodium silicate-activated slag binder to use as a control sample for the following samples to be compared to. This includes revealing the reaction kinetics and mechanisms during the initial days after mixing, the changes in phases and microstructure at different curing ages between 3 and 90 days, and physical properties – in the fresh-state immediately after mixing to assess workability and compressive strength measurements at 7 and 28 days for physical development. This chapter reveals the efficacy of sodium silicate as an activator for slag binders, having reacted within a day and to a sufficient degree, with C-A-S-H forming at an early age and continuing to polymerise over time, which in turn facilitates excellent compressive strength.

Chapter 5 explores the use of sodium carbonate as an activator for slag binders alongside a 50:50 wt.% blend of sodium carbonate and silicate, compared to the established sodium silicate-activated binder. Time-resolved data from calorimetry, DRIFTS and XRD reveal early-age reaction kinetics and mechanisms, specifically a preferential reaction occurring for the carbonate-activated slag that is delaying the onset of the main reaction. Subsequent phase evolution analysis shows stunted C-A-S-H development and limited strength and workability measurements compared to the control. The blend with sodium silicate greatly improves the performance of sodium carbonate-activated slag, comparable to that of the control.

Chapter 6 investigates the inclusion of additives calcium and magnesium oxide in small quantity replacements of slag within the sodium carbonate-activated system with the aim of improving the performance of said binders. The incorporation of CaO improved the rate of reaction of the cement system, but the mechanism generally remains the same, while MgO had little effect on the reaction or subsequent phase development. Both additive inclusions reduced the compressive strength measurements, and while CaO inclusion reduced the workability, MgO incorporation improved it.

Chapter 7 looks into the use of sodium sulphate for the activation of slag as well as a combination of both sodium sulphate and sodium silicate for the same use, all compared to the silicate-activated control sample. Analysis of the early reaction data for the sulphate-activated slag reveal an extreme delay in the onset of the main reaction, and there is limited development in the phase evolution, supporting the limited use of such materials. The blending with sodium silicate greatly improved the reaction rate and structural evolution.

Chapter 8 explores adding small amounts of CaO and MgO to the sulphate-activated slag systems to try to improve their limited performance. Both additives showed improvement in

the reaction kinetics of the binder, however, the mechanism did not change, and the extent of reaction and formation of products is still significantly limited.

Chapter 9 compares all the binder systems designed and produced herein and how their performance is inherently impacted by the activating solution. This includes a direct comparison of key reaction data measurements, the formation and polymerisation of the main binding phase, C-A-S-H, and the physical property development, where appropriate. Additionally, a preliminary assessment of carbon footprint of each mix design is assessed to determine indicative trends. Finally, key conclusions of the study are outlined as well as recommendations for future work.

Chapter 2: Literature Review

2.1 Construction Industry

2.1.1 Built Environment

It is estimated that globally the equivalent of a city the size of Paris is built every single week and will continue this way for the next 30 years [17]. Currently, the built environment and construction sector account for nearly 40 % of global energy- and process-related carbon emissions [18], with building-related CO_2 emissions rising by ~1 % per year since 2010 [17].

Concrete is the second most consumed material worldwide behind only water [19], [20], with an estimated 30 billion tonnes used annually, which is 3 times as much per capita as 40 years ago [1]. Its traditional binder, Portland cement, is a well-understood, long-established material that is structurally complex, designed to provide strength and durability over many years while being subjected to thermal, mechanical, and chemical stresses [2], [3]. However, the significantly high cement production volume required to match the immense quantities of concrete used results in undesirable environmental issues; Portland cement production is responsible for more than 8 % of global anthropogenic carbon emissions [4]–[6].

With the global population expected to grow by more than 20 % to 9.8 billion by 2050 [7], so too will the demand for materials and construction as it is estimated that 60 % of the infrastructure needed for such growth does not yet exist [8]. As such, there is a lot of focus on ways to decarbonise the construction industry, so we can build without destroying the planet in the process.

2.1.2 Sustainable Development in Construction

In 1987, the UN defined sustainability as "meeting the needs of the present without compromising the ability of future generations to meet their own needs" [21], highlighting the fair utilisation of resources available to industries. Concrete must fit mechanical specifications – good strength, durability, and resistance to stresses – but must also align with socio-economic factors, like affordability and environmental sustainability to satisfy requirements of the modern world. This poses the challenge for the construction industry to transition to a sustainable environmental, social, and economic approach while maintaining its efficacy.

Faced with this need to reduce industrial CO_2 emissions without reducing its capacity, the concrete industry has several key strategies targeted at cement-based emissions [22], [23], that include:

1. Using alternative fuels and/or raw materials to reduce the CO_2 output during the manufacture of Portland-based cements.
2. Implementing carbon capture and storage (CCS) and/or carbon capture utilisation and storage (CCUS).
3. Maximising Portland cement clinker replacement with low-carbon supplementary cementitious materials (SCMs) in concrete.
4. Developing low-carbon alternative binders, not based on Portland cement clinkers.

The first two proposed solutions encapsulate energy efficiency, which is applicable to all major industries and these strategies are typically being explored and implemented in most industry sectors. The latter two strategies, however, focus more on circular economy and waste valorisation, and are more specific to the built environment and construction industry.

Reducing the amount of clinker within concrete can be done via substitution with the likes of industrial by-products – fly ash from coal combustion and ground granulated blast furnace slag from iron and steel production – or recycled powders from materials including glass, brick, and concrete itself. However, the amount of clinker replacement is often limited by standards around the world, but some promising technologies are known to have a higher replacement, like limestone calcined clay cement (LC^3) where half of the clinker is substituted with a clay and some limestone and gypsum [22]–[24].

The development of environmentally friendly alternative binders that are not based on PC clinkers may offer the greatest potential for reduction of CO_2 emissions of the construction industry. Eradicating the need for traditional Portland cement manufacture, many alternatives utilise industrial waste or by-products and/or naturally occurring minerals and thus lower the carbon footprint associated with the cement industry, however, the local availability of such materials of an adequate quality can be a limiting factor. Alternative cements, that are not Portland-cement based, include sulphoaluminate cements, magnesium-based cements, alkali-activated materials, and bio-based cements [19], [22], [24], [25].

2.2 Portland Cement

2.2.1 Overview

Portland cement (PC) is the most commonly used cement type in general use globally as the fundamental binding element of mortar and concrete. The term “Portland cement” was first penned in 1824 in Joseph Aspdin’s patent of the material, where it was named for its association with the quality and prestige of Portland stone for which cement stuccos were designed to emulate [26]. Despite maintaining the name penned by Aspdin two centuries ago, the material has undergone various evolutions of its production process to become the material so widely used today. Modern Portland cement is a manufactured material with a basis of calcium oxide,

typically containing 62-68 % CaO by weight [27]. It is also a hydraulic binder, meaning the anhydrous cement chemically reacts with just water to set and harden [28], adding to its widespread availability and use.

Despite its versatility and wide-spread use, its production currently accounts for significant amounts of CO_2 emissions, which are predicted to continue rising over time with increasing population and urbanisation. The significant carbon footprint is primarily the result of the thermal decomposition of limestone to form the reactive calcium silicate and aluminate phases during pyro-processing in the kiln [2], where approximately 0.7 to 0.9 tonnes of carbon dioxide are produced per tonne of clinker formed [29], [30].

2.2.2 Manufacture

The raw materials needed for cement production are limestone, clay, and shale, amongst other minor ingredients. These materials are extracted or quarried, before being prepared for pyroprocessing through crushing, grinding and blending into a fine homogeneous mixture. From here, the manufacture of Portland cement can be defined by four main stages: preheater, rotary kiln, cooler, and finish grinding [27].

The ground dry blend of raw materials is fed into a suspension preheater and then an inclined rotary kiln, in order to minimise free lime and maximise mineral phase composition. During this process, the materials are heated to temperatures of 1350-1450 °C to facilitate calcination – the decomposition of calcium carbonate (limestone) to calcium oxide (lime) and carbon dioxide [27] – as well as the following reactions detailed in **Table 2-1** [31]. The pyroprocessing stage is responsible for around 0.7 to 0.9 tonnes of carbon dioxide per tonne of clinker [27], [29], [30] accounting for the majority of carbon emissions in the production of cement.

Table 2-1 *Principle chemical reactions in the kiln and their temperature ranges [31].*

Chemical Reaction	**Temperature Range (°C)**
$CaCO_3 \rightarrow CaO + CO_2$	~ 800-900
$2CaO + SiO_2 \rightarrow 2CaO.SiO_2$	800-900
$3CaO + Al_2O_3 \rightarrow 3CaO.SiO_2$	900-1300
$4CaO + Al_2O_3 + Fe_2O_3 \rightarrow 4CaO.Al_2O_3.Fe_2O_3$	900-1300
$CaO + 2CaO.SiO_2 \rightarrow 3CaO.Al_2O_3$	>1300

The kiln product, called clinker, consists mostly of four mineral solids: two calcium silicates, alite and belite, along with tricalcium aluminate and ferrite, which are detailed in **Table 2-2** with their cement chemistry notation. There are also small amounts of free lime present in the clinker, as well as much smaller amounts of impurities from the fuel used in heating the kiln and some sulphates (calcium, sodium, and potassium).

Table 2-2 *Phases and composition of typical Portland cement clinker with their cement chemist notation, where C is CaO, S is SiO_2, F is Fe_2O_3, and A is Al_2O_3 [27], [32].*

Chemical Description	**Phase Name**	**Chemical Composition**	**Oxide Composition**	**Cement Notation**	**Typical Content in PC (%)**
Tricalcium silicate	Alite	Ca_3SiO_5	$3CaO.SiO_2$	C_3S	50-65
Dicalcium silicate	Belite	Ca_2SiO_4	$2CaO.SiO_2$	C_2S	15-25
Tricalcium aluminate	Aluminate	$Ca_3Al_2O_6$	$3CaO.Al_2O_3$	C_3A	5-15
Tetracalcium aluminoferrite	Ferrite	$2(Ca_2AlFeO_5)$	$4CaO.Al_2O_3.Fe_2O_3$	C_4AF	5-15

Beyond the kiln, the clinker is cooled before fine grinding with a small amount of calcium sulphate (gypsum), to activate the cement clinker and give the desired setting characteristics and minimise shrinkage. The resulting product has a typical surface area between 2000 and 5000 cm^2/g and is marketed as Portland cement [27]. The industrial manufacturing process of Portland cement is energy-intensive, particularly in the high-temperature stages of pyro

processing, as well as in the cooler. The primary fuel for cement production is coal, but as with the current trend to replace fossil fuels, combustible wastes are gaining traction [3], [27].

2.2.3 Hydration Reaction

As previously mentioned, Portland cement is a hydraulic binder, meaning that it gains its structural properties from its interaction with water. Hydration refers to the reaction of an anhydrous cement powder with water, which facilitates both chemical and physicomechanical changes in the system, leading to setting and hardening of the cement binder [33]. Due to the clinker solids being highly unstable in the presence of water, they react rapidly displaying much heat evolution [27], as can be seen in **Figure 2-1**. The hydration reaction can be described in four distinct stages: the initial/pre-induction period, the dormant/induction period, the acceleration period, and the deceleration period.

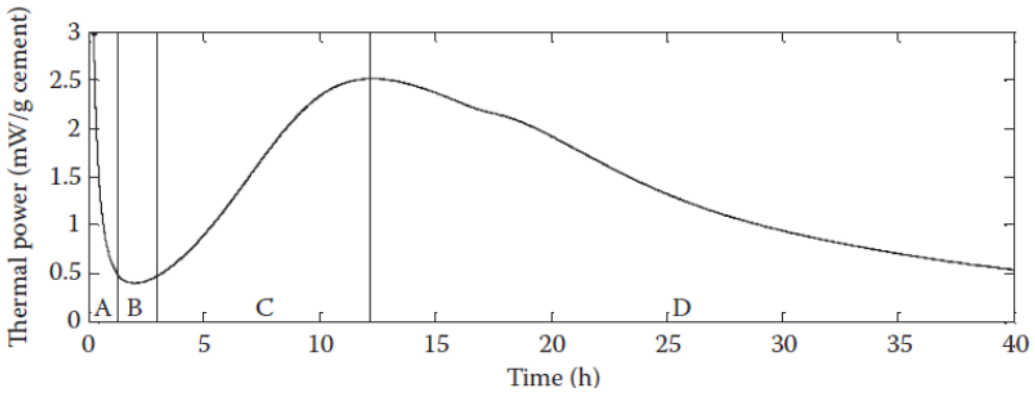

Figure 2-1 *Heat evolution of the hydration of Portland cement, displaying the mechanistic periods of the reaction: (A) initial/pre-induction period, (B) dormant/induction period, (C) acceleration period, and (D) deceleration period. Taken from [34].*

The pre-induction period begins at the introduction of water to the cement and is exothermic in nature. This heat release is attributed to the surface wetting and initial dissolution of soluble components – primarily calcium liberated from the clinker products, gypsum and other clinker sulphates – which creates a highly alkaline aqueous solution [27], [35], [36]. An aluminate-rich

gel is also formed from the mixing of the anhydrous cement with water facilitating a reaction of the aluminate phase [35].

This initial period is then followed by an induction or "dormant" period, which often lasts for several hours, in which the heat evolution is slow. The cement mix at this stage remains fluid and so can be moulded and pressed into shape [27], [33]. During this period, the aluminate-rich gel reacts with the sulphates in the solution to form early ettringite crystals [33], [35]. Once this dormant period has ceased, the cement paste will be too stiff to be worked or cast [33].

The acceleration period ensues, where a large heat release occurs, indicative of the nucleation, growth, and precipitation of the reaction phases. This period is particularly notable for the reactions involving the silica-containing clinker phases, alite and belite, which lead to the formation of calcium silicate hydrate (C-S-H) and calcium hydroxide (Portlandite), the primary binding phases of PC, as detailed in the following equations:

$$3CaO.SiO_2 + (3 + m - n)H_2O \rightarrow nCaO.SiO_2.mH_2O + (3 - n)Ca(OH)_2$$

$$2CaO.SiO_2 + (2 + m - n)H_2O \rightarrow nCaO.SiO_2.mH_2O + (2 - n)Ca(OH)_2$$

Additionally, during this period, the ettringite crystals transform into a more stable monosulphate phase when the sulphates in the solution deplete. This phase then undergoes a hydration reaction and forms AFm phases, containing less calcium sulphate [33], [35]. As hydration continues, the reacting particles diminish in size and the solid hydrate products accumulate to fill spaces between particles, which ultimately leads to the physical setting of the material, and marks the deceleration period. From this point, the strength of the cement continues to develop, with PC typically reaching 70-80 % hydration at around 28 days [27].

2.2.4 Structure

2.2.4.1 Calcium Silicate Hydrate

The main hydration product and strength-giving phase in Portland cement is calcium silicate hydrate (C-S-H), which has a highly disordered, partially crystalline structure [37]. It makes up more than 60 % by volume of the final hydration assemblage of the material [38], [39]. The content of calcium, silicon, and water in the phase is responsible for its final structure. With the content of calcium, silicon, and water in cement pastes being highly variable in nature, coupled with the disordered, poorly crystalline nature of the phase, the structure of C-S-H is difficult to pinpoint [38], [40], [41].

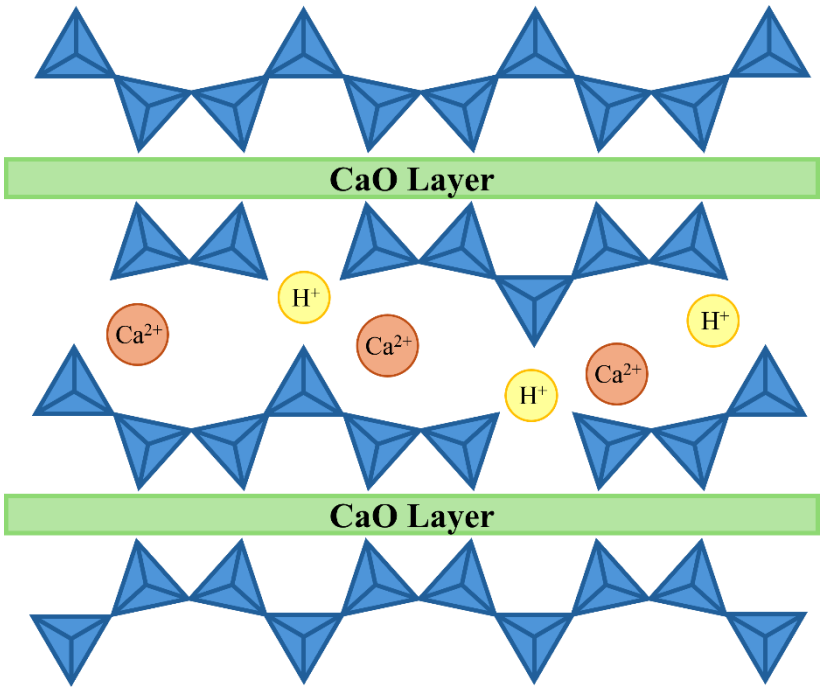

Figure 2-2 *Schematic of C-S-H, where the blue triangles represent tetrahedral Si sites.*

C-S-H is often described as having a structure similar to the crystalline minerals tobermorite and jennite, based on the calcium content of the phase. In PC systems with high calcium content and thus where Ca/Si ratios are greater than 1.5, the structure of C-S-H resembles a disordered jennite-like phase. Whereas, low calcium systems, including those blended with SCMs

(supplementary cementitious materials), C-S-H with a structure similar to tobermorite is believed to be formed [37], [38], [40], [41].

This phase is typically described as having a central calcium oxide sheet joined by disordered layers of silicate tetrahedra chains. The silicate tetrahedra form chains of a repeating kinked pattern, where each third connected tetrahedron sits so that it is not in contact with the calcium oxide layer, instead inhabiting the interlayer space. This forms the characteristic dreierketten unit associate with the phase. The first two silicate tetrahedra are referred to as paired sites, while the kinked tetrahedra are termed bridging sites [37], [41].

The length of the silicate chains dictating the C-S-H structure is dependent on the Ca/Si ratio, where higher calcium contents result in shorter mean chain lengths. This is due to the bridging sites being either vacant or containing charge-balancing interlayer cations, rather than consisting of silicate tetrahedra [37], [41]. The space between the layers of silicate chains allows for the infiltration of pore water, facilitating ion exchange with the pore solution for charge balancing by alkali cations [42].

2.2.4.2 Portlandite

Portlandite is a crystalline calcium hydroxide ($Ca(OH)_2$) with a layered lattice structure, where calcium layers are bonded to hydroxide layers with a hexagonal unit cell [37]. This phase composes of approximately 20 to 30 % of the total mass of hydration products in Portland cement [43]. The formation of Portlandite occurs through the hydration of the alite and belite phases in the clinker, and it is relatively highly soluble in nature compared to other cement hydration products. This high solubility makes this phase the key buffer for the high pH of pore water in Portland cement, which is typically around pH 12.5 [37], and in doing so, aids in protecting embedded reinforcing steel from corrosion as a result of carbonation [44], [45].

2.2.4.3 Calcium Aluminates (AFt and AFm Phases)

In cement science, calcium aluminates can be split into groups of minerals designated AFm and AFt, whose crystal structures allow for singular (mono-) or tri-substitution of anions, respectively. The use of these terms – AFt (Aluminate Ferrite tri (-sulphate, -hydroxide, etc.) hydrate) and AFm (Aluminate Ferrite mono (-sulphate, -hydroxide, etc.) hydrate) – allows the differentiation of phases dependent on their anion content [37].

Ettringite is the most common type of the AFt phases and initially forms during the hydration of the tricalcium aluminate in the presence of gypsum, which provides a sulphate-rich environment. Ettringite forms as rod-like hexagonal, prismatic crystals, which expand to occupy a large proportion of space within the hydrate assemblage [46], [47].

As the concentration of sulphate depletes, the ettringite phases begin to break down and transform into the more stable AFm type phases, including monosulphates. The conversion of ettringite into monosulphate is dependent on the SO_3 and CO_2 content of the cement paste [37], [47].

Minerals of AFm are structurally similar to hydrocalumite, which in turn is structurally similar to the layered lattice of Portlandite. The main difference in the structure of AFm is that every third divalent calcium atom is instead a trivalent cation, which is often aluminium but can sometimes be iron. This introduction of an extra positive charge causes a charge imbalance in the layer, which is rectified by the introduction of anions (typically sulphate, carbonate, and hydroxide) into the interlayer [37].

2.3 Alkali-Activated Cements

2.3.1 Overview

With the increasing concern of climate change, it is paramount that sustainable alternatives to PC are researched and developed to mitigate the negative environmental effect of the construction industry. A particularly promising replacement of PC is through the use of alkali-activated cements (AACs), which have a similar structure and also performance properties as their traditional counterpart [13], with the added bonus of the potential to reduce CO_2 emissions associated with cementitious materials by up to 80 % due to their utilisation of industrial waste and by-products as well as natural minerals [11]. The classification of these cements in comparison to traditional PC and other cementitious materials is demonstrated in **Figure 2-3**.

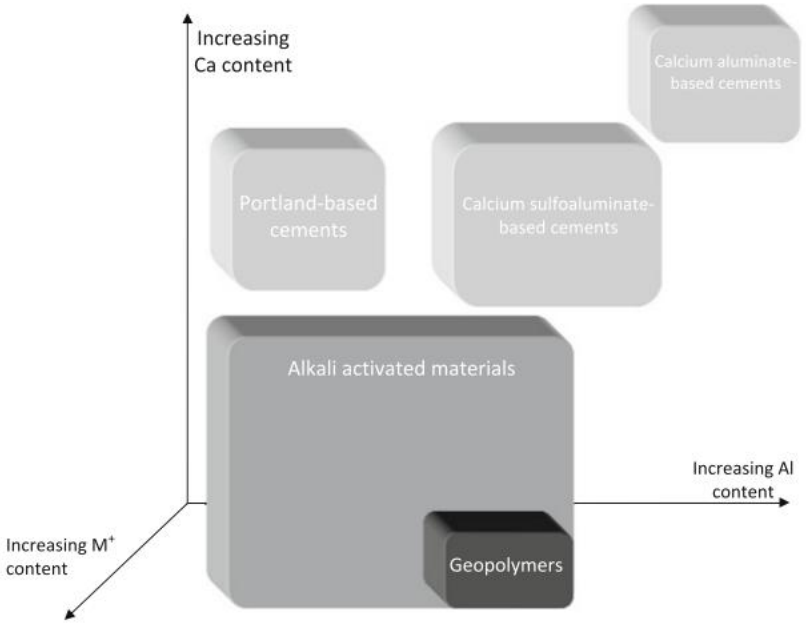

Figure 2-3 *Classifications of cements, including AAMs and Portland cement, taken from [48].*

AACs are materials with good binding properties formed from a reaction between an aluminosilicate precursor and an alkali solution. Their production makes use of industry waste and/or by-products as well as naturally occurring minerals, attributing to their superior sustainability over Portland cement [2], [49]. The specific chemistry of these cement binders

is still subject to much discussion within scientific literature but is known to be dependent on the nature of both the solid precursor and the alkali activator used [50].

2.3.2 Carbon Footprint of AACs

A life cycle assessment (LCA) [11] has revealed advantageous predictions of reducing CO_2 emissions associated with concrete production in line with the factor of four reduction objectives of the Intergovernmental Panel on Climate Change (IPCC) when utilising AAC over PC, and thus mitigating the global warming potential related to the construction industry. Habert and Oullet-Plamondon [11] found that a one-part geopolymer cement contributes less than 5 % of the global warming potential (GWP) of a binder of 100 % ordinary Portland cement, as can be seen in **Table 2-3**. The specific value varies depending on the cement mix used, i.e., the precursors and activators employed, and the material's component ratio.

Table 2-3 *The GWP of an example one-part geopolymer and its cement equivalent, taken from [11]*

	Mass (kg)	GWP (kg $CO_{2\text{-eq}}$)	
		No allocation	Economic allocation
Fly Ash	621	3	118
GBFS	621	10	81
Potash feldspar	41	0.1	0.1
Sodium hydroxide	25	23	23
Free water	476	0.1	0.1
Energy to activate K-Feldspar: 38 MJ		2.6	2.6
Total GWP		*39*	*224*
Cement equivalent (OPC)	1168	1016	1016
GWP comparison with OPC		4%	22%

A study by Pacheco-Torgal *et al.* [12] discusses the wide disparities in the values of carbon dioxide emissions of alkali-activated cement binders reported; depending on the study, AAC is estimated to reduce the cement carbon footprint by more than 80 %.

In 1990, Davidovits *et al.* [14] reported that per tonne of alkali-activated binder produced, only 0.184 tonnes of CO_2 were produced. Duxson *et al.* [15] calculated that for geopolymer binders

taken from literature, there are potential CO_2 reductions of more than 50 % when metakaolin is used and more than 80 % when fly ash is used compared to PC. Additionally, a commercial LCA discussed by Duxson and Van Deventer [10] reports an 80 % reduction of CO_2 emissions for a binder-to-binder comparison between Zeobond's E-Crete geopolymer and a standard OPC blend available in Australia, and a 60 % carbon emissions saving on the basis of a concrete-to-concrete comparison.

Overall, there are a wide range of values associated with the CO_2 emissions and sustainability reported for these alternative cementitious binders, and that these vary based on differences in raw materials, and their resulting properties. It is evident that there is need for a comprehensive LCA to be conducted around alkali-activated cements to properly consider all contributing factors, however, that is beyond the scope of this research study. Instead, this snapshot of the literature surrounding the carbon footprint of AACs serves as an indicator that regardless of mix design and the resulting performance, these binders inherently have lower carbon footprints than PC and therefore have the potential to reduce concrete-associated CO_2 emissions. That being said, it is reiterated that alkali-activated binders, nor any alternative binders for that matter, will serve as a single substitution for PC, and that specific applications must be identified as to where each alternative binder can replace PC-based systems in industry based on their performance .

2.3.3 Aluminosilicate Precursors

Aluminosilicate precursors fall into three main raw material classes: metallurgical slags, calcined clays (e.g. metakaolin), and coal fly ashes [51]. There are additional types of precursors including the likes of rice husks and municipal solid waste incineration ash, however, the aforementioned three categories are the most commonly used precursors presently [44]. The use of fly ashes is becoming increasingly scarce, particularly in Europe and Western

states, with the phasing out of coal-fired power stations. **Figure 2-4** illustrates the key chemical compositions of the key groups of raw materials used as precursors within alkali-activated cements in comparison with PC.

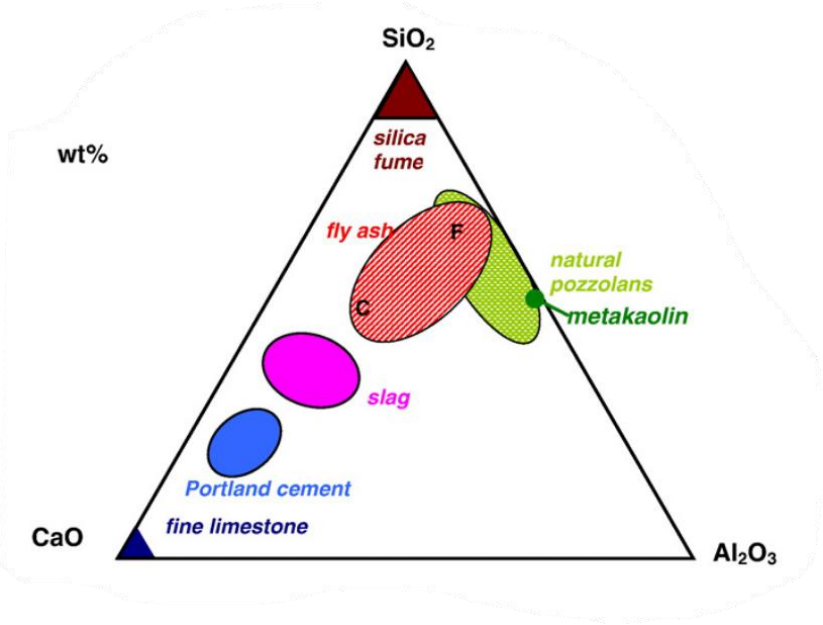

Figure 2-4 *CaO-SiO_2-Al_2O_3 ternary diagram showing precursor classes and their general compositions, in comparison to Portland Cement. Taken from [52].*

Based on their precursor and subsequent main hydration product, alkali-activated binders are categorised into two main types. Low calcium systems form the N-A-S-(H) phase and high calcium systems form the C-(A)-S-H phase as their main hydration product [53].

2.3.3.1 Low Calcium Content AACs

According to Provis and Van Deventer [48], low calcium systems are classified as geopolymers, a subset of AACs, with their binding phase being the sodium aluminium silicate hydrate (N-A-S-H) phase, which is a "highly disordered, highly cross-linked aluminosilicate gel" characterised by its amorphous or nanocrystalline nature [48] [54]. The N-A-S-(H) phase consists of "aluminium and silicon tetrahedra linked via oxygen bridges", with its chemical composition being dependent on the Si/Al ratio of the precursor material [55].

The reacting components typically have a low calcium content, and comprise of mostly aluminium and silicon, enabling the formation of a pseudo-zeolitic network. Typical precursors for low calcium content AAC includes metakaolin and other calcined clays, feldspars, natural zeolites, and low calcium fly ash and metallurgical slags [48].

For low calcium systems, the most prominent precursors are metakaolin and fly ash, which both have similar chemical properties to each other. Metakaolin is the product of heating calcinated kaolinite clays to a temperature between 500 and 800 °C [44], meaning it is one of the few precursors in alkali-activated binders that is not an industrial by-product and, as such, has greater embodied carbon than other precursors. On the other hand, fly ash is an artificial pozzolan and an otherwise-waste product of the coal combustion industry, consisting primarily of SiO_2 and Al_2O_3, although its specific composition is dependent on the coal used.

2.3.3.2 High Calcium Content AACs

High calcium cement systems are those produced when calcium- and silicon-rich materials are reacted in alkaline conditions. When discussing AAC, a high calcium system is defined as one having a Ca/(Si + Al) ratio of approximately 1. These binder systems produce the C-(A)-S-H phase as their main hydration product, which is similar to that produced in a hydrated Portland cement system (C-S-H). However, the C-A-S-H phase has a lower Ca/Si ratio than the C-S-H phase in a hydrated PC system; these ratios are 0.8-1.2 and 1.5-2.0, respectively [48], [56].

In these calcium-rich cement systems, secondary hydration phases include hydrotalcite, strätlingite, gismondine, and garronite. The formation and distribution of these secondary phases relates to composition of both the precursor used and the activating component used [48]. Precursors for high-calcium cement binders include metallurgical slags, bottom ash, and

municipal solid waste incineration ash, with blast furnace slag (BFS) being the most prominently used.

BFS is a calcium-silicate-based waste product of the steel industry, formed during the iron extraction from ore [57]. Slag mostly consists of CaO, SiO_2, MgO, and Al_2O_3, with approximately 90-95 % of its structure being a depolymerised calcium silicate. It is the most readily used precursor due to its availability and composition [56].

Slag is required to be of a certain specification for use in alkali-activated binders. It must display structural disorder, as a lower degree of polymerisation results in higher hydraulic activity. The BFS must also have a $CaO + MgO/SiO_2$ ratio greater than 1, making it pH-basic, as the lime content of the slag controls the activation reaction, and it should be ground to 400-600 m^2/kg, as specific surface is imperative to the intensity and rate of activation [54], [56].

Due to the similarity in chemical composition between PC and BFS, as well as the extensive research into slag-based AACs, the decision was made to use BFS as the precursor for this study. Additionally, it is emphasised that this study's main focus is on the mechanisms of reaction, and subsequent microstructure and physical properties, as determined by the alkaline solution used as an 'activator' and therefore the selection of precursor is less pertinent. Therefore, the precursor used herein is kept constant as BFS, and further discussion of specifically alkali-activated slag binders is detailed in the literature review.

2.3.4 Alkali Activators

One of the main distinctions between traditional Portland cement and alkali-activated cementitious binders is that where Portland cement requires only water to induce a reaction, alkali-activated materials require an alkaline solution to instigate the reaction. These solutions are often referred to as "activators" for their role of "activating" the material via inducing a

reaction. The primary role of the alkaline activators is to form a high-pH environment that initiates the dissolution of the anhydrous precursor as well as the consequent condensation and precipitation of reaction products [58]. Activating solutions with a pH value lower than 9.5 are said to not facilitate the sufficient dissolution and subsequent reaction of the slag precursor [59].

Alkali activators are aqueous solutions that, when added to an aluminosilicate precursor, form a material similar to Portland cement paste. Typically, these solutions comprise alkali hydroxides or alkali metal silicates, but some applications make use of the less used alkali metal carbonates and sulphates [2].

With the aim of alkali-activated materials to replace Portland cement being to reduce the carbon footprint of the cement and concrete industry, it is necessary to look at viable routes to further reduce their impact associated with carbon emissions. As such, it may be advantageous to explore the use of the less commonly used low-carbon alkali activators to reduce the environmental impact via CO_2 associated with AAC.

2.3.4.1 Commonly Used Activators

Sodium silicate and sodium hydroxide are some of the most widely used alkaline solutions in the production of alkali-activated slag cements [60]. Alkali metal hydroxides are produced via electrolysis of chloride salts. These activators are most commonly sodium- or potassium-based, with the limited large-scale use of lithium, rubidium, and caesium hydroxides due to their scarcity, cost, and lower solubility in water compared to the aforementioned [48].

Alkali silicates are typically produced by melting carbonate salts with silica to form glass or via dissolution of silicon dioxide in alkali salts [44]. Similar to hydroxides, sodium and potassium silicates are those most applicable to industrial alkali activation. The high cost and

limited production of rubidium and caesium silicates, and the insufficient solubility of lithium silicate, restricts their use at a large scale [48].

Most silicate activating solutions are buffered at approximately pH 11-13.5 by the silicate deprotonation equilibria due to the distribution of species and their respective pK_a values. As such, silicates typically provide a much higher level of 'available alkalinity' when compared to hydroxide solutions at the same pH due to the buffering effect providing a ready source of basic species [2], [48].

As previously stated, the effect of pH on the activation of BFS has great importance, primarily due to the fact that the solubility of calcium decreases with increasing pH. Hardened binders activated with an alkali hydroxide (pH >14) typically display a lower overall extent of reaction and lower mechanical strength than silicate-activated binder systems, where the initial activator pH is approximately 11-13.5 [2], [61]. This phenomenon is due to the reaction between the silicate species from the activator with the calcium and aluminium from the dissolving BFS forming binder products, and the gel nucleation process removes calcium from the solution phase, inducing the dissolution of precursor and thus, enhancing the extent of reaction [2].

Despite their common use due to quicker setting and hardening times, and good strength development, alkali metal hydroxides and silicates are identified as the primary contributor to the carbon footprint, as well as the production costs, of alkali-activated binders [62]. The production of sodium hydroxide and sodium silicate releases approximately 1.1 and 1.64 tonnes of CO_2 per tonne of activator, respectively [63], [64].

2.3.4.2 Low-carbon Activators

Alkali carbonates and sulphates are less commonly used in alkali-activated binders compared to the likes of silicates and hydroxides, be it due to properties, availability, or simply lack of

study. Carbonates are produced via the Solvay process, can be mined from carbonate salt deposits, which are plentiful worldwide, or can be produced from CO_2 sequestration processes, which shows obvious environmental benefits. On the other hand, alkali sulphates are either obtained from mining or as a by-product from the manufacture of many industrial chemicals, including ascorbic acid. Despite their availability, these activators possess lower alkalinity compared to hydroxides and silicates, which is thought to be responsible for their lengthy initial hardening time and poor early strength development [48], and thus their limited use.

However, due to the natural existence of alkali carbonates and sulphates, they can be directly mined from the environment, meaning their extraction is less energy intensive and emits less carbon dioxide than that required for hydroxides and silicates [65]. Further to this, there is growing interest in the use of carbonates and sulphates for lower carbon binders due to their lower monetary and environmental cost compared to silicates and hydroxides [66], [67].

2.3.4.2.1 Alkali Carbonates

As previously mentioned, alkali carbonates are naturally occurring, chemically processed or can even be produced via carbon sequestration processes, and thus have potential greenhouse gas emission savings as high as 97 % when used in AAC in comparison to Portland cement [68]–[70]. Moreover, these activators have a lower pH than the widely used hydroxides and silicates, giving potential benefits with regards to occupational health and safety [48], [71]. But this lower pH is thought to be responsible for the delayed hardening and strength development associated with carbonate-activated cement binders, leading to their early dismissal and limited use [72]–[74].

In recent years, the search for more cost-effective, and environmentally- and user-friendly alternatives to silicates and hydroxides has led back to sodium carbonate activation of blast

furnace slag garnering attention from academia and industry [69], [71]. The worldwide reserves of natural sodium carbonate are more than 25 billion tonnes, and this material is estimated to be ~2-3 times cheaper than sodium hydroxide or sodium silicate [75].

Sodium carbonate-activated slag cements require a much longer time to set - up to 5 days in some cases - compared to those activated with either sodium hydroxide or silicate [76]–[78]. This slow setting and hardening is due to the slow development in alkalinity, which is needed to initiate the dissolution of slag particles, with the initial pH of sodium carbonate being less than 12. A good consensus suggests that during the activation process, Ca^{2+} from the dissolved slag must react with the CO_3^{2-} from the activator to form carbonate salts (calcite and gaylussite) in order to increase the pH via the release of hydroxide ions [71], [77], [79]. With an excess of CO_3^{2-} ions in the system, the pH of the solution phase is slow to increase, but once these carbonate ions have been consumed, the later reaction stages are comparable to that of sodium hydroxide-activated slag binders [62], [71]. To overcome the challenges associated with hardening processes and the slow strength development of carbonate-activated slags, high-temperature curing has been proposed, but this would in turn limit the use of such materials commercially.

There have been mixed observations of the strength development of carbonate-activated binders. Provis *et al.* suggested that, despite the longer setting times and strength development, the mechanical strength in aged slag cements is higher when activated with carbonates over hydroxides [72], whereas, on the contrary, a study by Perumal *et al.* [80] observed that sodium carbonate-activated tailings showed excellent early-age strength development, but did not display improvement over time. Overall, an overarching observation is that the use of alkali carbonates in alkali-activated binders based on high-calcium precursor, early strength development is very poor and a highly porous material is produced, but at advanced times of

curing, the combination of the formation of a highly crosslinked C-A-S-H type phase, the densification of the material, and a decrease in porosity provides sufficient strength [81]–[85].

Overall, there appears to be a lack of comprehensive study into the use of metal carbonates for use in alkali-activated materials, in particular slag binders. Where research has been conducted into their use, some results and observations are contradictory meaning a sound conclusion as to the effectiveness of these activators is difficult to draw.

2.3.4.2.2 Alkali Sulphates

Similarly to alkali carbonates, alkali activation of aluminosilicate materials with alkali sulphates offers significant potential greenhouse savings as the salt is obtained either directly from mining – of which, there are estimated to be over 3.3 billion tonnes worldwide [86] – or a by-product of various industrial products, like viscose rayon, hydrochloric acid, and silica pigments. The availability of these salts, coupled with their reduced pH meaning less challenges with handling compared to the highly alkaline silicates and hydroxides, presents a viable option for a more environmentally friendly cementitious binder in the form of alkali sulphates in the production of AACs [48], [81], [87].

However, compared to various alkali activators, there are very limited studies investigating the activation of aluminosilicate precursors with sulphates, which may be due to its near-neutral pH causing a slow reaction, and thus longer setting times and lower early strength measurements [67], [88], [89] compared to hydroxide or silicate activators. Beyond this, alkali sulphate-activated slag has been proposed as a potential encapsulant for nuclear wastes containing reactive metals due to its reduced pH, reduced heat output during reaction, and less free water due to ettringite formation [90], [91].

Altogether, at face value, alkali sulphates offer an environmentally friendly, cost-effective, and safe-to-handle solution for use in alkali-activated binders, however, their limited study suggests hindered performance. As such, clear understanding of the underlying chemistry that governs the reaction and subsequent physical properties must be understood to assess their feasibility for use in these cementitious binders.

2.4 Alkali-Activated Slag Binders

2.4.1 Overview

Alkali-activated slag (AAS) cements are the product of mixing granulated blast furnace slag with highly alkaline solutions. Research into these materials has gained prominence in recent years due to their energy and environmental benefits over traditional Portland cement. With regards to mechanical properties, AAS binders are very comparable to PC, especially when activated with sodium silicate [61], [92]. Additionally, these materials exhibit greater durability than PC systems when exposed to acid, sulphates, and seawater [93], [94], but are thought to carbonate more readily [95].

2.4.2 Structure

2.4.2.1 C-A-S-H

The properties of slag binders are dependent on the nature and structure of their main reaction product, the C-A-S-H phase. As mentioned in the previous section, this phase is very similar in nature to the main hydration phase in Portland cement, C-S-H, however, C-A-S-H typically has a lower Ca/Si ratio than C-S-H, at 0.8-1.2 compared to 1.5-2.0, respectively [48], [56]. It comprises chains of tetrahedral silicates with a dreierketten structure, as can be seen in **Figure 2-5**. The chain length of the C-A-S-H phase in these slag cement systems is longer than that of the C-S-H phase in PC, with up to 13 tetrahedra compared to three to five tetrahedra, respectively. One of the primary differences between the two phases is that C-A-S-H contains

aluminium in its structure, replacing the silicon in bridging positions. A charge imbalance is caused by this substitution of Al^{3+} for Si^{4+}, which is remedied by the uptake of Na^{+} ions in the phase [2], [83], [96], [97].

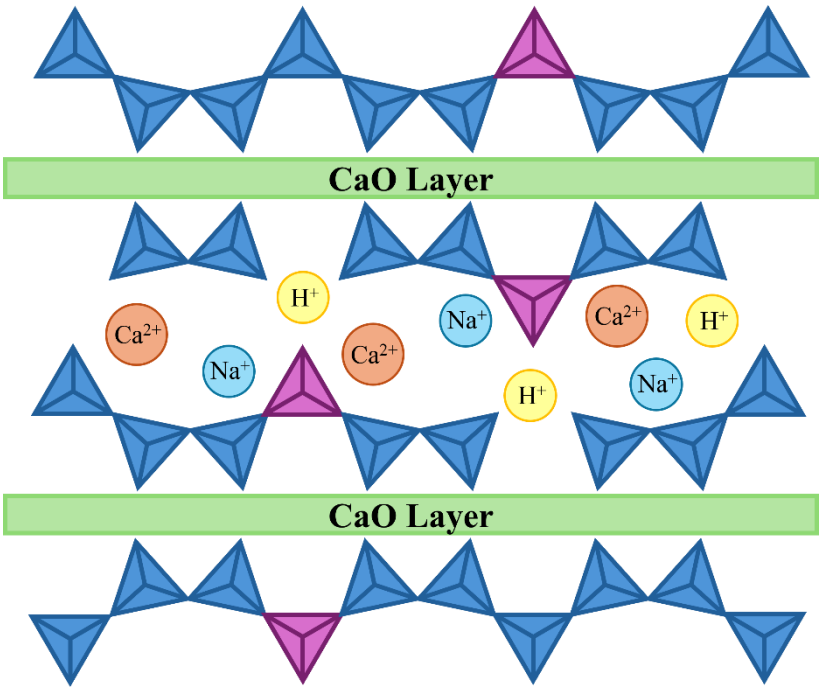

Figure 2-5 *Schematic of the generalised structure of C-A-S-H type phase, where the blue and purple triangles represent tetrahedral Si and Al sites, respectively.*

2.4.2.2 Secondary Hydration Phases

Secondary hydration phases present in alkali-activated slag binders include a Mg-Al rich crystalline phase of hydrotalcite ($Mg_6Al_2CO_3(OH)_{16}.4H_2O$) in systems with a high MgO content, as well as an AFm-type structure (tetracalcium aluminate hydrate, $(C,M)_4AH_{13}$) [16], [98]. The formation of a Mg-Al layered double hydroxide (LDH), also known as hydrotalcite, is via the precipitation of magnesium in the slag. This phase exhibits a layered crystal structure, where positively charged hydroxide layers are interlaced with layers comprising carbonate anions and water molecules [3], [99]. In systems with high aluminium but low magnesium content, zeolites (such as gismondine and garronite) also form as secondary hydrates [13], [98].

2.4.3 Alkali Activation Reaction

2.4.3.1 Overview

Studies have shown that the reaction mechanism for alkali-activation of blast furnace slag can often be described in the same four distinct stages as the hydration of Portland cement: the initial or pre-induction period, the induction period, the acceleration period, and the deceleration period. The initial, pre-induction period corresponds to the dissolution of solid aluminosilicate precursor, i.e. the dissolution of the slag particles, followed by the dormant, induction period, where there is rearrangement and exchange amongst dissolved species. The acceleration period is where there is typically a large release of heat, due to the gel nucleation and precipitation of reaction products. This stage is followed by a deceleration period, where the material begins to solidify, harden, and develop its strength [2], [62], [100], [101].

It has been found that in the first 24 to 48 hours of the reaction process, the reaction kinetics of BFS activated with alkali silicate, carbonate or hydroxide produce a heat flow curve generally similar to that expected for PC. However, the intensity and length of reaction periods of alkali-activated BFS binders during this time depends on the activator type [48]. Typically, BFS activated with NaOH or Na_2CO_3 produces a lower total heat release in the first 24 hours of reaction than that of silicate-activated binders, consistent with a slower reaction process [102]. Consequently, the reaction products, and thus the performance, of alkali-activated slag binders are heavily dependent on the nature of the alkali activator used [58], [103]–[105].

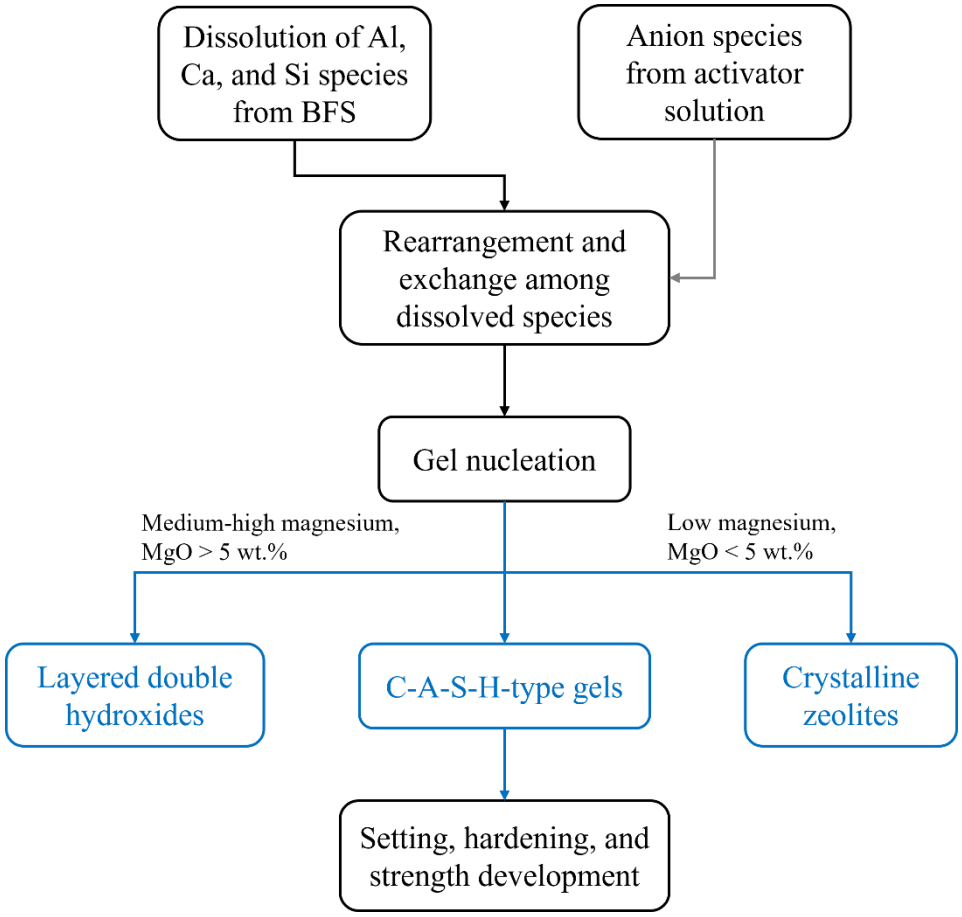

Figure 2-6 *Reaction process and products of alkali-activated slag binders. Adapted from Provis and Bernal [2].*

Blast furnace slag predominantly consists of the following oxides: CaO, SiO_2, MgO, and Al_2O_3 [100] and the variation in content of these aforementioned oxides is known to affect the reaction mechanisms and kinetics of alkali activation. An increase in MgO content results in a slower rate of reaction for silicate-activated slags, as observed by Bernal *et al.* [106], due to the formation of hydrotalcite as well as C-A-S-H. Whilst, another study observed that an increase in MgO content results in a higher degree of reaction at an early age in silicate-activated binders [107]. Furthermore, when the MgO content of slag was constant, an increase in Al_2O_3 saw a reduction in the rate of reaction for both hydroxide- and silicate-activated slag binders in the initial few days of curing [108].

During the first few hours of reaction, the dissolution of slag under high concentrations of OH^- facilitates the breaking of Ca-O, Mg-O, and T-O-T bonds (where T = Si or Al) within the slag particles. Due to the weaker bonding of Ca-O and Mg-O compares to T-O-T, greater amount of Ca and Mg dissolves in the water than Al and Si, and as such, a Si/Al-enriched layer forms rapidly on the slag surface. This altered phase structure of slag provides gaps for hydroxide ions to enter the bulk system and facilitate the primary reaction. Then, depending on activating solution chemistry, hydration products form in the space between particles previously occupied by OH^- ions [48], [104], [109]–[111].

2.4.3.2 Activation with Sodium Carbonate

As previously mentioned, sodium carbonate can be utilised in slag binders as a lower cost and more environmentally friendly alternative to hydroxide and silicate activators. The use of carbonates as activators promotes the development of a lower pH compare to other alkali-activated cement systems, which is cause for the material's slow setting times and early strength development, but is potentially beneficial with regards to occupational health and safety considerations [48], [77]. The understanding of the structural development of carbonate-activated slag binders is limited as these materials have garnered less interest from both academia and industry because of this delayed setting and strength development in comparison with BFS activated with sodium silicate or hydroxide [77].

During the early stages of BFS activation with sodium carbonate, it is believed that calcium carbonates and mixed sodium/calcium carbonate double salts form as a result of the Ca^{2+} ions from the slag preferentially reacting with the CO_3^{2-} ions of the carbonate activator, whilst the aluminosilicate component of the slag likely reacts with the sodium from the activator to form either a sodium aluminosilicate phase [58] or a crystalline zeolite, e.g. zeolite NaA [71]. These phases do not provide the high degree of cohesion required for high early strength development,

and the carbonate phases formed, in addition to the slow dissolution of slag under moderate pH from the Na_2CO_3 activator, retard the reaction, causing a longer induction period. However, once the CO_3^{2-} is exhausted, the activating reaction continues similarly to an NaOH-activated slag binder, forming the typical calcium aluminium silicate hydrate (C-A-S-H) and hydrotalcite phases [69], [71].

Furthermore, it has been suggested that the long-term activation reaction of slag binders with sodium carbonate occurs through a cyclic hydration process, where the Na_2CO_3 supplies a buffered alkaline environment, with the level of available CO_3^{2-} in the system maintained by the gradual dissolution of $CaCO_3$ within the pore solution releasing Ca^{2+} to react with the dissolved silicate from the BFS to form C-S-H-type products. However, there lacks detailed evidence as to how this mechanism might be established and then proceeds over the initial months of reaction [71], [82].

2.4.3.3 Activation with Sodium Sulphate

There is also interest in sodium sulphate for the alkali activation of aluminosilicate slag precursors, due to their availability and near-neutral pH making them more cost-effective, safer to handle, and lower in carbon intensity compared to their more commonly used counterparts, alkali silicates and hydroxides [48], [81], [87]. However, the aforementioned moderate pH lowers the amount of soluble silica released from the slag, and thus hinders the rate of reaction, the setting time, and early strength development of alkali-activated slags utilising sodium sulphate [67], [88], [89], [112], [113].

Alkali activation of slags with sodium sulphate typically leads to the formation of a C-A-S-H-type structure with a low Ca/Si ratio as the main reaction product and key binding structure [81], [114]. Depending on the chemistry of the slag, the main secondary reaction product for

sodium sulphate-activated slags is ettringite when the MgO content is low (<5 wt.%) and Al_2O_3 content is high, or sulphate-bearing layer double hydroxides (LDHs) when there is a higher MgO content [87], [88], [115]. Mobasher *et al.* [67] found that a greater quantity of C-A-S-H phase formed when the activator dosage increased due to a higher extent of reaction, while other studies revealed that slag fineness and curing temperature can greatly influence the reaction kinetics of sodium sulphate-activated slag binders [89], [114]. Although there is increasing interest in utilising sodium sulphate for alkali activation of slags, there is still limited knowledge of how the formulation chemistry affects the reaction-structure-property relationships.

2.4.4 Inclusion of Additives

It has been found that, although limited in overall research, early studies of the use of both sodium carbonate or sodium sulphate in the alkali activation of slags have generally conceded that the rate of reaction, setting time, and early strength development are less than desirable for cementitious binders applied in industry. As such, it is worth exploring avenues by which the performance of such slag binders can be improved without compromising on the lower carbon footprint and ease of handling that using these near-neutral salts afford.

Quite often where the desired performance of cementitious binders is not achieved, additional (mineral or chemical) components are incorporated into the mix design beyond the binder components – the aluminosilicate precursor and alkaline activator – with the aim of improving one or more properties [48]. For example, superplasticisers are possibly the most common admixture in alkali-activated materials used to improve the rheology and workability [116]–[118].

2.4.4.1 Inclusion of CaO and MgO for Improved Performance of AACs

With the knowledge that alkali hydroxides and silicates result in desirable properties for alkali-activated slag systems, the combination of these activators with the low-carbon activators has been explored as a happy medium between performance and environmental sustainability [69], [79], [119], [120].

Similarly, it is quite well known that slag composition can significantly affect reaction kinetics, phase assemblage, and mechanical properties of alkali-activated slag cements [106]–[108], [110], [121], [122], particularly the CaO, MgO, and Al_2O_3 content. As such, studies have incorporated calcium oxide and magnesium oxide to replace some quantities of slag within alkali-activated slag systems in order to improve properties; improved reaction kinetics, drying shrinkage, and strength has been noted for the inclusion of either MgO and CaO in alkali-activated slag binders [123]–[125], including those activated with sodium carbonate [125]–[127] or sodium sulphate [125].

MgO is typically used for the improvement of mechanical properties but has been ovserved to increase early reaction kinetics. According to Abdel-Gawwad [123], the replacement of slag with 5 wt.% of reactive MgO reduced the drying shrinkage, accelerated the hydration, and increased early compressive strength of slag binders activated with a sodium silicate and hydroxide blend. Moreover, He *et al.* [125] found that the inclusions of reactive MgO in quantities 4-6 wt.% greatly accelerates the hydration of Na_2CO_3- and Na_2SO_4-activated slag due to an increase in pH of the systems leading to an increased heat evolution rate and cumulative heat of reaction of AAS. This incorporation also saw the promotion of more reaction products and the densification of the matrix, which subsequently improves the mechanical properties. These findings are corroborated by Feng *et al.* [124].

Similarly, the addition of calcium oxide in alkali-activated slag systems has also seen mostly positive results in terms of reaction kinetics and setting time, however, reduced workability and limited changes in strength measurements [122]. The increase in reaction kinetics is due to the formation of $Ca(OH)_2$ facilitating the reaction between Ca^{2+} and $[SiO_4]^{4-}$ [128]. Reduced workability and setting time has been noted as being a result of the higher dissolution of aluminosilicate causing a shortage of water in the alkaline pore solution [122]. Furthermore, Wang *et al.* suggested that the inclusion of 2.5 wt.% of CaO with a 5 % dosage of Na_2CO_3 significantly increased the quantities of hydration products, resulting in a denser microstructure and a higher compressive strength. This was attributed to the generation of sodium hydrate and low crystalline calcium carbonate phases by the initial reaction of CaO and Na_2CO_3 facilitating the formation of calcium silicate hydrate and hydrotalcite-like phases [126].

Overall, though limited in study, it has been found that small inclusions of CaO and MgO in alkali-activated slag binders can alter the performance of such cements, be it their initial reaction kinetics, setting time, workability or compressive strength, however, the exact effects appear to depend on the mix chemistry.

2.5 Key Research Gaps and Aims of Study

It is evident that various approaches must be explored to lower the carbon footprint of the concrete industry, and one of those approaches is the use of alternative binders to reduce the reliance on PC. It is reasonable to suggest that there is no singular binder that will replace the role of PC, and so a variety of cementitious materials must be explored for the combined replacement of at least some proportion of PC in order to oppose the significant greenhouse effect of the concrete industry.

One of the most promising alternatives proposed is the use of alkali-activated slag binders, due to their key binding phase being analogous to that of PC, however despite this similarity, their structure-property relationships differ significantly. Where these materials have been studied and then used in practice, alkali silicates and hydroxides have been used, which have been noted for contributing the most to the material's carbon footprint. On the other hand, less commonly used activators, like alkali carbonates and sulphates, would contribute a lower carbon footprint but have been less studied.

This forms the basis of the research study herein, and the specific research gaps identified from the literature review are summarised below, alongside how these will be investigated in this study.

- Studies of low-carbon activators – alkali carbonates and sulphates – identify that the reaction is slow and resulting structure and properties are undesirable. However, there is clear lack of fundamental mechanistic knowledge as to how the activator results in such structure and properties. As such, a key focus of this study is to understand the fundamental chemistry governing the reaction kinetics and mechanisms, and subsequent phase evolution and physical properties. This understanding should in turn facilitate further study into optimisation of mix design to enhance performance and reduce the carbon footprint
- Some studies have proposed a probable theory as to the delay in main reaction of carbonate-activated slag binders – a preferential reaction occurring in the initial hours after mixing, whereby calcium ions from the slag are reacting with carbonate ions in the activator to form calcium carbonate polymorphs, which in turn prevents the increase in alkalinity required to induce the formation of key binding phases. Although a sound theory, there lacks clear evidence to verify this preferential reaction, and so there is

need for an *in-situ* investigation to validate the specific reaction mechanism. This verification is necessary in order to explore avenues for improving the rate of reaction associated with the limited use of such low-carbon activators.

- Along the lines of improving reaction kinetics and property development, approaches have been proposed where activating solutions are combined or even additional minerals are added to the system to improve performance. This study will therefore explore how low-carbon activators – sodium carbonate and sulphate – combined with sodium silicate affects the reaction and subsequent microstructure and property development, as a compromise between performance and carbon footprint. Additionally, minerals additives CaO and MgO – key compositional components of slags and other binders – will be incorporated into the system with the primary aim of improving the reaction kinetics of the low-carbon activator-based binders. As the primary overarching aim of this study is to assess viability of alternative activators while reducing the carbon footprint of AACs, only small amounts of these minerals will be used as replacements of the slag precursor, due to their own undesirable carbon footprint.

These gaps will be addressed in comparison to a sodium silicate-activated slag binder, which will act as a control formulation due to its known sufficient performance and use in the concrete industry in some applications around the world [92], [129]–[131].

Chapter 3: Materials and Experimental Methods

3.1 Materials

In this study, the choice was made to use cement paste rather than concrete in order to eradicate any effects of sand and aggregate, thus simplifying the analysis, and allowing the focus of the study to be on the cement itself. As such, samples were made using a blast furnace slag and alkaline solutions.

3.1.1 BFS

Samples were made using blast furnace slag supplied by Ecocem (Dunkirk, France). The oxide composition, which was determined by X-ray fluorescence (XRF), is detailed in **Table 3-1**. The particle size distribution (PSD) was determined using a Malvern Mastersizer 3000. A plot of the distribution is shown in **Figure 3-1** and the corresponding values detailed in **Table 3-2**.

Table 3-1 *Chemical composition of BFS determined by XRF, where LOI is the loss on ignition.*

Component	**CaO**	**SiO_2**	**Al_2O_3**	**MgO**	**TiO_2**	**Fe_2O_3**	**K_2O**	**Na_2O**	**Minor Comp.**	**LOI**
Mass Composition (%)	42.7	37.2	10.2	6.6	0.5	0.4	0.4	0.3	0.3	1.2

The same batch of BFS is used throughout this study, however, it should be noted that chemical composition of BFS varies batch-to-batch and therefore performance and properties of the resulting alkali-activated slag binders vary based on the initial precursor composition and PSD. The chemical composition of the BFS used herein is within 5 % of that for BFS in studies exploring alkali-activated slag binders, where the PSD is also in a similar range [69], [85], [119], [132] .

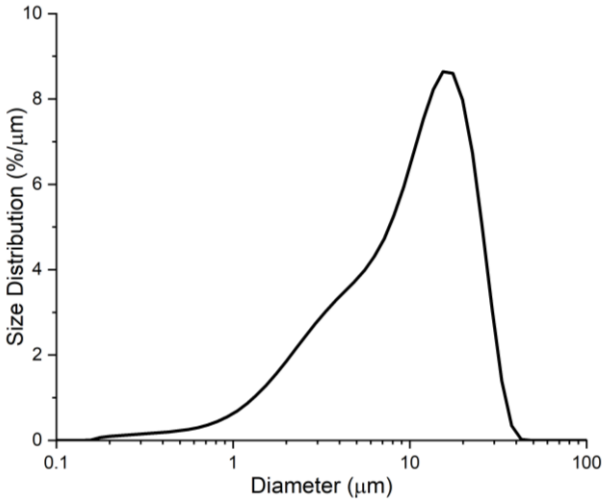

Figure 3-1 *Particle size distribution (PSD) of the blast furnace slag used.*

Table 3-2 *Particle size analysis of BFS.*

Sample	**Particle size analysis (µm)**		
	d_{10}	**d_{50}**	**d_{90}**
BFS	2.14	10.0	22.6

The XRD pattern of BFS shown in **Figure 3-2** indicates a mostly amorphous structure with a broad feature due to diffuse scattering centred at ~30° 2Θ. There are small amounts of crystalline structures present, namely calcium carbonate polymorphs (aragonite and calcite), likely due to some carbonation during material storage.

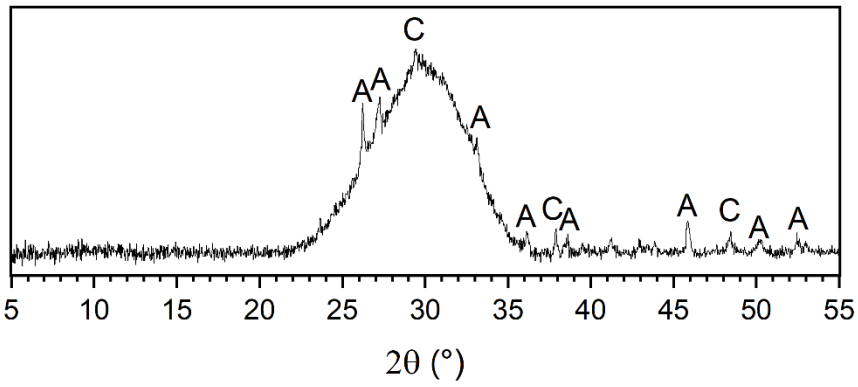

Figure 3-2 *XRD pattern of BFS with phases identified: A – Aragonite (PDF 04-008-5421) and C – Calcite (PDF 00-066-0867).*

Figure 3-3 displays the FTIR spectrum of the BFS. A broad band can be seen between ~800 and 1000 cm^{-1}, which appears to be two overlapping peaks, centred at ~920 and ~855 cm^{-1}, corresponding to asymmetric stretching vibrations (ν_a) of Si-O-T (where T = tetrahedral Si or Al) [133], [134] and asymmetric bending (δ_a) of C-O [135], [136], respectively. The latter can be attributed to atmospheric carbonation, consistent with the previous XRD pattern. Additionally, there is a minor resonance centred at ~690 cm^{-1} attributed to the Si-O out of plane bending (δ_a) [137]. The broadness of these peaks is indicative of the highly amorphous structure, predominantly consisting of silicates.

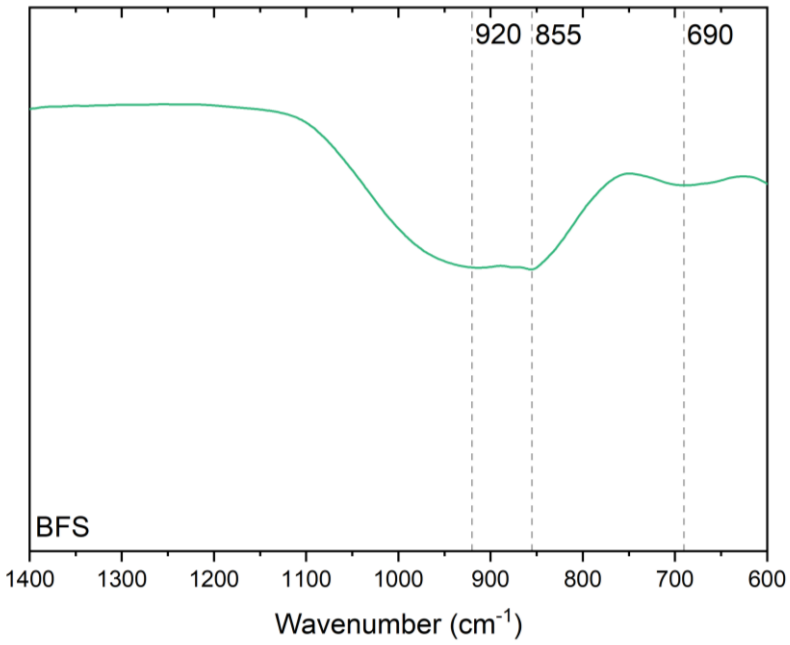

***Figure 3-3** FTIR spectrum of BFS.*

3.1.2 Activating Solutions

Five different alkaline solutions were used throughout the project using three reagents – sodium silicate, sodium carbonate, and sodium sulphate – either as the sole activator or in combination with each other. The pH of each solution was determined using a Mettler Toledo SevenCompact S220 pH meter, and these values are reported in **Table 3-3**.

Table 3-3 *pH values for activating solutions of 8 wt.% Na_2O of activator, taken in triplicate and averaged.*

Solution	pH
Na_2SiO_3	13.09
$Na_2SiO_3 + Na_2CO_3$	13.08
Na_2CO_3	11.74
$Na_2SiO_3 + Na_2SO_4$	12.96
Na_2SO_4	8.25

A commercial sodium silicate solution was used (PQ Silicas, Grade D), where the modulus, SiO_2/Na_2O, is equal to 2.0, and has the following mass composition: 55.9 wt.% H_2O, 14.7 wt.% Na_2O, and 29.4 wt.% SiO_2. Deionised water was added to the solution to achieve the desired water-to-solids ratio, and sodium hydroxide pellets were added to the solution to produce a modulus of 1.0. The solution was left to mix on a magnetic stirrer plate until the hydroxide pellets had completely dissolved and the solution cooled to the laboratory temperature (20 °C).

For the sodium carbonate activating solutions, reagent grade anhydrous sodium carbonate (Fischer Scientific, ≥99 % Na_2CO_3) was dissolved in deionised water at laboratory temperature.

In contrast, for sulphate solutions, reagent grade anhydrous sodium sulphate (Fischer Scientific, ≥99 % Na_2SO_4) was dissolved in deionised water whilst heated to ~50 °C on a magnetic stirrer hot plate. This solution was then allowed to cool to laboratory temperature (20 °C) before use. The temperature of 50 °C was selected based on the solubility characteristics of sodium sulphate as a function of temperature. At temperatures up to 32.4 °C, sodium sulphate decahydrate ($Na_2SO_4.10H_2O$, also known as mirabilite or Glauber's salt) has a higher solubility than the anhydrous form due to its stability. A eutectic point is reached at

32.4 °C, where the solubilities are equal for both sodium sulphate decahydrate and anhydrous sodium sulphate. Beyond this point, the anhydrous sodium sulphate is more soluble than the decahydrate form, and therefore, at a temperature of 50 °C, the complete dissolution of anhydrous sodium sulphate, and any sodium sulphate decahydrate potentially formed, is ensured [138].

For solutions with a combination of reagents, the solid reagent (sodium carbonate or sodium sulphate) was dissolved in deionised water before adding the sodium metasilicate solution (sodium hydroxide dissolved in sodium silicate solution) and allowing to cool to room temperature before experimental use.

Figure 3-4 shows the FTIR spectra for each of the five alkaline solutions used for making the alkali-activating slag samples in this project. All spectra contain a peak centring at ~1640 cm^{-1} corresponding to the bending vibration of the H-O-H bond of water [139]. Aptly, each sample containing: sodium silicate has a peak in its spectrum at ~985 cm^{-1} associated with Si-O stretching vibrations [53], [140]; sodium carbonate has a peak at ~1375 cm^{-1} in its spectrum assigned to the asymmetric stretching of C-O bonds of the carbonate ions [141], [142]; and sodium sulphate has a peak in its spectrum at ~1085 cm^{-1} aligning with the asymmetric stretching of the S-O bond within sulphate ions [143], [144].

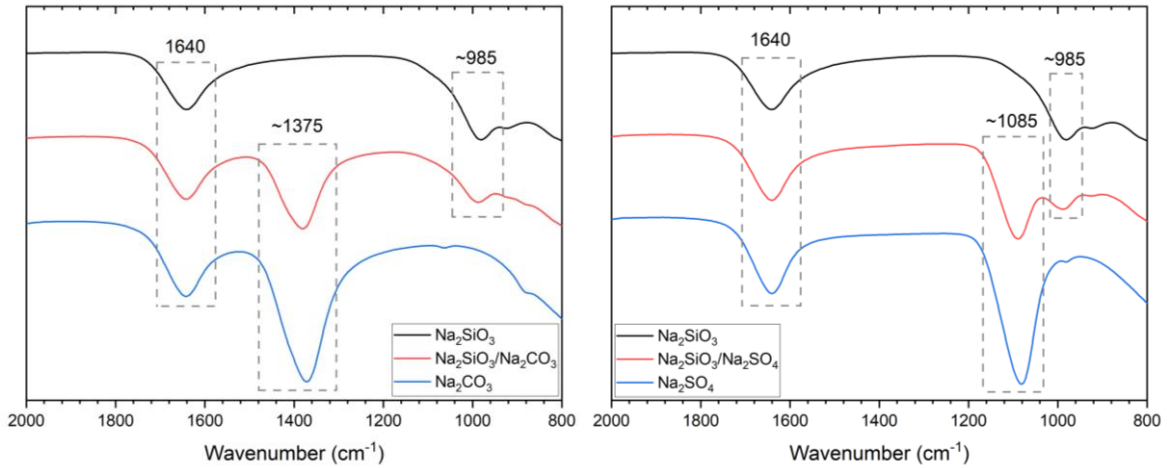

Figure 3-4 *FTIR spectra of alkaline solutions.*

3.1.3 Additives

Various chemicals and materials can be added to a cement mix to improve the performance of the overall material. The function of such additives includes reducing porosity, accelerating or reducing setting time, improving fluidity, and inhibiting corrosion. In this investigation, additives were incorporated in order to increase the rate of reaction of carbonate- and sulphate-activated slag cements so that their performance is more comparable to cementitious materials in practice.

Calcium oxide (CaO) and magnesium oxide (MgO) were chosen as appropriate additives for this experiment as they have previously been used in alkali-activated systems to improve the hydration and mechanical properties. These additives were used in small quantities (1 and 3 wt.%), where they replaced the BFS in the system.

3.1.4 Sample Preparation

Initial formulations (1-3) were designed to be comparable with previous investigations of microstructure and nanostructure of AACs produced using carbonate-based activators [58], [69], [71], where sodium silicate was used as a control sample. Further formulations were

designed with the same water-to-solids ratio and activator dosage to allow a comparable analysis. For all samples, water-to-solids (w/s) ratio is 0.4, and dosage, defined as the mass of Na_2O of the activator relative to the mass of anhydrous slag, is 8 wt.%. All formulations are detailed in **Table 3-4**.

Samples were mixed with an overhead high-shear mixer (Heidolph RZR2020) at 1200 rpm for 10 minutes until a homogeneous paste formed. Pastes were then transferred to 50 ml centrifuge tubes and cured at 20 °C for set times until solid-state characterisation. For fresh-state characterisation, sample pastes were transferred to the analytical apparatus in a promptly manner to acquire early reaction data.

Table 3-4 *Summary of sample formulations used in this study.*

No.	Formulation	Activator	BFS (g)	Activator Na_2O (g)	Additive	Additive mass (g)
1	**BFS_8%_SiO_3**	Na_2SiO_3	100	8	--	--
2	**BFS_8%_CO_3**	Na_2CO_3	100	8	--	--
3	**BFS_8%_SiO_3_CO_3**	Na_2SiO_3 + Na_2CO_3 (50:50 wt.%)	100	8	--	--
4	**BFS_8%_SO_4**	Na_2SO_4	100	8	--	--
5	**BFS_8%_SiO_3_SO_4**	Na_2SiO_3 + Na_2SO_4 (50:50 wt.%)	100	8	--	--
6	**BFS_8%_CO_3_1%_CaO**	Na_2CO_3	99	8	CaO	1
7	**BFS_8%_CO_3_3%_CaO**	Na_2CO_3	97	8	CaO	3
8	**BFS_8%_CO_3_1%_MgO**	Na_2CO_3	99	8	MgO	1
9	**BFS_8%_CO_3_3%_MgO**	Na_2CO_3	97	8	MgO	3
10	**BFS_8%_SO_4_1%_CaO**	Na_2SO_4	99	8	CaO	1
11	**BFS_8%_SO_4_3%_CaO**	Na_2SO_4	97	8	CaO	3
12	**BFS_8%_SO_4_1%_MgO**	Na_2SO_4	99	8	MgO	1

13	**BFS_8%_SO_4_3%_MgO**	Na_2SO_4	97	8	MgO	3

3.2 Testing Methods

3.2.1 Hardened State Chemical Analysis Methods

3.2.1.1 Hydration Stoppage via Solvent Exchange

Prior to analysis, the reaction of cementitious samples must be halted and the free water in the pore solution must be removed. The aim of reaction stoppage is to remove existing water within the pores without removing the water present in any hydration products, thus preserving the microstructure of the material. The hydration halting of samples is a desirable step before characterisation methods, where experimental runs are not performed immediately at a set time, and it is also utilised before epoxy saturation of samples for analysis with SEM [34], [145], [146].

Solvent exchange was used to stop the hydration prior to any solid-state analysis – FTIR, XRD, NMR, TGA, and SEM-EDX. Samples were fragmented at set time points and immersed in isopropanol for at least 48 hours and then dried ready for preparation for the aforementioned analysis methods. Once dry, samples were either crushed, ground and sieved to ~63 μm (for FTIR, XRD, NMR, and TGA) or mounted in epoxy resin for use in SEM-EDX.

Although solvent exchange for hydration stoppage is a well-established technique, it is noted that solvent exchange has its limitations, in particular the altering of metastable phases can occur and therefore, the acknowledgement that some redistribution or loss of species is possible, particularly for early-age samples [34], [146]. However, this is mitigated by using the same established method outlined in the previous paragraph and kept consistent for all samples. Furthermore, there have been various discussions of the limitations of using solvent exchange

when it comes to TGA, in particular the layer of inorganic carbon as a result of the solvent can lead to a greater amount of carbonation in the data [147]–[149]. That being said, within this study, TGA is utilised for indicative trends between mix designs and less for absolute values, and as previously mentioned, because the same method of solvent exchange was performed across all samples, any possible discrepancy can be resolved to systematic error.

3.2.1.2 Thermogravimetric Analysis (TGA)

Thermogravimetric analysis (TGA) is a method by which the mass of a sample is observed either as a function of increasing temperature or isothermally as a function of time. It is used for the characterisation of materials, by identifying phase changes as a result of undergone decomposition, oxidation, or dehydration.

TGA is used in the cement industry to understand the material's performance by identifying and quantifying mineralogical phases of the hydrated binder. Specifically, in this research study, TGA can be utilised to quantify hydration reactions as different cement hydrates will decompose in different temperature ranges during heating with TG. It can also be used to assess the degree of carbonation within a cementitious system, through decomposition at characteristic temperatures [150].

TGA data were acquired using a Perkin Elmer TGA 4000. Approximately 40 mg of powder sample in an alumina crucible was top loaded into the machine and heated from 30 to 900 °C at a rate of 10 °C per minute under a nitrogen flow of 40 ml per minute at 1 bar. An isothermal hold was applied at the start and end temperatures for 5 minutes. All data were normalised by the mass of the sample.

3.2.1.3 Fourier Transform Infrared (FTIR) spectroscopy

Fourier transform infrared spectroscopy is an analytical technique used for material identification and constituent quantification. It operates by passing infrared radiation (between 4000 and 500 cm^{-1}) through a sample, where some of the radiation is absorbed and the remainder passes through and is transmitted to a detector. This detected signal is processed via a Fourier transform (hence the name), and the absorbed wavelengths are extracted to produce a spectrum, of either transmittance or absorbance (%) as a function of wavenumber (cm^{-1}). Within the material, covalent bonds absorb the infrared beam, causing them to vibrate, which in turn facilitates the stretching and bending of different bonds. These vibrations occur at characteristic wavenumbers, and therefore, reveal the nature of the bond environment and the consequent molecular structure of the sample [151].

An infrared beam is generated and passed through a splitter in order to create two perpendicular beams. The incident beam is reflected off a moving mirror creating many different wavelengths within the beam, while the deflected beam is reflected off a fixed mirror. These two beams then converge at the beam splitter creating a single beam (the interferogram), containing both constructive and destructive interferences. The interferogram then passes through the sample, where wavelengths are absorbed at characteristic frequencies of the sample, and the remaining beam continues to the detector. This signal is then processed using a Fourier transform, creating an FTIR spectrum that can be analysed in conjunction with signals found in literature. **Figure 3-5** aids in illustrating the how FTIR spectroscopy works.

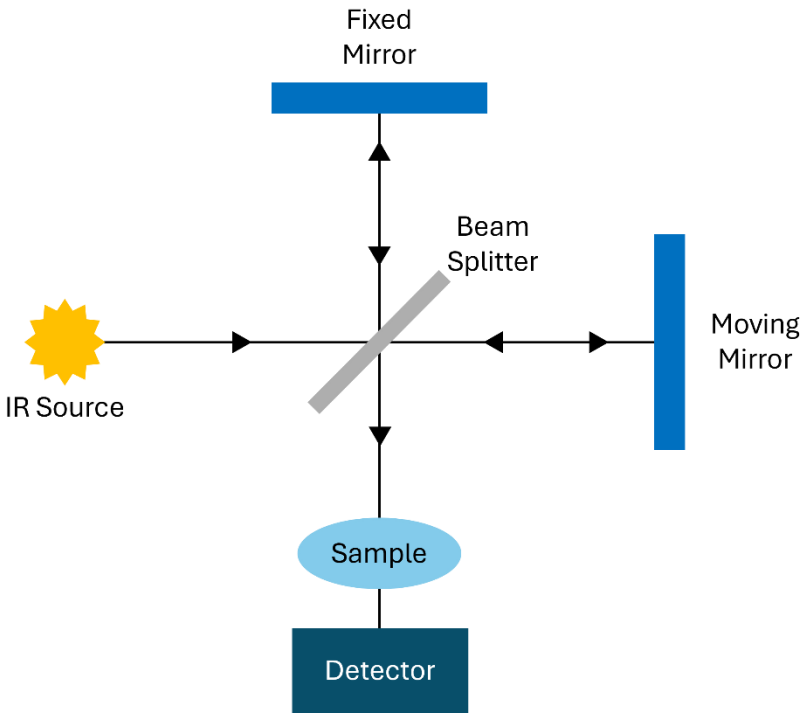

Figure 3-5 *Illustration of how FTIR spectroscopy works.*

Due to cement binders having an amorphous and highly cross-linked structure with structural disorder, the likes of XRD and other techniques for identification of crystalline phases, provide little insight into the nature of the material's structural network. On the other hand, FTIR spectroscopy does not require long range order within a sample, and is thus an ideal method for characterising individual bond environments in amorphous materials, like cementitious materials [151].

The Thermo Scientific™ Nicolet™ iS™ 5 FTIR Spectrometer was used to identify the bond environments present in the cured, ground samples at specific curing times over a range of 2000 to 500 cm^{-1} at a resolution of 16 cm^{-1} and 64 co-added scans to achieve an acceptable balance of signal-to-noise.

3.2.1.4 X-ray Diffraction (XRD)

X-ray diffraction (XRD) is a non-destructive analysis technique, which provides detailed information on the crystallographic structure, and the chemical composition of the crystalline phases of materials. It works on the principle of constructive interference of monochromatic X-rays and a crystalline sample. A sample material is irradiated with incident X-rays and the scattering angles and intensities of the X-rays leaving the material are measured, revealing the crystalline structure of the sample.

More specifically, a monochromatic X-ray beam with a single wavelength, which is similar to the characteristic distance of the atomic spacings of the sample material, is directed towards said sample. When the incident X-ray beam encounters the crystal lattice of a sample, they are diffracted by atoms present in the lattice planes that are spaced at a given distance. In accordance with Bragg's Law, the diffracted waves undergo constructive interference, and a characteristic diffraction intensity is produced as a function of the scattering angle:

$$n\lambda = 2d.\sin(\theta)$$

where n is a positive integer corresponding to the order of the diffraction peak, λ is the angle of the incident X-rays, d is the lattice spacing, and Θ is the angle between the incident X-ray beam and the crystal lattice planes [152]. An illustration of Bragg's Law is shown in **Figure 3-6**.

The resulting diffraction pattern can be used for the identification of crystalline phases, typically analysed with reference to databases containing known patterns for specific phases [34].

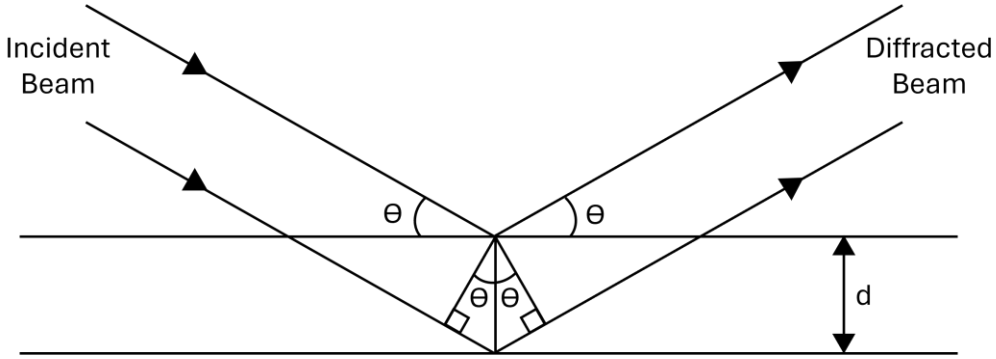

Figure 3-6 *Demonstration of Bragg's Law.*

Typically, quantitative XRD analysis is used to determine the phase composition of clinker and cement for quality control purposes. It is an advantageous tool that can be utilised to study phase changes during reaction and setting of binders in comparison to raw materials [34], [153], [154]. For AACs, XRD analysis is often used to identify the poorly crystalline C-A-S-H phase, secondary hydration phases in the form of gaylussite and zeolites, and calcium carbonates due to sample carbonation [69], [71], [155]. Diffractograms for alkali-activated binders have a distinctive diffuse scattering between 20 and 40° 2Θ, more specifically centred at ~29° 2Θ for high-calcium binder systems, indicative of the main binding phase within the material structural network [156], [157]. However, due to the primarily amorphous nature of alkali-activated binders, it is often used in conjunction with other analytical techniques, including FTIR and TGA, to verify findings.

XRD patterns of ground samples cured to specific time points were obtained use a PANalytical X'Pert^3 diffractometer operating in Bragg-Brentano geometry using a CuKα radiation source generated at 45 kV and 40 mA, which has been shown in the literature to be appropriate parameters when examining cementitious materials [154]. A scan from 5 to 70° 2Θ was used, with increments of 0.02° 2Θ and 2.2 s per step. Phase identification was carried out using DIFFRAC-EVA software and the ICDD PDF+4 database. For the sake of analysis, all diffractograms were normalised between 0 and 1.

3.2.1.5 Nuclear Magnetic Resonance (NMR) spectroscopy

NMR analysis involves detecting interactions between nuclei with intrinsic magnetic moments (i.e. non-zero spin) and applied magnetic fields. During an NMR experiment, a sample is held in a magnetic field (B_0), and pulses of radiofrequency radiation are applied to induce nuclear spin, where the electromagnetic response produced as the nuclei relax back to their equilibrium states is measured. This electromagnetic response is recorded as a free induction decay, which is converted to an NMR spectrum by the application of a Fourier transform. A spectrum contains characteristic resonances of near-neighbour atomic environments, as nuclei ca experience slightly different magnetic fields due to shielding from surrounding electrons. These resonance frequencies are denoted as a chemical shift (δ) relative to the known chemical shift on an external standard [42], [158].

For solids, NMR spectra are broadened due to the likes of dipolar interactions, anisotropy of the chemical shielding and quadrupolar interactions. As such, sample spinning methods must be applied to reduce broadening. The key method for this is magic angle spinning (MAS), by which a sample is spun at an angle of 54.74° relative to B_0, so that the dipolar interactions are suppressed and both chemical shielding anisotropy and first-order quadrupolar interactions are removed [42], [158], [159].

NMR allows the identification of local chemical environments of nuclei, irrespective of the crystallographic order of the material, which is ideal for the study of cementitious materials. In the application of cementitious materials, NMR is instrumental in determining reaction mechanisms and kinetics, and structural evolution to assess properties and performance of cements. And so, nuclei of interest included in alkali-activated slag binders are typically ^{1}H, ^{27}Al, and ^{29}Si [160].

Solid-state single pulse ^{27}Al and ^{29}Si magic angle spinning (MAS) NMR was conducted using a Bruker Avance III HD 500 spectrometer at 11.7 T with a 4.0 mm dual resonance cross-polarisation (CP) MAS probe producing a Larmor frequency of 130.32 MHz for ^{27}Al and 99.35 MHz for ^{29}Si. ^{27}Al MAS NMR spectra were acquired using a 1.7 µs nonselective ($\pi/2$) excitation pulse, a measured 5 s relaxation delay, a total of 512 scans, and at a spinning speed of 12.5 kHz. ^{29}Si MAS NMR spectra were collected using a 5.5 µs nonselective ($\pi/2$) excitation pulse, a spinning speed of 12.5 kHz, 60 s relaxation delay, and a total of 256 scans. The chemical shifts were compared to an external standard of 1.0 M $Al(NO_3)_3$ for all ^{27}Al spectra and pure tetramethylsilane (TMS) for all ^{29}Si spectra.

Gaussian peak profiles were used to deconvolute the ^{29}Si MAS NMR spectra. The minimum number of peaks possible were fitted, and the chemical shift and peak full width at half maximum (FWHM) of each resonance were required to be consistent across spectral deconvolutions for all samples. Peak intensities were required to be consistent with the structural constraints described by the "cross-linked substituted tobermorite model" (CSTM) for C-(N)-A-S-H phase products [161], so as to fit the following constraints:

$$Q^2(1Al) \geq 2Q^3(1Al)$$

$$Q^2 + Q^2(1Al) \geq 2(Q^3 + 2Q^3(1Al))$$

Six resonances were resolved and fitted using Gaussian peak profiles and the aforementioned constraints for tetrahedral Si sites within the C-A-S-H phase products, plus an additional resonance to account for the Si sites in remnant unreacted slag.

Using the CSTM in conjunction with ^{29}Si MAS NMR spectral deconvolutions, values for the mean chain length (MCL) and Al^{IV}/Si ratio of cross-linked C-(N)-A-S-H can be calculated using the following equations:

$$MCL_{crosslinked} = \frac{4[Q^1 + Q^2 + Q^2(1Al) + Q^3 + 2Q^3(1Al)]}{Q^1}$$

$$\frac{Al^{IV}}{Si} = \frac{Q^3(1Al)}{[Q^1 + Q^2 + Q^2(1Al) + Q^3 + 2Q^3(1Al)]}$$

3.2.1.6 Scanning Electron Microscopy with Energy Dispersive X-ray Spectroscopy (SEM-EDX)

SEM-EDX is a non-destructive analytical technique for chemical characterisation of a material at the micro scale via elemental identification and quantitative compositional data. SEM utilises a focused beam of electrons to produce high-resolution, magnified images of a samples surface topography, while EDX analysis is used to acquire the composition of a sample.

A stream of electrons is generated via an 'electron gun' and is then accelerated and focussed using a serious of electromagnetic lenses. This focused electron beam is then directed onto the surface of the sample, where several interactions can occur and a signal is generated based on the type of interaction undergone. When electrons undergo inelastic scattering, a resulting emission occurs of secondary electrons, backscattered electrons (BSE), and characteristic energy dispersive X-rays (EDX). In this study, the examination of BSE and characteristic X-rays are used for characterisation.

BSEs are the result of elastic collisions, where the electrons have been scattered back from within the sample. Their signals can distinguish materials by atomic number, and they are used to generate images with compositional contrast; brightness in BSE images corresponds to the

intensity of electrons, which is proportional to atomic number and material density. Additionally, an X-ray detector can be used to collect characteristic X-rays emitted from the specimen due to electron excitation and the corresponding EDX energies can provide semi-quantitative analysis on the elemental composition of the specimen. This can be displayed as elemental maps, line scans, or point analysis data.

In terms of cement chemistry, SEM-EDX provides vital information for quality control, including the degree of cement hydration by determining the formation and distribution of hydration products, homogeneity of the phase structure, and homogeneity of the cement. Additionally, this technique can be used to assess structural evolution of cementitious materials, including information on mineral phases in paste, pores, and cracks, morphology of phases, phase assemblage, and chemical composition of mineral phases [162]–[164].

BSE-SEM was conducted using a low vacuum benchtop Hitachi TM3030 coupled with an integrated Bruker Quantax 70 EDX detector, at an accelerating voltage of 15 kV and working distance of 8.5 to 9 mm. Sample preparation involved mounting hardened cement paste samples in epoxy resin, followed by grinding and polishing to a 0.25 μm finish using a diamond suspension. The polished surface was carbon coated prior to analysis.

Visual observation of the EDX spectra for each sampling point showed that for all spectra, the signal-to-noise ratio was sufficiently high that the noise could be considered negligible relative to the signal. EDX data were post-processed using the Quantax 70 software, where an evenly distributed selection of EDX data points across an 8 x 6 grid (48 points) were acquired for all samples. The EDX data points were normalised so that the sum of all elements observed at a single point equalled 100 mol%.

3.2.1.7 Compressive Strength Measurements

Compressive strength of selected alkali-activated cement pastes was determined after 7 and 28 days curing, according to amended ASTM C109 [165]. Slight deviation from this standard was followed, as cement paste samples were used rather than mortars, i.e. no sand was added to the mixture.

Cement pastes were mixed using a planetary mixer for 10 minutes before being transferred to 50 mm cube moulds, sealed, and placed in a curing chamber at 20 °C. Once hardened, usually after 24 hours, specimens were demoulded, resealed, and stored in the curing chamber until testing age.

A Controls Automax 5.0 uniaxial frame was used with a loading rate of 1250 N per second. Cubes were placed between the parallel plates with the "trowelled" or top-cast surface facing to the side of the instrument, to ensure the same orientation and for an even side-cast surface to meet the parallel plate. Strength values at each curing age were taken in triplicate and a mean value reported with a calculated standard deviation.

3.2.2 Fresh State Characterisation Methods

3.2.2.1 Isothermal Conduction Calorimetry (ICC)

Isothermal conduction calorimetry (ICC) is a test method designed to measure the heat production rate during reaction processes, including dissolution, hydration, and phase changes. The heat generated during the chemical reactions flows rapidly through a thermal conductor to a heat sink, which is maintained at a constant temperature, is recorded and then compared to an analogous reference sample running in parallel [166], [167].

ICC is a sensitive and versatile tool used to study the hydration process of cement, due to these reactions being highly exothermic in nature. The instrument allows the continuous monitoring

of heat generation, showing the reaction mechanisms, as well as reaction rates in the different phases, of the cement hydration process. By monitoring the heat evolution of cement during its formation, this method can be used, for example, to determine reaction kinetics, investigate the effect of contaminants and/or admixtures, explore temperature dependencies, and for quality control.

In this study, the TAM Air Isothermal Calorimeter was used, maintained at a constant temperature of 20 °C, to follow the heat output of the cement pastes for up to 150 hours. The cement paste was prepared following the above mixing procedure, before 20 g of sample was transferred to a glass ampoule and into the calorimeter. A reference of deionised water was used in a quantity equivalent to the mass of water in the cement paste sample. All values of heat flow are normalised by the mass of cement paste.

3.2.2.2 Diffuse Reflectance Infrared Fourier Transform Spectroscopy (DRIFTS)

Time-resolved data provide continuous information on a reacting system with no sample preparation (solvent exchange, drying, grinding, etc.) beyond initial mixing. The likes of isothermal calorimetry takes continuous measurements, allowing an overall insight into reaction kinetics, however, it is difficult to discern specific mechanisms – dissolution and precipitation – that can occur simultaneously during reaction. As such, using a technique like FTIR on a time-resolved basis will allow the study of reaction mechanisms *in situ*, through the tracking of changes in bond environments within consumed raw materials and precipitated reaction products over time.

Diffuse reflectance infrared Fourier transform spectroscopy (DRIFTS) is a type of FTIR spectroscopy, relying on scattering of infrared light within the sample. Within the spectrometer, an infrared beam strikes the sample, where three things happen: some of the beam is reflected,

some of the beam is absorbed in the sample and lost, and the remainder of the beam is transmitted into the sample. During the latter, the beam that scatters within the sample, then returns to the surface, and the light energy is diffusely reflected. This scattered light is then directed to an infrared detector, and the resulting data is processed into a spectrum. DRIFTS is typically used for analysis of powder samples or samples that are not easily analysed using traditional transmission methods, including those with rough surfaces and the likes of fibres [168].

Despite its typical uses, DRIFTS was used in this study as an *in-situ* technique to study the initial reactions of alkali-activated cement pastes by following the changes in bond environments with time. The Thermo Scientific™ Nicolet™ iS™ 5 FTIR Spectrometer was used with a PIKE EasyDiff attachment to measure IR spectra across a range of 2000 to 500 cm^{-1} at a resolution of 16 cm^{-1} and 64 co-added scans to achieve an acceptable balance of signal-to-noise. Samples were mixed and promptly loaded into a sample crucible and onto the spectrometer, and spectral scans were measured every 2 minutes for the first 2 hours after mixing.

Early-age changes in bond environments are essential for identifying the specific initial reaction mechanisms for sodium carbonate-activated slag binders, which has been proposed as a preferential reaction inducing the characteristic long induction period of the binder in previous studies [69], [71]. The intervals for DRIFTS spectra measurements were chosen to align with the initial heat release identified in calorimetry data for sodium carbonate-activated slag binders in this study, where the initial reaction peaks at ~2 hours.

3.2.2.3 XRD *in situ*

As previously mentioned, X-ray diffraction is a useful tool that can evaluate phase composition of cement samples, aiding in the identification of reaction products and structures over different curing ages. Also previously mentioned, time-resolved measurements from various analytical techniques can aid in the understanding of reaction mechanisms of cement hydration.

Typically, XRD is conducted on solid-state samples, and the parameters used for such powder samples in this project, mean a total scan time of ~2 hours per sample. However, to study reaction mechanisms *in situ*, a shorter total scan length is required, as reaction kinetics of cement suggest dissolution and precipitation of reaction products occur simultaneously at very early age, i.e. in the first few hours. As such, synchrotron XRD has been used successfully in recent years for the *in-situ* analysis of cement reactions [169]–[171], however, the limited existence of synchrotron facilities worldwide means high expenses and thus, limited access. Consequently, lab-scale diffractometers are more affordable and readily available and can also provide *in-situ* measurements.

The range of 2Θ was shortened and time per step size decreased to reduce overall scan time in order to effectively follow the reaction mechanism *in situ* while maintaining a suitable noise level to determine key phases. A range of 11 to 35° 2Θ was identified as of interest for key reaction products, including some calcium and sodium-calcium carbonates as well as the broad amorphous feature attributed to C-A-S-H, and time per step size was reduced to 1.0 s, meaning a total scan time of 15 min. To ensure a balance between scan time and noise was achieved as well as a suitable 2Θ range selected, a previously XRD-characterised powder sample was measured using these new scan parameters, which is shown in **Figure 3-7**.

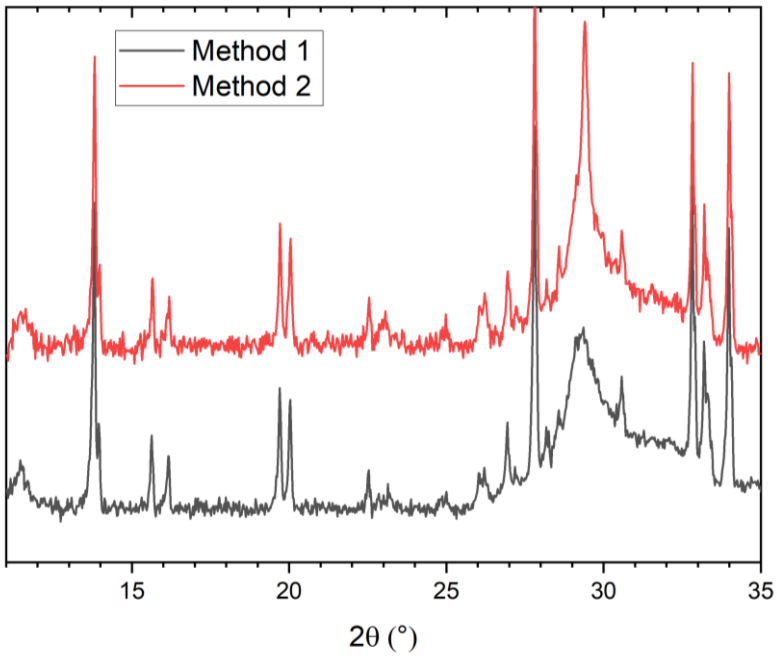

Figure 3-7 *Comparison of methods for XRD data acquisition, where 'Method 1' is the typical scan parameters used for powder analysis (0-70° 2Θ and 2 hours), and 'Method 2' is the shortened scan for in-situ measurements (11-35° 2Θ and 15 mins). N.B. the same sample was used for this test, however, when testing for 'Method 2', the sample age meant that carbonation had occurred during storage, hence the more crystalline feature at ~29° 2Θ.*

Alkali-activated cement pastes were mixed following the previously mentioned mixing procedure and transferred to a sample holder promptly. The paste was contained between 2 pieces of Kapton polyimide film to prevent any interference from the sample holder or the air. The use of this film results in a broad amorphous hump centred around ~20° 2Θ, however, crystalline structures around this 2Θ value are still identifiable.

3.2.2.4 Mini Slump Tests

A mini slump test is a fast, simple, and widely used method for assessing the workability of cementitious pastes in the fresh state. Typically for a slump test, a conical mould is filled with the testing material (cement), and then the mould is lifted to assess how the material flows. Neglecting inertial effects, the cement will flow once the mould is lifted and will stop flowing when the shear stress due to flow under gravity decreases to the value of the yield stress of the material [172], [173].

A mini slump test was conducted on fresh alkali-activated cement pastes immediately after mixing to determine the workability. A downscaled Abrams cone with a height of 57 mm, and internal top and bottom diameters of 19 and 38 mm, respectively, was used during the mini slump test. The slump cone was placed on a flat sheet and filled with fresh cement mixture, before the cone was then lifted as slowly as possible (< 1 cm/s). Flow diameter was measured using vernier callipers in two perpendicular directions, and tests were performed in triplicate, with a mean value of diameter and standard deviation calculated for each sample studied.

3.2.2.5 Rheology Measurements

With regards to cementitious systems, rheology is a measure of the yield stress and flow characteristics of the material, which can also be referred to as the workability of the paste. A rheometer can be used to measure how a viscous fluid responds to applied forces, thus providing an insight into stress-strain relationships to understand the flow and deformation properties of the material. Workability is an important characteristic relating to the fresh-state utilisation of cement pastes, including for the transportation, pouring, pumping, and shaping of the binder, and as such, rheology can be used to understand structural properties and performance of the material.

In this project, the acquisition of a shear rate vs shear stress curve allows one to see whether a paste undergoes Newtonian or non-Newtonian behaviour, as well as its yield stress [174]. Additionally, cement pastes have also been shown to display shear thinning or thickening behaviour [117], [175]. These behaviours are demonstrated in **Figure 3-8**.

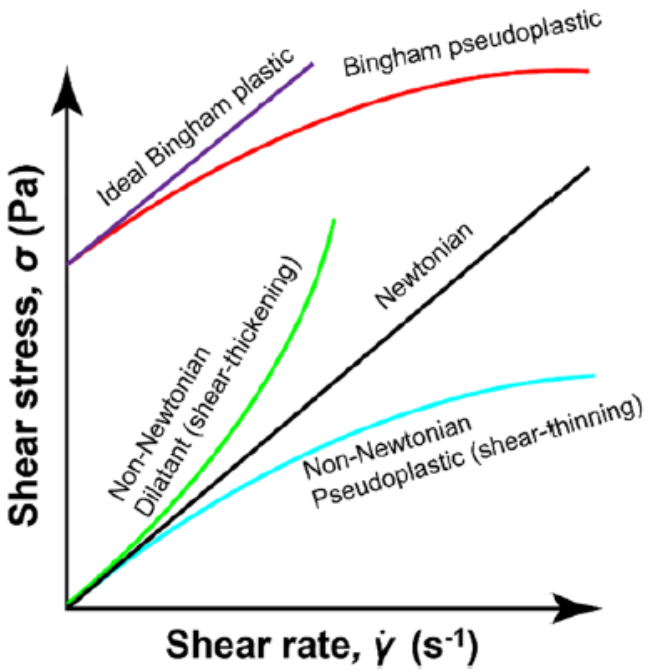

Figure 3-8 *Standard shear stress vs shear strain curves showing ideal pastes and fluid behaviours, taken from [176].*

Rheological behaviour of each sample was assessed using a six-blade vane coupled to a Thermo Scientific HAAKE Viscotester 550 to undertake plastic viscosity analysis, starting immediately after mixing had ceased. Data for processing was collected from the decreasing oscillating frequency curve, from 100 s^{-1} over a 60 s period. Working on the decreasing shear rate of flow curve allows for the minimisation of errors. If working with an increasing frequency from a stationary elastic fluid, then as the strain is applied, the inertia is high, and therefore, measurements would also include force required to overcome this inertia. Additionally, the Herschel-Bulkley model – a generalisation of the Bingham and power law models – was applied to the descending shear rate curve, and this is presented as an overlay to the measured data. The Herschel-Bulkley model is described via the following equation:

$$\tau = \tau_0 + k\dot{\gamma}^n$$

Where τ is shear stress, τ_0 is the yield stress, k is the consistency, $\dot{\gamma}$ is the shear rate, and n is the flow index. When n is equal to 1, the material follows Bingham plastic behaviour, and when greater than or less than 1, the material follows shear thickening or shear thinning behaviour, respectively.

3.2.2.6 Setting Time Measurements

Vicat apparatus is used to measure consistency and thus setting times of concrete, mortar, and cement paste, in accordance with BS EN 196-3 [177]. The setting time is indicative of the final phase of the cement hydration reaction, as well as the material's workability [178].

The Vicat method was used to acquire values for initial and final setting times of fresh alkali-activated cement pastes during this project, using a Matest VICATRONIC apparatus equipped with a 1.13 mm-diameter needle. Fresh pastes were transferred immediately after mixing into a conical frustum mould of height 40 mm, and top and bottom internal diameters of 60 and 70 mm, respectively.

The initial setting time was determined as the point when the distance from the base plate and the needle is 6 ± 3 mm. This point is noted as being when the cement paste starts to lose its plasticity and begins to stiffen; the paste is no longer workable and difficult to re-mix. The final setting time was recorded when the sample cannot be penetrated by more than 0.5 mm. This time is when the cement has completely lost its plasticity and has gained sufficient stiffness; the cement paste has fully transitioned from a fluid to solid state and can now resist external pressure.

Chapter 4: Sodium Silicate-activated Slag Binders – Control Sample

4.1 Introduction

Alkali silicates are one of the most commonly used agents for the alkali activation of slag and other aluminosilicates (fly ash and metakaolin), due to their high pH resulting in the quick onset of reaction after mixing, the subsequent sufficient hardening and setting, and a resulting structure similar to that of Portland cement with comparable strength values. Such alkali-activated slag cements have been used in China, Eastern Europe, Scandinavia, and the former USSR [92], [129]–[131].

Problems have been noted with the use of sodium silicate for use in AACs, with very short setting times and subsequent shrinkage observed [92], [179]. Additionally, the strong alkalinity in combination with their viscous nature means these activators are often difficult to handle safely beyond a laboratory setting [92], [129]. Furthermore, these alkali salts possess a higher-than-desired carbon footprint due to the energy consumption and CO_2 output during their production; they are produced from carbonate salts and silica via calcination, followed by dissolution in water [44], [56]. However, due to the relatively low content (by mass) of activators in the majority of AAC systems, the rate of carbon emissions induced by calcination during the production of silicates is much lower per tonne of binder than that of Portland cement production [180], [181].

The aim of this chapter is to assess the performance of a sodium silicate-activated slag binder and understand how the formulation chemistry has influenced the reaction kinetics and mechanisms, microstructure, and fresh-state and physical properties. This formulation will act

as a control sample by which further formulations are compared to due to its known functionality.

4.2 Methodology

Blast furnace slag was reacted with sodium silicate solution ($SiO_2/Na_2O = 1.0$) to form cement samples for either immediate fresh-state testing or cured for solid-state characterisation at various time points. The sample formulation has been defined in *Chapter 3* and is detailed in **Table 4-1**.

Table 4-1 *Sample formulation used herein this chapter, acting as a control for further samples to be compared to.*

No.	Sample Name	Activator	BFS (g)	Activator Na_2O (g)	Additive	Additive mass (g)
1	**BFS_8%_SiO_3**	Na_2SiO_3	100	8	--	--

The reaction rate and mechanisms were determined using time-resolved data from isothermal calorimetry, and DRIFTS and XRD measurements taken *in situ* immediately after mixing. Additional fresh-state characterisation was performed – mini slump testing and viscometry – to understand the workability of the paste, while further physical properties, setting time and 7- and 28-day compressive strength, were also determined. Furthermore, the phase assemblage and structural evolution were determined via FTIR spectroscopy, TGA, XRD, ^{27}Al and ^{29}Si MAS NMR spectroscopy, and SEM-EDX analysis.

4.3 Results and Discussion

4.3.1 Reaction Mechanisms and Kinetics

As indicated in **Figure 4-1**, the heat evolution of the silicate-activated slag binder follows four distinct stages of reaction, similar to that observed in the hydration reaction of PC. The pre-induction period is observed as an initial high heat in the first few hours of reaction, which

corresponds to the surface wetting and initial dissolution of slag particles. In this study, these data are not a true representation of the heat evolution during the first 10 minutes of reaction, due to the mixing of the samples outside of the calorimeter. Instead, there is a large heat of reaction at the offset, representing this initial dissolution period. The pre-induction period is then followed by a dormant stage, where there is a very low rate of heat release, which is associated with the progressive dissolution of slag particles as well as some initial condensation and precipitation of reaction products. Following this, a second, more significant stage of heat release ensues, consistent with the acceleration period of cementitious binders, indicative of the nucleation, growth, and precipitation of a great amount of reaction products. Finally, a deceleration period occurs, where the reaction rate gradually slows after setting [62], [100].

As is expected, the silicate-activated slag reacts quickly, with a very short dormant period observed after dissolution and the main reaction occurring within 20 hours in **Figure 4-1**. Additionally, the significant degree of cumulative heat output demonstrates the likely great extent of the reaction – high amounts of structurally ordered reaction products. This aligns with the known advantageous quick reaction and setting of binders activated with alkali silicates.

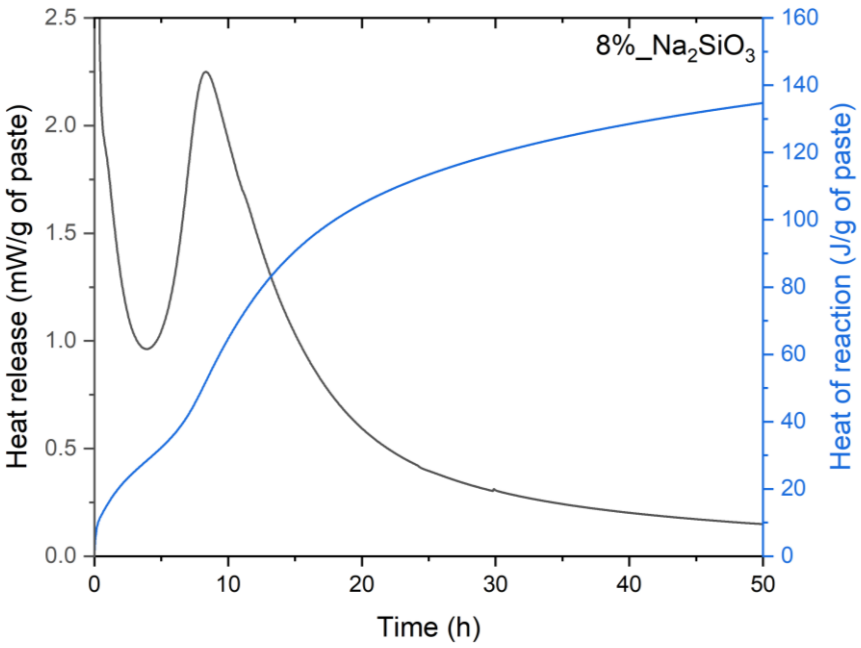

Figure 4-1 *Heat release rate and heat of reaction of sodium silicate-activated BFS.*

During the initial dissolution of slag particles, the sodium silicate solution dissociates into its ions, and further (with the reaction of water) into silicate species and hydroxide ions, which disperse in the bulk structure between slag grains. As there is little dormancy observed in the calorimetry data, it is expected that the nucleation and precipitation of reaction products occurs quite rapidly following dissolution. Sodium silicate typically favours the rapid formation of an aluminium-rich calcium (sodium) aluminosilicate hydrate, with hydrotalcite forming as a secondary product [58], [83], [182].

DRIFTS spectral measurements were collected *in situ* in 2-minute intervals during the initial 2 hours of reaction after mixing to aid in the understanding of the reaction mechanisms and kinetics of the sodium silicate-activated slag binder. Similarly to ICC data, the very early dissolution reaction occurring in the first 10 minutes during mixing cannot be observed as this was performed outside of the DRIFTS setup.

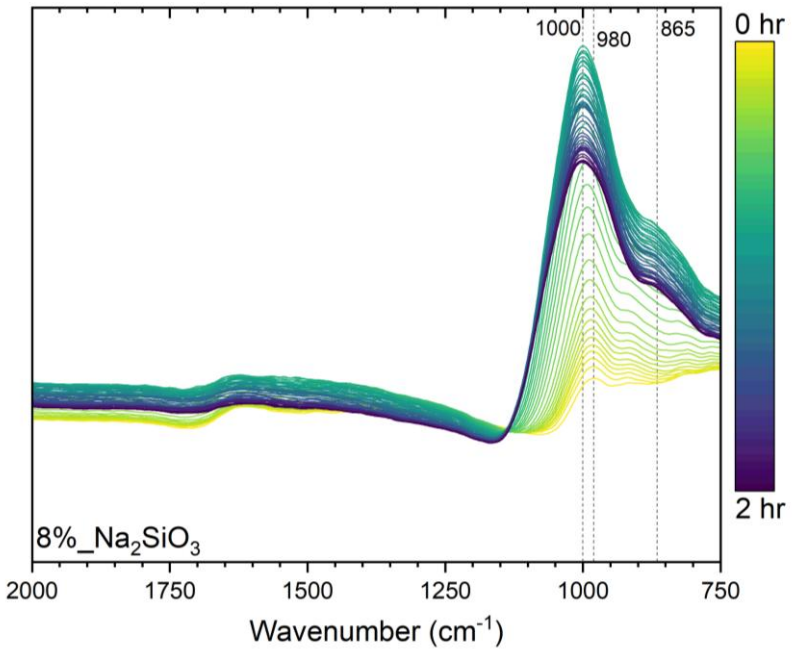

Figure 4-2 *DRIFTS spectra of sodium silicate-activated BFS over the first 2 hours of reaction.*

Figure 4-2 shows an initial low-intensity peak at ~980 cm^{-1}, attributed to asymmetric stretching of Si-O-T bonds (where T represents tetrahedral Si or Al). Quite rapidly over time, this peak shifts to a higher wavenumber and increases in intensity, centring at ~1000 cm^{-1}, maintaining in the attributed range of Si-O-T bonding. The initial lower wavenumber aligns with Si-O-Al, likely from the precursor slag particles, and the upwardly shifted wavenumber equates to a stronger bond interaction within Si-O-Si within the C-A-S-H structure [53], [133]. Due to the slightly broader nature of this peak, its span across a range of wavenumbers encompassing the asymmetric stretching of T-O-T bonds, and the varying intensity (increase then decrease), it is likely that this is likened to an isosbestic point, i.e. the breaking of T-O-T bonds during the dissolution of slag particles is occurring simultaneously with the formation of different T-O-T bonds within aluminosilicate reaction products.

Furthermore, a shoulder to the T-O-T peak, centring at ~865 cm^{-1}, can be seen developing over time at a similar rate to the main peak, which is attributed to the asymmetric bending of C-O

within calcium carbonate [135], [136], [183]. The existence of this peak is likely due to atmospheric carbonation – CO_2 in the air infiltrating the pore matrix of the bulk and reacting with calcium ions from the slag – as the sample surface is exposed to the atmosphere in the DRIFTS setup, and no carbonate ions are supplied in the formulation chemistry of the sample.

XRD patterns were collected every 15 minutes for the first couple of hours of reaction post-mixing to further probe the mechanisms of reaction for silicate-activated BFS binders (**Figure 4-3**).

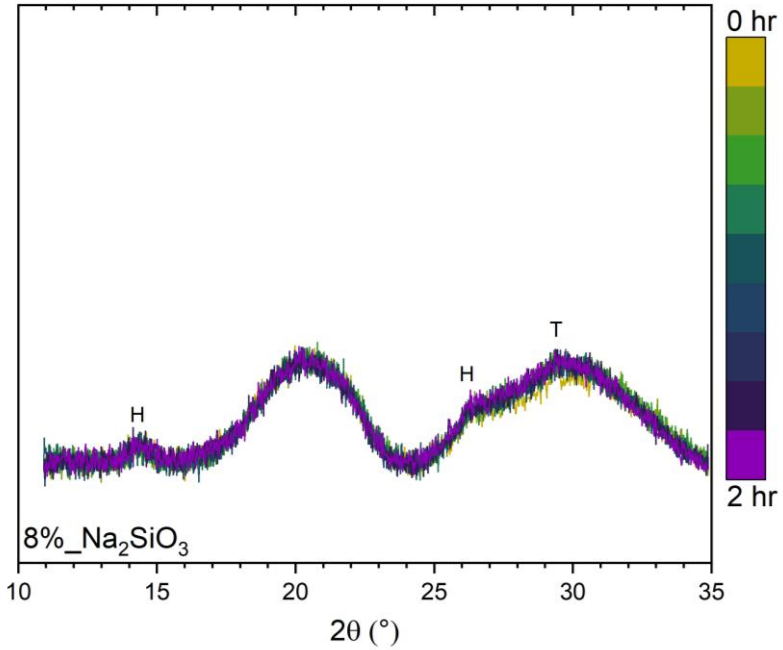

Figure 4-3 *XRD pattern of silicate-activated BFS over the first 2 hours of reaction, with identified phases labelled: H – Hydrotalcite (PDF 01-088-9171), and T – Tobermorite (PDF 04-014-8455).*

Generally, the sample presents as predominantly amorphous in structure, with few to no crystalline phases present. The broad hump observed due to diffuse scattering centred at ~20° 2Θ is attributed to the polyimide – an amorphous polymer – film encompassing the paste sample within the diffractometer, to eliminate interactions with the air. Besides this, a second broad hump is observed, centred at ~30° 2Θ, indicative of an alumina/silica phase, more

specifically a tobermorite-like structure (C-A-S-H). Additionally, small increases in intensity can be seen at points corresponding to the existence of hydrotalcite from an early age.

4.3.1.1 Summary

The time-resolved data obtained from ICC, DRIFTS, and XRD neatly describe the reaction kinetics and mechanisms of the sodium silicate-activated during early age curing. It is observed that the formation of key hydration phases, C-A-S-H and hydrotalcite, is occurring rapidly and almost simultaneously with the dissolution of the slag particles, during the initial few hours of reaction. The main reaction is reaching its peak at ~10 hours and decelerating over the following 10 hours into a period of continuous reduced reaction over its lifetime. The formation of somewhat structurally ordered C-A-S-H – the main binding and strength-giving phase within AACs – at such an early age in theses silicate-activated slag cements suggests the efficacy of such materials as a replacement to traditional Portland cement.

4.3.2 Structural Evolution

4.3.2.1 ATR-FTIR

ATR-FTIR spectra were measured for silicate-activated slag samples at different curing ages to identify bond environments and explore phase evolution during curing. In **Figure 4-4**, it is noted that the spectra show minimal changes, agreeing with, not only the fast rate of reaction, but also the great extent of reaction from an early age occurring in silicate-activated slag systems.

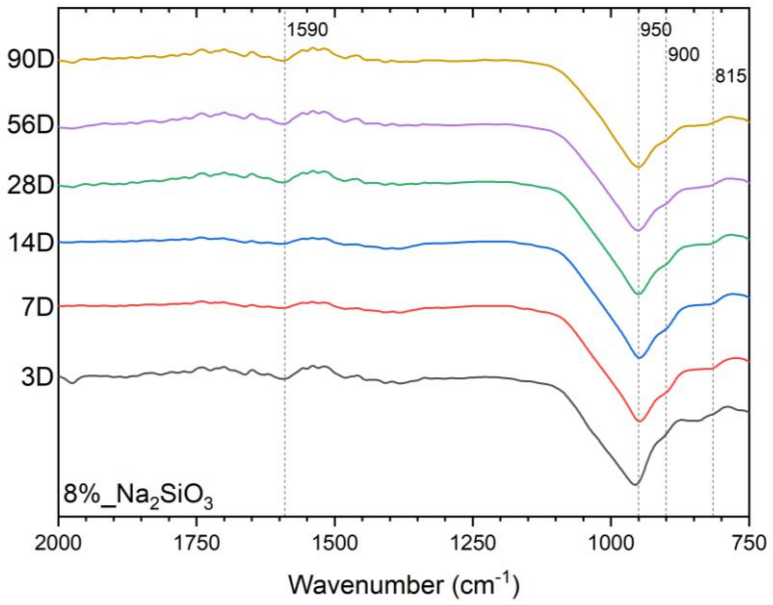

Figure 4-4 *FTIR spectra of sodium silicate-activated BFS at various time points.*

A shallow, but notable, band is observed at ~1590 cm^{-1}, a characteristic vibration for C-O in the calcium carbonate polymorph, vaterite [184]. Additionally, the shoulder peak at ~900 cm^{-1} is associated with the out-of-plane bending of C-O in calcite, another calcium carbonate polymorph [135], [136], [185]. This shoulder becomes more prominent over time, owing to an increased level of carbonation proportional with curing age. The existence of these calcium carbonates in the sample set is associated with atmospheric carbonation – carbon dioxide from the atmosphere infiltrating the sample and reacting with calcium hydroxide in the sample – during preparation and curing.

The most prominent peak observed in all spectra at ~950 cm^{-1} and the smaller peak at ~815 cm^{-1} are attributed to the asymmetric stretching of Si-O-T bonds, specifically Q^2 and Q^1 sites, respectively, indicative of the presence of a C-A-S-H structure [53], [133], [134]. An increased wavenumber represents increased polymerisation and crosslinking within the phase, and typically a sharp peak indicates that a greater structural ordering of C-(A)-S-H evolves as the reaction proceeds [53], [183]. It is noted that the presence of both of these peaks is observed at

the earliest curing age (3 days), with no notable change over time; the peak at ~950 cm^{-1} maintains its sharpness and the band at 815 cm^{-1} holds its low intensity over time, indicating the existence of the C-A-S-H phase from an early age, further supporting the high rate of and extent of reaction associated with silicate-activated BFS.

4.3.2.2 TGA

Thermogravimetric analysis (TGA) was undertaken with the aim of quantifying the extent of reaction by identifying and quantifying reaction products present in the sodium silicate-activated slag binder at different curing ages. Generally, increasing overall mass losses were observed at longer curing ages (26.6, 25.9, 25.3, 27.5, and 30.8 wt.% at 3, 7, 14, 28, and 90 days, respectively) in **Figure 4-5**, indicative of an increasing extent of reaction, i.e. more reaction products are forming.

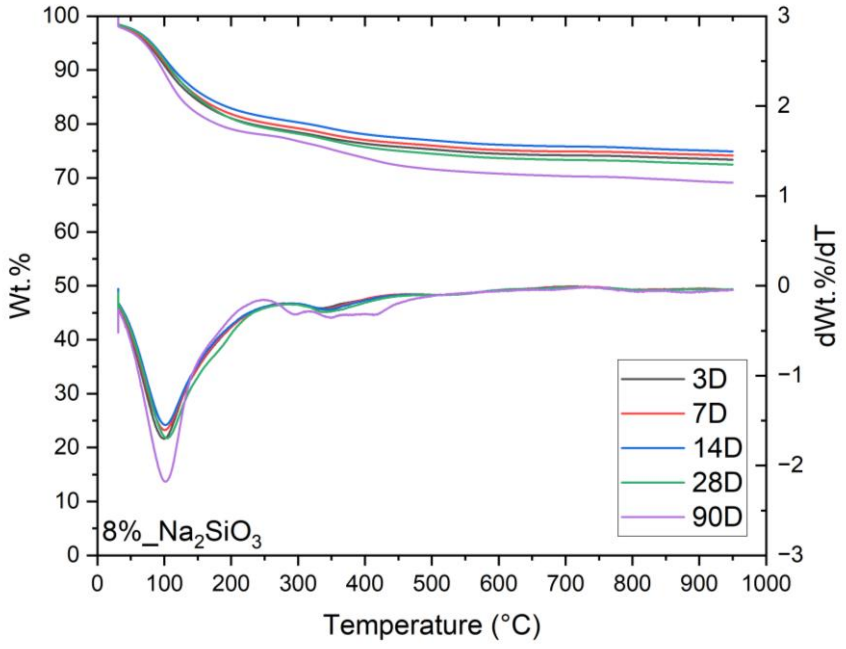

Figure 4-5 *TG/dTG trends of sodium silicate-activated BFS, cured for various lengths of time, as labelled.*

The first observation from the TGA curves is that there is a mass loss of up to 20 wt.% between 60 and 200 °C for all curing times, generally increasing with age. This is in agreement with

associated mass losses from loss of free or slightly bound water from the calcium aluminosilicate hydrate (C-A-S-H) [186], [187]. A shoulder to the aforementioned mass loss peak is observed for the 28- and 90-day old samples at ~170 °C, which is attributed to the first stage of thermal dehydration of hydrotalcite [188], [189]. Additionally, the mass loss between 300 and 500 °C, observed for each curing age, is attributed to the loss of chemically bound water in and dehydroxylation of hydrotalcite-type phases [186], [188], [190]. The increased total mass loss, as well as the observation of multiple mass losses, during this temperature profile for the 90-day sample is likely due to the existence of more strongly bound reaction products, consistent with the increased extent of reaction. Furthermore, a notable mass loss is visible in the region 250-350 °C, associated with the presence of katoite (a calcium aluminium garnet) and/or other hydrous calcium aluminate phases [188], [191]. In the region of 500-700 °C, there is a progressive but notable mass loss, attributed to the continuing dehydration of the C-S-H type phase and dehydroxylation of the hydrotalcite phases [186], [188]. A final progressive but minor mass loss can be observed between 700 and 900 °C, which is likely due to the decomposition of calcium hydrates [186], as well as being associated with the decarbonation of some calcium carbonates – calcite, vaterite, and aragonite – which are likely present due to atmospheric carbonation of the sample [188], [192], [193].

4.3.2.3 XRD

Similarly to the ATR-FTIR spectra, there is little to no change in structure over time in the XRD patterns for the silicate-activated slag binder (**Figure 4-6**), indicative of stable, structurally ordered phase development at an early age. There is a broad hump observed, centred at ~30° 2Θ, indicative of an alumina/silica phase, more specifically a tobermorite-like structure (C-A-S-H), as well as few sharp, crystalline phases, demonstrating the primarily amorphous structure of AACs utilising silicates as an alkali activator. The diffractograms also reveal additional tobermorite peaks, as well as some amounts of hydrotalcite, with small

amounts of calcite appearing over time. The presence of tobermorite-like C-A-S-H and hydrotalcite from the earliest curing age (3 days) with little change over time further suggests that the bulk of the main reaction has occurred by this time point and that these reaction products have strongly formed. The occurrence of the calcium carbonate polymorph, calcite, and its slight increase in intensity over time, again indicates that atmospheric carbonation has ensued during sample preparation and curing, where CO_2 in the atmosphere has penetrated the sample and reacted with $Ca(OH)_2$ in the bulk to form calcium carbonate.

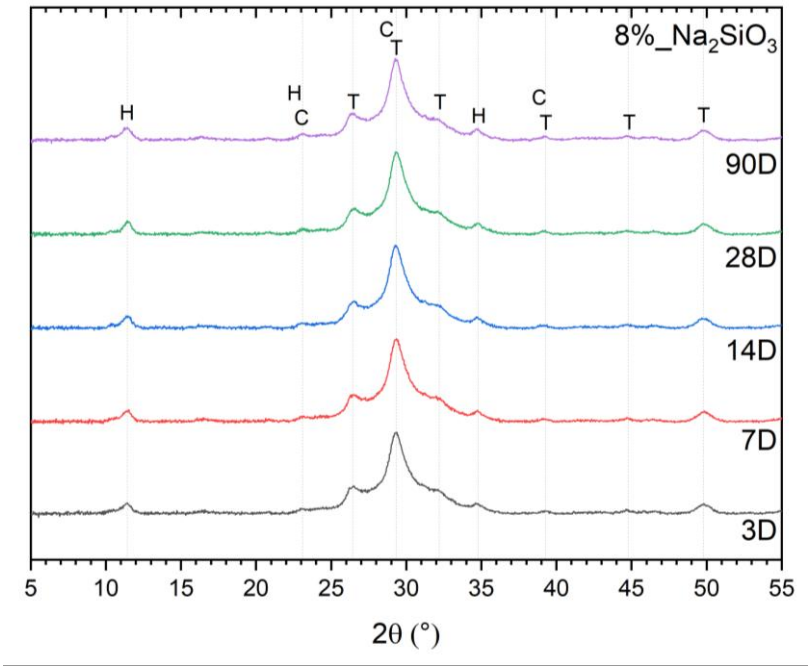

Figure 4-6 *XRD patterns of silicate-activated BFS, at various curing times, as labelled. Phases identified have been labelled: C – Calcite (PDF 00-066-0867), H – Hydrotalcite (PDF 01-088-9171), and T – Tobermorite (PDF 04-014-8455).*

4.3.2.4 NMR

Solid-state ^{27}Al and ^{29}Si magic angle spinning (MAS) nuclear magnetic resonance (NMR) spectroscopy are used to reveal how the nanostructure, cross-linking, and local hydration of C-(A)-S-H in silicate-activated slag cements evolves over time.

4.3.2.4.1 ^{27}Al MAS NMR Spectroscopy

The ^{27}Al MAS NMR spectra in **Figure 4-7** displays a broad tetrahedral Al resonance spanning from 80 to 60 ppm, containing contributions from multiple Al sites, for all curing ages for the silicate-activated slag binder sample, indicative of the formation of C-A-S-H phases. Here, a narrower resonance represents a greater degree of polymerisation as the reaction proceeds with time. Signals at δ_{obs} = 74 and 68.4 ppm represent Al in well-defined Al^{IV} coordination and incorporated in bridging tetrahedra, q^2(I) and q^2(II), respectively, whereby Al tetrahedra are bonded to Q^2(1Al) Si sites [58].

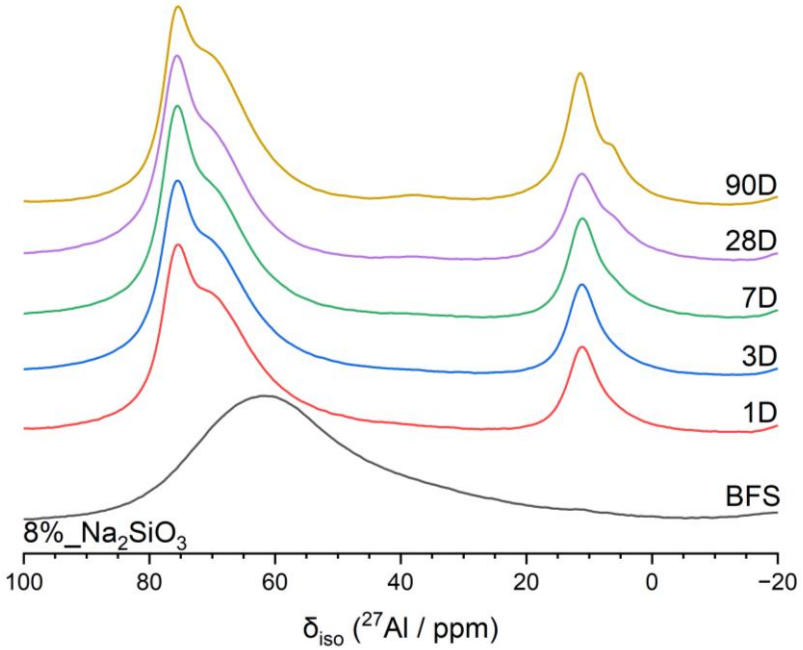

Figure 4-7 *^{27}Al MAS NMR spectra of BFS and sodium silicate-activated BFS at various curing times, as marked.*

Additionally, a broad octahedral Al resonance spanning from 20 to 0 ppm is observed, also containing contributions from multiple Al sites. The signal at δ_{obs} = 11 ppm corresponds to two Al^{IV} environments in octahedral formation within hydrotalcite group compounds [194], [195], evidencing the formation of such products, consistent with the TGA and XRD data. Furthermore, a signal at δ_{obs} = 5 ppm is observed as growing at longer curing ages. This signal

is typically attributed to a "third aluminate hydrate" (TAH), an amorphous nanoscale aluminate hydrate phase precipitated at the surface of C-(N)-A-S-H in calcium-rich binders, including alkali-activated slag binders [16], [188], [194], [196], however, recent studies utilising one- and two-dimensional dynamic nuclear polarisation-enhanced MAS NMR experiments accredited this resonance to silicate-bridging $[AlO_2(OH)_4]^{5-}$ sites in C-A-S-H and suggested that TAH does not exist [197]. This latter attribution is based on atomistic simulations, and so, this resonance may still resemble an amorphous aluminate phase on the C-A-S-H surface, interacting with nearby Q^1 silicate sites.

Moreover, a slight broad resonance spanning 40 to 30 ppm is observed, consistent with a pentahedral Al, tentatively assigned to a charge-balancing species within C-(N)-A-S-H interlayers [194]. The existence of this Al^V within the C-A-S-H interlayer has been hypothesised in the literature [196], [198], [199], however, the current structural model of C-A-S-H does not include this species [161]. The observation of a new ^{27}Al MAS NMR resonance associated with an Al^V environment whose intensity cannot solely be attributed to remnant anhydrous slag particles is possible here, as this signal is observed only at longer curing ages, i.e. typically there are fewer remnant slag particles as reaction time increases. The intensity of Al^V increasing as a function of curing time in this study is consistent with experimental ^{27}Al MAS NMR spectra of AAS cements [194], [200], [201], lab-synthesised C-(N)-A-S-H gels [198], [199], and hydrated PC-based materials [196], [202], [203].

The existence of this Al^V environment has also been observed by ^{27}Al multiple quantum MAS NMR analysis of synthesised C-(N)-A-S-H gels, where the relative amount of this Al^V environment within the C-(N)-A-S-H was noted to increase with increasing Al content. They hypothesised that the structural limitations on the amount of aluminium substitution into

tetrahedral sites within aluminosilicate chains of the C-(N)-A-S-H means an excess aluminium content results in increased charge-balancing Al^{V} species in the interlayer [204].

In this study, it is possible that there is an increased substitution of Si for Al in the aluminosilicate chains in C-(N)-A-S-H over time due to the high activator SiO_3^{2-} content and an increase in excess Al species means availability for charge-balancing. Spectral deconvolutions of ^{27}Al MAS NMR spectra and ^{27}Al MQ_MAS NMR data would aid in this confirmation.

4.3.2.4.2 ^{29}Si MAS NMR Spectroscopy

On the other hand, ^{29}Si MAS NMR spectra in **Figure 4-8** reveals a broad hump centred at ~73 ppm due to unreacted anhydrous slag (more specifically δ_{obs} = -71 and -74 ppm attributed to Q^0 and Q^1 sites in slag, respectively) is present at all curing ages and generally lessens over time, indicating extent of reaction increasing with increasing curing time, as expected. There are three main resonances between -75 and -85 ppm that are all present at each time point however in different coordination. These resonances, δ_{iso} = -78.6, -81.4, and -84.4 ppm, are attributed to Q^1(I), Q^2(1Al), and Q^2 units, respectively, indicating the formation of a C-A-S-H phase with a tobermorite-like structure, more specifically a sodium and aluminium substituted calcium silicate hydrate (C-(N)-A-S-H) phase [58], [161], [205], consistent with previous observation for sodium silicate-activated slag cements [188]. A general increase in Q^2 sites relative to Q^1 sites over time is observed, indicative of an increased degree of polymerisation within the C-A-S-H. Additionally, a signal at δ_{obs} = -87 ppm is visible at older curing ages, which is attributed to Q^3(1Al), demonstrating the significant extent of cross-linking in the C-(N)-A-S-H structure for sodium silicate-activated slag binders, as observed in previous studies [96].

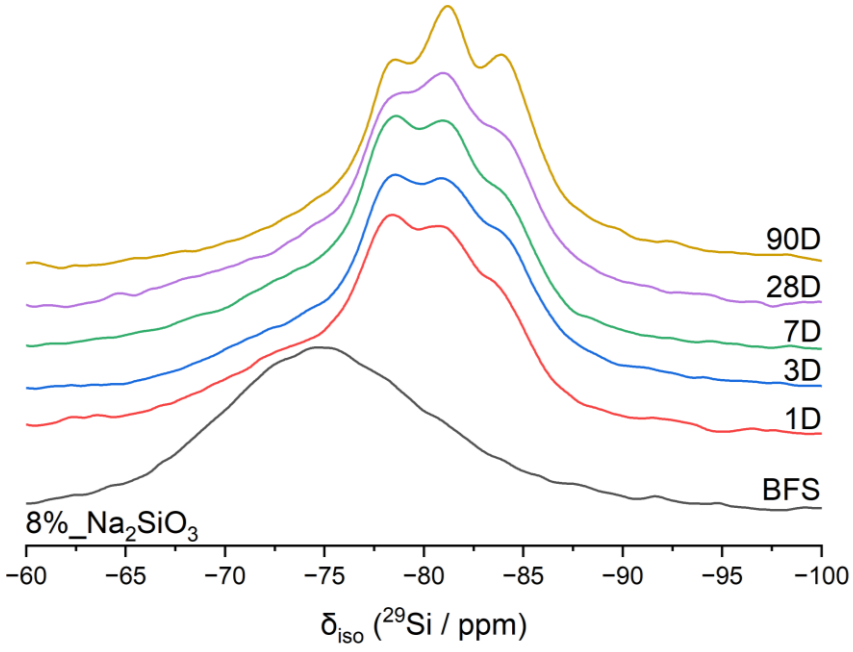

Figure 4-8 *^{29}Si MAS NMR spectra of BFS and sodium silicate-activated BFS at various curing times, as marked.*

The three main resonances identified above in the region of δ_{obs} = -75 and -85 ppm are further highlighted in the deconvolution of ^{29}Si MAS NMR spectra (**Figure 4-9**), as well as the presence of five additional Si environments in each sample, resonating at δ_{iso} = -76.0, -87.0, and -92.0 ppm. These resonances at δ_{iso} = -76.0, -87.0, and -92.0 are attributed to Q^1(I), Q^3(1Al) or Q^4(4Al), and Q^3 or Q^4(3Al), respectively, within the C-(N)-A-S-H. Additionally, no Q^0 Si sites were identified in the spectral deconvolutions, however, the broad Gaussian peak representing remnant anhydrous slag particles centres at δ_{iso} = -75.0 ppm and likely encompasses at least some of the Q^0 and Q^1 environments at δ_{iso} = -72.0 and -76.0 ppm, respectively.

The identification of two distinct Q^1 sites, denoted as Q^1(I) and Q^1(II), corresponds to differences in shielding experienced by Q^1 species charge-balanced by Ca^{2+}, Na^+, or H^+, as calculated in molecular dynamics studies [206], and observed in ^{29}Si MAS NMR spectra for previous studies of silicate-activated slag binders [58], [194]. Based on electronegativity, H^+

and Na^+ will shield the Si nuclei to a greater extent than Ca^{2+} will, and therefore Q^1(I) and Q^1(II) sites are attributed to Q^1 species charge-balanced by Na^+ or H^+ and Ca^{2+}, respectively.

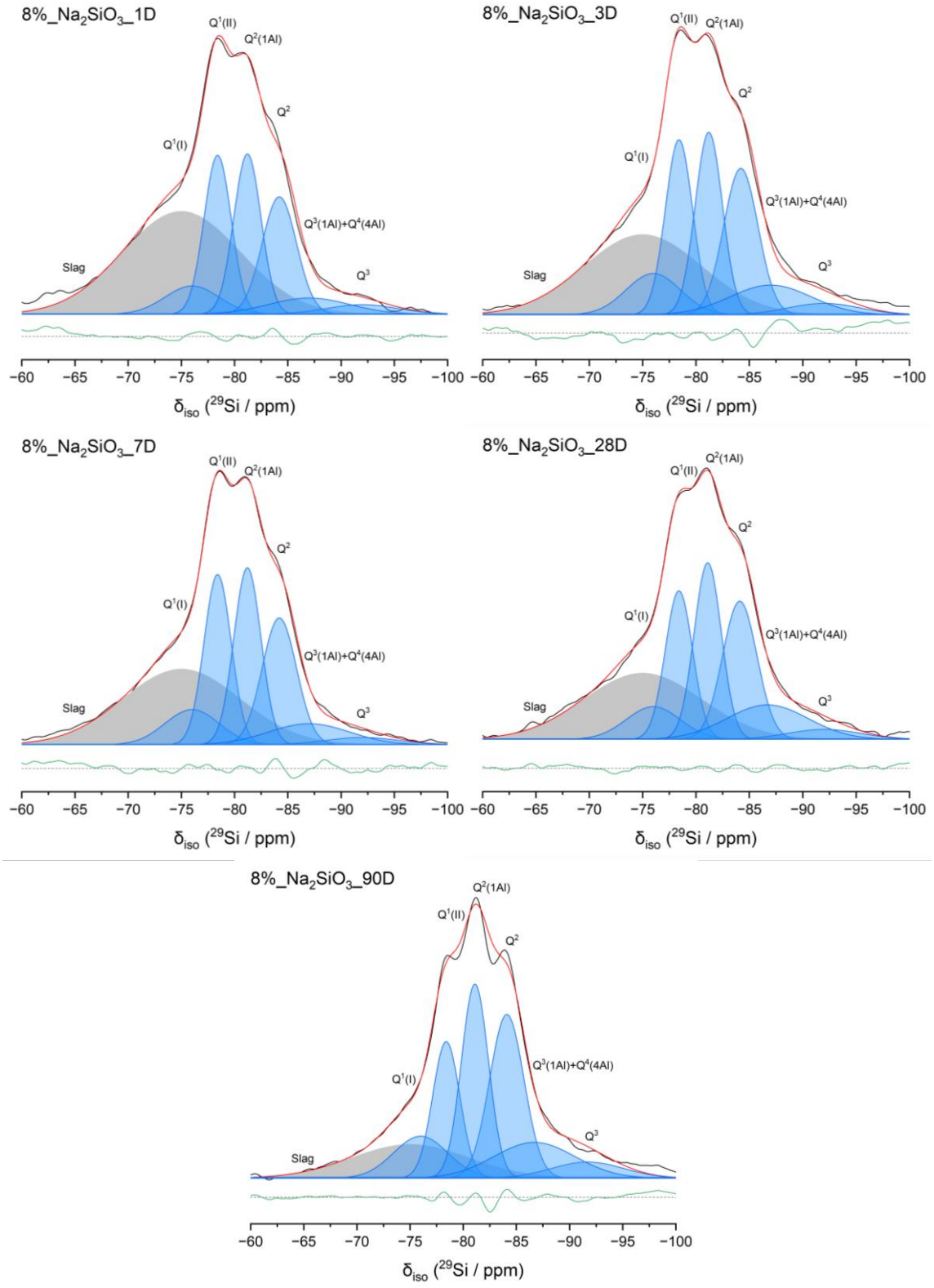

Figure 4-9 *Deconvolutions of ^{29}Si MAS NMR spectra for silicate-activated slag. In each case, the data are shown in black, the fit (shown in red) is the sum of the deconvoluted peaks, and the difference between the data and the fit is shown in green. Peaks attributed to Si sites in C-(N)-A-S-H are shaded in blue, while those attributed to sites within remnant anhydrous slag are shaded in grey.*

A notable resonance intensity at approximately δ_{iso} = -92 ppm is observed, particularly at a later curing age, whose chemical shift can be assigned to Q^3 and/or Q^4(3Al) environments [160], [207]. To satisfy the structural constraints for a mixed cross-linked/non-cross-linked C-(N)-A-S-H phase described by the CSTM, the peak at -92 ppm is assigned to Q^4(3Al) in a polymerised Al-rich N-A-S-H, rather than to Q^3 in C-(N)-A-S-H. In this system, due to the presence of high Al and Na content, a N-A-S-H phase, comprising of Q^4(4Al) and Q^4(3Al) sites, has formed in addition to C-(N)-A-S-H, in line with other studies on silicate-activated slags [58], [194]. Moreover, the resonance at -87 ppm, which generally increases in intensity with curing time, is typically attributed to cross-linked Q^3(1Al) Si sites in C-(N)-A-S-H but also contains contributions from overlapping resonances of Q^4(4Al) environments within this additionally formed N-A-S-H, again consistent with the structural model proposed by Myers *et al.* [161] and studies on silicate- and carbonate-activated slags [58], [83], [92], [188], [194], [208]. It is necessary here to attribute part of this resonance to Q^4(4Al) due to the assignment of Q^4(3Al) sites in the spectral deconvolutions needing the presence of additional Q^4-type units, as no aluminosilicate phase can consist of solely Q^4(3Al) sites [209]. Previous studies have shown that Al-rich geopolymers contain almost exclusively Q^4(3Al) and Q^4(4Al) environments, supporting the existence of these units in the spectral deconvolutions here, indicating that alkali-activated slag cements may include disordered, zeolite-type products similar to N-A-S-H typically formed where low-calcium aluminosilicate precursors are used [55], [209], [210].

Quantification of Si sites, determined through deconvolution of the ^{29}Si MAS NMR spectra as a function of curing age is reported in **Table 4-2**. ~57 % of the slag is seen to have reacted within the first day of curing, and ~84 % after 90 days, showing a steady consumption of anhydrous slag particles with time, indicative of the continual dissolution of slag and uptake of silica supplied by the activator into the solid binder.

Table 4-2 *NMR parameters for silicate-activated slag samples, extracted from the deconvoluted ^{29}Si MAS NMR spectra.*

Sample	Parameter	Assignment								
		Unreacted slag	**Q^0**	**Q^1(I)**	**Q^1(II)**	**Q^2**	**Q^2(1Al)**	**Q^3 or Q^4(3Al)**	**Q^3(1Al)**	**Q^4(4Al)**
	δ_{iso} (ppm)	*-75*	*-72*	*-76*	*-78.6*	*-84.4*	*-81.4*	*-92*	*-87*	*-87*
	FWHM (ppm)	*13*	*5*	*6*	*3*	*3.8*	*3*	*8*	*9*	*9*
SiO_3_1D	Relative integral area (%)	42.7	0.0	5.4	15.2	14.2	15.4	2.4	3.9	0.7
SiO_3_3D	Relative integral area (%)	31.8	0.0	7.6	16.0	17.0	16.7	2.8	7.0	1.2
SiO_3_7D	Relative integral area (%)	33.1	0.0	7.1	17.2	16.3	17.9	2.0	5.2	1.2
SiO_3_28D	Relative integral area (%)	29.2	0.0	6.7	15.1	17.8	18.0	2.7	7.6	2.9
SiO_3_90D	Relative integral area (%)	15.9	0.0	9.2	14.9	22.6	21.1	4.7	8.5	3.2

There are notable amounts of Q^2(1Al) sites present, indicating high levels of Al substitution in the C-(N)-A-S-H, and the steady existence of Q^3(1Al) units suggest that the C-(N)-A-S-H is significantly cross-linked. Increased quantities of Q^4(4Al) and Q^4(3Al) environments from 28 days of curing onwards suggest the precipitation of N-A-S-H at later curing ages.

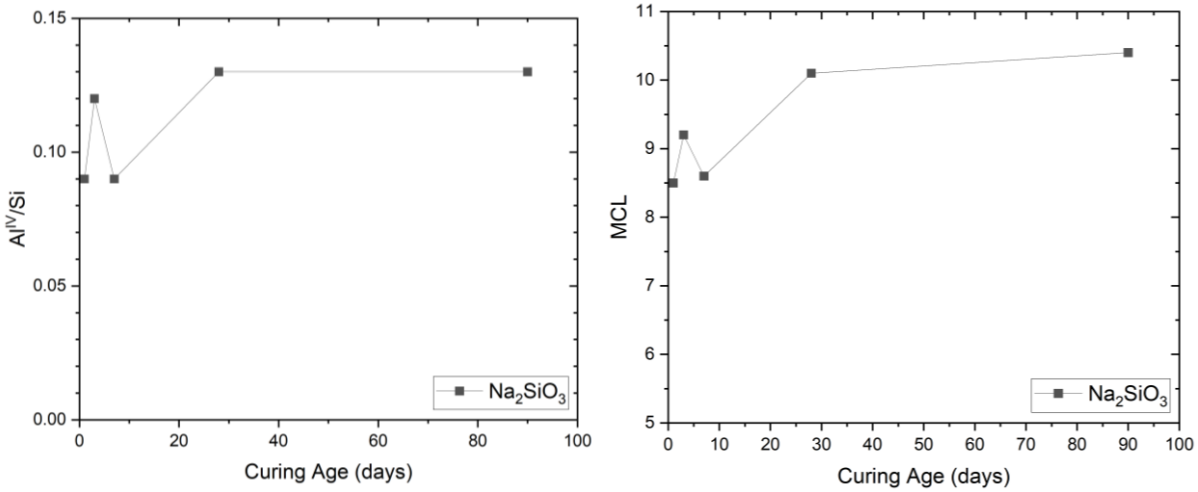

Figure 4-10 *Al^{IV}/Si ratio and MCL of crosslinked C-(N)-A-S-H in silicate-activated BFS over time, calculated using the CSTM and 29Si MAS NMR spectral deconvolutions.*

Additionally, the relative amount of Q^1(II) sites remains relatively constant from 1 to 90 days of curing, while that of Q^1(I) increases with increasing curing time. The increasing prevalence of Q^1(I) sites as well as an increase in Q^2(1Al) and Q^3(1Al) sites over time correlates with the increasing mean chain length (MCL) of C-(N)-A-S-H, in **Figure 4-10**, as time of curing increases. Moreover, the increasing trend in relative percentage of Q^3(1Al) sites is consistent with increasing concentration of Q^2(1Al) sites, as well as apparent increase in Al^{IV} sites in **Figure 4-7**, supporting the slight increase in Al^{IV}/Si as curing time increases (**Figure 4-10**), thus indicating that the degree of cross-linking of C-(N)-A-S-H increases over time.

Typically, the formation of the additional disordered Q^4-containing product (N-A-S-H) at extended curing ages would result in a reduction in cross-linking of the C-(N)-A-S-H, which in turn would cause a similar decreasing trend in MCL and Al/Si ratio. This is not the case in this study.

It is hypothesised that the increase in Al^{IV}/Si ratio, MCL, and cross-linking as curing time increases, coupled with the apparent growth of Al^V sites (**Figure 4-7**), means that either maximum crosslinking potential is satisfied or the binding potential of Al in C-(N)-A-S-H is attained, as crosslinked C-(N)-A-S-H have much lower Al-binding capacities than their non-crosslinked counterparts [194], and thus, there is no more uptake of Al in C-(N)-A-S-H. Consequently, the Al-rich secondary reaction product, N-(A)-S-H is forming, but in small amounts, as well as Al^V sites forming as free tetrahedra for charge-balancing in the interlayer, altogether creating a more stabilised structural network.

4.3.2.5 SEM-EDX

Scanning electron microscopy is useful for examining the general surface structure of cementitious materials and coupled with energy dispersive X-ray (EDX) analysis, the

elemental compositional changes over time can also be studied. SEM images for alkali-activated slag cements, as demonstrated in **Figure 4-11**, show unreacted slag particles as light grey shapes amongst a dark grey bulk structure, representing hydrate phases, including the main binding phase, C-A-S-H, as well as the secondary structures, hydrotalcite and calcium carbonates. Additional features include cracks and striations, possibly as a result of fracturing the cement paste samples rather than cutting in this study. Furthermore, no pores are visible at this magnification, which does not mean that none exist for this material, but rather it likely has low porosity and/or any pores are on the nanoscale.

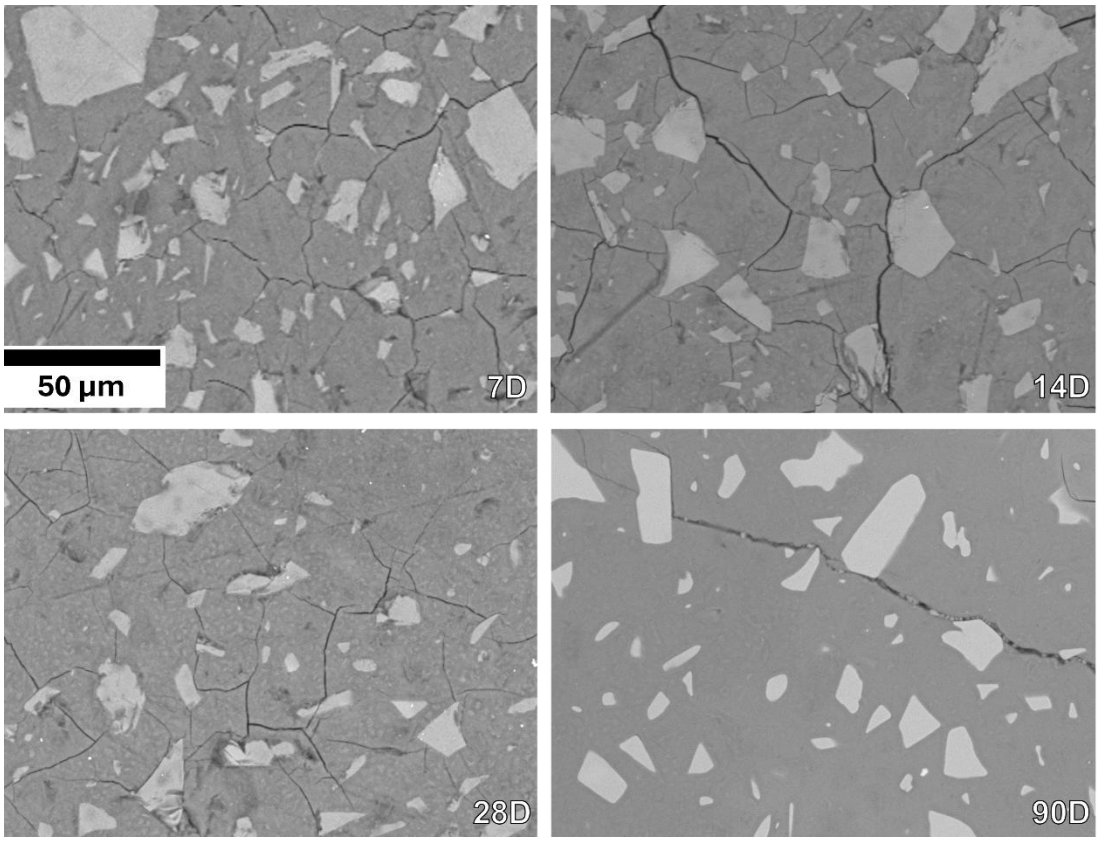

Figure 4-11 *SEM images for silicate-activated BFS, at 1000x magnification, for various curing times, as labelled.*

The SEM images for the silicate-activated slag binder (**Figure 4-11**) show little difference in structure over time. All samples contain some unreacted slag particles amongst a generally cohesive surrounding hydrate structure, further showcasing the great extent of reaction

achieved from early curing ages. A general reduction in slag particles and increase in cohesion of the phase bulk structure are observed over time, particularly at 90 days curing, as is expected as the reaction proceeds steadily beyond initial activation.

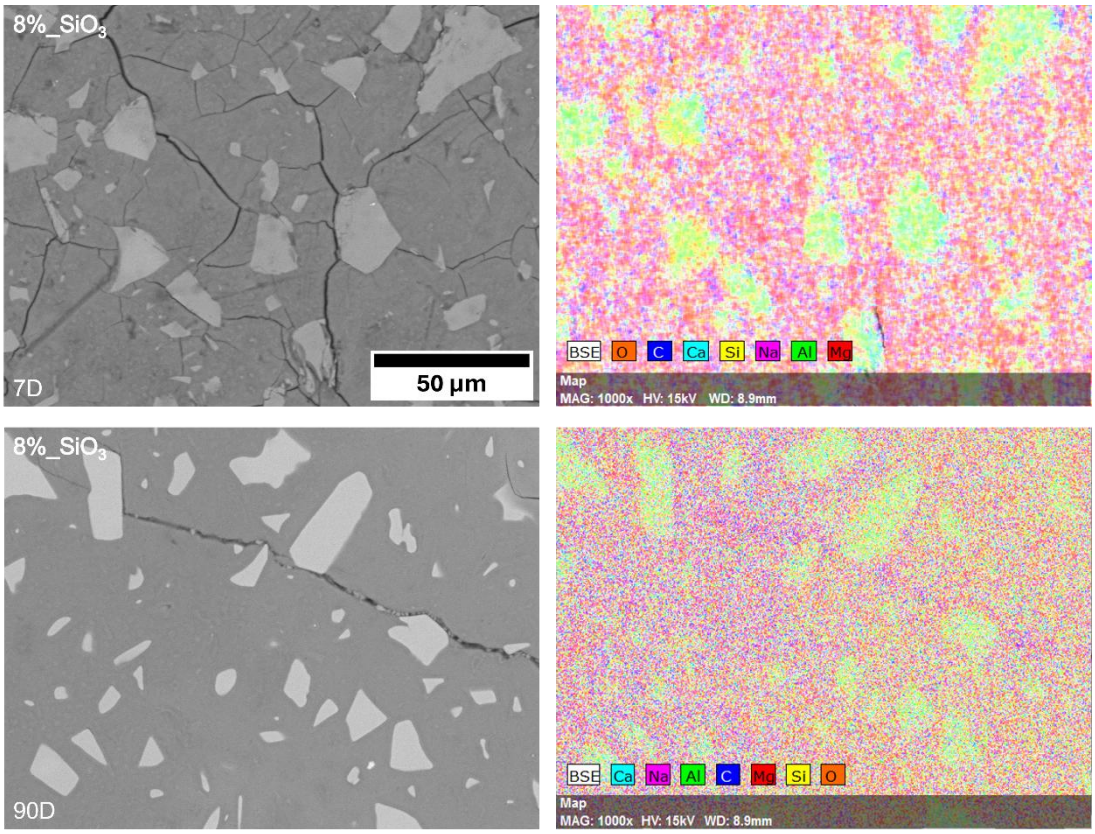

Figure 4-12 *Elemental mapping for silicate-activated BFS, cured at 7 and 90 days, as labelled.*

Elemental mapping for the silicate-activated BFS sample (**Figure 4-12**) at 7 days curing, indicates a clear difference in elemental concentration for slag particles and the hydrate phases; the unreacted slag particles are rich in silicon, aluminium and calcium, while the surrounding hydrate structure predominantly consists of sodium, magnesium and oxygen, with some amounts of calcium and silicon in the hydrate phases. However, for the same sample cured for 90 days, there appears to be a more even distribution of all elements across the bulk structure, with some concentrations of silicon, aluminium, and calcium maintained in the areas of remnant anhydrous slag particles. The difference in elemental composition over curing time is

indicative of the greater extent of reaction achieved at later ages – the increased bulk elemental composition suggests a greater amount of hydrate phases forming as the reaction continually proceeds with time.

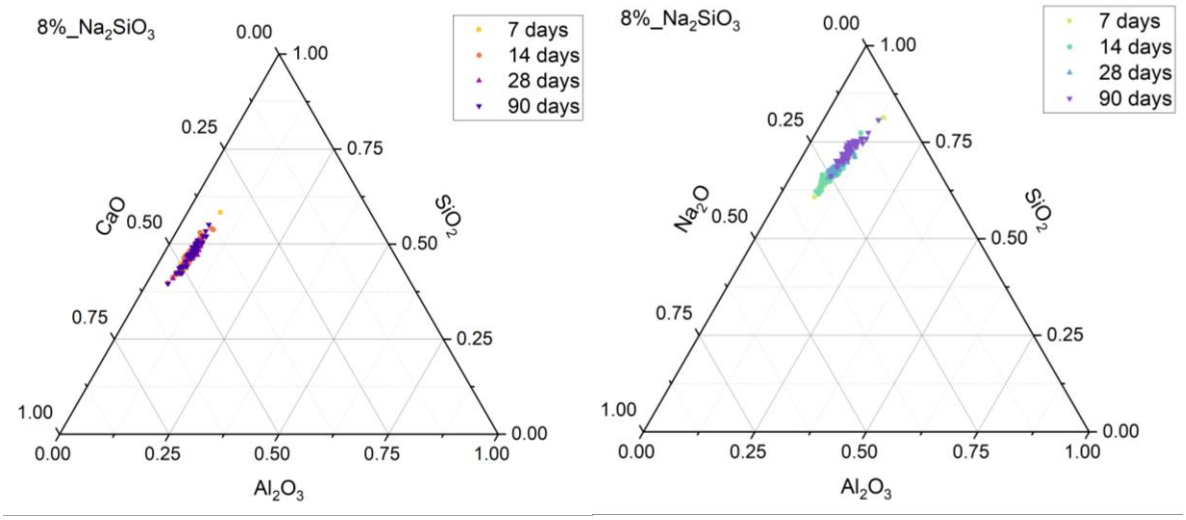

Figure 4-13 *Ternary systems of silicate-activated slag cured for 7, 14, 28, and 90 days, as determined by SEM-EDX analysis. (L) Ternary CaO – Al_2O_3 – SiO_2 system (neglecting Na_2O content), and (R) Ternary Na_2O – Al_2O_3 – SiO_2 system (neglecting CaO) content, showing elemental composition.*

Using elemental compositional data from EDX, ternary systems for samples were developed to further illustrate the phase evolution over time. The ternary CaO-Al_2O_3-SiO_2 system in **Figure 4-13** remains generally consistent as curing age increases, with the bulk structure corresponding to previous studies of alkali-activated slag [53], [211], [212] as well as that of synthetic C-(A)-S-H and N-A-S-H gels formed by a sol-gel method [213]. The chemistry of the sample at all curing ages lies within the region associated with the C-(N)-A-S-H [53], [161], [214], with the Al/Si ratio maintaining relatively constant over time. A slight increase in calcium over time may be observed, indicating that over time, an increased amount of calcium from the slag precursor is integrating into, and thus widening, the interlayer space of the C-(N)-A-S-H. This aligns with the increased crosslinking at higher curing ages determined from NMR spectroscopy.

For the ternary Na_2O-Al_2O_3-SiO_2 system in **Figure 4-13**, a general decrease in Na_2O over time, which is unexpected as typically there would be an increase in sodium ions in the interlayer space, like with calcium, as curing progresses. Additionally, a slight increase in Al/Si over time is noted, which aligns with findings from NMR spectroscopy, where both Al^{IV} and Al^{V} was observed to increase over time. This increase in aluminium content with time may be indicative of the greater formation of Al-rich secondary reaction product, N-(A)-S-H, as the reaction progresses.

4.3.3 Physical Properties

Physicomechanical properties of cementitious systems are determined to understand their behaviour and determine potential applications; they are often influenced by the chemical structure, which in turn is determined by the initial sample formulation. This section explores how the physical properties relate to the chemistry and bulk phase composition of the silicate-activated slag binder.

Table 4-3 *Physical properties of silicate-activated slag.*

Physical Property	**Determined value**
Mini slump diameter	115.87 ± 0.69 mm
Initial Set	1 h 25 m
Final Set	2 h 25 m

Sodium silicate typically acts as a dispersant in particulate suspensions, meaning a low yield stress of silicate-activated cement pastes [215], resulting in a greater spread in a mini-slump test [172]. Tan *et al.* [172] found that for a very similarly composed slag as in this project activated with sodium silicate at a water-to-binder ratio of 0.4, slump diameters of 72.5, 105.0 and 120.9 mm were measured for 4, 8, and 12 wt.% activator doses, respectively, using the

same mini slump setup. This increase appears to be non-linear, possibly exponential, suggesting that increasing the activator dosage further would have reduced improvements on the slump diameter. The measured value of 115.87 mm (**Table 4-3**) in this study is comparable to that found in the previous study, corresponding to the dispersive nature of sodium metasilicate.

Additionally, the initial and final setting times were determined with a simple automatic Vicat apparatus setup. As is known for silicate-activated slags, the values for setting times is relatively low, reaching initial set at 1 hour 25 min and final set at 2 hour 25 min, aligning with quick setting times previously measured on such materials [182], [215]–[218]. This quick setting time is often linked to its fast rate of reaction, where the dissolves Ca^{2+} and aluminate species of the slag interact with Na^{+} and silicate ions from the activator solution, leading to large formations of reaction products [216], [218]. However, this main reaction, where the bulk of products are formed, was found to occur between 6 and 12 hours for the silicate-activated sample in this study (**Figure 4-1**), while the heat release due to slag dissolution aligns more with the setting time, occurring within the first ~2 hours. The dissolution of species in the bulk fresh cement, as well as some precipitation of reaction products, filling spaces between slag particles likely causes the hardening of the material.

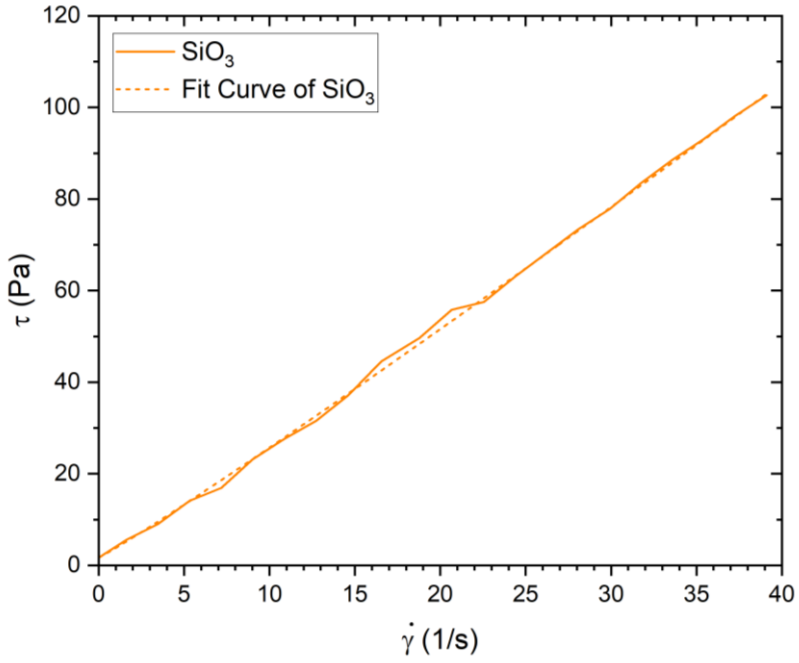

Figure 4-14 *Rheology of silicate-activated BFS.*

Rheological properties and behaviour were determined for the silicate-activated slag cement sample via a shear stress vs shear rate curve (**Figure 4-14**), and a Herschel-Bulkley model fitted to the data. **Figure 4-14** in conjunction with the model parameters for the fit detailed in **Table 4-4** reveal that the sodium silicate-activated slag cement displays Bingham-type behaviour, having a flow index (n) of ~1, with a very low yield stress of ~1.7 Pa, meaning that the paste behaves as a rigid body at very low stresses but once a stress of 1.7 Pa is exceeded, it flows as a viscous fluid. Bingham-type behaviour has been observed in previous studies for AACs [117], [215], [216], as have the particularly low yield stresses for silicate-activated slag cements [172], [217], [219].

Table 4-4 *Herschel-Bulkley model parameters for silicate-activated BFS, fitted to the curve in* ***Figure 4-14****.*

Sample	**τ_0**	**k**	**n**
8%_Na_2SiO_3	1.69	2.11	1.06

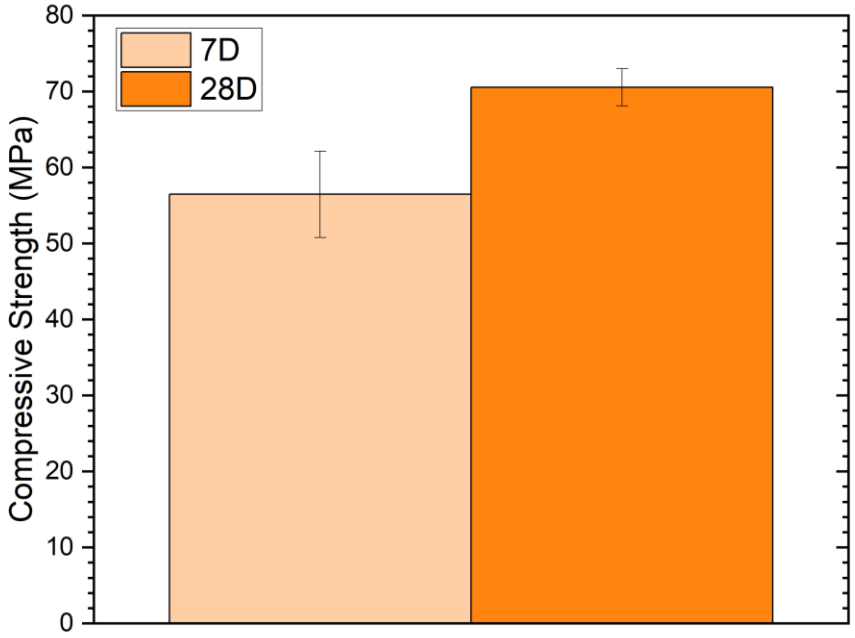

Figure 4-15 *Compressive strength values of silicate-activated BFS at 7 and 28 days.*

The compressive strength for the silicate-activated slag binder at 7 and 28 days of curing is comparable to that found in the literature for sodium silicate-activated materials [69], [92], [132], [220], however, it is noted that here, cement pastes were used rather than the mortar specified by ASTM C109 [165]. Despite this amendment, the values measured here are within ~5 % of the values determined by Bernal *et al.* [69] for mortars including similar binder formulation at the same curing ages.

Compressive strength values at 28 days of curing are generally used as the design value of the material, and it is noted that the value at this time-point is expected to be ~99 % of the material's potential compressive strength, while the value at 7 days should be at least roughly 65 % of the material's ultimate 28-day compressive strength [221]. Here, the value at 7 days is closer to ~80 % of the 28-day value for compressive strength, indicating that there is rapid early strength development, akin to the fast rate and degree of reaction.

Typically, specifications require concrete to have a compressive strength value at 28 days of: ~17 to 28 MPa for general use in foundations, slabs and footings; ~34.5 MPa for high-strength concrete uses for the likes of beams and girders; and at least ~52 MPa for high-load-bearing structures, including high-rise columns, according to ACI standards [221]. Considering the knowledge that concrete is stronger than cement due to the inclusion of sand and aggregates in addition to cement, the values measured here for sodium silicate-activated slag cement suggest that the use of this binder within concrete would result in a high-strength concrete material, comparable to those utilising Portland cement. Furthermore, the likely highly crosslinked nature of main binding phase C-(N)-A-S-H determined at later curing ages (28 and 90 days) from NMR spectroscopy means the cement structure becomes more interconnected, which is generally found to correspond to a reduced porosity and better load transfer, which in turn results in high compressive strength values [61], [222], [223], as determined here for the silicate-activated slag binder, however, it is noted that porosity measurements would aid in this understanding.

4.4 Conclusions

The use of sodium silicate for the alkali activation of blast furnace slag has been evaluated via the characterisation of early reaction, structural evolution, and fresh-state and mechanical properties, to be used in this project as the control sample by which further samples will be compared to, due to its validity and functionality for use in industry.

It was found that the sodium silicate-activated slag binder reacts very quickly due to the high alkalinity provided by the activating solution, with the main reaction occurring and reaching completion within ~18 hours, with very little dormancy in the heat release. Further to this, a C-N-A-S-H structure forms quickly and continues to polymerise over time to create a cohesive and strong material, with some amounts of secondary products forming over time, including

N-A-S-H, hydrotalcite and calcium carbonate polymorphs from atmospheric carbonation. Moreover, the use of sodium silicate leads to sufficient workability due to its dispersive nature, as well as influencing the rheological behaviour of the binder, forming a Bingham-like fluid with a low yield stress. The sufficient workability and viscosity means that the material flows well and can be shaped effectively in practice before it sets. Furthermore, compressive strength testing reveals that the binder has a 7-day strength of ~60 MPa, which continues to develop to ~70 MPa by 28 days, verifying its sufficient formation of the strength-giving C-A-S-H phase and its subsequent feasibility for industrial applications.

Chapter 5: Sodium Carbonate-activated Slag Binders

5.1 Introduction

The use of alkali-activated cements has been proposed as a potential strategy to minimise cement-associated carbon emissions, due to their incorporation of industrial waste and/or by-products, as well as naturally occurring minerals [11]. Despite this, commonly used activators – alkali silicates and hydroxides – carry greater embodied carbon than their less commonly used counterparts, alkali carbonates, which are naturally occurring, or can be produced via industrial chemicals manufacture and even through CO_2 sequestration [180], [224]–[226]. Additionally, the use of silicates and hydroxides also pose significant challenges in handling due to their caustic and viscous nature [92], [129], where alkali carbonates do not.

Despite being advantageous in their carbon footprint and handling compared to alkali silicates and hydroxides, there is limited use of these alkali carbonates in the current production of AACs. This is attributed to lengthy initial setting and hardening times as well as poor early strength development as a result of the moderate to near-neutral pH of these solutions, reducing their capacity for dissolution of slag particles and the subsequent release of silica [48], [71], [78]. However, there is limited knowledge of how the formulation chemistry intrinsically influences the reaction-structure-property relationships.

Therefore, this chapter explores the use of sodium carbonate for the alkali activation of blast furnace slag in comparison with sodium silicate-activated slag. As such, the combination of sodium silicate and sodium carbonate in a 50:50 wt.% blend will also be assessed as an activator for slags. The reaction mechanisms and kinetics are studied *in situ* to determine the specific pathway by which the cementitious binder forms, followed by a probing of the microstructure at various curing times to understand the structural evolution, and finally the

fresh-state and mechanical properties will be determined. The knowledge determined here for carbonate-activated slag binders will direct further research into improving the performance of such cementitious materials in order to certify their use for industry implementation.

5.2 Methodology

Cement samples were made by mixing blast furnace slag with either sodium carbonate solution or a blended sodium carbonate and silicate solution at 50:50 wt.%, for both fresh-state testing immediately after mixing, and solid-state characterisation at numerous time points. The performance of these formulations was compared to the sodium silicate-activated sample in *Chapter 4*. The sample formulation for this chapter are as described in **Table 5-1**.

Table 5-1 *Sample formulations used in Chapter 5.*

No.	Sample Name	Activator	BFS (g)	Activator Na_2O (g)	Additive	Additive mass (g)
1	**BFS_8%_SiO_3**	Na_2SiO_3	100	8	--	--
2	**BFS_8%_CO_3**	Na_2CO_3	100	8	--	--
3	**BFS_8%_SiO_3_CO_3**	Na_2SiO_3 + Na_2CO_3 (50:50 wt.%)	100	8	--	--

Reaction kinetics and mechanisms were explored using isothermal conduction calorimetry as well as *in-situ* IR spectra and XRD patterns. The structural evolution, including the general microstructure and nanostructural phase assemblage, were probed using multiple solid-state techniques: ATR-FTIR spectroscopy, TGA, XRD, ^{27}Al and ^{29}Si MAS NMR spectroscopy, and SEM-EDX analysis. Additionally, physical and mechanical properties were tested: setting time using a Vicat apparatus, workability by mini slump testing and viscometry measurements, and compressive strength at 7 and 28 days.

5.3 Results and Discussion

5.3.1 Reaction Mechanisms and Kinetics

5.3.1.1 ICC

As previously stated and supported by **Figure 5-1**, the heat evolution of slag binders follows four distinct stages of reaction, similar to the hydration reaction associated with Portland cement: a pre-induction period corresponding to surface wetting and dissolution of anhydrous precursor; a dormant period where a very low rate of heat is released as progressive dissolution of slag particles occurs with some initial precipitation of reaction products; an acceleration period, where a significant increase in heat release occurs, indicative of the nucleation, growth, and precipitation of many reaction products; and a deceleration period, where the reaction steadily reduces after setting [62], [100].

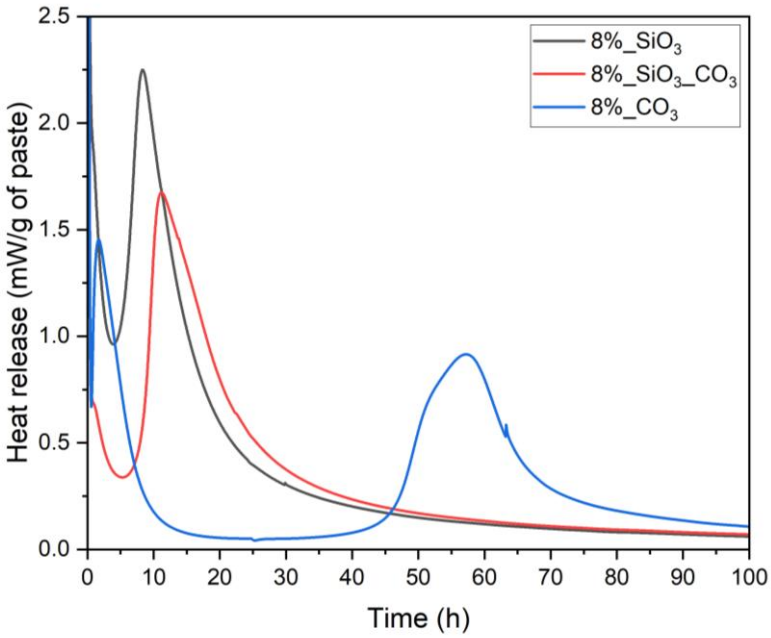

Figure 5-1 *Heat release rate of alkali silicate- and carbonate-activated slag binders.*

Figure 5-1 shows that the slag sample activated solely with sodium carbonate has a much longer induction period than those binders activated with sodium silicate, which both display

very short induction periods. There is an almost 50-hour different between the onset of the acceleration periods, which is consistent with the known slower setting times of carbonate-activated slag cements [62], [71]. The sample prepared using the combination of both sodium silicate and sodium carbonate reacts at a quicker rate than the solely carbonate-activated sample, aligning with the use of combined activators as a compromise to reduce carbon emissions whilst achieving a more desirable setting time. Additionally, the carbonate-activated slag sample possesses a much broader acceleration peak than the other two samples, with the silicate-activated sample having a very sharp heat release and the combined activator sample also displaying a sharp peak but with a slight shoulder, likely due to the sodium carbonate present.

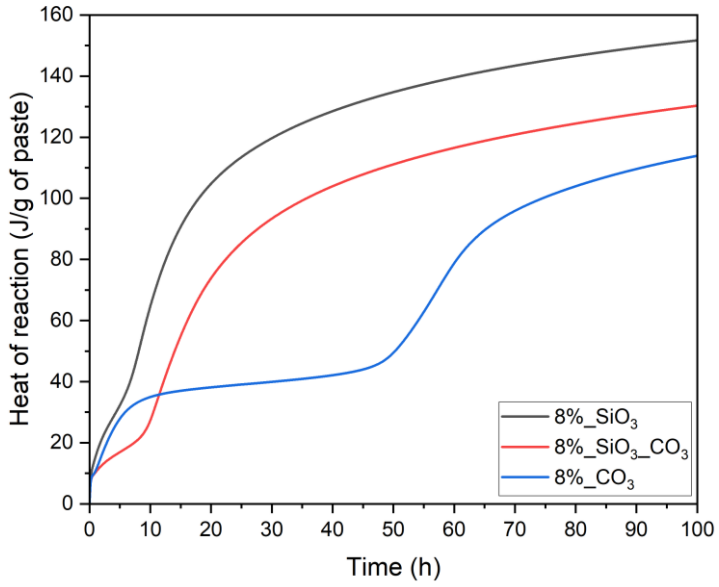

Figure 5-2 *Heat of reaction of alkali silicate- and carbonate-activated slag binders.*

Additionally, the cumulative heat of reaction further details the reaction kinetics for each of the slag samples. As expected, and discussed in previous Chapter 4, sodium silicate-activated BFS has the greatest heat of reaction, and the carbonate-activated binder has the least. Quite neatly, the mixed activator sample displays an overall heat of reaction in between both sole activator

samples. This pattern indicates that the inclusion of sodium silicate greatly improves the extent of reaction, i.e. there is a greater precipitation and formation of reaction products compared to a solely carbonate-activated binder.

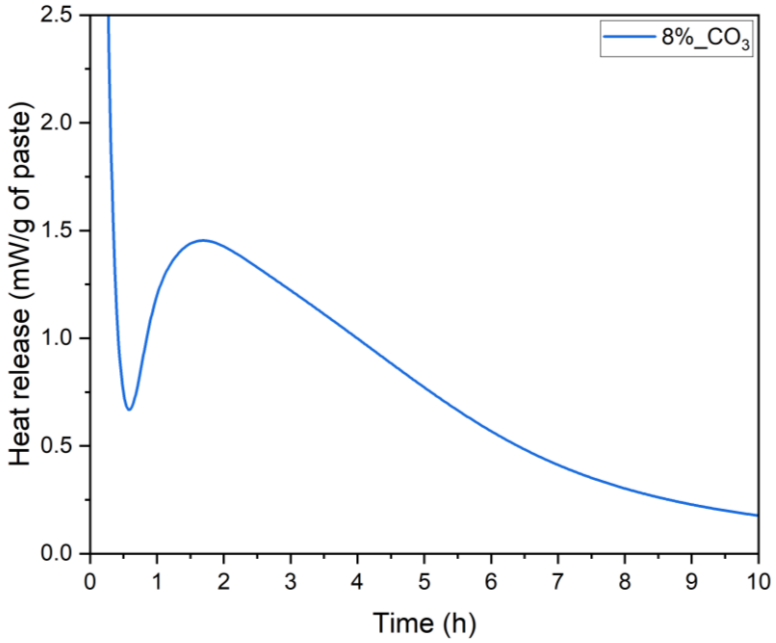

Figure 5-3 *Initial heat release rate of sodium carbonate-activated slag binder for the first 10 hours of reaction.*

Additionally, in **Figure 5-1** and more clearly in **Figure 5-3**, there is a significant heat release in the first few hours of reaction for the sodium carbonate-activated samples in addition to the later acceleration-deceleration peak. This early-age hump is likely due to the formation of carbonates from a preferential reaction between the Ca^{2+} ions from the slag and the CO_3^{2-} ions of the activator. Previous studies have suggested that also occurring at this early stage is a reaction between the aluminosilicate component of the slag with the sodium from the activator to form either a sodium aluminosilicate phase [58] or a crystalline zeolite, e.g. zeolite NaA [71]. These phases do not provide the high degree of cohesion required for high early strength development, and the carbonate phases formed inhibit an increase in pH, retarding the reaction, and causing a longer induction period.

5.3.1.2 DRIFTS

Diffuse reflectance infrared Fourier transform spectroscopy (DRIFTS) was conducted to explore changes in bond environments of the carbonate-activated slag binder *in situ* during the first hours of reaction, to align with the initial peak observed in the ICC data (shown in **Figure 5-1** and highlighted in **Figure 5-3**). IR spectra collected every 2 minutes after mixing for the initial 2 hours are shown in **Figure 5-4**.

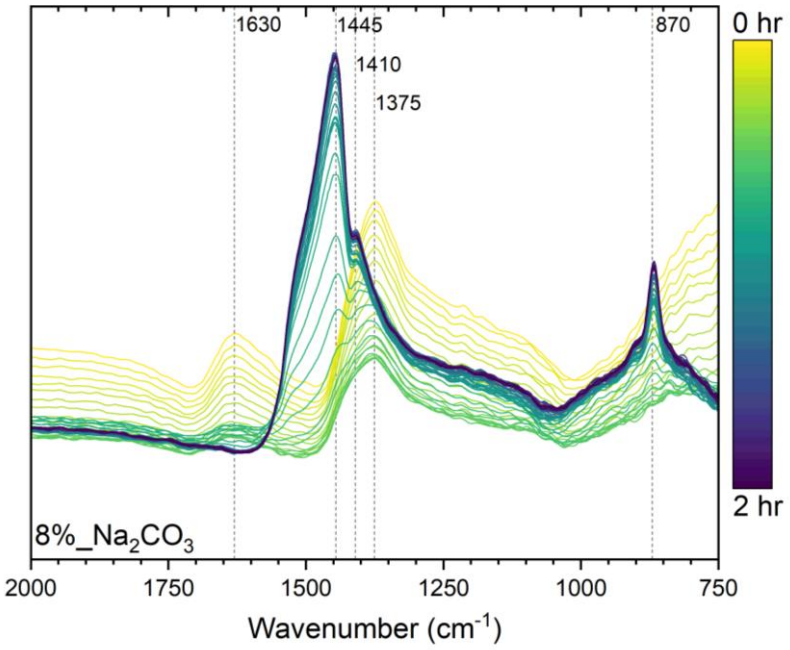

Figure 5-4 *DRIFTS spectra of sodium carbonate-activated BFS over the first 2 hours of reaction.*

Peaks at ~1630 and ~1375 cm^{-1} result from the sodium carbonate activating solution, more specifically the bending of O-H bonds in water [135], [183] and the asymmetric stretching of C-O bonds of the carbonate ions [141], [142], respectively. Once mixed with the BFS, both peaks decrease in intensity, with the peak at ~1630 cm^{-1} reducing completely, over 30 minutes, indicative of the consumption of these species. Similarly, the peak that was at ~1375 cm^{-1} shifts to a higher wavenumber and increases in intensity, from ~40 minutes, into a sharp peak at ~1445 cm^{-1} with a small shoulder at ~1410 cm^{-1}. Both of these peaks are attributed to the

asymmetric vibration of the C-O bond of carbonate ions, likely calcium carbonate and sodium calcium carbonate [95], [141], [183], respectively, indicative of the formation of carbonate species.

It is noted that the specific type of carbonate in the region of 1370 to 1450 cm^{-1} cannot be identified from IR spectra alone due to the overlapping of vibrational bands for various calcium carbonate polymorphs – including calcite, vaterite, aragonite – as well as for the sodium carbonate hydrate, natron. However, due to knowledge of activator chemistry as well as the likely preferential reaction occurring, it is considered that the band at ~1375 cm^{-1} is due to sodium carbonate as it is present in the spectrum immediately after mixing before being consumed, and that the peaks at ~1445 and 1410 cm^{-1} can be attributed to calcium carbonate polymorphs or other calcium carbonate-containing structures that have precipitated.

Further to this, a broad feature spanning the region of 750 to 1000 cm^{-1} develops slowing into a clearly defined peak at ~865 cm^{-1} after 1 hour and continues to grow and sharpen for the following hour. This peak is assigned to the asymmetric bending of C-O in calcium carbonate [135], [136], [141], [183].

Additionally, DRIFTS was conducted *in situ* for the silicate-modified sodium carbonate-activated slag over the first 2 hours of reaction following mixing, shown in **Figure 5-5**.

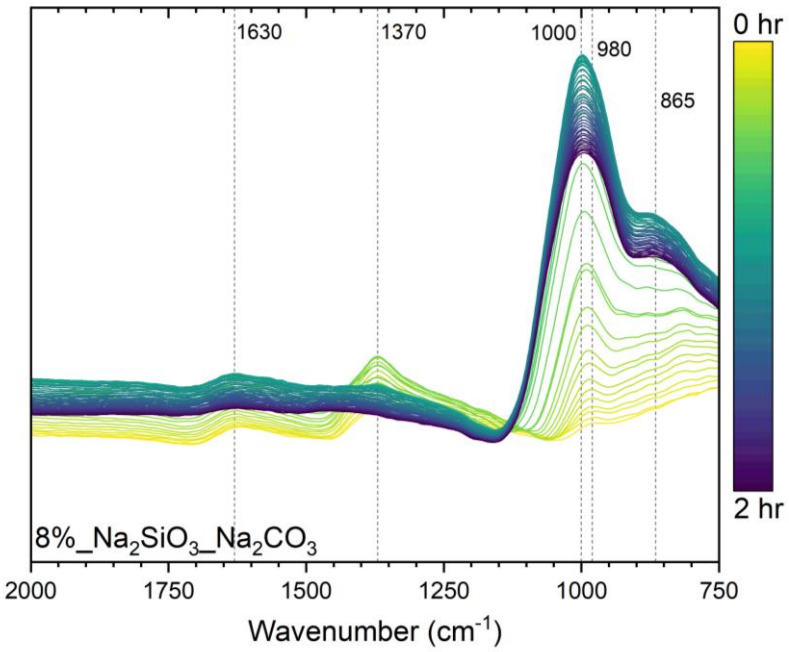

Figure 5-5 *DRIFTS spectra of BFS activated with both sodium silicate and carbonate over the first 2 hours of reaction.*

Similarly to the solely carbonate-activated sample, there are initial peaks at ~1630 and ~1370 cm^{-1}, assigned to the bending of the O-H bonds in water and the asymmetric stretching of the C-O bonds within carbonate ions, corresponding with the sodium carbonate solution within the mixed activator. In contrast, there is an initial signal at ~980 cm^{-1}, aligning with the asymmetric stretching of a Si-O-Si bond, which can be ascribed to the silicate solution, or the asymmetric stretching of a Si-O-Al bond within the aluminosilicate precursor [53], [133], [134].

The increase in intensity of all the aforementioned peaks in the first ~30 minutes is likely due to the supersaturation of activator species in solution. Those attributed to the carbonate species within the activator then reduce greatly, while the peak due to metasilicate anions in the activating solution (or the BFS) increases in intensity and shifts slightly to a higher wavenumber, forming a clearly defined peak centred at ~1000 cm^{-1}, assigned to a more crystalline Si-O-Si bond, likely within C-A-S-H species [53], [133]. Simultaneously, a shoulder

at ~865 cm^{-1} takes shape from ~40 minutes onwards, corresponding to the asymmetric stretching of the C-O bond within calcium carbonate, either due to some reaction between the carbonate anions in the activator with calcium ions in the slag or from atmospheric carbonation. Due to the nature of the mixed activating solution and the setup of the DRIFTS apparatus (in a temperature-controlled environment, but exposed to air), it is difficult to ascribe the presence of calcium carbonate structures in these binders to either reaction, but it is likely owing to contributions from both reactions (activation and carbonation), as shown in the solely silicate- or carbonate-activated slag samples.

5.3.1.3 *In-situ* XRD

X-ray diffraction (XRD) was utilised *in situ* to further probe the reaction mechanisms of the sodium carbonate-activated binder, by identifying the crystalline structures and their changes during the initial hours of reaction post-mixing **Figure 5-6**. As mentioned in the previous section, it can be difficult to distinguish carbonate-containing structures, particularly the likes of calcium carbonate and sodium carbonate polymorphs, using FTIR alone. However, because of the crystalline nature of these carbonates, XRD was expected to be a useful tool for differentiating between the carbonate phases consumed and formed, thus resolving the initial reaction mechanisms for carbonate-activated slag binders.

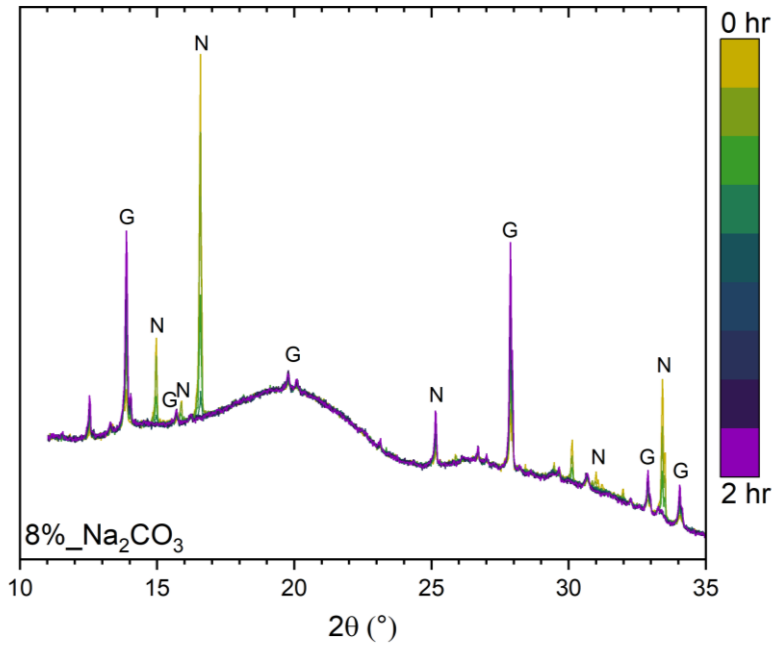

Figure 5-6 *XRD pattern of carbonate-activated BFS over the first 2 hours of reaction. Key crystalline peaks labelled: G – Gaylussite (PDF 00-021-0343), and N – Natron (PDF 00-015-0800).*

Peaks corresponding to natron ($Na_2CO_3.10H_2O$), a hydrated sodium carbonate, are present initially but generally reduce over time, with most representative peaks gone by ~1 hour. Simultaneously, the crystalline phase, gaylussite ($Na_2Ca(CO_3)_2.5H_2O$), a sodium calcium carbonate hydrate, begins to form from 0 hours and grows over time into sharp peaks. This further supports the theory of a preferential reaction, suggesting the depletion of sodium carbonate from the activator and formation of calcium carbonates with the incorporated calcium coming from the precursor, slag.

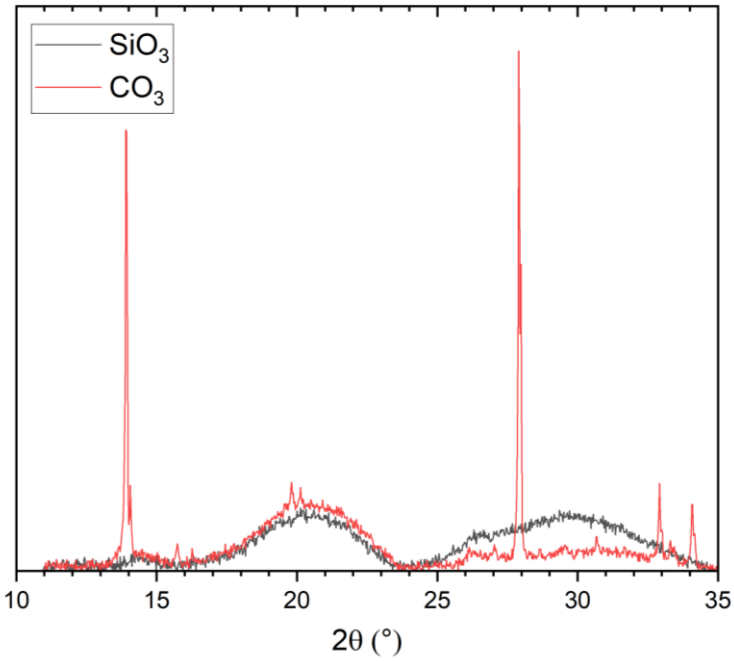

Figure 5-7 *Comparison of XRD patterns at 2 hours post-mixing, for carbonate-activated and silicate-activated BFS.*

Figure 5-7 shows the similarities and differences in XRD measurements for the silicate- and carbonate-activated slag binders. There is generally very little similarity between the patterns, other than the amorphous hump centred at ~20° 2Θ, which is credited to the polyimide film used for sample preparation. Furthermore, there is a very subtle amorphous hump centred at ~30° 2Θ forming in the carbonate-activated sample compared to that same hump being very clearly present in the silicate-activated sample. This broad feature due to diffuse scattering is shown to be present in the anhydrous precursor (**Figure 3-2**), however, it is also indicative of an alumina/silica phase, identified in AAC binders as belonging to the tobermorite-like C-A-S-H phase [156]. Combining observations for XRD and DRIFTS measurements taken *in situ*, it is reasonable to suggest that this broad feature is more likely attributed to a reaction product – C-A-S-H – than the unreacted precursor.

In contrast to the XRD pattern for the silicate-activated slag, that for the carbonate-activated binder contains various crystalline peaks (**Figure 5-7**), identified as being numerous carbonate

phases. The lack of these structures in the silicate-activated slag diffractogram, in conjunction with the absence of carbonate supplied in the sample formulation and the air-sensitive nature of the sample preparation for the XRD measurements *in situ*, suggests that any carbonate phases observed for the solely silicate-activated sample (in solid state characterisation or otherwise) are owed to atmospheric carbonation – CO_2 from the air infiltrating the samples and reacting.

5.3.1.4 Summary

Data from XRD combined with that from DRIFTS, both taken *in situ*, evidence that a preferential reaction is occurring in the initial few hours for sodium carbonate-activated slag binders, corroborating the observations from ICC data. The combination of these data suggests that the calcium ions from the slag are reacting with the carbonate anions of the activator to form calcium carbonate and sodium calcium carbonate polymorphs, in both hydrous and anhydrous forms. These carbonate phases, as well as the slower dissolution of slag under moderate pH conditions (from the Na_2CO_3 activator), retard the reaction, causing the longer induction period. Moreover, the main reaction period is inhibited due to the calcium ions from the precursor being occupied – preferentially bound in $CaCO_3$ – rather than incurring supersaturation in solution and the subsequent precipitation of primary reaction product, C-(A)-S-H. However, once the CO_3^{2-} ions are exhausted, the activating reaction is expected to continue similarly to other alkali-activated slag binders.

On the other hand, the reaction of the mixed silicate-carbonate-activated slag sample appears to be heavily influenced by its silicate component rather than the carbonate inclusion, having its peak of reaction occurring much nearer in time to that of the silicate-activated slag. Additionally, the DRIFTS data for the blended silicate-carbonate-activated sample follows a similar mechanism to the solely silicate-activated sample, favouring the likely formation of C-

A-S-H within the first 2 hours of reaction, however with more calcite forming, likely due to the inclusion of carbonate ions from the activating solution.

5.3.2 Structural Evolution

5.3.2.1 ATR-FTIR

ATR-FTIR spectra were taken at different curing ages for the carbonate-activated and the mixed silicate-carbonate-activated slag samples to identify bond environments and explore phase development over time. For both sample sets, the respective normalised spectra in **Figure 5-8** and **Figure 5-9** show little variation over time, indicative of a steady rate of reaction from 3 to 90 days of curing.

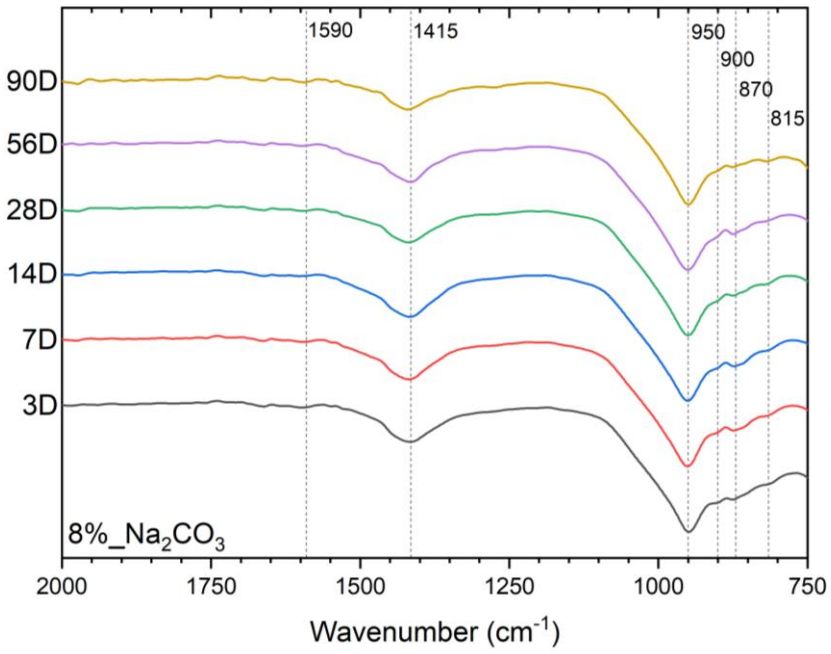

Figure 5-8 *FTIR spectra of sodium carbonate-activated BFS at various time points.*

For both sample sets, there is a shallow but notable band at ~1590 cm^{-1} in each sample's spectra, which is characteristic of the C-O vibration within the calcium carbonate polymorph, vaterite [184]. Additionally, a band centred at ~1415 cm^{-1} can be observed in the spectra for both samples, corresponding to the asymmetric stretching of C-O bonds of carbonate ions

[141], [142], likely encompassing sodium carbonate from the activator, hence its better prominence in the solely carbonate-activated sample, but it could possibly indicate additional carbonate phases forming. Further to this, the shoulder peak at ~900 cm^{-1} corresponds to the out-of-plane bending of C-O in calcite, another calcium carbonate polymorph [135], [136], [185]. Generally, this band becomes slightly more prominent over time, due to the increasing atmospheric carbonation with curing time. Moreover, a peak at ~870 cm^{-1} is observed in all spectra for both samples, but somewhat more pronounced in the spectra for the solely carbonate-activated slag sample, associated with the asymmetric bending of C-O in calcium carbonate [135], [136], [141], [183], as observed in the DRIFTS spectra after 1 hour in ***Section 5.3.1.2***.

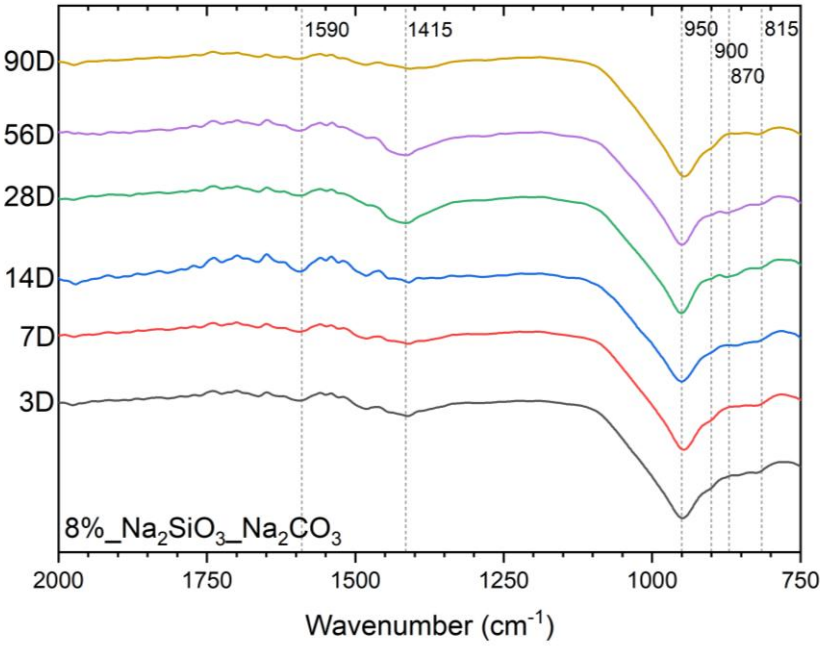

Figure 5-9 *FTIR spectra of BFS activated with both sodium silicate and carbonate at various time points.*

A band at ~950 cm^{-1} is the most prominent in all spectra for both samples, which is attributed to the asymmetric stretching of Si-O-T bonds, as is the smaller peak observed at ~815 cm^{-1}, more specifically, these two bands correspond to Q^2 and Q^1 sites, respectively, within the C-A-S-H structure [53], [133], [134]. The presence of both of these peaks is observed at 3 days with

no prominent change over time – the peak at ~950 cm^{-1} appears to sharpen slightly over time for the mixed silicate-carbonate-activated sample, indicating increased structural ordering of C-(A)-S-H as the reaction proceeds [53], [183], while the band at 815 cm^{-1} appears to hold its low intensity over time for both sample sets, however, is more prominent in the mixed activator sample, suggesting an increased amount of C-A-S-H in said sample, compared to the carbonate-activated sample.

5.3.2.2 TGA

Thermogravimetric analysis was conducted to understand the reaction progression by identifying and quantifying reaction products present in the sodium carbonate-activated and mixed sodium silicate- and carbonated-activated slag binders at various curing ages. For both samples, a general increase in overall mass loss was observed with increasing curing times, indicative of an increased extent of reaction over time: 23.0, 24.0, 26.5, 24.4, and 31.8 wt.% at 3, 7, 14, 28, and 90 days, respectively, for the carbonate-activated sample (**Figure 5-10**); and 27.1, 26.5, 24.6, and 26.8 wt.% at 3, 7, 14, and 90 days, for the mixed silicate-carbonate-activated sample (**Figure 5-11**).

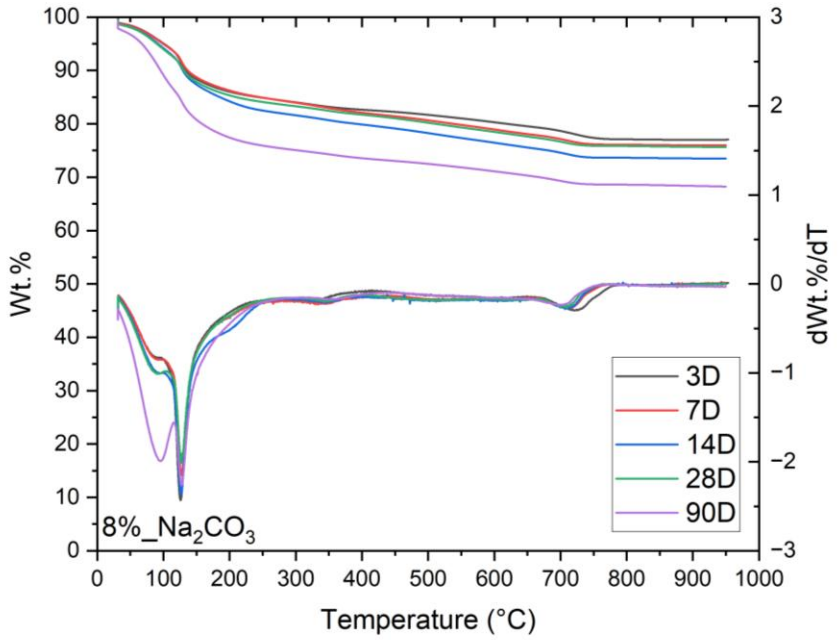

Figure 5-10 *TG/dTG trends of sodium carbonate-activated BFS, cured for various lengths of time, as labelled.*

The TGA curves for carbonate-activated slag display a first mass loss between 60 and 200 °C of up to 15 wt.% at curing ages up to and including 28 days, generally increasing with age, and ~25 wt.% at 90 days. A loss in this region is attributed to the loss water from the calcium aluminosilicate hydrate (C-A-S-H) [186], [187]. It is observed that for the carbonate-activated sample, there are two sharper mass losses in this region compared to the single broad mass loss observed for the silicate- and mixed silicate-carbonate-activated binder samples. The second of the two mass losses, centring at ~130 °C, remains similar in intensity regardless of curing age, equating to ~5 wt.% for each curing age, however, the first peak at ~100 °C increases slightly with curing age between 3 and 28 days before dramatically increasing at 90 days. This peak is typically associated more with the loosely bound water within C-S-H phases, meaning a likely increase in the quantity of such phases as curing time progresses, as expected due to the continual reaction over time after setting.

Similarly to the silicate-activated sample, TGA data for both carbonate- and mixed silicate-carbonate-activated samples display a shoulder to the initial mass loss peak(s) at ~170 °C for later curing ages, which is attributed to the initial thermal dehydration of hydrotalcite [188], [189]. Further to this, a mass loss in the region of 300-500 °C is observed in both samples for each curing age, which is associated with further loss of chemically bound water within hydrotalcite phases [186], [188], [190]. For the solely carbonate-activated sample, there is very little difference in mass loss over time in this second hydrotalcite-associated region, indicative of the small but established quantity of more stable hydrotalcite phases within the sample. On the other hand, the silicate-carbonate-activated sample has a slightly more pronounced, but still relatively constant-over-time, mass loss in this region, suggesting an increased quantity of hydrotalcite in the mixed activator samples.

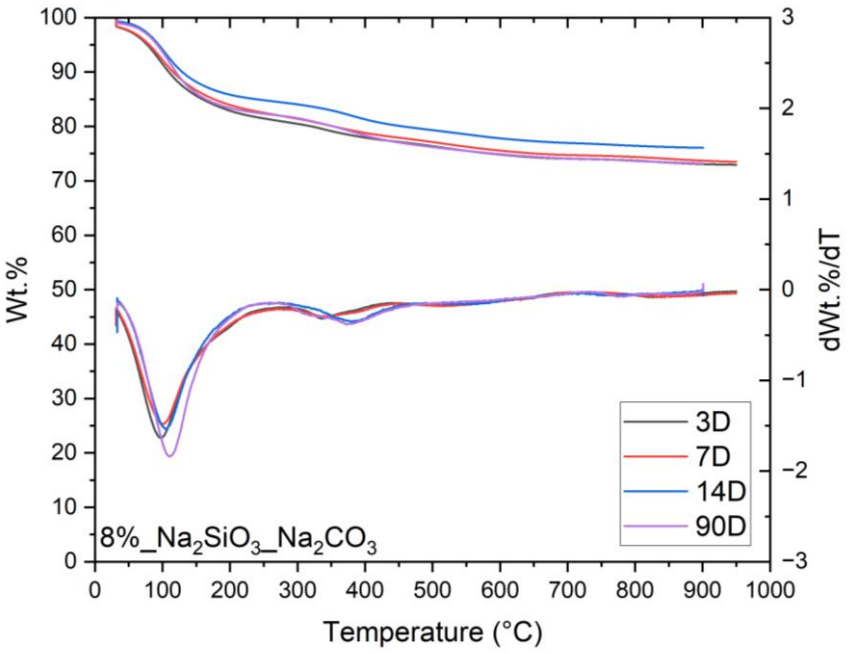

Figure 5-11 *TG/dTG trends of BFS activated with both sodium silicate and carbonate, cured for various lengths of time, as labelled.*

Additionally, a notable and progressive mass loss is present between 500 and 700 °C for the mixed silicate-carbonate sample, associated with the continual dehydration of C-A-S-H-type

phases and dehydroxylation of hydrotalcite phases [186], [188]. Although a mass loss in this region may be visible for the carbonate-activated sample, it is significantly less noticeable than for the samples activated with solely silicate or with both silicate and carbonate, indicating that the inclusion of silicate results in an increase in strongly bound C-A-S-H and hydrotalcite phases, paralleling with the increased rate and extent of reaction for such samples.

Finally, a mass loss can be observed in the region of 700-900 °C for both samples at all time points, but more so for the carbonate-activated binder. This loss is due to the decomposition of calcium hydrates [186] and the decarbonation of calcium carbonates, including calcite, vaterite, and aragonite [188], [192], [193], but can also be attributed to sodium (calcium) carbonates. The presence of such carbonate polymorphs in any sample can be credited to atmospheric carbonation of samples, however, the increased quantity in the sodium carbonate-activated sample observed here, coupled with the knowledge discerned from the *in-situ* characterisation in ***Section 5.3.1***, can be ascribed to the formation of such phases due to the presence of carbonate ions from the activator reacting with sodium and calcium ions from the slag precursor.

5.3.2.3 XRD

XRD patterns were measured for the carbonate-activated and mixed silicate-carbonate-activated slag binders at various curing ages as shown in **Figure 5-12** and **Figure 5-13**, respectively. Similarly to ATR-FTIR spectra and TGA plots for these samples, there is very little to no change in structure over time in the diffractograms, suggesting a stable, structurally ordered phase development from an early curing age. Both samples at all time points display a broad hump centred at ~30° 2Θ, characteristic of an alumina-silica phase, specifically a tobermorite-like C-A-S-H structure, in line with observations from TGA and FTIR spectra. Additionally, where the mixed silicate-carbonate-activated sample has a primarily amorphous

nature with little crystalline features, the solely carbonate-activated slag exhibits significant amounts of sharp peaks, likely due to the increased presence of crystalline carbonate phases. The crystallinity for the sodium carbonate-activated slag and the lack thereof for the blended sodium silicate/carbonate sample aligns with what is seen in literature [58], [69]. Additional tobermorite peaks, as well as those for hydrotalcite, can be observed in XRD patterns for both sample sets at all time points, in addition to small amounts of calcium carbonate polymorphs, calcite and vaterite.

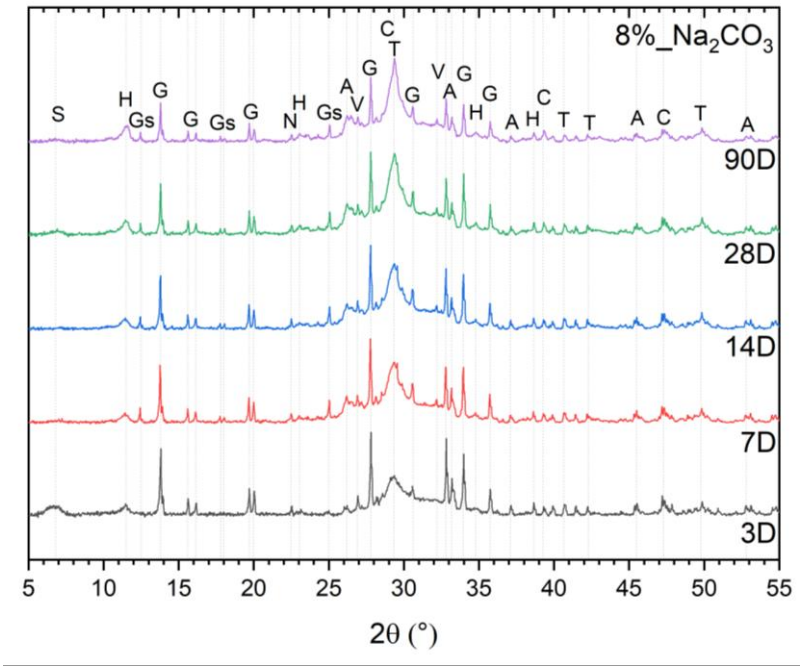

Figure 5-12 *XRD patterns of carbonate-activated BFS, at various curing times, as labelled. Phases identified have been labelled: A – Aragonite (PDF 04-008-5421), C – Calcite (PDF 00-066-0867), G – Gaylussite (PDF 00-021-0343), Gs – Gismondine (PDF 01-089-6321), H – Hydrotalcite (PDF 01-088-9171), N – Natron (PDF 00-015-0800), S – strätlingite (PDF 04-012-1915), T – Tobermorite (PDF 04-014-8455), and V – Vaterite (PDF 00-060-0483).*

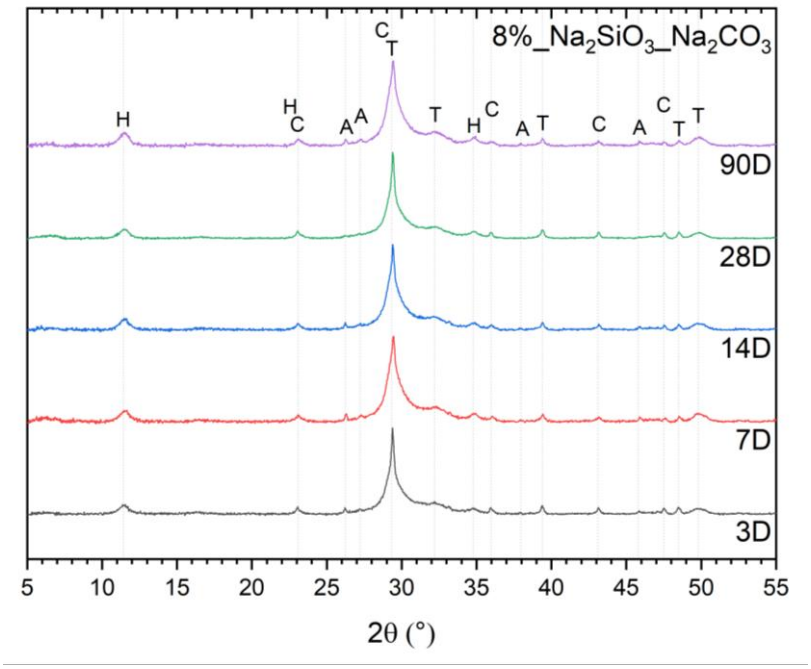

Figure 5-13 *XRD patterns of silicate/carbonate-activated BFS, at various curing times, as labelled. Phases identified have been labelled: A – Aragonite (PDF 04-008-5421), C – Calcite (PDF 00-066-0867), H – Hydrotalcite (PDF 01-088-9171), and T – Tobermorite (PDF 04-014-8455).*

The almost identical diffractograms for the mixed silicate-carbonate-activated sample at various time points (**Figure 5-13**), with the existence of tobermorite-like C-A-S-H and hydrotalcite from early age, highlights that a great degree of the main reaction has occurred by 3 days and the main reaction phases have formed stably. The existence of calcium carbonate polymorphs – calcite and vaterite – in the patterns for this sample again indicates that atmospheric carbonation has taken place during sample preparation and curing, but only in small amounts. The similarities between the XRD patterns for the mixed silicate-carbonate activated and solely silicate-activated slag samples once more suggest that the inclusion of sodium silicate in the mixed activator sample has a greater bearing on the mechanisms of reaction than its carbonate counterpart, with the main difference being the sharpness of the peak at ~30° 2Θ, which can be ascribed to the carbonate content of the binder.

For the solely carbonate-activated slag binder (**Figure 5-12**), the primary amorphous peak centring at ~30° 2Θ associated with C-A-S-H, although existing from an early age, grows in intensity and sharpens over time, suggesting an increase in structural ordering and stability with curing age. Further to this, the existence of this peak suggesting the existence of the aluminium-substituted tobermorite-like phase, as well as the presence of small amounts of hydrotalcite from early age (3 days), which are typically the main reaction products of sodium silicate- and hydroxide-activated BFS, suggest that once the CO_3^{2-} ions supplied by the sodium carbonate activator is largely consumed in the formation of carbonate compounds during the initial preferential reaction highlighted in ***Section 5.3.1***, the mechanism of sodium carbonate-activated slags proceeds in a similar fashion to the silicate- or hydroxide-activated slag systems.

Additionally, multiple peaks associated with calcium carbonate polymorphs – calcite, vaterite, and aragonite – exist at all curing ages, demonstrating that once these phases form, either due to the preferential reaction between calcium ions from the precursor with carbonate ions from the activator or via atmospheric carbonation of samples during preparation and curing, they remain stable and in the bulk structure. Unlike for the silicate-activated and mixed silicate-carbonate-activated samples, the presence of three phases – gismondine, gaylussite, and natron – are observed for the solely carbonate-activated slag binder. Natron, a hydrated sodium carbonate, likely exists due to unreacted activator species, and gaylussite was observed to form in the early hours of reaction between the carbonate activator and sodium and calcium species in the system, as illustrated by the XRD measurements taken *in situ* (see ***Section 5.3.1.3***). On the other hand, the presence of gismondine – a hydrated zeolite with chemical formula, $CaAl_2Si_2O_8.4(H_2O)$ – in the diffractograms for the carbonate-activated slag is observed in small amounts from 7 days onwards, suggests that different C-A-S-H-type phases are forming, once the initial preferential reaction has run its course.

5.3.2.4 NMR

Solid-state ^{27}Al and ^{29}Si magic angle spinning (MAS) nuclear magnetic resonance (NMR) spectroscopy were conducted in order to probe how the nanostructure of the carbonate-activated and silicate-carbonate-activated slag cements evolves over time.

5.3.2.4.1 ^{27}Al MAS NMR Spectroscopy

The ^{27}Al MAS NMR spectra for the carbonate-activated and mixed silicate-carbonate-activated slag samples in **Figure 5-14** and **Figure 5-15**, respectively, both display a broad tetrahedral resonance spanning the region of 80 to 60 ppm, which clearly contains contributions from multiple Al sites, for all curing ages. Resonances at δ_{obs} = 74 and 68.4 ppm correspond to well-defined Al^{IV} sites incorporated in bridging tetrahedra, $q^2(I)$ and $q^2(II)$, respectively, where tetrahedral Al are bonded to $Q^2(1Al)$ Si sites [58], charge-balance by Na^+/H^+ and Ca^{2+} ions, respectively, indicative of the formation of C-A-S-H . A narrower signal here represents a greater degree of polymerisation as the reaction continues over time. The spectra for the mixed silicate-carbonate slag varies very little in this region over time, similar to what was observed for the silicate-activated sample in **Figure 4-7**, having a sharp resonance at ~74 ppm from 1 day and maintaining this over time. Conversely, for the carbonate-activated sample in **Figure 5-14**, the resonance at ~74 ppm is barely distinguishable from that at ~68.4 ppm at 1-day curing, but becomes gradually sharper over time, suggesting a slow early formation of C-A-S-H, aligning with the preferential reaction of carbonate ions from the activator with calcium species from the slag inhibiting the onset of the main reaction within the first few days. For both carbonate-activated and silicate-carbonate-activated samples, the peak at ~68.4 ppm appears to increase in intensity over time, becoming more prominent at 90 days, like the observation for the silicate-activated slag, indicative of more $q^2(II)$ forming over time, i.e. more calcium is incorporating in the C-A-S-H interlayer. As such, it can be said that the inclusion of

sodium silicate accelerates the kinetics of the blended silicate-carbonate-activated system, by way of a reaction between the silicon species from the activator and the calcium ions supplied by the dissolving slag, forming calcium aluminium silicate hydrates within the first day of reaction.

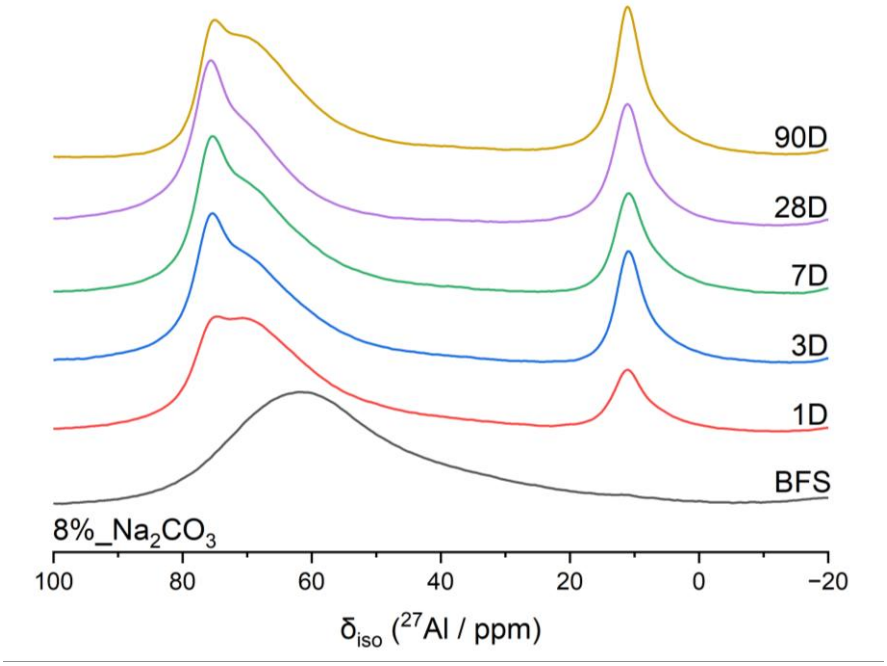

Figure 5-14 *^{27}Al MAS NMR spectra of BFS and sodium carbonate-activated BFS at various curing times, as marked.*

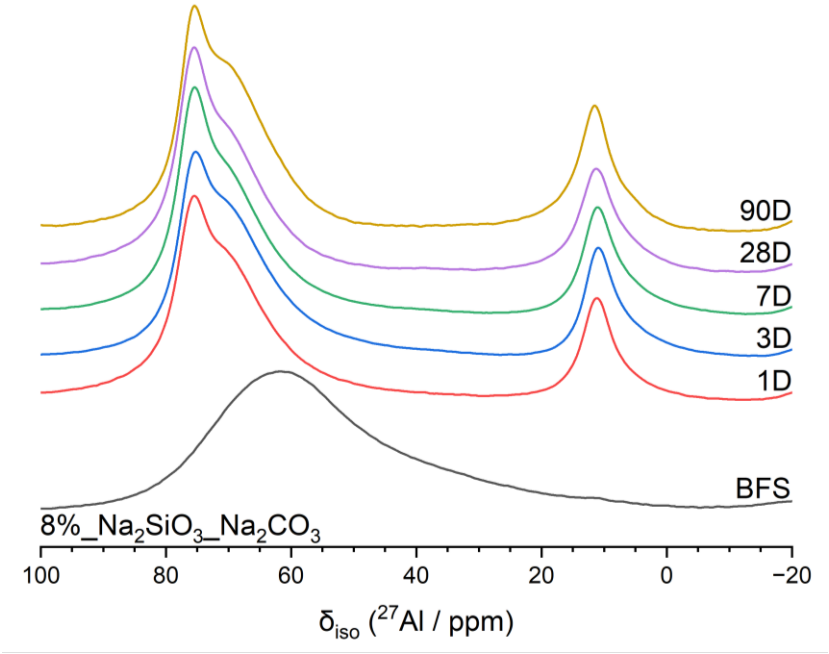

Figure 5-15 *^{27}Al MAS NMR spectra of BFS and silicate/carbonate-activated BFS at various curing times, as marked.*

An additional resonance is observed for both sample sets spanning the region from 20 to 0 ppm, possibly containing contributions from multiple Al sites, with the signal at δ_{obs} = 11 ppm corresponding to two Al^{IV} environments in octahedral formation within a hydrotalcite-type layered double hydroxide reaction product [194], [195], verifying the formation of such products, in line with observations from the TGA and XRD data. Like the observation for the resonance in the 80-60 ppm region, this hydrotalcite-associated resonance is very low in intensity at 1 day curing for the carbonate-activated sample, further indicating the lack of main reaction occurring at this time point, but then grows in intensity over time consistent with the continuous main reaction beyond the first few days. Furthermore, unlike for the silicate-activated slag, it is not clear if a signal at δ_{obs} = 5 ppm is present, corresponding to either a "third aluminate hydrate" on the surface of C-(N)-A-S-H [16], [188], [194], [196] or a silicate-bridging $[AlO_2(OH_4)]^{5-}$ site within C-A-S-H [197], suggesting that the silicate-activated slag

binders exhibit a greater extent of reaction than both the carbonate-activated and silicate-carbonate-activated samples.

Additionally, the slight broad resonance spanning 40 to 30 ppm that was observed for the silicate-activated slag sample and was tentatively linked to a charge-balancing pentahedral Al within the C-(N)-A-S-H gel interlayer, is not observed in the spectra for carbonate- or silicate-carbonate-activated slag. The presence of a resonance at δ_{iso} = 4.6 ppm corresponding to such Al sites has been observed in the study by Walkley *et al.* [58], not just for silicate-activated slag but also for mixed silicate-carbonate- and carbonate-activated slag binders of similar formulations to this study, in deconvolutions of ^{27}Al MAS NMR spectra, suggesting the formation of this pentahedral Al environment occurs regardless of the activator anion.

5.3.2.4.2 ^{29}Si MAS NMR Spectroscopy

For the ^{29}Si MAS NMR spectra of carbonate-activated and mixed silicate-carbonate-activated slag samples, in **Figure 5-16** and **Figure 5-17**, respectively, a broad mound is observed centring at ~73 ppm associated with unreacted slag particles, at all curing ages and generally reduces over time, consistent with the increasing extent of reaction at longer curing ages. Additionally, three clear resonances are visible between -75 and -85 ppm for both samples at all time points, however, their intensities vary. The signals at δ_{iso} = -78.6, -81.4, and -84.4 ppm correspond to Q^1(II), Q^2(1Al), and Q^2 units, respectively, indicative of the growth of a tobermorite-like C-S-H phase, likely to be a sodium and aluminium substituted calcium silicate hydrate (C-(N)-A-S-H) [58], [161], [205], consistent with previous studies into the structure of sodium silicate- and carbonate-activated slag cements [58], [69], [188], [205]. For both sample sets, there is an increase in Q^2 sites relative to Q^1 sites over time, which suggests an increase in the degree of polymerisation within the C-A-S-H phase. Moreover, a slight resonance at δ_{obs} = -87 ppm becomes visible at longer curing times, noticeably so in the spectra for the carbonate-activated

sample, which is attributed to Q^3(1Al), and whose presence means there is a significant amount of cross-linking in the C-(N)-A-S-H structure [58], [96].

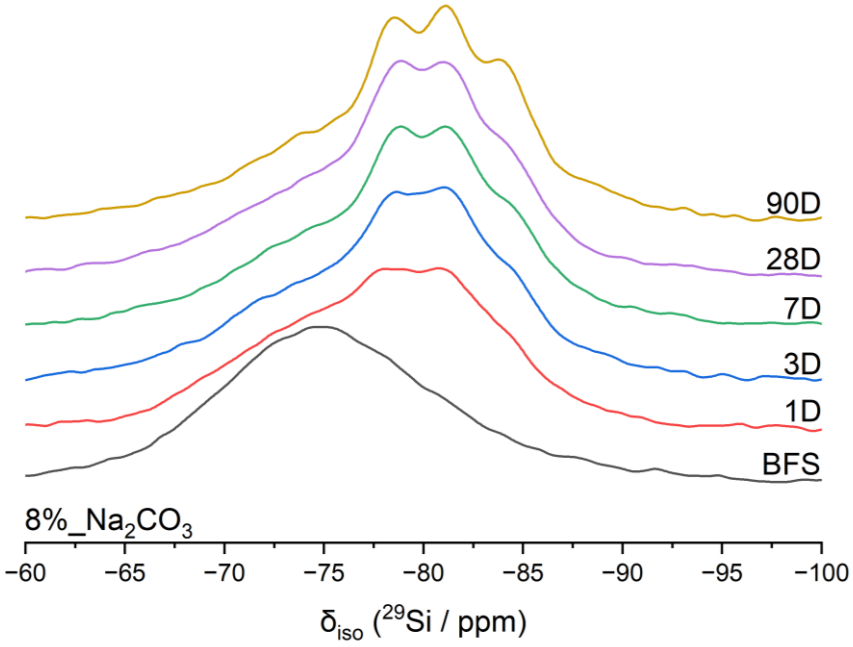

Figure 5-16 *^{29}Si MAS NMR spectra of BFS and sodium carbonate-activated BFS at various curing times, as marked.*

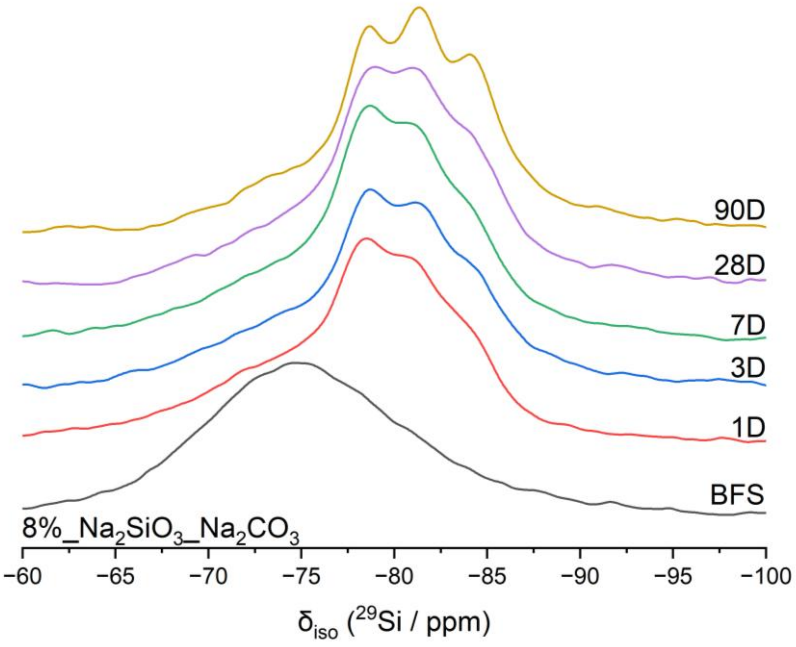

Figure 5-17 *^{29}Si MAS NMR spectra of BFS and carbonate/silicate-activated BFS at various curing times, as marked.*

The three main resonances identified in the region between δ_{obs} = -75 and -85 ppm are further probed in the deconvolution of the ^{29}Si MAS NMR spectra for both carbonate- and silicate-carbonate-activated slag samples, as shown in **Figure 5-18** and **Figure 5-19**, respectively. Additionally, the presence of a further five Si environments are identified in each sample, with signals at δ_{iso} = -76.0, -87.0, and -92.0, attributed to Q^1(I), Q^3(1Al) or Q^4(4Al), and Q^3 or Q^4(3Al), respectively, within the C-(N)-A-S-H. The identification of two distinct Q^1 sites in all samples, designated Q^1(I) and Q^1(II), correspond to the shielding variation from charge-balancing Na^+ or H^+ and Ca^{2+}, respectively, as determined by molecular dynamic studies [206].

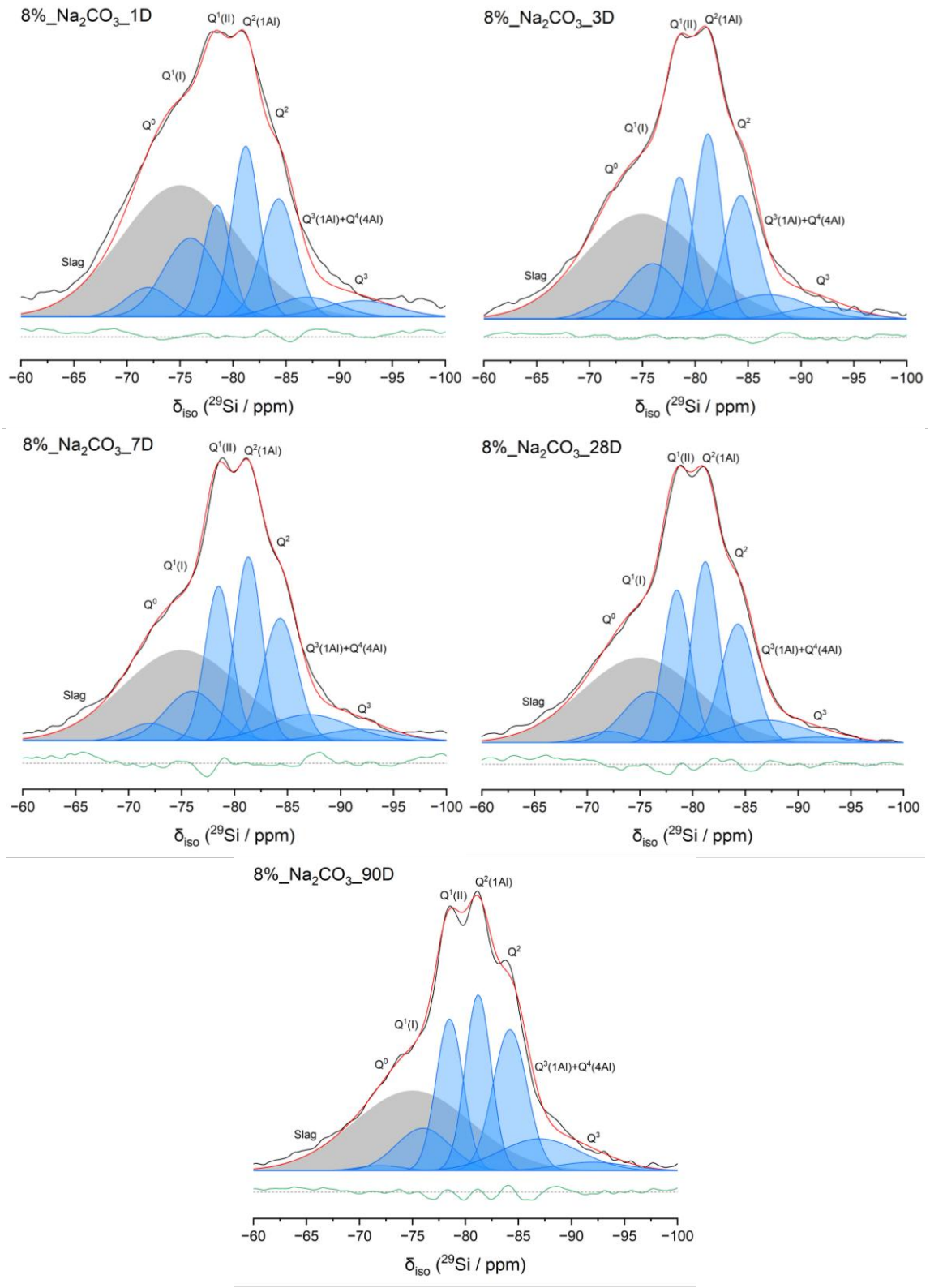

Figure 5-18 *^{29}Si MAS NMR spectra for slag activated with sodium carbonate, and their associated deconvolutions. In each case, the data are shown in black, the fit (shown in red) is the sum of the deconvoluted peaks, and the difference between the data and the fit is shown in green. Peaks attributed to Si sites in C-(N)-A-S-H are shaded in blue, while those attributed to sites within remnant anhydrous slag are shaded in grey.*

Small amounts of Q^0 sites are identified in the spectral deconvolutions at a resonance δ_{iso} = -72.0 ppm, as well as quantities of remnant anhydrous slag particles, represented by the broad Gaussian peak centring at δ_{iso} = -75.0 ppm, both of which reduce in quantity with curing time. Relative quantifications of Si sites as a function of sample curing age were determined by the deconvolution of ^{29}Si MAS NMR spectra and are recorded in **Table 5-2** and **Table 5-3** for carbonate- and silicate-carbonate-activated slag samples, respectively. For the carbonate-activated binder, ~56 % of slag particles have reacted in the first day and ~67 % after 90 days of curing, while the mixed activator sample demonstrated that ~64 % and ~82 % of slag had reacted at 1 and 90 days, respectively, in comparison to ~57 % after 1 day and ~84 % after 90 days for the silicate-activated sample. This proves the continual dissolution of slag over time in all of the activated slag binders, and an improved reaction for the two silicate-activated samples due to the uptake of silica into the solid binder.

Table 5-2 *NMR parameters for carbonate-activated slag samples, extracted from the deconvoluted ^{29}Si MAS NMR spectra.*

Sample	Parameter	Assignment								
		Unreacted slag	**Q^0**	**Q^1(I)**	**Q^1(II)**	**Q^2**	**Q^2(1Al)**	**Q^3 or Q^4(3Al)**	**Q^3(1Al)**	**Q^4(4Al)**
	δ_{iso} (ppm)	*-75*	*-72*	*-76*	*-78.6*	*-84.4*	*-81.4*	*-92*	*-87*	*-87*
	FWHM (ppm)	*13*	*5*	*6*	*3*	*3.8*	*3*	*8*	*9*	*9*
CO_3_1D	Relative integral area (%)	43.9	3.8	12.1	8.6	11.5	13.2	3.4	3.5	0.0
CO_3_3D	Relative integral area (%)	38.3	2.6	9.4	12.0	13.2	15.6	2.8	5.8	0.4
CO_3_7D	Relative integral area (%)	34.9	2.6	8.8	13.8	13.8	16.4	2.8	6.2	0.9
CO_3_28D	Relative integral area (%)	34.8	1.8	9.7	14.5	14.3	17.2	1.4	5.5	1.0
CO_3_90D	Relative integral area (%)	32.7	0.8	8.1	14.4	16.9	15.9	2.2	7.1	2.0

There is a resonance at δ_{iso} = -92.0 ppm, assigned to Q^3 and/or Q^4(3Al) Si environments, as well as one another at δ_{iso} = -87.0 ppm, assigned to either Q^3(1Al) or Q^4(4Al) [160], [207]. The resonance at δ_{iso} = -87.0 ppm increases steadily over time for both carbonate- and silicate-carbonate-activated samples, whilst the peak at signal δ_{iso} = -92.0 ppm increases for the mixed

activator sample and decreases for the carbonate-activated sample over time. For these alkali-activated samples, the resonance at δ_{iso} = -87.0 ppm is assigned to both the typical crosslinked Q^3(1Al) Si environments in C-(N)-A-S-H and also some Q^4(4Al) environments in a polymerised Al-rich N-A-S-H phase, aligning with the structural constraints of the "cross-linked substituted tobermorite model" (CSTM) proposed by Myers *et al.* [161]. This N-A-S-H phase forms in addition to C-(N)-A-S-H in systems with high Al and Na content, and is made up of Q^4(4Al) and Q^4(3Al) sites, as seen in previous studies on silicate-activated slag binders [58], [194]. Moreover, it is necessary to attribute part of the resonance at signal δ_{iso} = -92.0 ppm to Q^4(3Al) as well as Q^3, as no aluminosilicate phase can contain solely Q^4(4Al) units [209], and as such an additional representation of Q^4-type units is required. The existence of this N-A-S-H gel in addition to the more typical C-(N)-A-S-H has been observed in previous studies of both silicate- and carbonate-activated slag binders [58], [71], [83], [92], [188], [194], [208]. Some studies demonstrated that aluminium-rich geopolymers contain almost entirely Q^4(3Al) and Q^4(4Al) units, which supports such identifications in the spectral deconvolutions in this study, suggesting that alkali-activated slag binders could include disordered, zeolite-like products likened to the N-A-S-H structures usually found in low-calcium aluminosilicate precursor-based AACs [55], [209], [210]. The observation of the decreased quantities of Si sites assigned to δ_{iso} = -92.0 ppm over time for the carbonate-activated binder, indicates a decrease in Q^3 sites, rather than Q^4(3Al), due to the increase of Q^4(4Al) sites observed and the requirement of both Q^4(3Al) and Q^4(4Al) to co-exist in the formation of a N-A-S-H.

There are notable amounts of Q^2(1Al) sites present in both sample sets from day 1 of curing, which steadily increases with curing age, indicating high levels of aluminium substitution in the C-(N)-A-S-H structure, and the notable existence of Q^3(1Al) units at early age and their growth over time suggests that C-(N)-A-S-H is significantly crosslinked and this crosslinking only improves with curing. The growth of Q^4(4Al) and Q^4(3Al) environments begins from 7

days curing and steadily increases with time, indicating the precipitation of N-A-S-H at similar rates for both carbonate- and silicate-carbonate-activated slag binders.

Table 5-3 *NMR parameters for silicate and carbonate-activated slag samples, extracted from the deconvoluted ^{29}Si MAS NMR spectra.*

Sample	Parameter	Assignment								
		Unreacted slag	**Q^0**	**Q^1(I)**	**Q^1(II)**	**Q^2**	**Q^2(1Al)**	**Q^3 or Q^4(3Al)**	**Q^3(1Al)**	**Q^4(4Al)**
	δ_{iso} (ppm)	*-75*	*-72*	*-76*	*-78.6*	*-84.4*	*-81.4*	*-92*	*-87*	*-87*
	FWHM (ppm)	*13*	*5*	*6*	*3*	*3.8*	*3*	*8*	*9*	*9*
SiO_3_CO_3_1D	Relative integral area (%)	35.7	2.3	8.7	16.7	14.5	16.5	3.0	2.7	0.0
SiO_3_CO_3_3D	Relative integral area (%)	29.4	2.3	8.4	16.4	15.3	16.8	6.1	5.0	0.3
SiO_3_CO_3_7D	Relative integral area (%)	29.6	1.5	8.7	19.2	15.6	17.7	2.4	4.8	0.5
SiO_3_CO_3_28D	Relative integral area (%)	23.5	1.5	9.0	17.8	18.3	18.5	3.0	7.6	0.8
SiO_3_CO_3_90D	Relative integral area (%)	18.4	1.6	7.8	17.6	20.7	19.6	4.4	7.9	2.1

Moreover, the relative sum of Q^1(I) and Q^1(II) sites remains relatively constant from 1 to 90 days for both sample sets; for the mixed activator the relative amounts of the individual sites remains the same, while for the carbonate-activated sample, the relative amount of Q^1(I) sites decreases at a similar rate to the increase in relative amounts of Q^1(II) sites as time progresses. This suggests an increased amount of calcium ions in the interlayer of the C-(N)-A-S-H structure over time, consistent with the slower dissolution of slag particles for carbonate-activated binders.

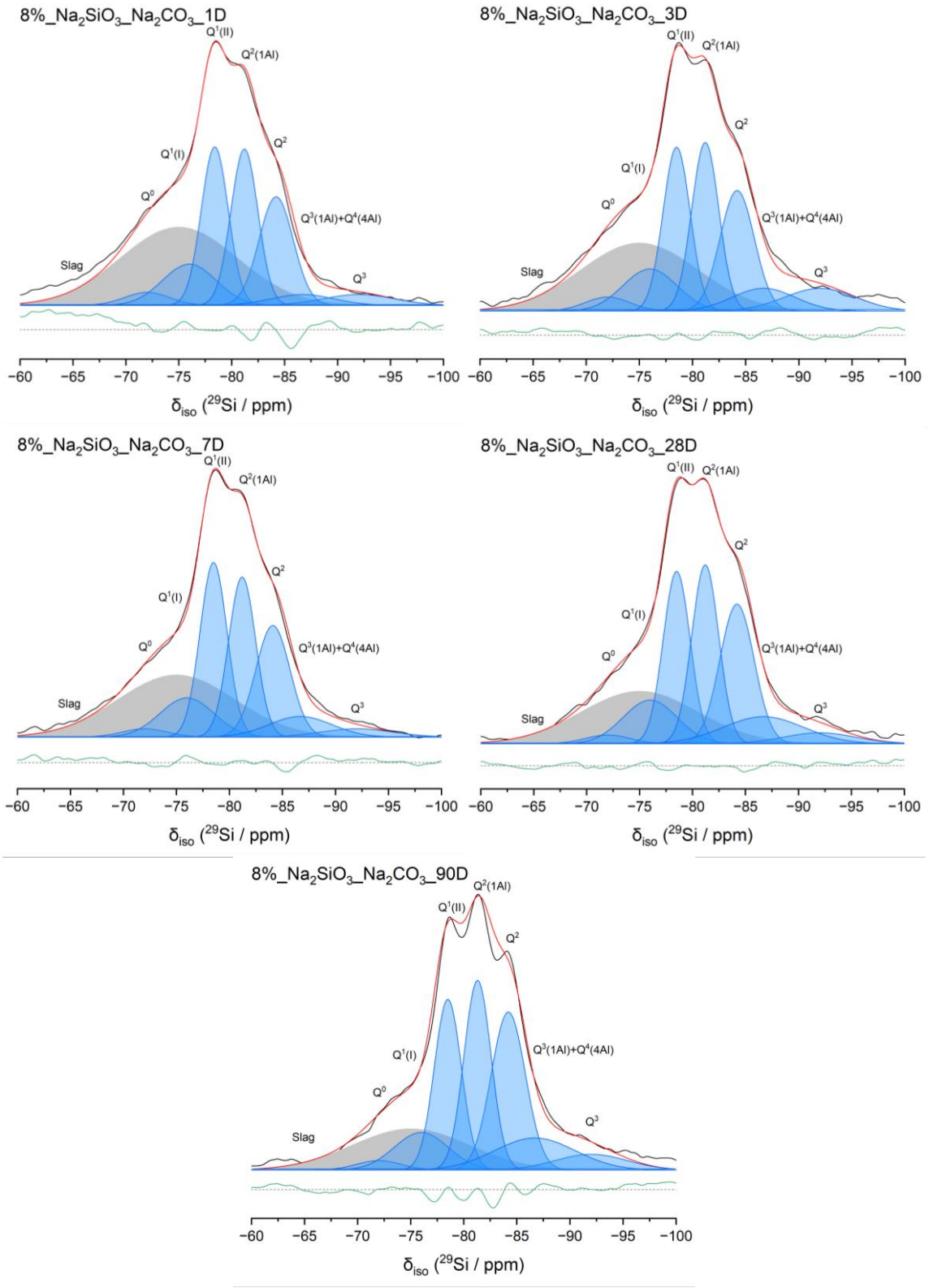

Figure 5-19 *^{29}Si MAS NMR spectra for BFS activated with sodium silicate/carbonate, and their associated deconvolutions. In each case, the data are shown in black, the fit (shown in red) is the sum of the deconvoluted peaks, and the difference between the data and the fit is shown in green. Peaks attributed to Si sites in C-(N)-A-S-H are shaded in blue, while those attributed to sites within remnant anhydrous slag are shaded in grey.*

An increase in quantity of $Q^2(1Al)$ and $Q^3(1Al)$ is observed for both samples over time, which correlates to the increase in mean chain length of the C-(N)-A-S-H as curing time increases (**Figure 5-20**). Furthermore, the increase of these sites aligns with the apparent increase in tetrahedral Al sites in **Figure 5-14** and **Figure 5-15** for both carbonate-activated and silicate-carbonate-activated BFS, respectively, which in turn aligns with the general increase in Al^{IV}/Si over time shown in **Figure 5-20**, which further suggests the greater extent of crosslinking of C-(N)-A-S-H as curing time progresses. The formation of the disordered Q^4-containing product, N-A-S-H, typically causes a reduction in crosslinking of C-(N)-A-S-H structure, however, the quantifications based on spectral deconvolutions of such Q^4 sites suggest very small amounts of N-A-S-H is forming in these carbonate-activated slag cements, likely not sufficient enough to affect the crosslinking of the main reaction product.

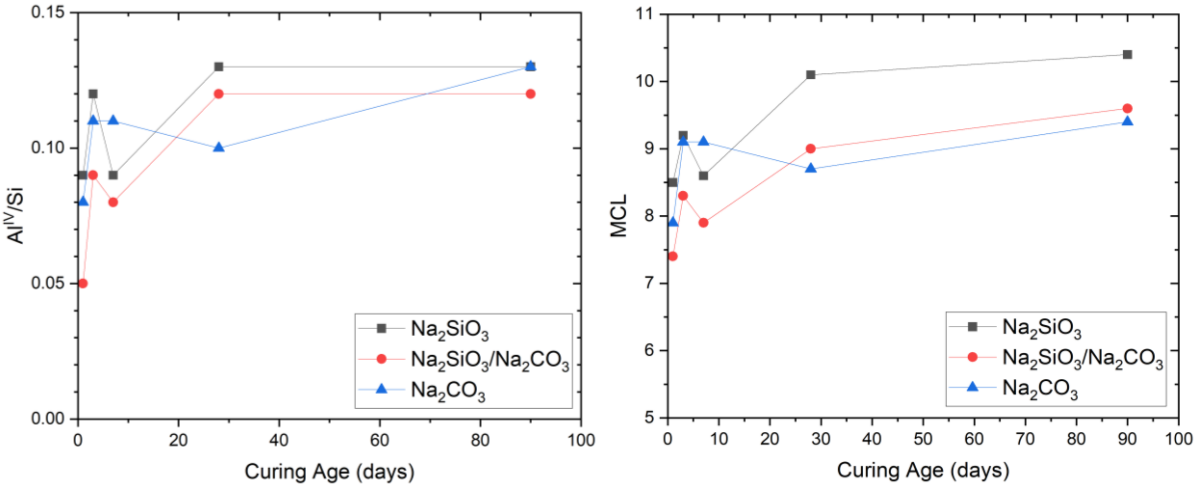

Figure 5-20 *Al^{IV}/Si ratio and MCL in carbonate- and silicate/carbonate-activated BFS over time, calculated using the CSTM and 29Si MAS NMR spectral deconvolutions.*

5.3.2.5 SEM-EDX

Scanning electron microscopy can be used for probing the surface structure of cementitious binders, and when partnered with energy dispersive X-ray (EDX) analysis, the elemental composition of the sample surface can be determined, allowing the study of structural evolution

over different curing lengths. SEM images for alkali-activated slag binders, as seen in **Figure 5-21** and **Figure 5-22**, display a generally dark grey bulk structure, representing reaction phases, including the likes of C-A-S-H, hydrotalcite, and calcium carbonate polymorphs amongst others, surrounding lighter grey unreacted slag particles. Features, such as cracks and striations, may also be visible, due to the use of fractured samples rather than cutting in this study. Additionally, some pores are visible at this magnification, but it is likely that most pores exist on the nanoscale and so are not as prominent in these images.

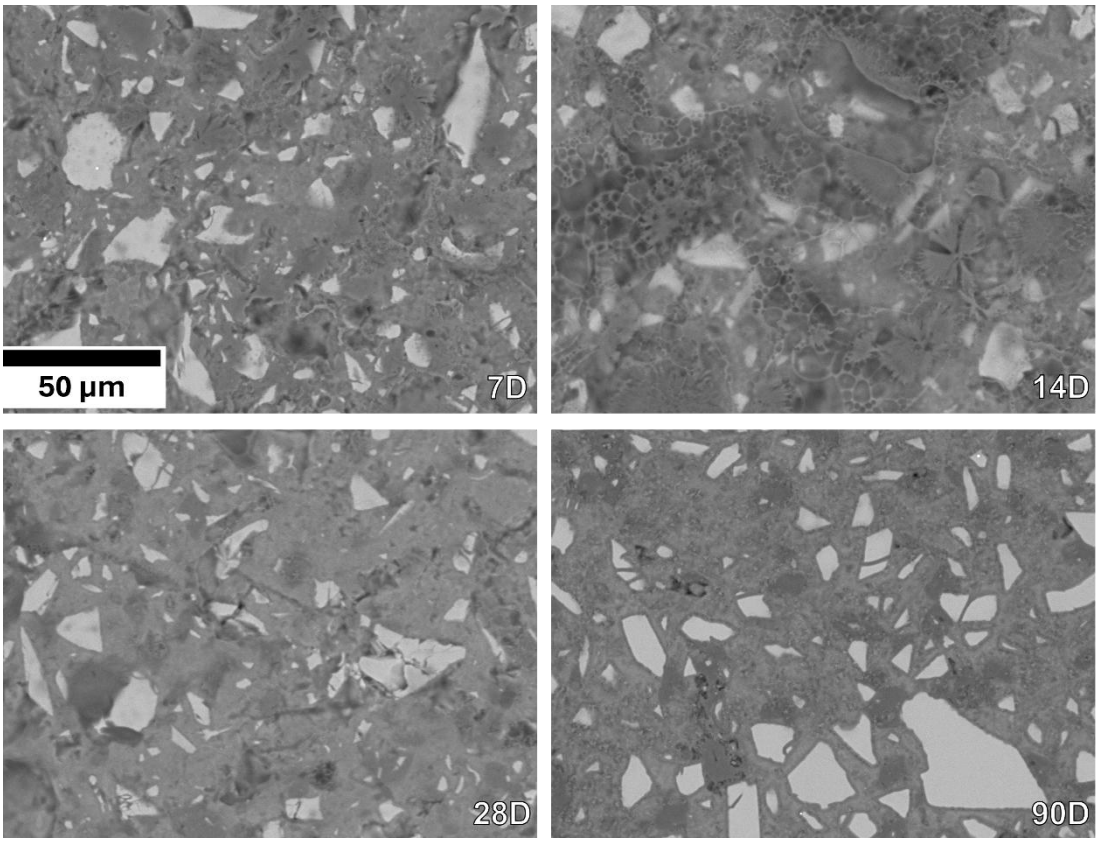

Figure 5-21 *SEM images for carbonate-activated BFS, at 1000x magnification, for various curing times, as labelled.*

Images for the carbonate-activated BFS sample (**Figure 5-21**) show minimal physical change over time, other than the bulk structure becoming more cohesive, particularly noticeable at 90 days curing, surrounding similar amounts of unreacted slag particles. In comparison, the mixed silicate-carbonate-activated sample (**Figure 5-22**), also contains unreacted slag particles but in

much smaller amounts and of a smaller size, indicative of the silicate activator component increasing the dissolution of slag. Similarly to both carbonate- and silicate-activated samples, the mixed-activated slag binder displays a much more cohesive bulk structure at 90 days with further reduced amounts of slag particles in the bulk, aligning with the increased extent of reaction with curing time. It is noted that the solely carbonate-activated sample in **Figure 5-21** includes bloom-like features on the surface, noticeable at 7 and 14 days, which may be due in part to the solvent exchange and epoxy impregnation during sample preparation.

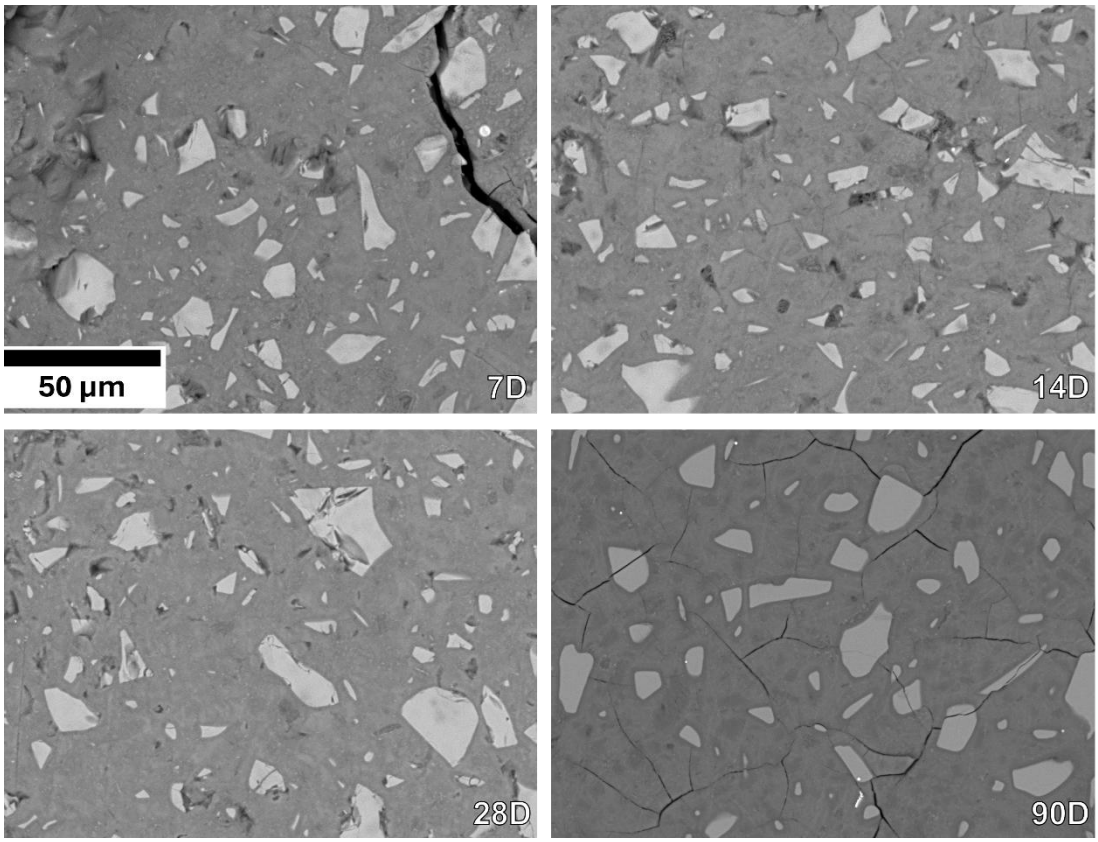

Figure 5-22 *SEM images for silicate and carbonate-activated BFS, at 1000x magnification, for various curing times, as labelled.*

Elemental mapping for the carbonate-activated sample in **Figure 5-23** shows a clear distinction between slag particles – rich in silicon, aluminium and calcium – and the surrounding hydrated bulk structure, which mostly consists of sodium, magnesium, and carbon, at 7 days of curing. However, by 90 days, the slag particles, although still clearly distinguishable from the bulk

structure, consist mostly of silicon with small amount of aluminium, likely due to the aluminium from the slag incorporating more easily into the C-A-S-H structure due its weaker bonding nature. Furthermore, the bulk hydration structure appears to have more elements incorporated more evenly at this later curing age. These observations for evolution of chemical composition align with the expected increased reaction extent with time, meaning a greater amount of hydrate phases forming. For both 7- and 90-day samples, there are distinct areas of high sodium concentration, likely due to the sodium ions from the activating solution existing on the surface rather than incorporating in C-A-S-H or forming the secondary N-A-S-H phase, as supported by the ^{29}Si MAS NMR spectral deconvolutions discussed in *Section 5.3.2.4.2.*

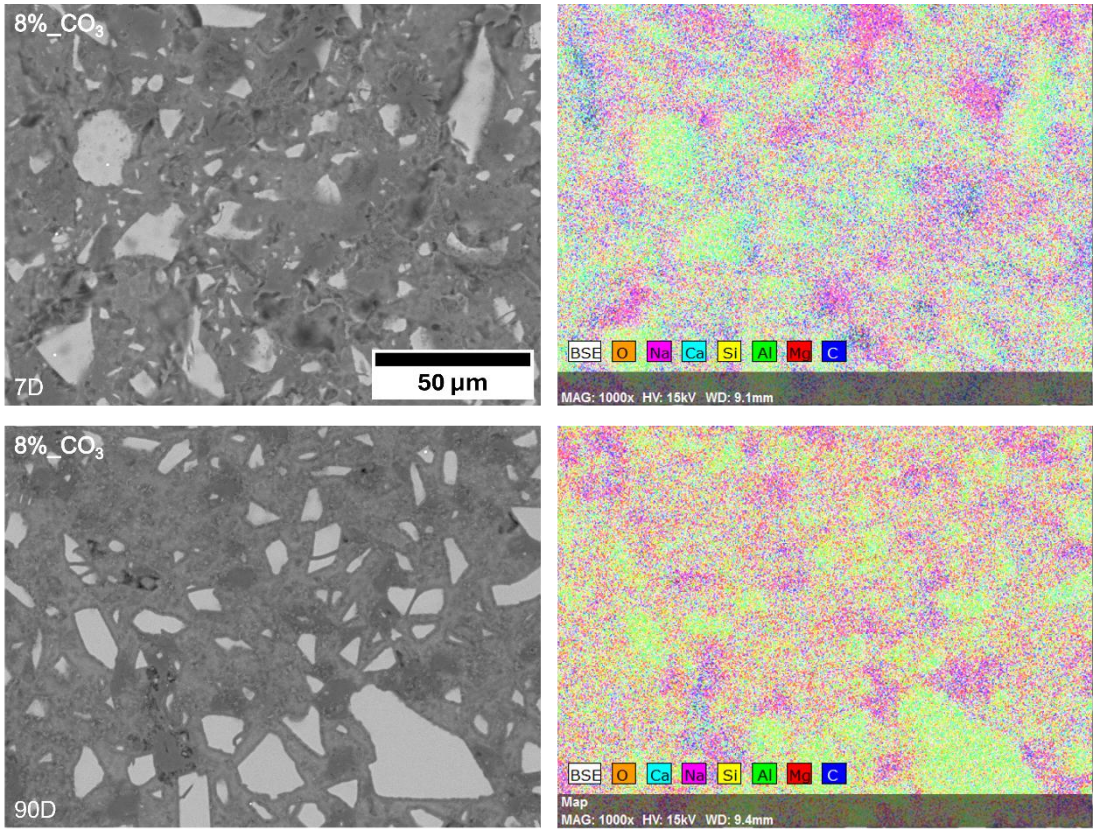

Figure 5-23 *Elemental mapping for carbonate-activated BFS, cured at 7 and 90 days, as labelled.*

Furthermore, the elemental maps acquired via EDX for the mixed silicate-carbonate-activated slag binder in **Figure 5-24** also display areas rich in aluminium and silicon associated with

remnant slag particles surrounded by a bulk structure containing mostly calcium, magnesium, sodium and oxygen, and some silicon, with an observed increase in silicon and magnesium at 90 days, indicative of increased amounts of hydrate phases, C-(N)-A-S-H and/or N-A-S-H and hydrotalcite, respectively, at later curing ages, aligning with observations from ^{27}Al and ^{29}Si MAS NMR spectra.

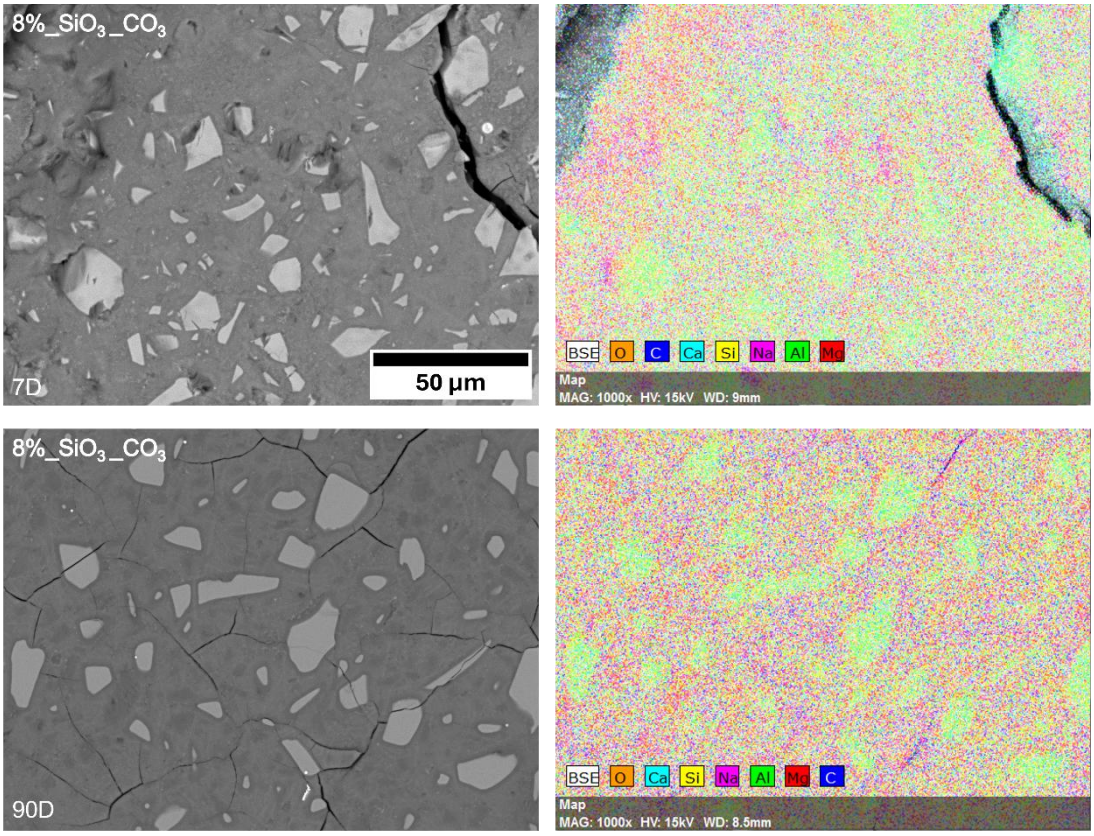

Figure 5-24 *Elemental mapping for silicate/carbonate-activated BFS, cured at 7 and 90 days, as labelled.*

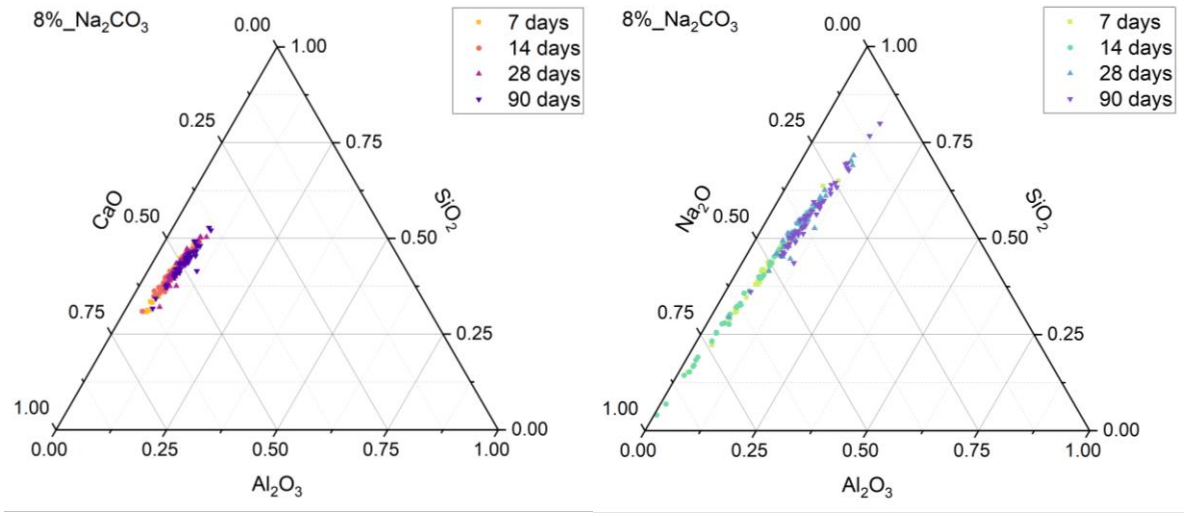

Figure 5-25 *Ternary systems of carbonate-activated slag cured for 7, 14, 28, and 90 days, as determined by SEM-EDX analysis. (L) Ternary CaO – Al_2O_3 – SiO_2 system (neglecting Na_2O content), and (R) Ternary Na_2O – Al_2O_3 – SiO_2 system (neglecting CaO) content, showing elemental composition.*

Ternary systems for samples have been developed based on the elemental composition data from EDX for carbonate- and mixed silicate-carbonate-activated slag samples, as illustrated in **Figure 5-25** and **Figure 5-26**, respectively, to aid in the understanding of phase evolution with curing age. The ternary CaO-Al_2O_3-SiO_2 system for both samples remains generally consistent as curing age increases, with the structure here aligning with previous studies of alkali-activated slag binders [53], [211], [212] as well as that of synthetic C-(A)-S-H and N-A-S-H gels formed by a sol-gel method [213]. The composition of both samples at all curing ages lies within the region associated with the C-(N)-A-S-H gel [53], [161], [214], and the Al/Si ratio remains relatively constant over time for the mixed activator sample, but increases slightly for the carbonate-activated sample. Furthermore, there is a small decrease in calcium for the carbonate-activated sample over time, while for the silicate-carbonate-activated binder, the calcium content maintains mostly constant. This slight decrease may be due to the reduced amounts of slag particles observed in the sample over time, meaning the calcium may not be on the sample surface, but rather integrated deeper in the sample.

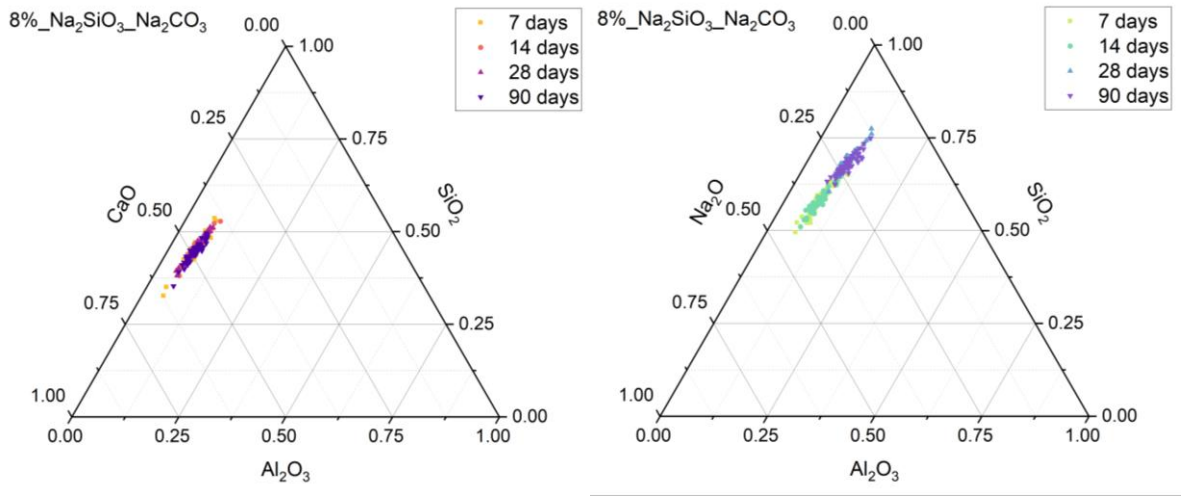

Figure 5-26 *Ternary systems of silicate/carbonate-activated slag cured for 7, 14, 28, and 90 days, as determined by SEM-EDX analysis. (L) Ternary CaO – Al_2O_3 – SiO_2 system (neglecting Na_2O content), and (R) Ternary Na_2O – Al_2O_3 – SiO_2 system (neglecting CaO) content, showing elemental composition.*

On the other hand, the ternary Na_2O-Al_2O_3-SiO_2 system for the mixed silicate-carbonate-activated sample (**Figure 5-26**) reveals a general decrease in Na_2O over time, which is unexpected as typically sodium ions integrate into the interlayer space of C-A-S-H phases over time, however, it is noted that as SEM-EDX measurements are of the top layer of the sample, it is probable that the sodium is more integrated in the sample over time, rather than remaining on/near the surface. In contrast, the same ternary system for the carbonate-activated sample (**Figure 5-25**) shows a massive reduction in sodium over time, with the 14-day sample containing significant amounts. Using the assumption that the sodium that is incorporated in the interlayer of C-A-S-H is not detected by the EDX measurements, it is likely that the sodium here exists on the surface of the sample from the slag particles and activator, and is likely the bloom-like features observed in the SEM images of the early age sample (**Figure 5-21**). Additionally, for both samples, a slight increase in Al/Si is observed as curing time increases, which corroborates the findings from the NMR spectroscopy, where Al^{IV} was seen to increase with time, likely indicating the further integration into the C-A-S-H phase or the formation of an aluminium-rich secondary reaction product, as the reaction progresses.

5.3.3 Physical Properties

The understanding of physical behaviour and mechanical properties of cementitious binders is necessary to determine appropriate applications. These properties are often influenced by chemical phase structure, which is typically dependent on the initial mixing formulation. As such, the physicomechanical properties of the carbonate- and silicate-carbonate slag binders will be explored in this section, as well as how the chemistry and phase composition impacts such properties.

5.3.3.1 Workability and Setting Time

The average mini slump diameters (**Figure 5-27**) illustrate the influence of the silicate activator on the workability of alkali-activated slag binders, with the blended silicate/carbonate-activated sample having a much greater spread than the solely carbonate-activated sample, not too dissimilar from the solely silicate-activated sample. This is likely due to the known behaviour of sodium silicate to act as a dispersant in particle suspensions, as previously discussed, which results in a low yield stress and subsequent greater mini-slump spread for silicate-activated slag pastes [172], [215]. On the other hand, the carbonate-activated slag sample has a rather low slump diameter at ~70 mm, reflecting a less than desirable workability. Stefanini *et al.* [227] used a similarly composed BFS activated with sodium carbonate at a 5 wt.% Na_2O dosage and a water-to-binder ratio of 0.38, and found the slump diameter 30 minutes after mixing to be 79 mm, using the same mini slump apparatus as in this study. This value is comparable to that measured here as the higher activator dosage in this work is likely to further reduce the workability. Another study, conducted by de Hita and Criado [127], found for a similar slumping apparatus, the slump diameter of sodium carbonate-activated BFS immediately after mixing to be ~42 mm, however, the slag used had a lower SiO_2 content (32.3 wt.%) and a higher CaO content (45.7 wt.%) than that used in this study, and a dosage of 8 wt.% Na_2CO_3 was used compared to the 8 wt.% Na_2O of the activator here. The effective

increase in Na_2O content of the activator in addition to the reduced CaO and increased SiO_2 content in the slag used here likely cause the slightly improved workability compared to the study by de Hita and Criado [127]. The values measured here, as well as those from literature, suggest poor workability within the first few minutes after mixing, which is known to lessen further in mere minutes [76], [228], [229]. Ideally for use in industrial practice, a stable rheology is required between the end of mixing and use, which typically varies between 1 and 3 hours.

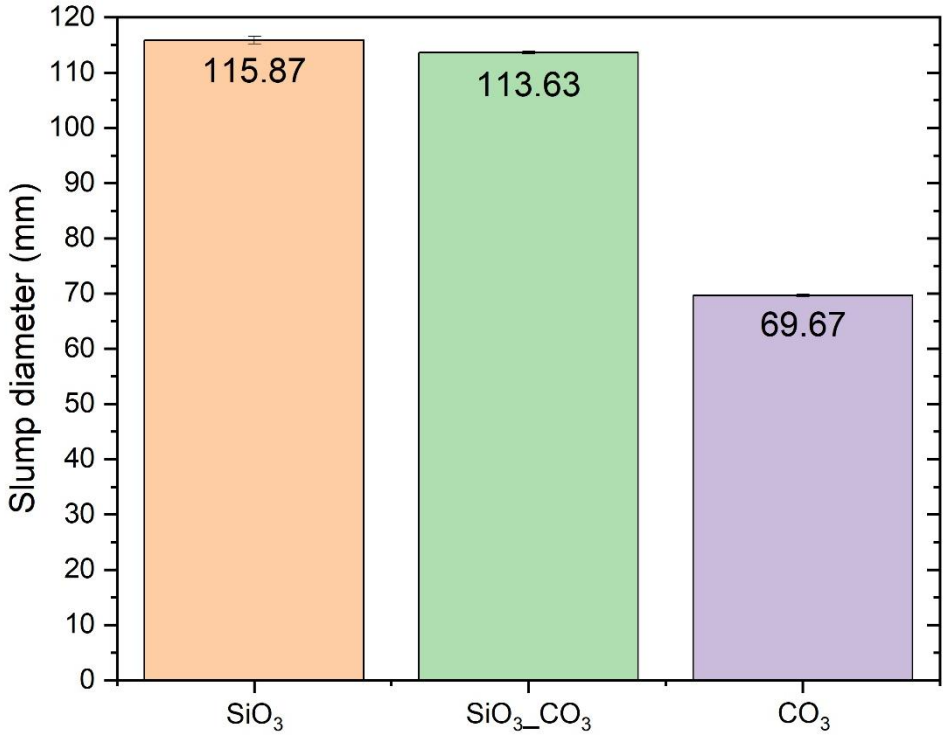

Figure 5-27 *Mini slump diameter values for carbonate-activated BFS, in comparison to silicate-activated BFS, as labelled.*

Furthermore, initial and final setting times were determined using a simple automatic Vicat apparatus. As expected, the carbonate-activated sample took the longest to fully set according to the Vicat setup, while the silicate-activated sample set the fastest, and the mixed activator sample set in between the sole activator samples. Despite following the expected trend, the carbonate-activated sample set quite quickly, unlike previous reports of much longer setting

times in the range of days rather than hours [71], [73], [74], [77], [227]. However, the setting times measured here for the sodium carbonate-activated sample are comparable to those found in previous studies [84], [127], [230] with similar sample formulations, indicating that the much slower activation reaction does not necessarily equate to a longer setting time. Similarly to the silicate-activated sample, as discussed in *Section 4.3.3*, the timing of the heat release due to the dissolution of precursor illustrated in the calorimetry data, is more similar to the setting than the onset of the main reaction, where the strength-giving phases form, which is typically associated with setting time. As such, it is likely that the dissolution of species immediately after mixing as well as the initial formation of any reaction products, be it C-A-S-H for the samples activated with sodium silicate or calcium carbonate polymorphs for the solely carbonate-activated sample, fills spaces between slag particles and thus causes the hardening of the material. Furthermore, it is more likely that the pH of the activating solution, which influences the rate of slag dissolution, is responsible for the initial setting time, while the formation of reaction products is the prime influencer of the final setting time, and thus hardening of the binder.

Table 5-4 *Setting times for carbonate-activated BFS, in comparison with silicate-activated BFS, as determined by Vicat apparatus.*

Sample	Setting Time	
	Initial	**Final**
8%_Na_2SiO_3	1 h 25 m	2 h 25 m
8%_Na_2SiO_3_Na_2CO_3	2 h 25 m	4 h 10 m
8%_Na_2CO_3	3 h 10 m	4 h 40 m

5.3.3.2 Viscometry

Figure 5-28 presents the flow curves of alkali-activated slag cements with the corresponding Herschel-Bulkley model parameters outlined in **Table 5-5**, which can be used to evaluate the

fresh properties of the binders based on their activating solution. The sodium carbonate-activated slag exhibits the highest yield stress, while the inclusion of sodium silicate as well as sodium carbonate greatly reduces the yield stress to a value very similar to the solely silicate-activated slag. These observations are consistent with the previously discussed mini slump data. The mixed activator sample appears to behave as a Bingham-type fluid, having a flow index (n) of ~1, similar to the silicate-activated sample, while the carbonate-activated slag binder exhibits shear thinning behaviour as its flow index is lower than 1, consistent with previous studies [117], [119], [231], meaning that its viscosity decreases with increasing stress. This indicates that the addition of sodium silicate into a carbonate-activated system not only improves the rate of reaction, but also the rheological properties, favouring the dispersive nature of silicate to improve its workability.

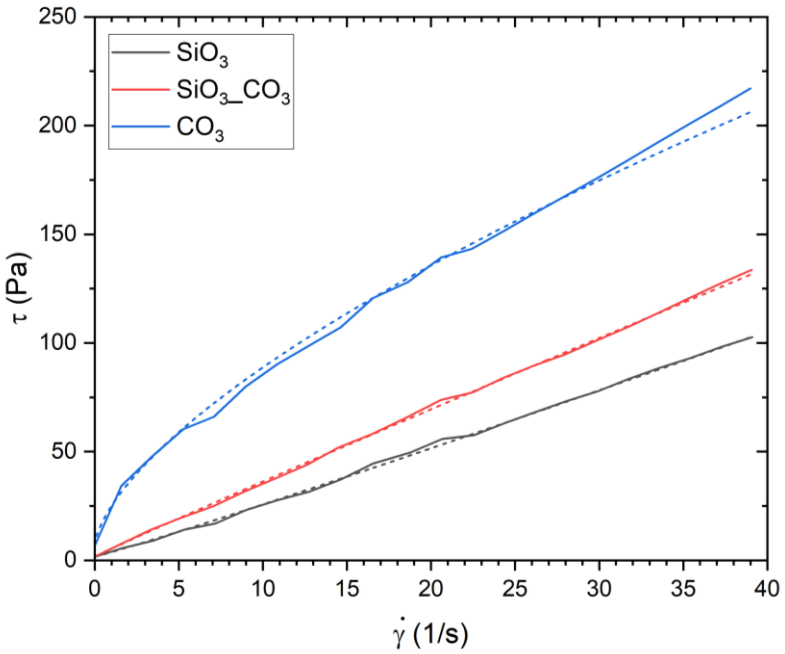

Figure 5-28 *Rheology of carbonate-activated BFS, in comparison with silicate-activated BFS. Experimental data are the solid lines, and the model fits are the dotted lines.*

Table 5-5 *Herschel-Bulkley model parameters for carbonate-activated BFS, fitted to the curve in* ***Figure 5-28****.*

Sample	**τ_0**	**k**	**n**
8%_Na_2SiO_3	1.69	2.11	1.06
8%_Na_2SiO_3_Na_2CO_3	1.56	3.25	0.99
8%_Na_2CO_3	6.77	18.22	0.65

5.3.3.3 Compressive Strength

Compressive strength measurements at 7 and 28 days of curing for the carbonate- and blended silicate-carbonate-activated slag pastes are presented in **Figure 5-29** in comparison with the strength values previously discussed for the silicate-activated slag sample.

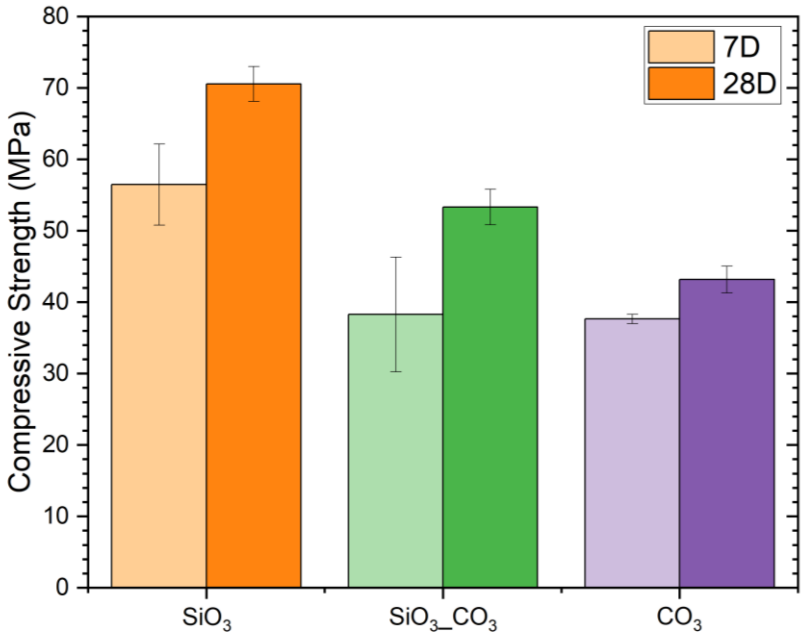

Figure 5-29 *Compressive strength values for carbonate-activated BFS at 7 and 28 days, in comparison to silicate-activated BFS, as labelled.*

The values measured here for both 7- and 28-day compressive strength for the carbonate-activated slag sample are much higher than most found in the literature with a similar experimental composition – water-to-binder ratio and activator dosage [69], [71], [84], [230],

[232]. However, it is noted that the use of pastes in this study is associated with some increase in strength compared to mortars, which were used in the aforementioned studies. A study by Jin and Al-Tabbaa [233] found that for BFS activated with Na_2CO_3 at a dosage of 8 % by weight of BFS, but a water-to solids ratio of 0.32, the compressive strength values of pastes at 7 and 28 days curing were higher than reported here at values of ~52 and ~62 MPa, respectively. This elevated value is likely due to the slight difference in formulation, including the lower water-to-binder ratio as well as their dosage being defined as the entire activator at 8 % by weight of precursor compared to 8 wt.% of Na_2O in this study. Generally, the lower strength development of carbonate-activated slag binders is associated with the low initial pH and the formation of sodium calcium carbonate and other calcium carbonate polymorphs, retarding the reaction process and thus the subsequent precipitation of C-A-S-H – the main strength-giving phase of alkali-activated slag binders.

Unlike findings for reaction kinetics and mechanisms, structural evolution, and fresh-state physical properties, the blended silicate-carbonate-activated binder appears to tend towards the solely carbonate-activated sample rather than the silicate-activated sample when it comes to compressive strength, with 7-day strength values for the silicate-carbonate- and carbonate-activated samples being within 1 % of each other. However, it is noted that the large calculated standard deviation for the strength of the mixed activator sample at 7 days means that its strength may possibly sit halfway between the two sole activator samples, aligning with the increased formation of the strength-giving C-A-S-H phase associated with the silicate-containing sample. Moreover, the 28-day compressive strength value for the silicate-carbonate-activated sample is approximately halfway between the values for silicate- and carbonate-activated slag samples, indicating that, despite the silicate component heavily influencing the reaction mechanisms and kinetics and the fresh-state properties, the strength and likely durability are more equally influenced by both silicate and carbonate components in the

activator. This somewhat corroborates studies by Bernal *et al.* [69], [71], where a blended sodium silicate/carbonate slag mortar system of very similar formulation to that used in this study resulted in compressive strength values of 44 and 50 MPa, however, their findings suggested a tendency towards the physical behaviour of silicate-activated slag binders at a later age.

Typically, 28-day compressive strength values are used as a guide for the viability and subsequent appropriate application of a cementitious building material, with the strength at this time expected to be approximately 99 % of the total potential strength of the material. Similarly, a benchmark of 65 % of the 28-day strength of the material is expected to be reached by 7 days. In this case, the 7-day compressive strength is approximately 87 and 72 % of the measured 28-day strength for the carbonate- and silicate-carbonate-activated slag pastes, respectively, indicating a rapid early strength development.

According to the American Concrete Institute [221], concrete (made using Portland cement) specifications require a 28-day compressive strength value of: ~17-28 MPa for use in foundations, slabs, and footings; ~34.5 MPa for high-strength uses including beams and girders; and at least 52 MPa for high-load-bearing structures. As concrete is known to be stronger than cement, due to the incorporation of aggregates in the matrix, the values measured in this study for both the solely carbonate- and silicate-carbonate-activated binders suggest that these alkali-activated binders are suitable in applications where Portland cement-based concrete is utilised.

5.4 Conclusions

This chapter explored the use of sodium carbonate for the alkali activation of blast furnace slag, with a comparison to sodium silicate-activated slag, as well as a binder activated with a

50:50 wt.% blend of sodium silicate and sodium carbonate. The early age reaction was explored, as well as the binders' structural evolution and their fresh-state and mechanical properties, in order to assess the influence of the activator on the performance of alkali-activated slag binders.

Calorimetry findings show that for the carbonate-activated slag, the onset of the main reaction occurs after ~48 hours and lasts for nearly 24 hours, with a lower but continual heat output, evidencing a slower reaction compared to the silicate-activated sample. Furthermore, there is an initial heat output peaking in the first 2 hours after mixing, which is then followed by a long dormant period, before the main reaction eventually occurs, suggesting an initial preferential reaction that inhibits the main reaction. Further *in-situ* characterisation revealed that the carbonate ions from the activator are preferentially reacting with the calcium from the slag (and the sodium in the system) to form (sodium) calcium carbonate polymorphs in the early hours of reaction, which in turn is preventing the formation of C-A-S-H and causing the observed dormant period. Once these carbonate ions are exhausted, the main reaction then occurs. In terms of phase assemblage and structural evolution, analysis techniques (TGA, XRD, FTIR) revealed that by 3 days, there was clear formation of a calcium aluminosilicate phase, which continued to form and polymerise over time, verified by ^{27}Al and ^{29}Si MAS NMR spectroscopy, which also showed the eventual formation of a N-A-S-H structure in addition to the earlier formed C-N-A-S-H, but in lower quantities than observed for the silicate-activated binder. Additionally, hydrotalcite was detected as a secondary reaction product, as well as the initially formed calcium carbonates, which increased in quantity slightly with some atmospheric carbonation. Furthermore, the fresh-state properties of the carbonate-activated slag binder were less than desirable, with a higher yield stress determined compared to the silicate-activated sample, and the sample having a shear-thinning nature, which also resulted in a smaller slump diameter than the control sample. In terms of compressive strength, the carbonate-activated

sample has a slower development between 7 and 28 days than the control sample, and its 28-day strength, which is often taken as an indicator for ultimate compressive strength, is ~40 % less than the silicate-activated sample, likely due to the slower formation and reduced polymerisation rate of C-A-S-H . Nonetheless, the strength values determined are within the applicable range for use in the construction of foundations, slabbing, and girders, but not high load-bearing structures.

On the other hand, one might expect the mixed silicate-carbonate-activated slag system to behave in the middle of both the solely carbonate- and silicate-activated systems due to its 50:50 wt.% nature, however, it is observed to behave more similarly to the solely silicate-activated slag binder, favouring a quicker rate of reaction, with the main reaction occurring within 24 hours after mixing. Furthermore, DRIFTS analysis revealed the rapid dissolution of species and the subsequent formation of Si-O-Si bonds, suggesting the early formation of C-A-S-H, analogous to the early reaction of the solely silicate-activated binder. Additionally, the structural evolution and physical properties of the mixed activated-sample tended towards the behaviour of the silicate-activated sample, with the slight exception of compressive strength, whose values did sit more centrally between those for the silicate- and carbonate-activated samples. With regards to structural phase evolution, C-A-S-H-type phases were observed to form within the first day after mixing, with some N-A-S-H structures forming at later curing ages, however, the former saw a slower rate of polymerisation and increase in crosslinking than for the control sample, but still higher than that for the carbonate-activated sample. Additional reaction products were observed, such as hydrotalcite and calcium carbonate polymorphs, however, the latter formed in much lower quantities than for the carbonate-activated sample, due to the influence of sodium silicate preventing the initial preferential reaction associated with sodium carbonate from occurring, and instead these products are a result of atmospheric carbonation, similar to the silicate-activated sample. Moreover, the inclusion of sodium silicate

positively influenced the fresh-state properties, with the slump diameter, and rheological behaviour of the mixed activated samples being very similar to the control sample.

Overall, the use of sodium carbonate in the formation of alkali-activated slag binders leads to a slow rate of reaction due to both its lower alkalinity and an initial preferential reaction hindering the formation of the primary binding and strength-giving phase, C-A-S-H. Additionally, the early formation of calcium carbonate polymorphs negatively affects the fresh-state properties of the carbonate-activated binders, increasing the materials yield stress and reducing its flowability. Once the main reaction does occur, the eventual formation of C-A-S-H occurs in lower quantities and polymerises at a slower rate than for the slag binders activated with sodium silicate, which in turn contributes to its slower strength development and ultimate compressive strength value. Furthermore, the modification of the activating solution to include sodium silicate as well as sodium carbonate in a 50:50 wt.% blend greatly improves the rate of reaction, the formation and polymerisation of C-A-S-H, and the physicomechanical properties, proving that a combination of activator components can achieve a compromise between the material's performance and its carbon footprint.

Chapter 6: Sodium Carbonate-activated Slag Binders – Incorporation of Additives

6.1 Introduction

Based on existing knowledge and the further knowledge obtained in the previous chapter, sodium carbonate has the potential to reduce carbon emissions and industrial handling challenges when used as an activator for alkali-activated slag binders compared to the more commonly used alkali salts. However, the early reaction is hindered by the initial preferential reaction between calcium ions from the slag and carbonate ions from the activator forming calcium carbonates rather than the precipitation of C-A-S-H, which in turn increases setting and hardening times and limits strength development.

Additional chemical and mineral components has previously been explored to improve the performance and tune properties of alkali-activated binders, including combining precursors [127], [211], [227], combining activator solutions [69], [79], [119], [120], or incorporating the likes of magnesium oxide or calcium oxide [123]–[127]. With the aim of utilising the less commonly used sodium carbonate-activated binders in order to reduce embodied carbon and handling issues, incorporating very small amounts of additives is the most sensible option, and therefore, the choice to include calcium oxide and magnesium oxide in the sample matrix was made. Although both CaO and MgO do not necessarily have low carbon footprints associated with their production, used in relatively small quantities, there is likely a cost-benefit balance achieved if the performance of carbonate-activated slags is improved.

This chapter will therefore assess the performance of sodium carbonate-activated slag binders with 1 and 3 wt.% replacements of slag with both calcium oxide and magnesium oxide. The reaction mechanisms and kinetics will be explored through *in-situ* analysis, followed by

structural evolution assessment with solid-state analysis techniques, and finally the fresh-state and physical properties will be determined. This understanding will aid the optimisation of alkali-activated slag binders for enhanced properties while mitigating CO_2 emissions where possible.

6.2 Methodology

Cement paste samples in this chapter were made by mixing BFS with sodium carbonate solution, in similar proportions to those in the *Chapter 5*, however, small quantities of additives, calcium and magnesium oxide, were incorporated via replacement of slag in the system. These samples were compared to both the non-additive-containing carbonate-activated sample and the sodium silicate-activated slag binder in terms of performance. The formulations used hereafter in this chapter are summarised in **Table 6-1**.

Table 6-1 *Sample formulations used in Chapter 6.*

No.	Sample Name	Activator	BFS (g)	Activator Na_2O (g)	Additive	Additive mass (g)
2	**BFS_8%_CO_3**	Na_2CO_3	100	8	--	--
6	**BFS_8%_CO_3_1%_CaO**	Na_2CO_3	99	8	CaO	1
7	**BFS_8%_CO_3_3%_CaO**	Na_2CO_3	97	8	CaO	3
8	**BFS_8%_CO_3_1%_MgO**	Na_2CO_3	99	8	MgO	1
9	**BFS_8%_CO_3_3%_MgO**	Na_2CO_3	97	8	MgO	3

Isothermal calorimetry as well as IR spectra and XRD patterns measured *in situ* were utilised to explore the early reaction rate and mechanisms of the cement pastes. While the structural evolution, including phase assemblage, were investigated using the following solid-state techniques: ATR-FTIR spectroscopy, TGA, XRD, ^{27}Al and ^{29}Si MAS NMR spectroscopy, and SEM-EDX analysis. Furthermore, the physical performance of these cements was assessed

using Vicat apparatus for setting time measurements, mini slump testing, and viscometry measurements to understand workability, and compressive strength testing at 7 and 28 days of curing.

6.3 Results and Discussion

6.3.1 Reaction Mechanisms and Kinetics

6.3.1.1 ICC

Figure 6-1 again shows that the heat evolution of carbonate-activated slag binders at early age exhibits four stages of reaction: pre-induction, induction or dormancy, acceleration, and deceleration. These correspond to an initial heat output equivalent to the surface wetting and dissolution of slag particles, a very low rate of heat release as continual dissolution occurs and some initial reaction products may nucleate, followed by a substantial heat release relating to the precipitation of many reaction products, and then a decline in heat release as the reaction steadily slows after the binder hardens and sets [62], [100]. In this case, the effect of the inclusion of additives on the reaction kinetics of carbonate-activated slag binders can be assessed from the time-resolved calorimetry data.

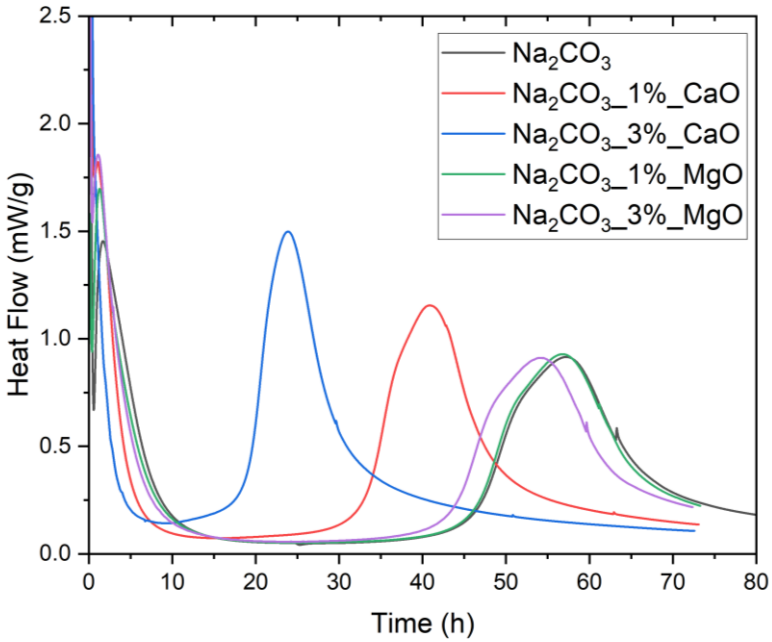

Figure 6-1 *Heat release rate of carbonate-activated binders with inclusion of additives, calcium oxide and magnesium oxide, as labelled.*

It is observed that the addition of magnesium oxide has little to no impact on the reaction kinetics, with the peak of heat release for the 3 wt.% magnesium oxide dosage is at ~54 hours compared to the ~57 hours for the non-additive carbonate-activated sample, and the peak for 1 wt.% dosage is achieved only 20 minutes sooner than that for the carbonate-activated slag. Additionally, the shape of the heat flow curve for non-additive and magnesium oxide-containing carbonate samples being almost identical during the main reaction phase indicates no change in reaction mechanisms, i.e. the same types of reaction product forming at the same rate. As can be seen in **Figure 6-2**, the heat evolution associated with the initial preferential reaction identified for the carbonate-activated binder, also occurs with the inclusion of magnesium oxide, however, the extent of heat release increases with the increased inclusion of additive and reduces more quickly than that of the non-additive sample. This suggests that a preferential initial reaction occurs regardless of the inclusion of MgO and is completed more

quickly than without MgO in the system, however, this has minimal effect on the length of the dormant period that ensues afterward.

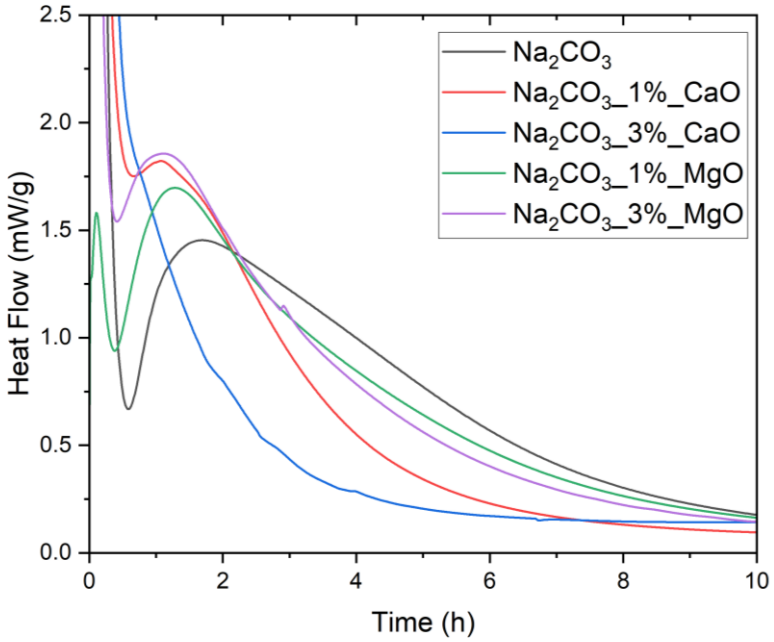

Figure 6-2 *Initial heat release rate of sodium carbonate-activated slag with additives, for the first 10 hours of reaction.*

On the other hand, the introduction of calcium oxide into the carbonate-activated binder system has a much more notable effect on the reaction kinetics compared to the inclusion of magnesium oxide. Firstly, the peak of the heat evolution associated with the main reaction occurs much sooner with the inclusion of calcium oxide, at ~41 and ~24 hours for 1 and 3 wt.% dosage, respectively, compared to the peak at ~57 hours for the non-additive sample, likely due to a higher alkalinity in the matrix due to the formation of $Ca(OH)_2$. Additionally, the shape of the heat evolution curve during the main reaction for 1 wt.% inclusion of CaO is quite similar to that of the carbonate-activated sample, having a right-leaning peak and a shoulder to the left, however, narrower, and taller. Conversely, the heat evolution during this period for the 3 wt.% CaO-doped sample does not appear to have this same initial shoulder preceding its peak, but rather, is tall and narrow in shape, similar to what is observed for silicate-activated samples, as is demonstrated in **Figure 6-4**. Furthermore, the initial preferential reaction identified in

carbonate-activated samples occurs and is completed more quickly in the sample including 1 wt.% CaO and appears to possibly be completely supersedes for the 3 wt.% CaO sample (**Figure 6-2**).

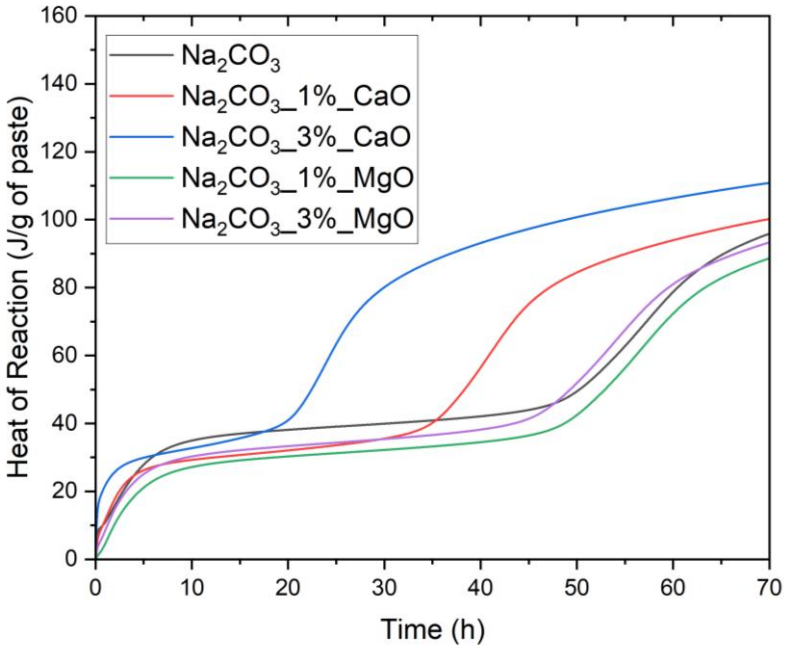

Figure 6-3 *Heat of reaction of carbonate-activated BFS and additives, calcium oxide and magnesium oxide.*

Despite the differences in the rate of reaction – the time when each reaction phase is occurring – the overall heat of reaction after 70 hours for carbonate-activated slag binders varies only marginally with the inclusion of additives in **Figure 6-3**. Generally, by this time point, the magnesium oxide-containing samples have a slightly lower (~7 %) overall heat of reaction, while those including calcium oxide show an increase of 5 and 15 % in heat of reaction for dosages of 1 and 3 wt.%, respectively. Thus, for small dosages of calcium oxide, it can be theorised that the heat of reaction of carbonate-activated slag binders can be improved by 5 % for every 1 g of slag replaced with the additive per 100 g. An increased heat of reaction typically aligns with an increase in the amount of reaction products being formed or more strongly bound reaction products being formed. Furthermore, **Figure 6-3** indicates that the heat

of reaction for the initial preferential reaction, when it does occur, is the greatest for the carbonate-activated slag binder without any additives, meaning that a greater number of calcium carbonate polymorphs may be forming at this point than for any of the additive-doped samples. The reaction products and phase evolution can be further probed through solid-state characterisation at various curing ages to confirm how the sample formulation chemistry influences the reaction.

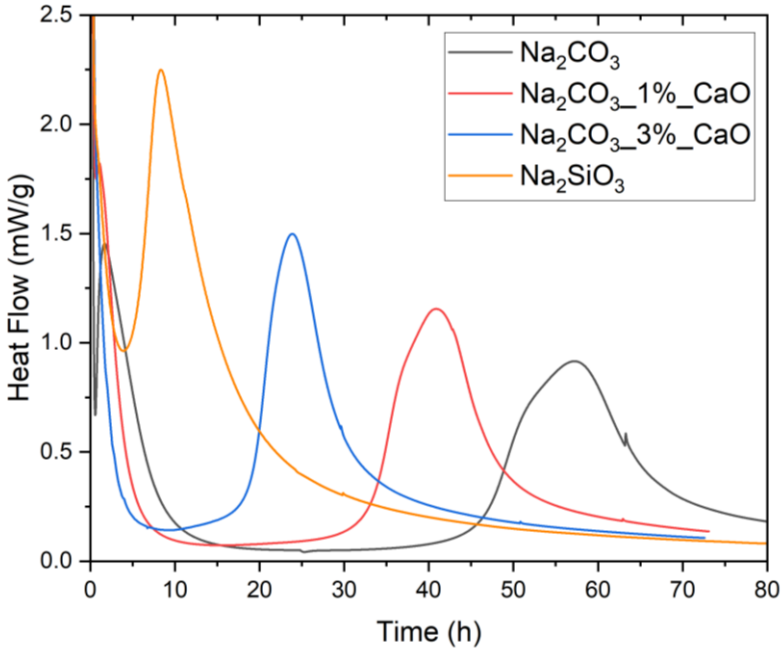

Figure 6-4 *Heat release rate of carbonate-activated BFS with calcium oxide, in comparison with silicate-activated BFS.*

As **Figure 6-4** illustrates, the rate of reaction of sodium carbonate-activated slag binders can be improved with small amounts of calcium oxide, somewhat comparable to sodium silicate-activated binders. There is a reduction in the time of the peak of the main reaction heat output by 16 and 34 hours for 1 and 3 wt.% calcium oxide replacements of slag within the system, respectively, as well as a change in the shape of the "hump" from wide and blunt with a shoulder to a sharper and narrower peak with increasing inclusion of calcium oxide.

An increase in the replacement of slag with calcium oxide beyond 3 wt.% may further improve the reaction rate to be more similar to the silicate-activated sample, whose reaction peaks at ~8.5 hours, than the non-additive carbonate-activated sample. However, due to the observed rate of change of the peak reaction time of the CaO-doped samples decreasing with increasing dosage at an exponential rate, it is likely that no calcium oxide dosage will achieve the same peak reaction time as the sodium silicate-activated slag binder. An exponential fit for rate of change of peak reaction time with calcium oxide dosage (**Figure 6-5**) suggests a minimum peak reaction time of ~11 hours can be achieved at a dosage of 15 wt.%, however, the derivative curve suggests that there is very little improvement in peak reaction beyond 8 wt.% calcium oxide. According to the extrapolation of the exponential fit in **Figure 6-5**, a dosage of 5 wt.% calcium oxide suggests a peak reaction time of ~16.5 hours, which may be more appropriate in finding a balance between carbon footprint and reaction time. It is noted that additional data points should be obtained to verify the relationship (linear or exponential or otherwise) between peak reaction time and the dosage of calcium oxide for carbonate-activated slag binders.

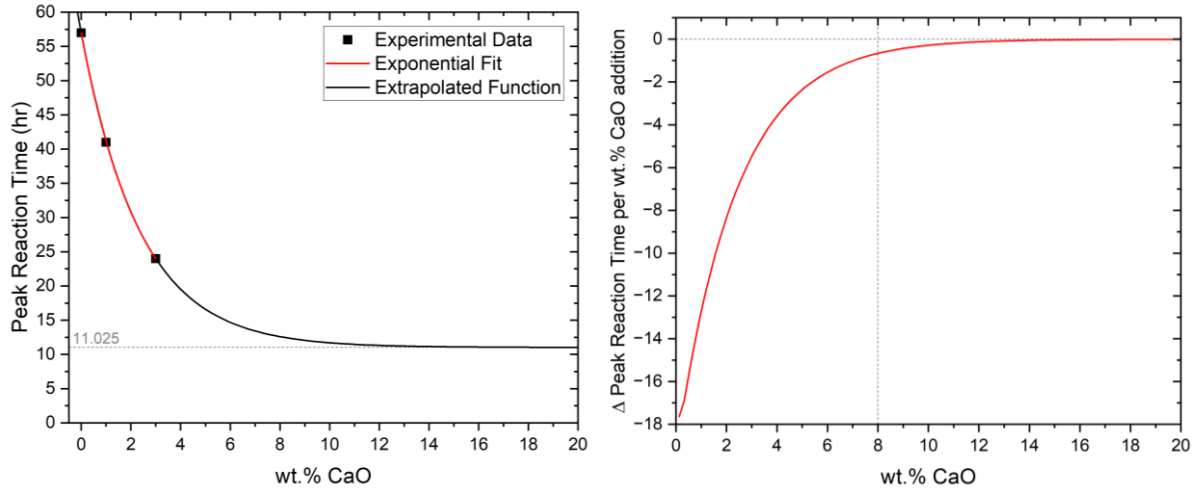

Figure 6-5 *Exponential fit for peak reaction time with dosage of CaO (L), and its derivative (R).*

6.3.1.2 DRIFTS

The mechanisms of reaction during the initial hours following mixing were probed using DRIFTS to take measurements every 2 minutes *in situ*. The change of bond environments during this time for carbonate-activated slag binders doped with magnesium oxide and calcium oxide is illustrated in **Figure 6-6** and **Figure 6-7**, respectively.

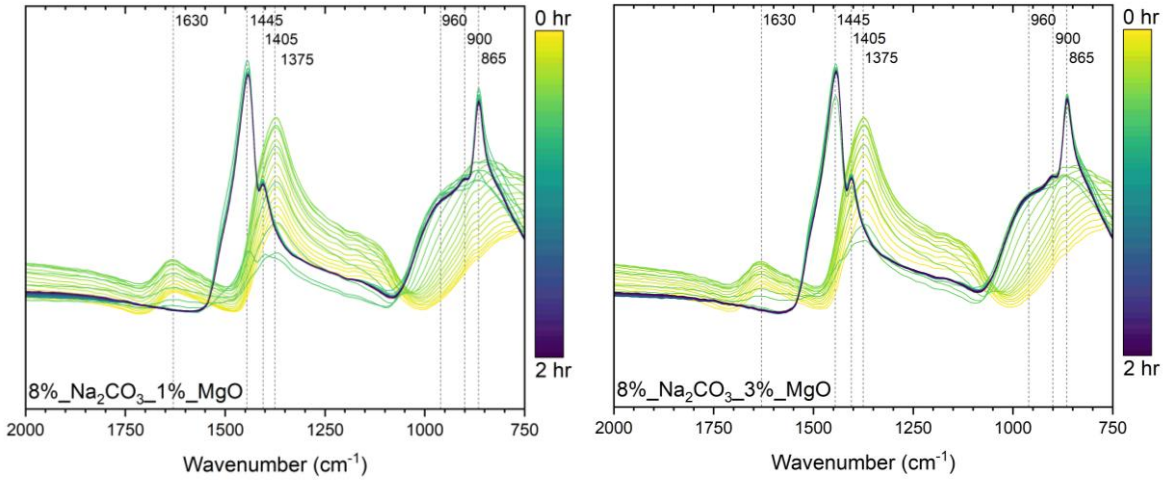

Figure 6-6 *DRIFTS spectra for carbonate-activated BFS with magnesium oxide, as marked, over the first 2 hours of reaction.*

For the carbonate-activated samples including magnesium oxide (**Figure 6-6**), it is observed that the mechanism occurring during the early hours of reaction is very similar and almost identical to what occurs in the non-additive carbonate-activated sample, as well as not varying much between dosage of magnesium oxide. Peaks at wavenumbers 1630 and 1375 cm^{-1} increase in intensity slightly in the first 20 minutes after mixing before reducing massively, with the peak at 1630 cm^{-1} reducing completely within 90 minutes. The peaks at these wavenumbers result from the sodium carbonate solution, specifically the asymmetric bending of O-H bonds in water [135], [183] and the asymmetric stretching of C-O bonds of carbonate ions [141], [142], respectively. The peak at 1375 cm^{-1} shifts to a higher wavenumber and increases in intensity to a sharp peak at ~1445 cm^{-1} with a smaller shoulder at ~1405 cm^{-1}, both attributed to the asymmetric vibration of the C-O bond within carbonate ions, likely calcium

carbonate and sodium carbonate, respectively [95], [141], [183], indicative of the formation of these species. It is noted that the specific type of carbonate cannot be identified solely from IR spectra, as the wavenumber regions for multiple calcium carbonate polymorphs and sodium calcium carbonate hydrate – natron – overlap. Additionally, a broad hump spanning 750 to 1000 cm^{-1} develops slowly into a clearly defined peak at ~865 cm^{-1} after 1 hours, corresponding to the asymmetric bending of C-O in calcium carbonate [135], [136], [141], [183].

In contrast to the DRIFTS spectra of the carbonate-activated slag binder, in **Figure 5-4**, a broad shoulder to the aforementioned peak at ~865 cm^{-1} also forms at a similar rate, with notable peaks at ~900 and ~950 cm^{-1}, both in the region associated with asymmetric stretching of T-O-T bonds (where T represents tetrahedral Si or Al). Typically, a lower wavenumber in this region aligns with bonds Al-O-Al or Si-O-Al, likely in slag particles, and the increasing wavenumber in this region corresponds to the stronger bonding of Si-O-Si within the C-A-S-H structure [53], [133]. Unlike the spectra for the silicate-activated slag sample, due to the broad peak encompassing both peaks corresponding to T-O-T bonds only increasing in intensity and doing so after some time, it is likely that these bonds are contained within the C-A-S-H structure (rather than from the slag particles).

Although the general mechanism for sodium carbonate consumption and calcium carbonate formation is the same for both 1 and 3 wt.% magnesium oxide (**Figure 6-6**), it is noted that the rate at which this mechanism occurs is slightly quicker for the increased dosage. Similarly, the formation of the peaks aligning with the T-O-T bonds also occurs at a higher rate for the 3 wt.% magnesium oxide-containing sample. Altogether, the DRIFTS data aligns with the reaction kinetics observed in the calorimetry data in **Figure 6-1**.

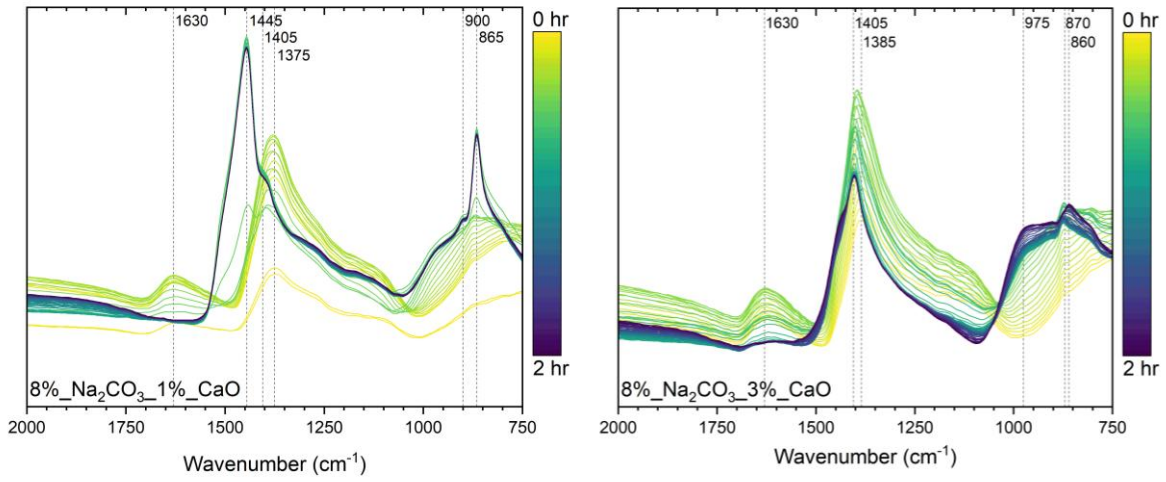

Figure 6-7 *DRIFTS spectra for carbonate-activated BFS with calcium oxide, as marked, over the first 2 hours.*

For the carbonate-activated slag binder with the addition of 1 wt.% calcium oxide, the DRIFTS spectra in **Figure 6-7** demonstrates a very similar mechanism for the consumption of sodium carbonate from the activating solution and the associated (sodium) calcium carbonate polymorph formation to that identified in the non-additive carbonate-activated sample (**Figure 5-4**) and the magnesium oxide-modified samples (**Figure 6-6**), with the exception of the shoulder peak at ~1405 cm^{-1} being less prominent. Additionally, the growth in intensity of the peaks associated with T-O-T bonds is also similar to the magnesium oxide-doped carbonate-activated slag samples. Despite the general reaction mechanism remaining the same, the rate of change in bond environments for the 1 wt.% CaO sample is greater than that for MgO samples as well as for the non-additive carbonate sample, corresponding with the calorimetry data in **Figure 6-1**.

On the other hand, the carbonate-activated sample incorporating 3 wt.% of calcium oxide displays a different DRIFTS spectrum (**Figure 6-7**) compared to the other carbonate-activated binders. In a similar manner, the peaks associated with the sodium carbonate activating solution reduce and associated peaks at ~1405 and ~865 cm^{-1} take shape, indicative to the formation of calcium carbonate phases. However, these carbonate peaks are much less prominent than those

that appear in the spectra for the other carbonate-activated slag binders, and the peak forming at ~975 cm^{-1}, associated with T-O-T bonds likely within the C-A-S-H structure, forms more quickly and is more prominent than with the other samples. This indicates that the extent of reaction at 2 hours after mixing is much greater than that for the other carbonate-activated samples, and that although the initial preferential reaction does still occur, the formation of main reaction products occurs almost simultaneously.

Overall, the appearance and change in intensity of wavenumbers associated with various bond environments in the time-resolved DRIFTS spectra for the carbonate-activated slag binders with the inclusion of additives suggests the general reaction mechanisms and kinetics occurring at early age, in line with the observations from the calorimetry data, shown in **Figure 6-1**.

6.3.1.3 *In-situ* XRD

XRD patterns were collected every 15 minutes after mixing for the initial few hours of reaction to further explore the reaction mechanisms and kinetics of sodium carbonate-activated slag binders including calcium oxide, by identifying the changes in crystalline structures during this time to corroborate findings from the DRIFTS measurements in **Figure 6-7**.

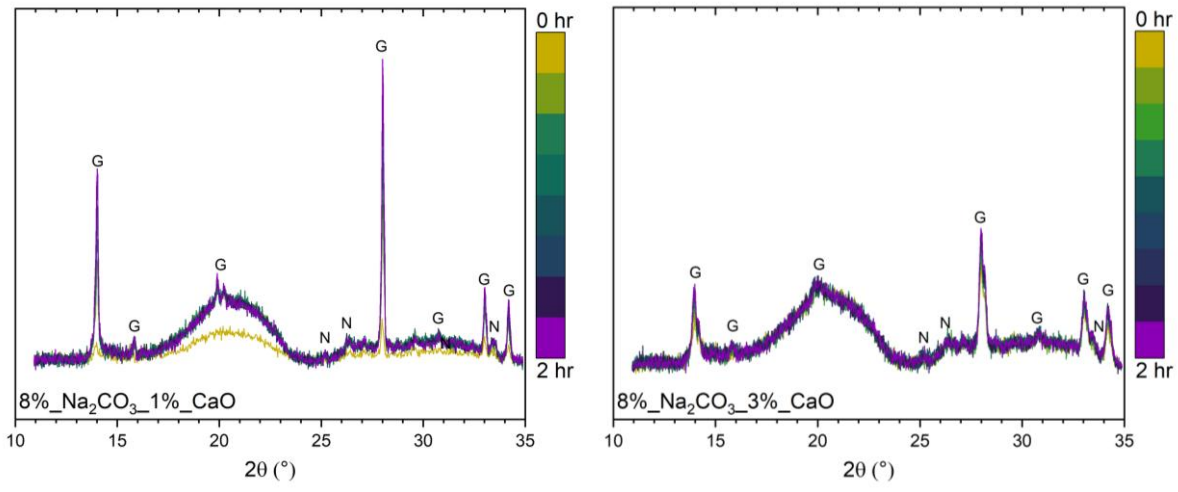

Figure 6-8 *XRD pattern of carbonate-activated BFS with calcium oxide over the first 2 hours of reaction. Key crystalline peaks labelled: G – Gaylussite (PDF 00-021-0343), and N – Natron (PDF 00-015-0800).*

The XRD patterns in **Figure 6-8** for both 1 and 3 wt.% calcium oxide in the sample matrix show the same crystalline structures present, however, there is variation in the peak intensities between the two dosages. Similarly to the XRD measurements taken *in situ* for the non-additive carbonate-activated slag in **Figure 5-4**, peaks corresponding to natron ($Na_2CO_3.10H_2O$), a hydrated sodium carbonate, are present in both doped samples, but unlike their non-additive counterpart, these peaks are much lower in intensity at the offset. This indicates that this phase, corresponding to the alkali activating solution, is consumed at a much faster rate when calcium oxide is added to the carbonate-activated slag system. Additionally, the crystalline phase, gaylussite ($Na_2Ca(CO_3)_2.5H_2O$), a sodium calcium carbonate hydrate, is identified in the diffractograms for the carbonate-activated slag sample and for those with the addition of calcium oxide. For the 1 wt.% calcium oxide addition, the peak begins to form from 0 hours and grows steadily over 2 hours into sharp peaks, whereas, for the 3 wt.% calcium oxide addition, the peaks associated with gaylussite exist from the offset and increase very marginally over the 2 hours. The existence of this phase confirms that the preferential reaction between carbonate ions from the activator and calcium ions is still occurring for the calcium oxide-doped carbonate-activated samples, but at a different rate to the non-additive system. The already depleted intensities of natron peaks for the calcium oxide samples suggests that the activating solution splits into its separate species almost instantly in the presence of the calcium oxide, and the inclusion of this additive facilitates the formation of calcium carbonates very quickly, likely due to the increase of calcium ions in the system – from both the precursor and the calcium oxide. The pre-existence, but reduced peak intensity, of gaylussite in the sample with an inclusion of 3 wt.% calcium oxide is likely due to the preferential reaction happening almost immediately after or even simultaneously to dissolution and dispersion of slag particles during and after mixing, due to the massive increase of calcium ions in the system. The lack of

increase in intensity in these phase peaks during the initial 2 hours after mixing suggests that the extent of this preferential reaction may have been reached during this time, inducing the dormant period almost immediately. This observation aligns with the calorimetry and DRIFTS data in **Figure 6-1** and **Figure 6-7**, respectively.

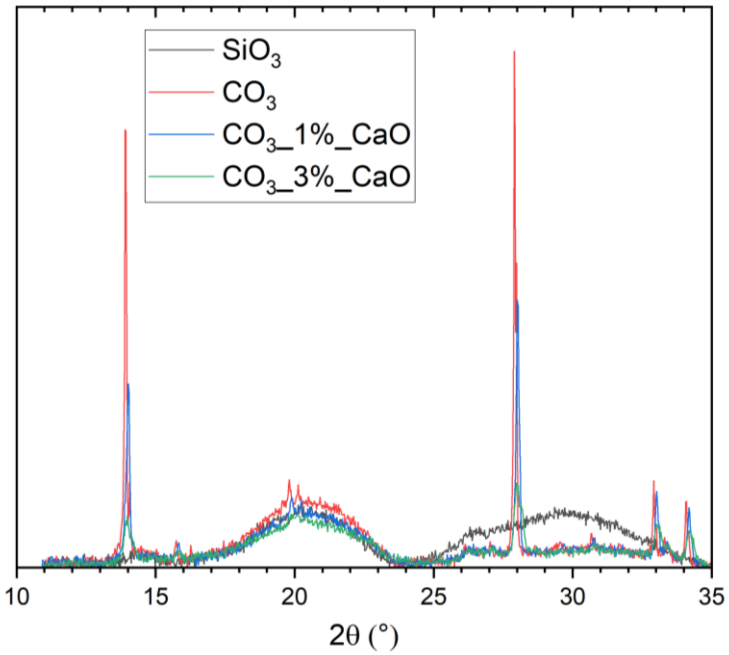

Figure 6-9 *Comparison of XRD patterns at 2 hours, for carbonate-activated BFS, with and without calcium oxide, and silicate-activated BFS.*

A comparison between XRD patterns measured at 2 hours for carbonate-activated slags excluding and including calcium oxide with the silicate-activated slag sample in **Figure 6-9** reveals how activator and additive influences the reaction mechanisms of alkali-activated slag cements at early age. Despite the initial suggestion that 3 wt.% calcium oxide inclusion causes the initial preferential reaction resulting in calcium carbonate polymorphs to be superseded based on the calorimetry data in **Figure 6-2**, all samples activated with sodium carbonate reveals the existence of the sodium calcium carbonate hydrate, gaylussite, and thus the preferential reaction between calcium ions and the activating solution does still occur but almost immediately that an initial heat release peak does not appear for this sample in its

calorimetry data. As **Figure 6-9** illustrates, despite the increased rate of reaction of the carbonate-activated sample including 3 wt.% calcium oxide, it does not follow the same reaction mechanism as the silicate-activated slag binder, but rather all of the carbonate-activated samples follow the same reaction mechanism in the early hours of reaction, but just at different rates.

6.3.1.4 Summary

Combining data from calorimetry, DRIFTS, and XRD taken *in situ* during the initial reaction after mixing, the influence of small inclusions of additives, magnesium oxide and calcium oxide, on the reaction mechanisms and kinetics of carbonate-activated slag binders is revealed. The inclusion of magnesium oxide at both 1 and 3 wt.% has little to no impact on the rate of reaction, despite its use in previous studies for the same purpose. The lack of effect on the reaction is possibly due to the type of magnesia used and its method of production; the reactivity of MgO is directly linked to its production process, where “light-burned” magnesia is characterised by its high surface area and rapid hydration in water, while “hard-burned” magnesia is calcined at higher temperatures and results in a lower surface area and reduced reactivity compared to light-burned MgO.

Alternatively, calcium oxide in small amounts can greatly improve the overall reaction rate, likely due to the increased presence of calcium ions in the bulk facilitating the initial preferential reaction between calcium ions – usually from the precursor – with the carbonate ions from the activator at a quicker rate. According to the calorimetry data, this improved reaction is likely more exothermic in nature, meaning an increase in heat in the system, which also aids in increasing the rate of reaction.

6.3.2 Structural Evolution

6.3.2.1 ATR-FTIR

Spectral measurements of ATR-FTIR spectroscopy were taken at different ages of curing for the carbonate-activated samples doped with calcium oxide and magnesium oxide, in order to identify bond environments and the change of phase assemblage over time. For each sample set, the normalised spectra (**Figure 6-10** and **Figure 6-11**) display minimal changes over time, indicating a steady rate of reaction from early age (3 days) to late curing (90 days).

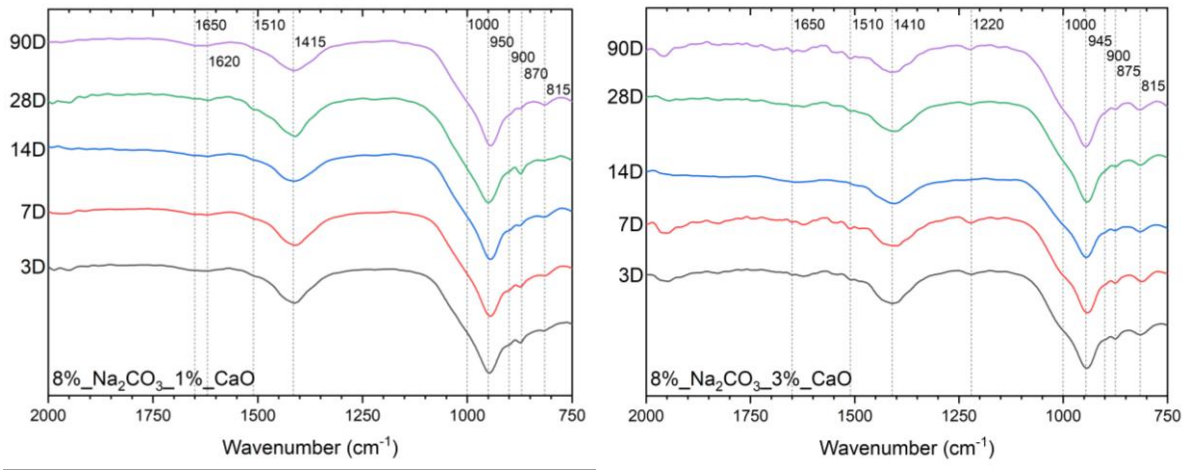

Figure 6-10 *FTIR spectra of sodium carbonate-activated BFS with calcium oxide, at various time points, as labelled.*

The IR spectra for all carbonate-activated slag sample sets containing additives, either calcium or magnesium oxide, contain peaks at 875 and at 900 cm^{-1}, which are both attributed to the asymmetric bending of C-O bonds in calcium carbonates [135], [136], [141], [183], with the latter ascribed specifically to the calcium carbonate polymorph, calcite [135], [136], [185]. The band at ~ 875 cm^{-1} is quite prominent from an early curing age due to the early formation of such calcium carbonates during the initial reaction stage, as detailed by the DRIFTS analysis in the previous section, however, its prominence reduces with curing age due to the formation of other reaction products over time. Additionally, the intensities at ~1410 and ~1510 cm^{-1} also correspond to the C-O vibration within carbonate polymorphs [141], [142], [125], with the

band at ~1410 cm^{-1} specifically belonging to the C-O bonds within sodium carbonate, possibly directly from the activator or the sodium calcium carbonates forming in the early reaction stages, while the band at ~1510 cm^{-1} corresponds to calcite or dolomite ($CaMg(CO_3)_2$) [234], [235]. Furthermore, the small band intensities visible at 1620 and 1650 cm^{-1} are characteristic of the O-H bonds in water, which is likely embedded in the reaction product, C-A-S-H, indicating its presence in the system.

As is the case with all previous samples, and is expected for alkali-activated slag binders, the highest intensity band in all spectra for all sample sets is at ~950 cm^{-1}, which is attributed to the asymmetric stretching of Si-O-T bonds (where T = tetrahedra of either Si or Al), as is the smaller band observed at ~815 cm^{-1}, which can more specifically be assigned to Q^2 and Q^1 Si sites respectively, within the C-A-S-H structure [53], [133], [134]. These peaks are present from 3 days with no major change with time; the band at ~950 cm^{-1} appears to slightly sharpen over time, particularly for the calcium oxide-doped samples, representing increased structural ordering of C-(A)-S-H as the reaction proceeds [53], [183], while the small peak at ~815 cm^{-1} maintains its low intensity over time for all sample sets, however, appears to have a slightly greater intensity for the sample containing 3 wt.% CaO, suggesting that the greater inclusion of calcium oxide increases the amount of C-A-S-H.

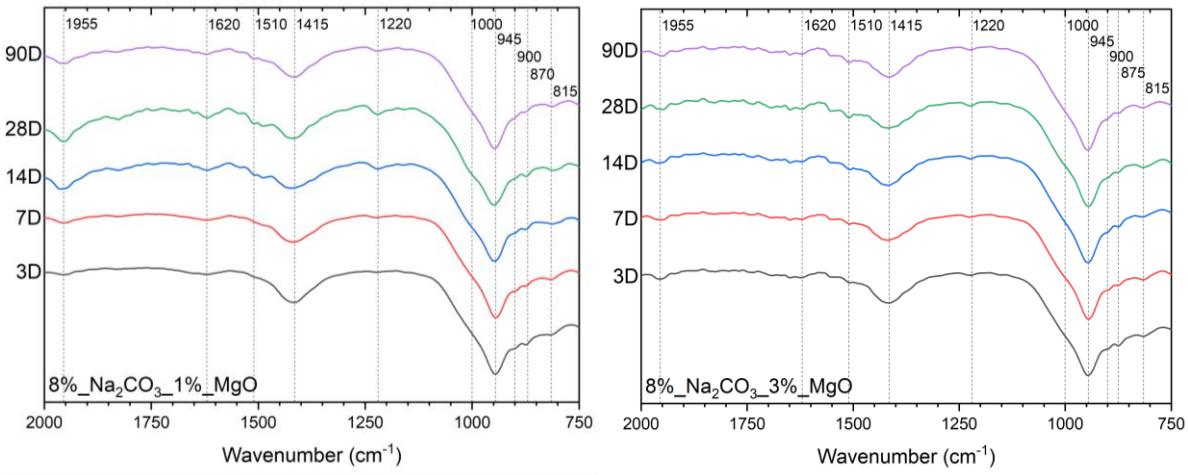

Figure 6-11 *FTIR spectra of sodium carbonate-activated BFS with magnesium oxide, at various time points, as labelled.*

The band highlighted at 1220 cm^{-1}, which is present in the carbonate-activated slag with the addition of 3 wt.% calcium oxide and 1 and 3 wt.% magnesium oxide is not typically found in IR spectra for alkali-activated cements. However, a study into amorphous silica and calcined MCM-41 (Movil Composition of Matter No. 41) identified an intensity at this wavenumber to be the vibration of external linkages for Q^4 silicate species [236]. This assignment here is not completely sound, as a band at ~1220 cm^{-1} does not appear in any previous samples, including the silicate-activated, which was found to have Q^4 Si sites from early curing ages according to ^{29}Si MAS NMR spectral deconvolutions. It is possible that this low intensity may be another carbonate bond, belonging to a calcium carbonate polymorph, but this cannot be stated with certainty.

6.3.2.2 TGA

Thermogravimetric analysis was undertaken to aid in understanding the reaction progression in sodium carbonate-activated slag binders containing either calcium or magnesium oxide in small amounts through the identification and quantification of reaction products at a range of curing ages. There is a general increase in the overall mass loss as curing time progresses for all sample sets, indicating an increased extent of reaction over time, as expected. The values for these overall mass losses are in **Table 6-2**.

Table 6-2 *Overall mass loss values for additive-containing carbonate-activated slags, as determined from TGA data characterised in* ***Figure 6-12*** *and* ***Figure 6-13****.*

	Curing Age				
Sample	**3 days**	**7 days**	**14 days**	**28 days**	**90 days**
Na_2CO_3_1%_CaO	23.3	23.8	23.8	25.5	28.1
Na_2CO_3_3%_CaO	24.5	25.5	26.7	25.8	27.4
Na_2CO_3_1%_MgO	24.5	24.4	27.6	24.9	27.2
Na_2CO_3_3%_MgO	25.0	24.7	27.2	25.7	27.2

TGA curves for both the calcium oxide- and magnesium oxide-containing carbonate-activated samples demonstrate an initial mass loss between 60 and 200 °C of up to ~15 wt.% for all curing ages, generally slightly increasing with curing age, with the exception of both of the 1 wt.% additive samples displaying a moderate increase in mass loss between 28 and 90 days. This mass loss is attributed to the loss of water from the calcium aluminosilicate hydrate (C-A-S-H) [186], [187], and the moderate increase at 90 days compared to earlier ages for the 1 wt.% additive-containing samples suggests a delayed extent of reaction beyond the initial month after curing. As discussed in the previous chapter, this mass loss is observed as the sum of two sharper mass losses for carbonate-activated samples compared to a single broad mass loss for silicate-activated samples. The latter of the two mass losses, which centres at ~130 °C, remains mostly similar with minor reductions in intensity over time, while the first peak at ~100 °C increases slightly with curing time between 3 and 28 days before drastically increasing at 90 days for all samples.

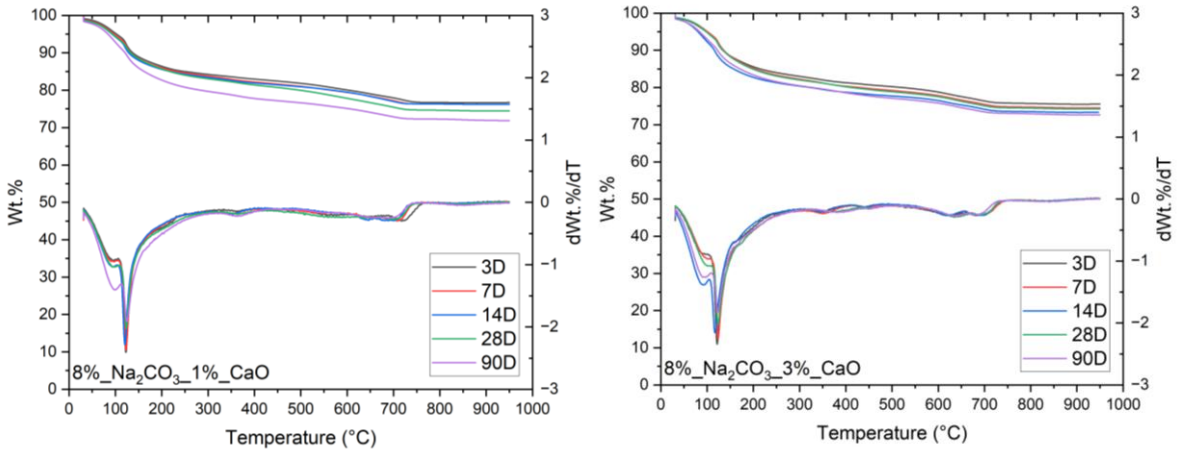

Figure 6-12 *TG/dTG trends of sodium carbonate-activated BFS with calcium oxide, cured for various lengths of time, as labelled.*

Similarly to the TGA observations for the previous samples, all of the additive-containing carbonate-activated samples display a shoulder to the right of the initial mass loss peak(s) at

~170 °C becoming particularly prominent at later curing ages, which is associated with the initial thermal degradation of hydrotalcite [188], [189]. Additionally, in the region of 300 to 500 °C, another mass loss can be observed at each curing age for all sample sets, which is attributed to additional loss of chemically bound water within hydrotalcite phases [186], [188], [190]. With the exception of the 3 wt.% calcium oxide-containing sample set, this second hydrotalcite-associated mass loss varies very little with time and remains centred at ~350 °C, suggesting that a small but established quantity of stable hydrotalcite phases form at early age and remain over time. However, for the carbonate-activated sample containing 3 wt.% calcium oxide, there are two mass losses in this region – centred at ~350 and ~450 °C – at curing ages up to and including 14 days, and just a single mass loss centred at ~385 °C from 28 days onwards. This difference may suggest the formation of multiple hydrotalcite-like (magnesium-aluminium-based) phases with varying stability at early age, which then rearrange and form more stable AFm (calcium-aluminium-based) products as the reaction progresses at a later age due to the increased calcium content in the system from the additive. Despite hydrotalcite being magnesium-rich, the quantity of this phase in the magnesium oxide-doped samples appears to be the same or similar to the solely carbonate-activated sample, further indicating the limited effect that the inclusion of this additive has on this system.

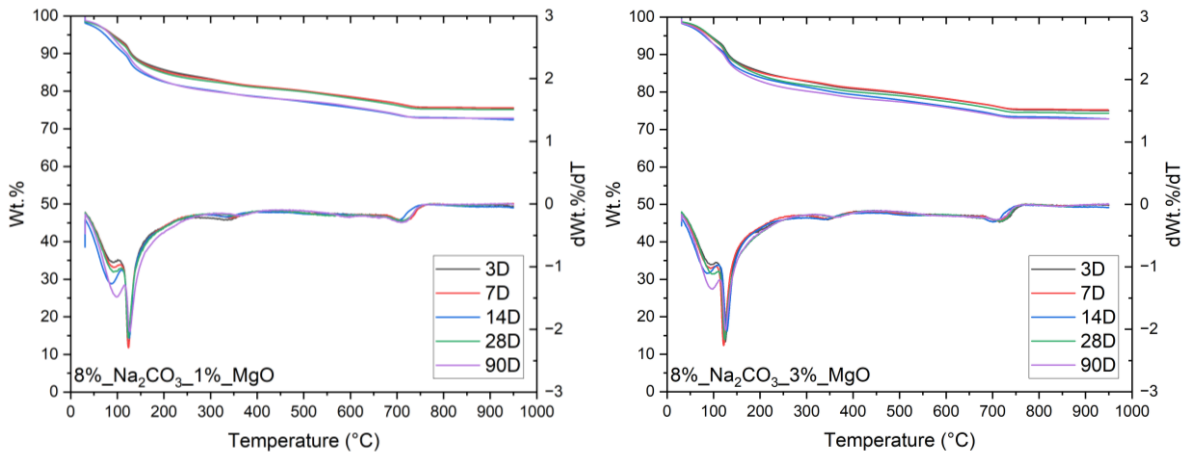

Figure 6-13 *TG/dTG trends of sodium carbonate-activated BFS with MgO, cured for various lengths of time, as labelled.*

A mass loss in the region of 500 to 700 °C is associated with the continual dehydration of C-A-S-H-type phases as well as the dehydroxylation of hydrotalcite phases[186], [188]. There is a small, progressive mass loss in this area for the magnesium oxide-containing carbonate-activated samples, similar to that seen in the TGA for the carbonate-activated slag sample (**Figure 5-10**), compared to a more notable progressive mass loss centring at ~650 °C for the calcium oxide-doped samples, which overlaps slightly with the rightmost mass loss. The existence of this mass loss in the calcium oxide-doped samples but not in the magnesium oxide-containing samples suggests that the former possesses more strongly bound C-AS-H and hydrotalcite phases, which aligns with the noted increased rate and extent of reaction.

Finally, the rightmost mass loss that sits in the region of 700-900 °C for all samples at all time points is due to the decomposition of calcium hydrates [186], in addition to the decarbonation of carbonates, including calcium carbonate polymorphs – calcite, vaterite, and aragonite [188], [192], [193]. The presence of these carbonate polymorphs is often accredited to atmospheric carbonation of samples, but the large quantity observed here is more likely due to the sample formulation, i.e. the activation with sodium carbonate. The existence of such calcium carbonates determined with TGA supports observations from the *in-situ* characterisation in *Section 6.3.1*, where carbonate ions (CO_3^{2-}) from the activating solution preferentially reacted with calcium (Ca^{2+}) from the slag. The mass loss in this region for the calcium oxide-containing samples overlaps slightly with the mass loss ascribed to dehydration of C-A-S-H-type phases, which may be further indicative of the existence of AFm-type phases, specifically the likes of a calcium monocarbonate ($3CaO.Al_2O_3.CaCO_3.nH_2O$), forming as a result of the increased CaO content.

6.3.2.3 XRD

Diffractograms were taken for the carbonate-activated slag samples containing small amounts of either additional calcium or magnesium oxide at various curing ages (**Figure 6-14** and **Figure 6-15** respectively) to further explore the influence of the additives on reaction products and phase evolution. As with ATR-FTIR and TGA data for these samples, the XRD patterns show little to no change in structure over time, indicating a stable and structurally ordered phase development from at least 7 days onward.

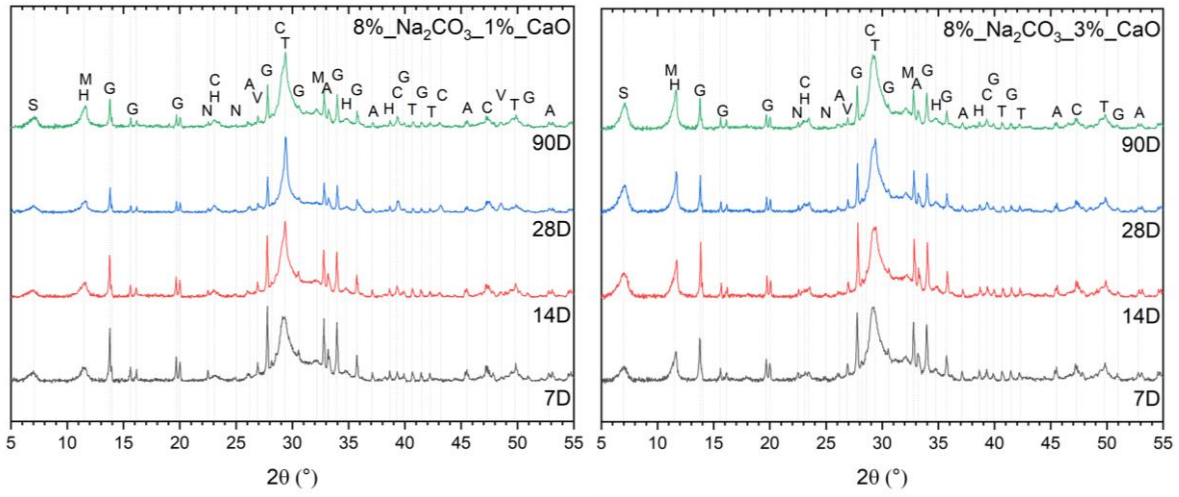

Figure 6-14 *XRD patterns of carbonate-activated BFS with calcium oxide, at various curing times, as labelled. Phases identified have been labelled: A – Aragonite (PDF 04-008-5421), C – Calcite (PDF 00-066-0867), G – Gaylussite (PDF 00-021-0343), H – Hydrotalcite (PDF 01-088-9171), M – Monocarbonate (Taken from Georget et al. [237]), N – Natron (PDF 00-015-0800), S – strätlingite (PDF 04-012-1915), T – Tobermorite (PDF 04-014-8455), and V – Vaterite (PDF 00-060-0483).*

Both sample sets at all curing ages display a broad "mounded" peak centred at ~30° 2Θ, which is assigned to an alumina-silica phase, in this case specifically a tobermorite-like C-A-S-H structure, which aligns with observations from TGA and FTIR data. In addition to this, the diffraction patterns for all samples feature significant amounts of sharp peaks, dissimilar to the silicate- and silicate-carbonate-activated samples, due to the presence of crystalline carbonate phases, analogous to previous studies of carbonate-activated slag binders [58], [69]. All samples contain additional tobermorite peaks, some quantities of hydrotalcite and various

peaks associated with calcium carbonate polymorphs – aragonite, calcite, and vaterite – corroborating observations from the other solid state analysis techniques, in addition to the sodium carbonate hydrate, natron, and hydrated sodium calcium carbonate, gaylussite, as observed at very early reaction stages with XRD *in situ* (**Figure 5-6** and **Figure 6-8**).

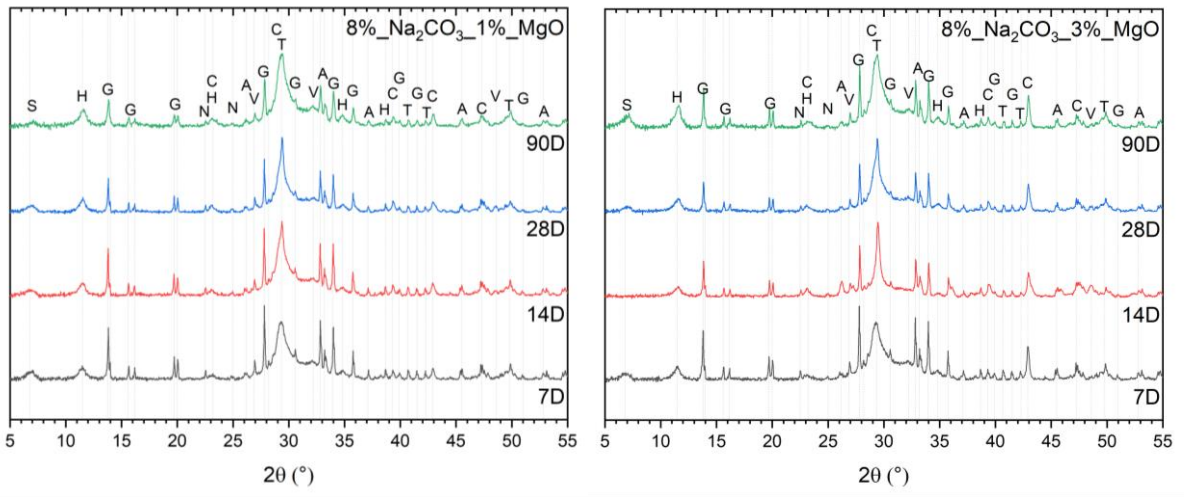

Figure 6-15 *XRD patterns of carbonate-activated BFS with magnesium oxide, at various curing times, as labelled. Phases identified have been labelled: A – Aragonite (PDF 04-008-5421), C – Calcite (PDF 00-066-0867), G – Gaylussite (PDF 00-021-0343), H – Hydrotalcite (PDF 01-088-9171), N – Natron (PDF 00-015-0800), S – strätlingite (PDF 04-012-1915), T – Tobermorite (PDF 04-014-8455), and V – Vaterite (PDF 00-060-0483).*

The primary amorphous peak centring at ~30° 2Θ associated with the main reaction product, C-A-S-H, exists from an early curing age, but grows in intensity and sharpens with time, suggesting increasing structural ordering and stability with curing age, signifying a greater extent of reaction, as expected. The presence of both this peak and the quantities of hydrotalcite at 7 days and each further time point suggests that once the initial preferential reaction – CO_3^{2-} ions from the activator reacting with Ca^{2+} ions from the precursor – is satisfied, the reaction for carbonate-activated slag binders proceeds similarly to a silicate- or hydroxide-activated slag system. Moreover, various peaks assigned to calcium carbonate polymorphs (aragonite, calcite, and vaterite) are observed at all curing ages, indicating that when these products form, be it

during the initial preferential reaction or via atmospheric carbonation, they remain in the bulk structure.

As is the case for the carbonate-activated sample not containing additives, the presence of gaylussite and natron are observed for all samples from an early curing age. Natron – sodium carbonate decahydrate – likely exists where there are unreacted activating species, while gaylussite – hydrated sodium calcium carbonate – was observed to form in the initial hours of reaction between the sodium carbonate activator and sodium and calcium species in the system, highlighted for the carbonate-activated slag cements in *Section 5.3.1.3*.

Despite being mostly identical the diffraction patterns of the calcium oxide-containing samples differ from those containing magnesium oxide with the presence of peaks aligning with monocarbonate (11) phases at ~12 and ~33° 2Θ. The observation of this phase aligns with that seen in the TGA, where some of the less stable magnesium-containing LDH – hydrotalcite – appears to transform into the more stable calcium-containing LDH – monocarbonate, with a strätlingite-like structure for the sample containing 3 wt.% calcium oxide. Here in the XRD patterns for both 1 and 3 wt.% calcium oxide-containing samples, peaks aligning with strätlingite and monocarbonate appear to increase in intensity over time, increasingly so for the higher CaO content. For the magnesium oxide-containing samples, the presence of strätlingite is noted and does increase slightly with time, however the intensity of hydrotalcite increases at more significantly. These observations align with the increased magnesium and calcium of each system, but again, the calcium oxide appears to have a greater influence on the reaction and thus phase evolution compared to the magnesium oxide.

6.3.2.4 NMR

Due to its greater influence on the reaction and phase evolution of the carbonate-activated slag binder samples, the nanostructure of samples containing additional calcium oxide was probed over time using solid-state ^{27}Al and ^{29}Si magic angle spinning (MAS) nuclear magnetic resonance (NMR) spectroscopy.

6.3.2.4.1 ^{27}Al MAS NMR Spectroscopy

The ^{27}Al MAS NMR spectra for the carbonate-activated slag binders containing 1 and 3 wt.% of calcium oxide are illustrated in **Figure 6-16**. All spectra for both sample sets display a broad tetrahedral resonance across the region of 80-60 ppm, clearly containing contributions from multiple Al sites.

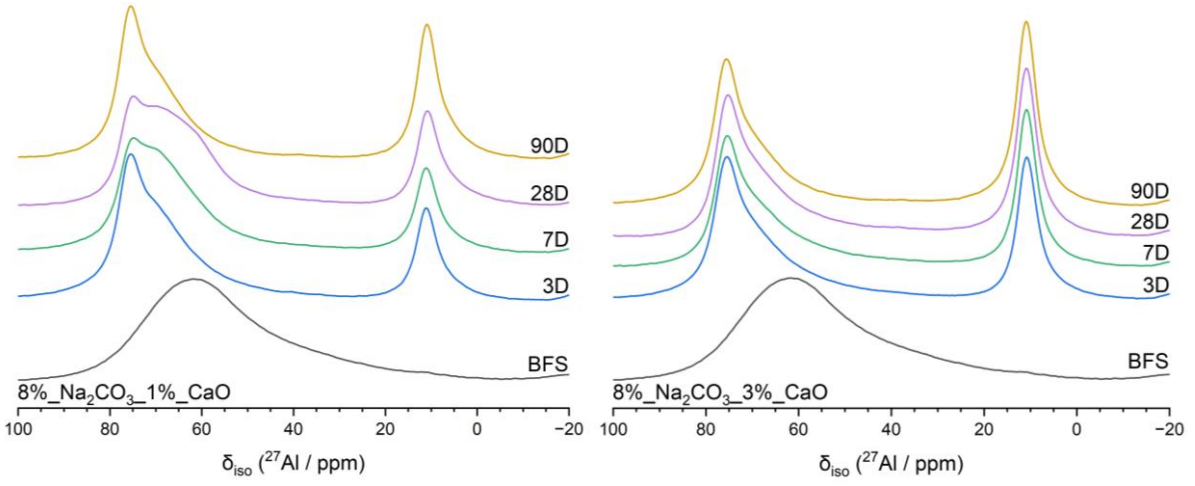

Figure 6-16 *^{27}Al MAS NMR spectra of BFS and carbonate-activated BFS with CaO at various curing times, as marked.*

Resonances at δ_{obs} = 74 and 68.4 ppm are due to Al in well-defined Al^{IV} coordination and incorporated in bridging tetrahedra, $q^2(I)$ and $q^2(II)$, respectively, whereby Al tetrahedra are bonded to Q^2 (1Al) Si sites [58], which are charge-balanced by Na^+/H^+ and Ca^{2+} ions, respectively, indicating the formation of C-A-S-H-type structures. Typically, a narrower signal here represents a greater degree of polymerisation, which is associated with a greater degree of

reaction, and this narrowing over time occurs continuously for the 3 wt.% calcium oxide-doped sample. On the other hand, the sample containing an additional 1 wt.% of calcium oxide shows a narrowing of this resonance at 90 days from its initial 3-day spectra, however, the spectrum in this region differs at 7 and 28 days, displaying a broad bulge forming to the right before reducing greatly to a small shoulder thereafter. This is likely due to an increased number of q^2(II) sites in the sample, meaning more calcium ions occupying the interlayer once the initial preferential reaction is exhausted (see 7 day spectrum), and then slowly these calcium ions integrate into reaction products (rather than as charge balancing species) like monocarboaluminates, leading to the sharpening of the resonance between 80 and 60 ppm after 28 days.

Another resonance is observed for both sample sets in the region from 20 to 0 ppm, possibly also containing contributions from multiple Al sites. The signal at δ_{obs} = 11 ppm corresponds to two Al^{IV} environments in octahedral formation often associated with a hydrotalcite-type LDH reaction product [194], [195], attesting to the formation of such products observed in the TGA and XRD data. Although previously assigned to only hydrotalcite, it is likely that this resonance also encapsulates the bonding of the AFm-type calcium monocarbonates with a strätlingite-like structure [238], discussed in previous sections. This resonance maintains an almost constant intensity up to and including 28 days of curing for the sample with 1 wt.% calcium oxide, before increasing in intensity significantly by 90 days, while for the sample of 3 wt.% replacement of calcium oxide, this resonance is sharper and has a greater intensity at 3 days, steadily increasing with sample age, similarly to observations made for the TGA curves (**Figure 6-12**).

6.3.2.4.2 ^{29}Si MAS NMR Spectroscopy

The ^{29}Si MAS NMR spectra for carbonate-activated slag incorporating calcium oxide at 1 and 3 wt.% (**Figure 6-17**) each display a broad hump centring at ~73 ppm, which is associated with the remnant slag particles and reduces in intensity over time, most noticeably beyond 3 days for the sample containing 1 wt.% of CaO, consistent with the continued reaction as curing occurs. Furthermore, there are three distinct resonances in the region of -75 to -85 ppm for both sample sets, which vary slightly for the 3 wt.% of calcium oxide-containing samples and differ significantly for the 1 wt.% calcium oxide-containing samples as curing time progresses. These signals at δ_{iso} = -78.6, -81.4, and -84.4 ppm correspond to Q^1(II), Q^2(1Al), and Q^2 units, respectively, indicative of the formation of a tobermorite-like C-S-H phase, likely a sodium and aluminium substituted calcium silicate hydrate, C-(N)-A-S-H [58], [161], [205], consistent with this study's ^{29}Si MAS NMR spectra (*Section 5.3.2.4.2*) as well as previous studies into the structure of sodium carbonate-activated slag binders [58], [69], [188], [205]. Although the intensity of the resonances for Q^2 sites increase slightly with curing age, as expected and as seen with the carbonate- and silicate-activated samples, the resonance corresponding to Q^1(II) maintains the greatest intensity, unlike what was discerned from the ^{29}Si MAS NMR spectra for the carbonate-activated slag sample (**Figure 5-16**). However, the increase in Q^2 sites relative to the increase in Q^1 sites over time suggests an increase in the degree of polymerisation within the C-A-S-H structure. Moreover, there is a resonance at δ_{iso} = -87 ppm becoming slightly visible in these spectra at later curing ages, which is attributed to Q^3(1Al), whose presence demonstrates a significant amount of cross-linking in the C-(N)-A-S-H's structure [58], [96].

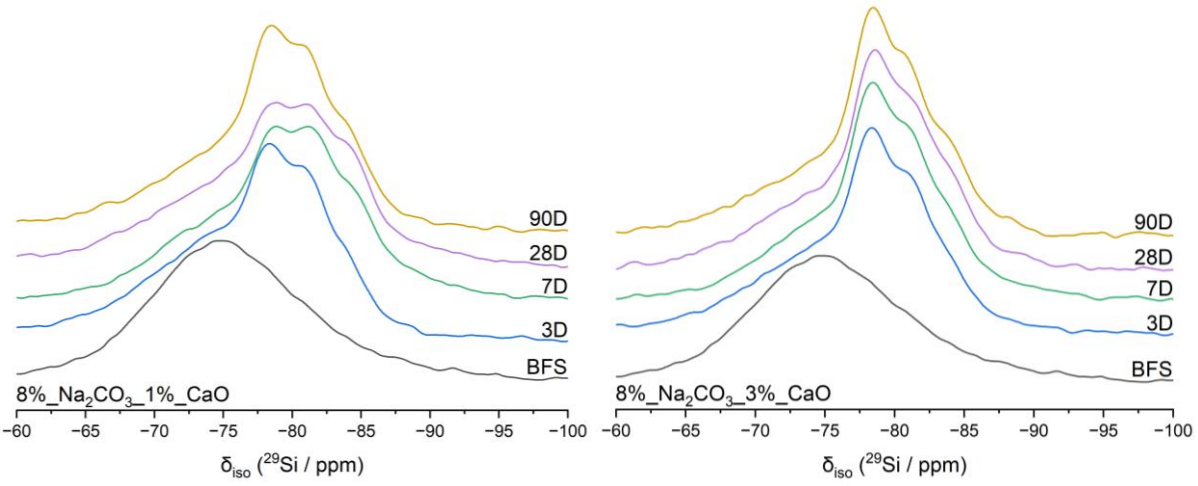

Figure 6-17 *^{29}Si MAS NMR spectra of BFS and carbonate-activated BFS with CaO at various curing times, as marked.*

The deconvolution of the ^{29}Si MAS NMR spectra (**Figure 6-18** and **Figure 6-19**) allows further exploration of the main three resonances identified in the region of -75 to -85 ppm, as well as a further five Si sites identified at δ_{iso} = -76.0, -87.0, and -92.0, assigned to Q^1(I), Q^3(1Al)/Q^4(4Al), and Q^3/Q^4(3Al), respectively, within the C-(N)-A-S-H phase. The existence of two apparent Q^1 sites that are presence in all sample spectra, designated as Q^1(I) and Q^1(II), are named based on the shielding variation from charge-balancing cations, Na^+/H^+ and Ca^{2+}, respectively, as calculated by molecular dynamic studies [206].

Table 6-3 *NMR parameters for carbonate-activated slag with 1 wt.% CaO samples, extracted from the deconvoluted ^{29}Si MAS NMR spectra.*

Sample	Parameter	Assignment							
		Unreacted slag	**Q^0**	**Q^1(I)**	**Q^1(II)**	**Q^2**	**Q^2(1Al)**	**Q^3**	**Q^3(1Al)**
	δ_{iso} (ppm)	*-75*	*-72*	*-76*	*-78.6*	*-84.4*	*-81.4*	*-92*	*-87*
	FWHM (ppm)	*13*	*5*	*6*	*3*	*3.8*	*3*	*8*	*9*
CO_3_1%CaO_3D	Relative integral area (%)	49.4	1.9	7.9	14.9	9.4	15.1	1.3	0.0
CO_3_1%CaO_7D	Relative integral area (%)	39.0	1.5	7.9	13.5	14.8	15.9	4.2	3.1
CO_3_1%CaO_28D	Relative integral area (%)	38.7	1.2	9.7	13.0	17.9	13.0	3.0	3.5
CO_3_1%CaO_90D	Relative integral area (%)	36.3	1.5	8.6	18.3	15.4	16.0	1.7	2.3

Minor quantities of Q^0 environments are calculated from the spectral deconvolutions for a signal at resonance δ_{iso} = -72.0 ppm, as well as remnant anhydrous slag particles represented by a broad Gaussian curve centring at δ_{iso} = 75.0 ppm, both of which generally decrease in area (and thus quantity) with curing time. All relative quantities of Si sites as a function of curing age were determined by the ^{29}Si MAS NMR deconvolutions of the carbonate-activated samples containing 1 and 3 wt.% of calcium oxide, and are detailed in **Table 6-3** and **Table 6-4**, respectively. For the 1 wt.% calcium oxide-containing sample, ~51 % of slag particles have reacted in the first 3 days and ~64 % at 90 days of curing, while for the 3 wt.% calcium oxide-containing sample, ~56 and ~67 % of slag had reacted by 3 and 90 days, respectively. This evidences the continual dissolution and reaction of slag over time, and an increased rate of reaction when including 3 wt.% of calcium oxide rather than 1 wt.%. Interestingly, the quantities calculated for remnant slag particles at 3 days of curing are greater when calcium oxide is incorporated in the system than without, which counters the increased rate of reaction observed initially when carbonate-activated slag is doped with calcium oxide, however, by 90 days, the remnant slag quantities are very similar regardless of the inclusion of or amount of

calcium oxide in the system, indicating that the reaction eventually plateaus to a similar rate for all carbonate-activated samples.

Table 6-4 *NMR parameters for carbonate-activated slag with 3 wt.% CaO samples, extracted from the deconvoluted ^{29}Si MAS NMR spectra.*

Sample	Parameter	Assignment							
		Unreacted slag	**Q^0**	**Q^1(I)**	**Q^1(II)**	**Q^2**	**Q^2(1Al)**	**Q^3**	**Q^3(1Al)**
	δ_{iso} (ppm)	*-75*	*-72*	*-76*	*-78.6*	*-84.4*	*-81.4*	*-92*	*-87*
	FWHM (ppm)	*13*	*5*	*6*	*3*	*3.38*	*3*	*8*	*9*
CO_3_3%CaO_3D	Relative integral area (%)	43.9	1.9	7.9	19.5	9.4	15.1	1.3	1.2
CO_3_3%CaO_7D	Relative integral area (%)	38.1	1.2	7.8	20.5	10.8	16.6	2.6	2.3
CO_3_3%CaO_28D	Relative integral area (%)	38.1	1.0	6.4	21.6	12.1	16.0	1.1	3.7
CO_3_3%CaO_90D	Relative integral area (%)	33.5	1.3	8.3	23.2	12.4	16.5	0.0	4.8

Furthermore, the relative sum of Q^1(I) and Q^1(II) sites remains relatively constant between 3 and 28 days, before notably increasing by 90 days for both sample sets, with both sites growing in quantity but the latter at a greater rate. This indicates an increased number of charge-balancing ions in the interlayer – both Na^+ or H^+ and Ca^{2+} – consistent with the slower dissolution of slag particles associated with carbonate-activated binders, and also likely due to the increased calcium in the system from the additive.

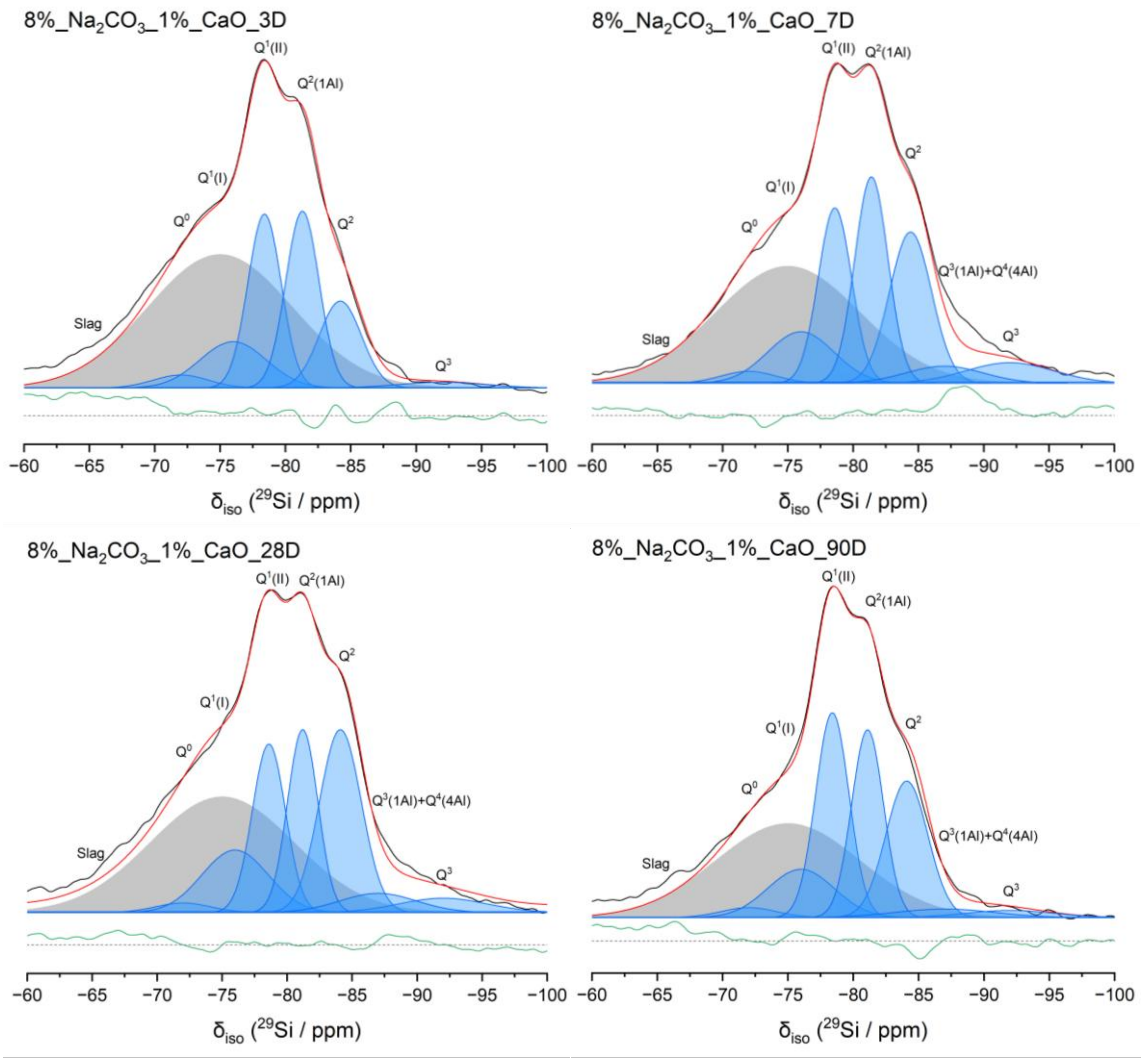

Figure 6-18 *^{29}Si MAS NMR spectra for carbonate-activated BFS with 1 wt.% CaO, and their associated deconvolutions. In each case, the data are shown in black, the fit (shown in red) is the sum of the deconvoluted peaks, and the difference between the data and the fit is shown in green. Peaks attributed to Si sites in C-(N)-A-S-H are shaded in blue, while those attributed to sites within remnant anhydrous slag are shaded in grey.*

As previously stated, two of the resonances are assigned to two Si sites each: δ_{iso} = -92.0 ppm represents Q^3 and/or Q^4(3Al), while δ_{iso} = -87.0 ppm is associated with Q^3(1Al) and Q^4(4Al) [160], [207]. The signal at δ_{iso} = -87.0 ppm increases steadily with time for the carbonate-activated sample containing 3 wt.% of CaO but increases from 3 to 28 days before reducing by 90 days for the sample containing 1 wt.% of CaO. Similarly, the resonance at δ_{iso} = -92.0 ppm increases between 3 and 7 days and then significantly decreases by 90 days for both CaO-containing carbonate-activated samples. For alkali-activated slag samples, the resonance at δ_{iso}

= -87.0 ppm is assigned to both the typical crosslinked Q^3(1Al) Si site in C-(N)-A-S-H and also some Q^4(4Al) sites in a polymerised aluminium-rich N-A-S-H phase, in accordance with structural constraints of the "cross-linked substituted tobermorite model" (CSTM) determined by Myers *et al.* [161]. The N-A-S-H phase consists of Q^4(3Al) and Q^4(4Al) sites and forms as an additional product to C-(N)-A-S-H in systems with high aluminium and sodium content, as observed in previous studies into alkali-activated slag cements [58], [194]. Likewise, some of the resonance at signal at δ_{iso} = -92.0 ppm must be attributed to Q^4(3Al) as well as Q^3, if Q^4(4Al) units have been determined, because no aluminosilicate phase can consist of only Q^4(4Al) units [209]. The formation of N-A-S-H in addition to the typical C-(N)-A-S-H structure has been demonstrated in previous studies of alkali-activated slag binders, including those activated with sodium carbonate [58], [71], [83], [92], [188], [194], [208], and some studies into geopolymer-rich geopolymers found them to contain almost entirely Q^4(3Al) and Q^4(4Al) environments [55], [209], [210]. The observed increase and subsequent decrease in quantity of Si environments at both -87.0 and -92.0 ppm for the samples with an addition of 1 wt.% of calcium oxide coupled with the lack of discernible Q^4(4Al) to meet CSTM structural constraints means that the existence of any Q^4 sites cannot be confirmed with certainty. On the other hand, for the carbonate-activated sample with 3 wt.% calcium oxide, the observed increase in quantity of the signal at δ_{iso} = -87.0 ppm and its subsequent complete depletion, paired with the steady increase in quantity of the resonance at δ_{iso} = -92.0 ppm reveals either a complete depletion of all Q^4 Si sites by 90 days (due to no aluminosilicate phase consisting solely of Q^4(4Al) sites) or the complete lack of such environments altogether. As such, it is entirely possible that no Q^4 Si environments exist within these samples at any curing age, suggesting that the aluminium-rich N-A-S-H does not form in carbonate-activated samples incorporating calcium oxide, therefore the signals at resonances δ_{iso} = -87.0 and -92.0 ppm are herein assigned to Q^3(1Al) and Q^3 Si sites. It is likely that the lack of Q^4 sites bonded to

aluminium tetrahedra is due to these aluminium tetrahedra being occupied within the aforementioned AFm-type calcium monocarboaluminates.

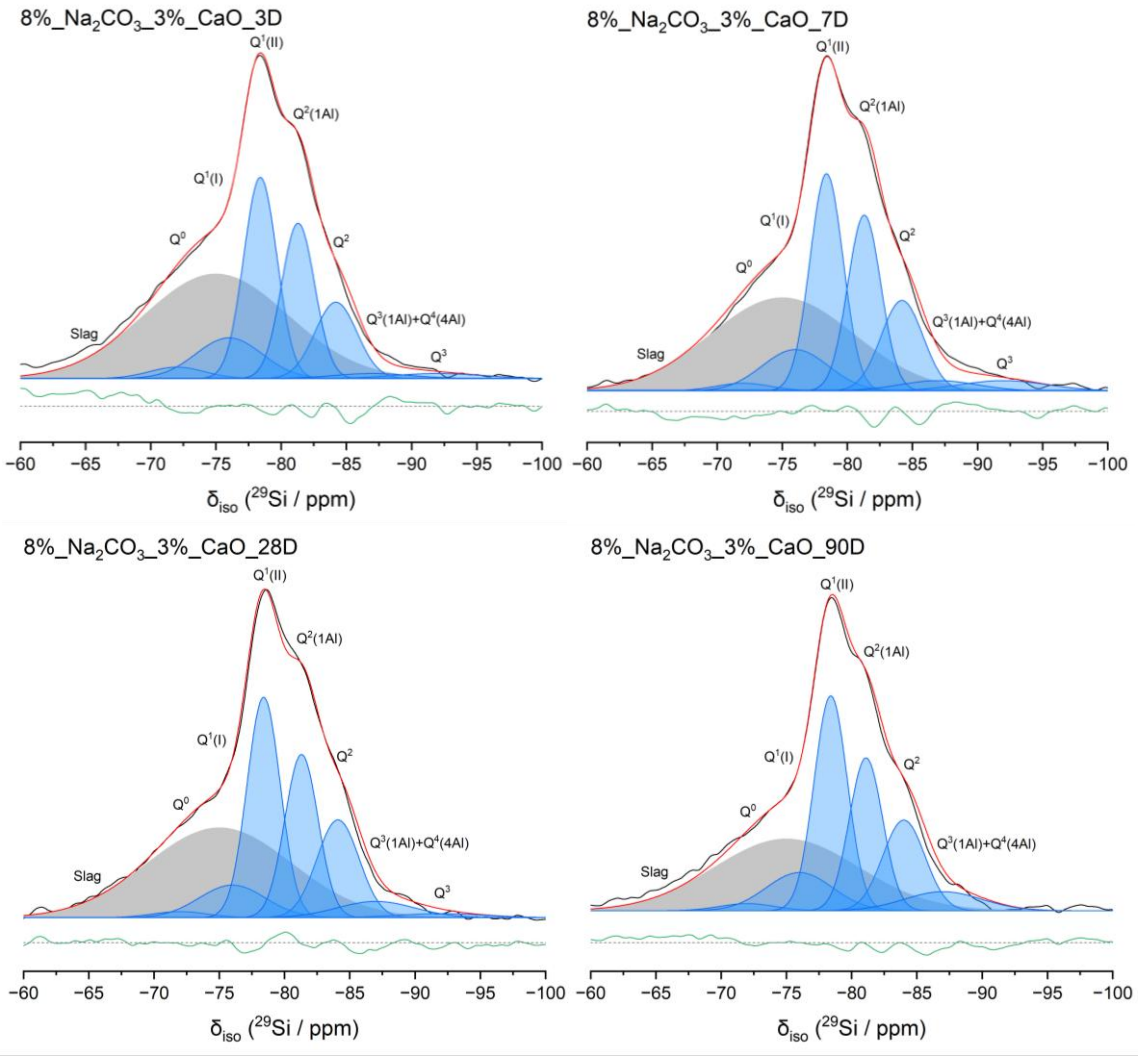

Figure 6-19 *^{29}Si MAS NMR spectra for carbonate-activated BFS with 3 wt.% CaO, and their associated deconvolutions. In each case, the data are shown in black, the fit (shown in red) is the sum of the deconvoluted peaks, and the difference between the data and the fit is shown in green. Peaks attributed to Si sites in C-(N)-A-S-H are shaded in blue, while those attributed to sites within remnant anhydrous slag are shaded in grey.*

There are notable amounts of Q^2(1Al) sites present in both samples, ~15 %, from 3 days of curing, which remains relatively constant and slightly increases to ~16 % by 90 days, indicating a steady level of aluminium substitution in the C-(N)-A-S-H structure, likely hindered by the occupation of Al tetrahedra in AFm phases. Furthermore, the existence of Q^3(1Al) units at an early age and their general increase in quantity over time suggests that the C-(N)-A-S-H is

significantly crosslinked, which only improves with increasing $Q^3(1Al)$ sites. This is the case for the sample containing 3 wt.% of calcium oxide, however, the carbonate-activated sample with 1 wt.% of calcium oxide included shows a slower increase in such sites before a reduction in quantity between 28 and 90 days of curing, meaning a reduction in crosslinking at later ages. This observation corroborates the change in Al^{IV}/Si ratios with curing age shown in **Figure 6-20**.

Additionally, the quantities of $Q^2(1Al)$ and Q^3 (including $Q^3(1Al)$) sites correlate with the mean chain length of the C-(N)-A-S-H. As $Q^2(1Al)$ remains relatively constant over time for both samples, the change in quantity of Q^3 theoretically should have the greater influence on mean chain length; for 1 wt.% of calcium oxide in the system, the amount of Q^3 sites peaks at 7 days and then gradually reduces by 90 days, while the 3 wt.% of calcium oxide-containing sample reveals an increase in Q^3 sites from 3 to 7 days, before maintaining this quantity through to 90 days, both following a similar pattern as the MCL shown in **Figure 6-20**.

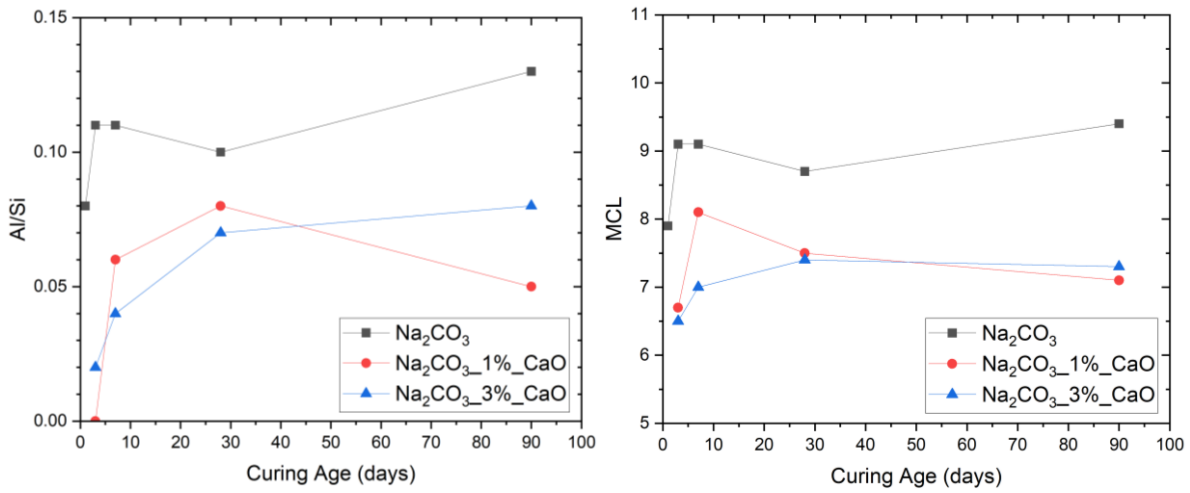

Figure 6-20 *Al/Si ratios and mean chain length for carbonate-activated BFS with CaO over time, calculated using the CSTM and ^{29}Si MAS NMR spectral deconvolutions.*

6.3.2.5 SEM-EDX

Scanning electron microscopy was conducted to examine the surface structure of cementitious binders, and in conjunction with energy dispersive X-ray (EDX) analysis, the elemental composition of the sample surface was determined, providing data on structural evolution over different curing lengths. SEM images for the additive-containing carbonate-activated slag binders, as seen in **Figure 6-21**, **Figure 6-22**, **Figure 6-27**, and **Figure 6-28** as with typical micrographs for alkali-activated slags, show a generally darker grey bulk structure containing the reaction products – C-A-S-H, hydrotalcite, AFm phases, and calcium carbonates – surrounding lighter grey remnant slag particles. Additional feature like cracks or striations can sometimes be seen, as fractured samples rather than cut samples were used in this study. Finally, some pores may be visible at this magnification, but the majority of pores in cement samples exist on the nanoscale and thus cannot be seen in these images.

6.3.2.5.1 Calcium Oxide-containing Carbonate-activated Slag

Images for the calcium oxide-containing carbonate-activated samples at 1 and 3 wt.% slag replacement, in **Figure 6-21** and **Figure 6-22** respectively, show little major change over time, with only the bulk structure becoming notably more cohesive and the amount of slag particles slightly reducing as time progresses. The sample with 3 wt.% of CaO shows a generally more cohesive bulk structure from early age compared to the sample containing 1 wt.% of CaO, aligning with the increased rate of reaction and extent of reaction associated with the sample.

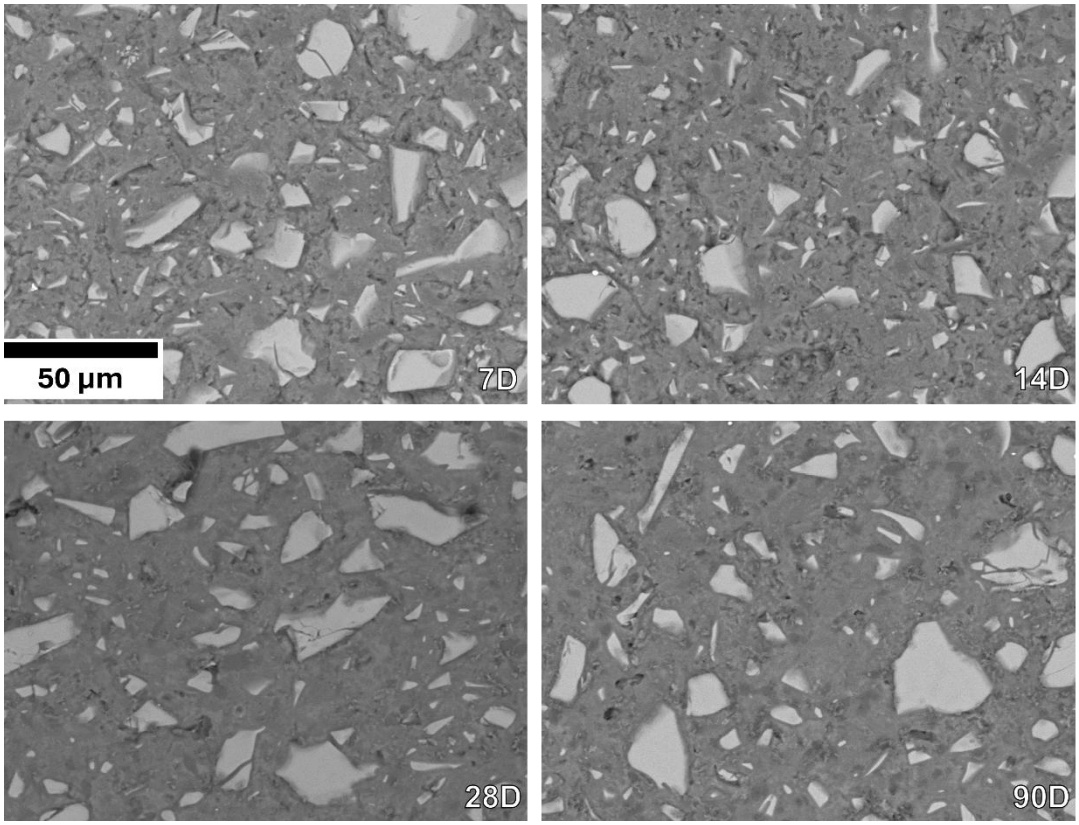

Figure 6-21 *SEM images for carbonate-activated BFS with 1 % CaO, at 1000x magnification, for various curing times, as labelled.*

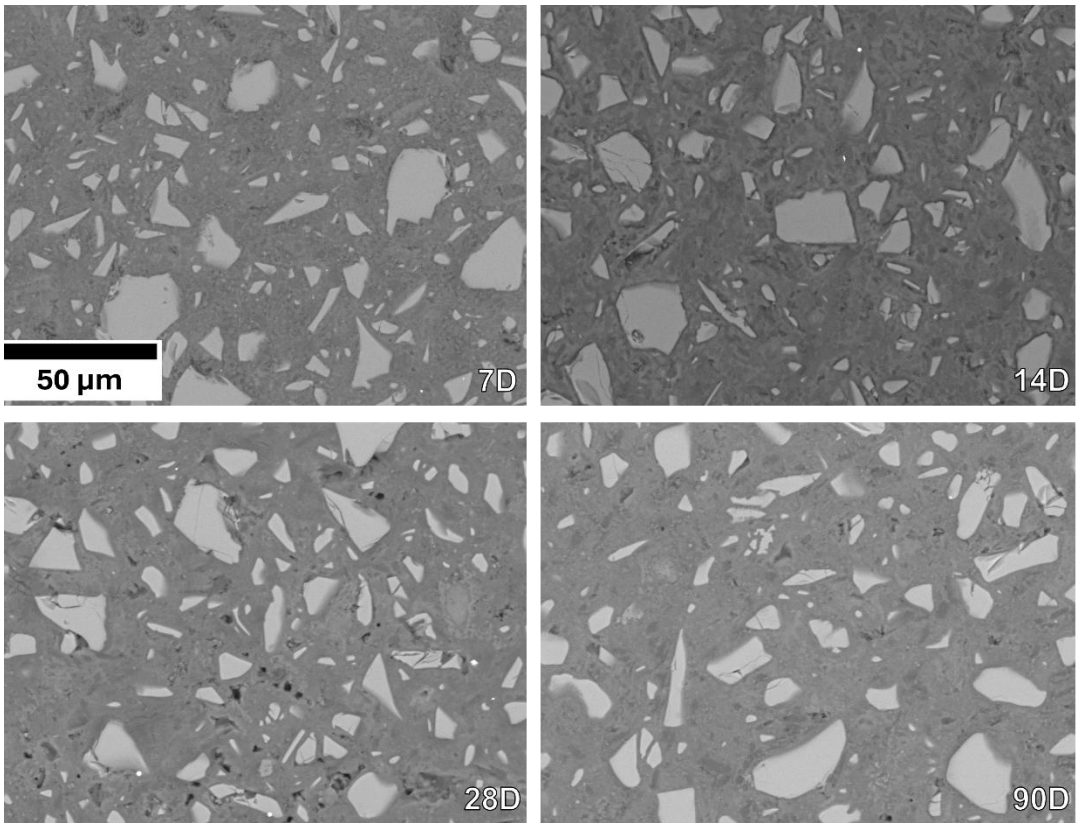

Figure 6-22 *SEM images for carbonate-activated BFS with 3 % CaO, at 1000x magnification, for various curing times, as labelled.*

The elemental mapping for both calcium oxide-containing carbonate-activated samples (**Figure 6-23** and **Figure 6-24**) show a very clear distinction at 7 days between slag particles, consisting heavily of calcium, silicon, and aluminium, and the surrounding bulk structure, which mostly consists of sodium, magnesium, and some calcium. The sample including 3 wt.% of calcium oxide appears moderately more cohesive in the bulk structure compared to its 1 wt.% CaO counterpart, whose bulk structure is much more sodium-dense at this age likely from both the activator and slag, while the former sample has more elements more evenly distributed throughout the bulk, further indicating the difference in rate of reaction. However, by 90 days, the 1 wt.% calcium oxide-containing sample has achieved a more evenly distributed bulk structure, akin to the sample with 3 wt.% of calcium oxide. Additionally, there does appear to be a greater inclusion of carbon and calcium in the bulk structure when the extent of reaction increases, possibly relating to the formation of AFm-type calcium monocarbonates.

Ternary systems for the samples were developed to further probe the phase evolution, based on the elemental composition data from the EDX scans, as illustrated in **Figure 6-25** and **Figure 6-26** for the carbonate-activated slags with 1 and 3 wt.% replacement with calcium oxide, respectively. The ternary CaO-Al_2O_3-SiO_2 system for both dosages of calcium oxide varies very little with curing time, and aligns with previous studies of alkali-activated slag binders [53], [211], [212] in addition to studies of synthetic C-(A)-S-H and N-A-S-H gels formed via a sol-gel method [213]. The region that both samples occupy is associated with the C-(N)-A-S-H phase structure, [53], [161], [214], as expected, aligning with previous observations in this study of C-(N)-A-S-H being the main reaction product for carbonate-activated samples. Additionally, there is a general maintenance of the amount of calcium in the system over time for both dosages of calcium oxide, with the 3 wt.% inclusion containing more CaO than the 1 wt.%, as one would expect.

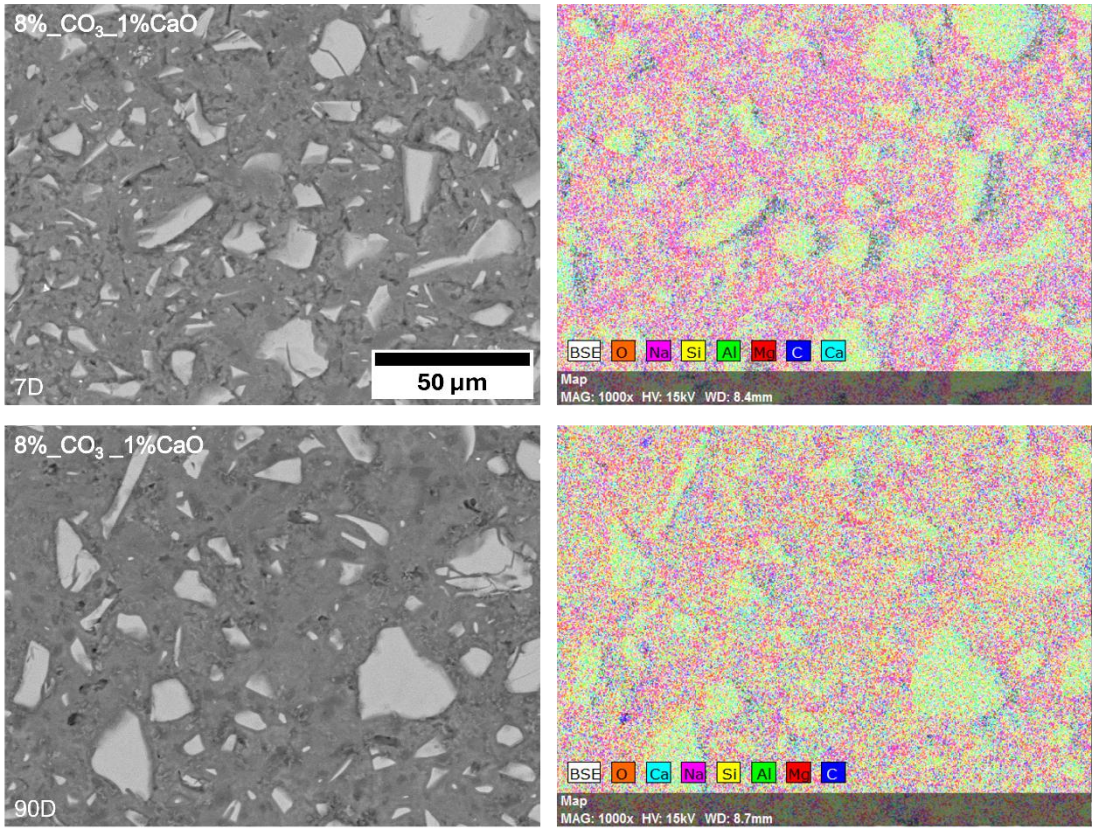

Figure 6-23 *Elemental mapping for carbonate-activated BFS with 1 % CaO, cured at 7 and 90 days, as labelled.*

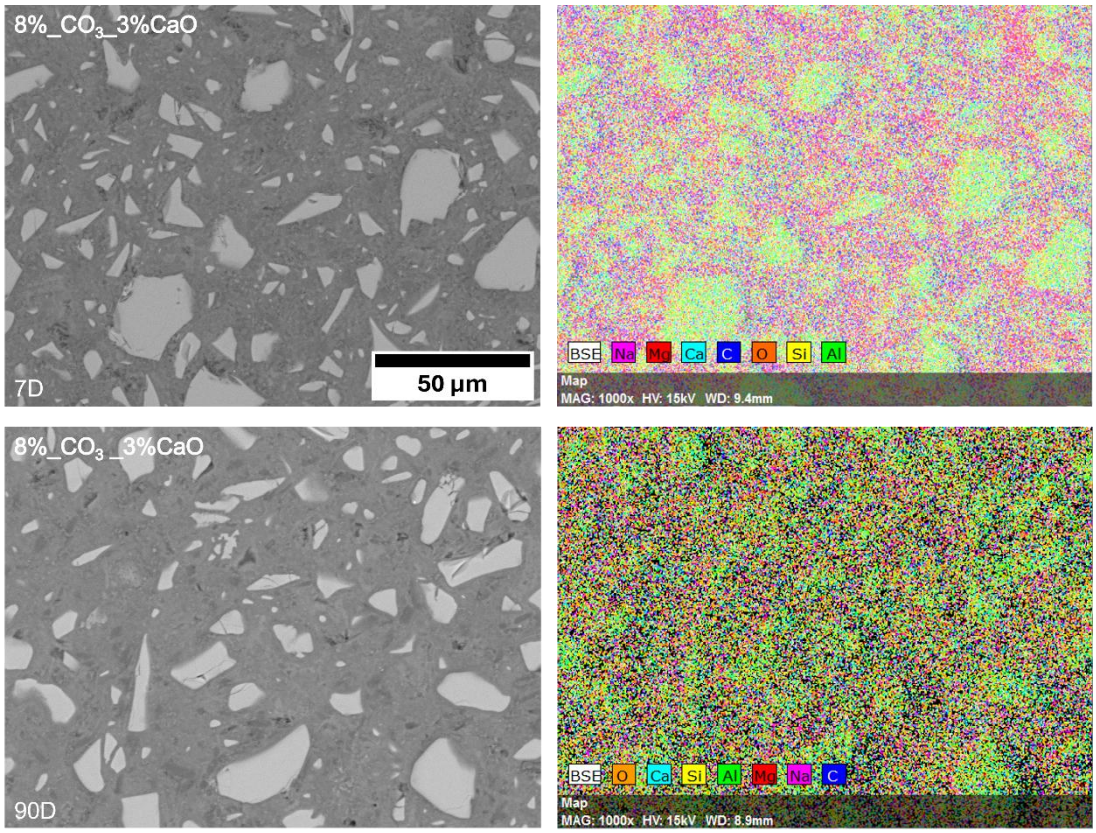

Figure 6-24 *Elemental mapping for carbonate-activated BFS with 3 % CaO, cured at 7 and 90 days, as labelled.*

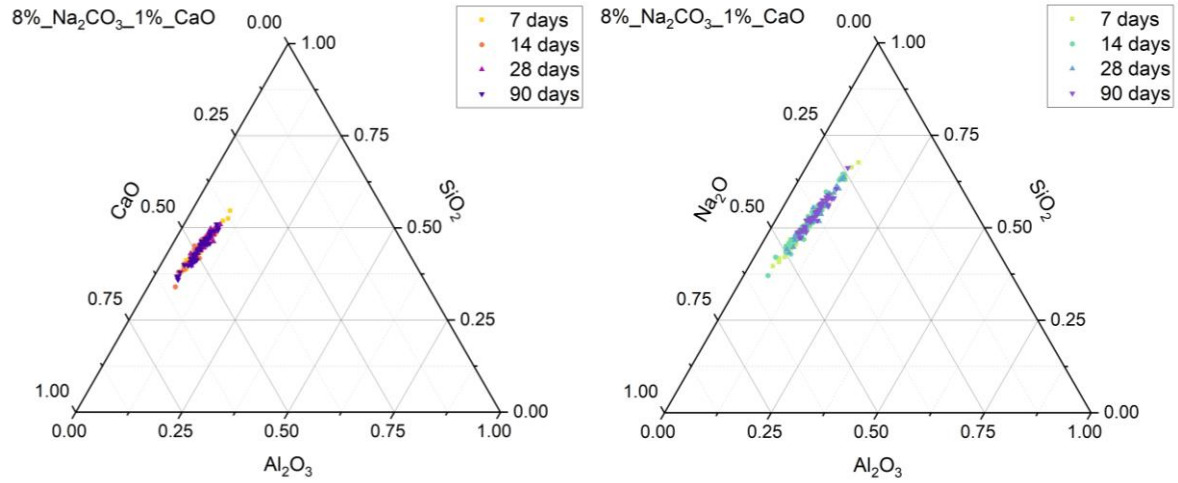

Figure 6-25 *Ternary systems of carbonate-activated slag with 1 % CaO cured for 7, 14, 28, and 90 days, as determined by SEM-EDX analysis. (L) Ternary CaO – Al_2O_3 – SiO_2 system (neglecting Na_2O content), and (R) Ternary Na_2O – Al_2O_3 – SiO_2 system (neglecting CaO) content, showing elemental composition.*

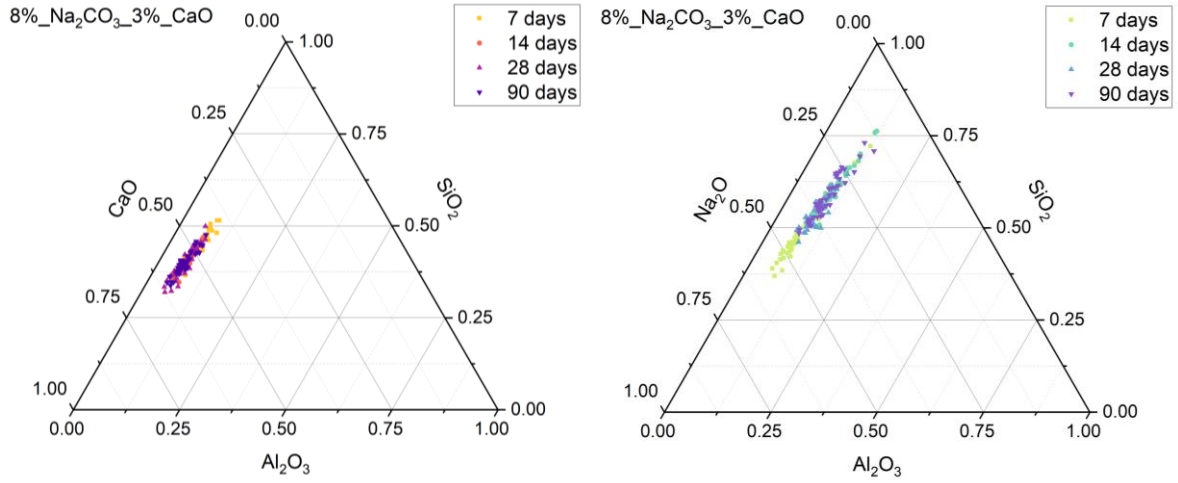

Figure 6-26 *Ternary systems of carbonate-activated slag with 3 % CaO cured for 7, 14, 28, and 90 days, as determined by SEM-EDX analysis. (L) Ternary CaO – Al_2O_3 – SiO_2 system (neglecting Na_2O content), and (R) Ternary Na_2O – Al_2O_3 – SiO_2 system (neglecting CaO) content, showing elemental composition.*

In contrast, the ternary Na_2O-Al_2O_3-SiO_2 system for both sample sets reveals a general decrease in Na_2O over time, which is somewhat unexpected as sodium ions are known to integrate into the interlayer of C-A-S-H phases over time.

6.3.2.5.2 Magnesium Oxide-containing Carbonate-activated Slag

Similarly to the samples containing calcium oxide, the carbonate-activated samples doped with 1 and 3 wt.% of magnesium oxide, shown in **Figure 6-27** and **Figure 6-28** respectively, have very little variation over time, other than the bulk structure surrounding the remnant slag particles becoming more cohesive. This appears to be occurring slightly faster for the higher replacement with magnesium oxide, with its 7-day samples appearing to have a smoother main structure, indicative of a slightly quicker rate of reaction. For these samples, there does appear to be areas within the bulk structure, particularly at early age, which display needle-like features, possibly due to the secondary phases filling pores. Additionally, darker spots can be observed for these magnesium oxide-containing samples, which are likely high concentrated areas of unwanted structures or unreacted components, or they may possibly be due to sample preparation.

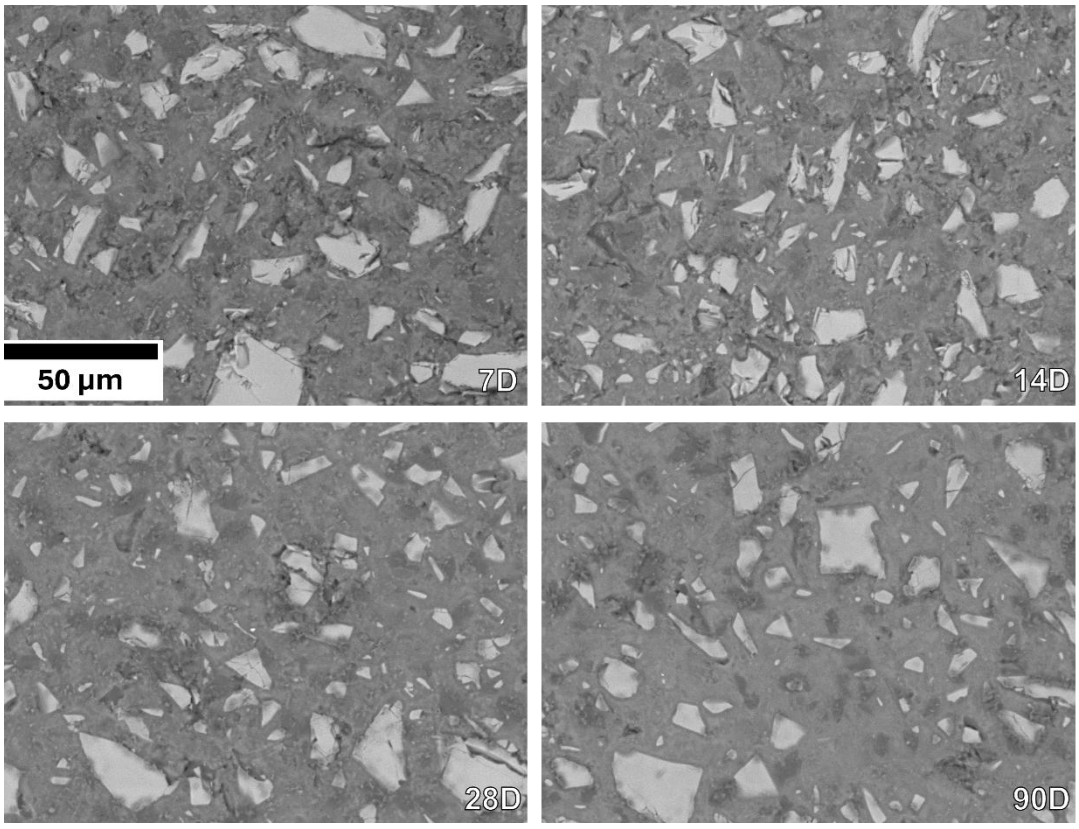

Figure 6-27 *SEM images for carbonate-activated BFS with 1 % MgO, at 1000x magnification, for various curing times, as labelled.*

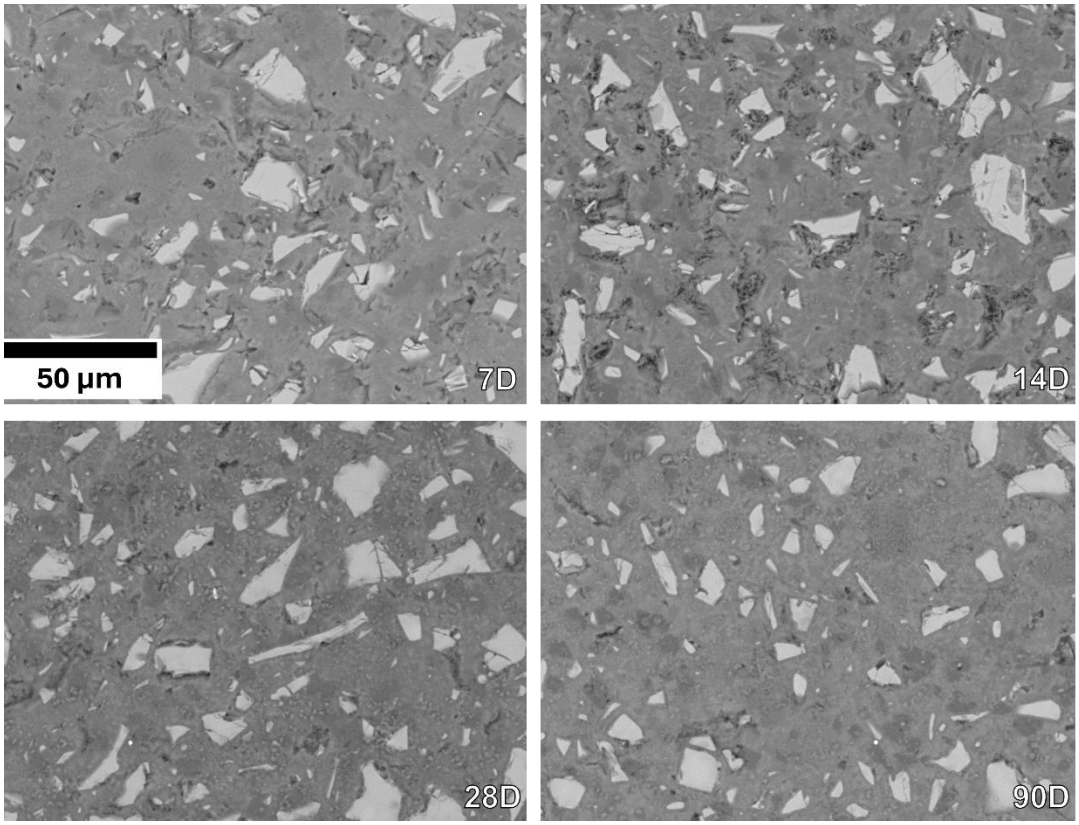

Figure 6-28 *SEM images for carbonate-activated BFS with 3 % MgO, at 1000x magnification, for various curing times, as labelled.*

Elemental mapping for the samples doped with magnesium oxide, shown in **Figure 6-29** and **Figure 6-30** for a replacement of slag by 1 and 3 wt.% respectively, appear to vary in chemical composition concentration by dosage. Both dosages reveal the remnant slag particles to consist mostly of silicon, aluminium and calcium, which becomes less clearly defined (i.e. less concentrated) from 7 to 90 days as the continual dissolution of slag particles proceeds. However, the composition of the bulk structure varies between the two sample sets; for the 1 wt.% of magnesium oxide, the bulk structure is very sodium dense with some magnesium, calcium, and carbon evenly throughout at 7 days, which tends to a more silicon-rich bulk containing sodium, calcium and aluminium by 90 days, indicative of a C-N-A-S-H-based structure, while for the sample including 3 wt.% of magnesium oxide, the bulk structure is very sodium- and carbon-rich at 7 days with distinct areas concentrated with magnesium, likely due to the MgO not reacting or incorporating into the system as planned. Similarly, by 90 days, the

3 wt.% of magnesium oxide-containing sample maintains areas of high magnesium concentration, but the bulk structure has become enriched with calcium, silicon, and aluminium as well as the previously observed sodium and carbon, indicative of C-A-S-H formation.

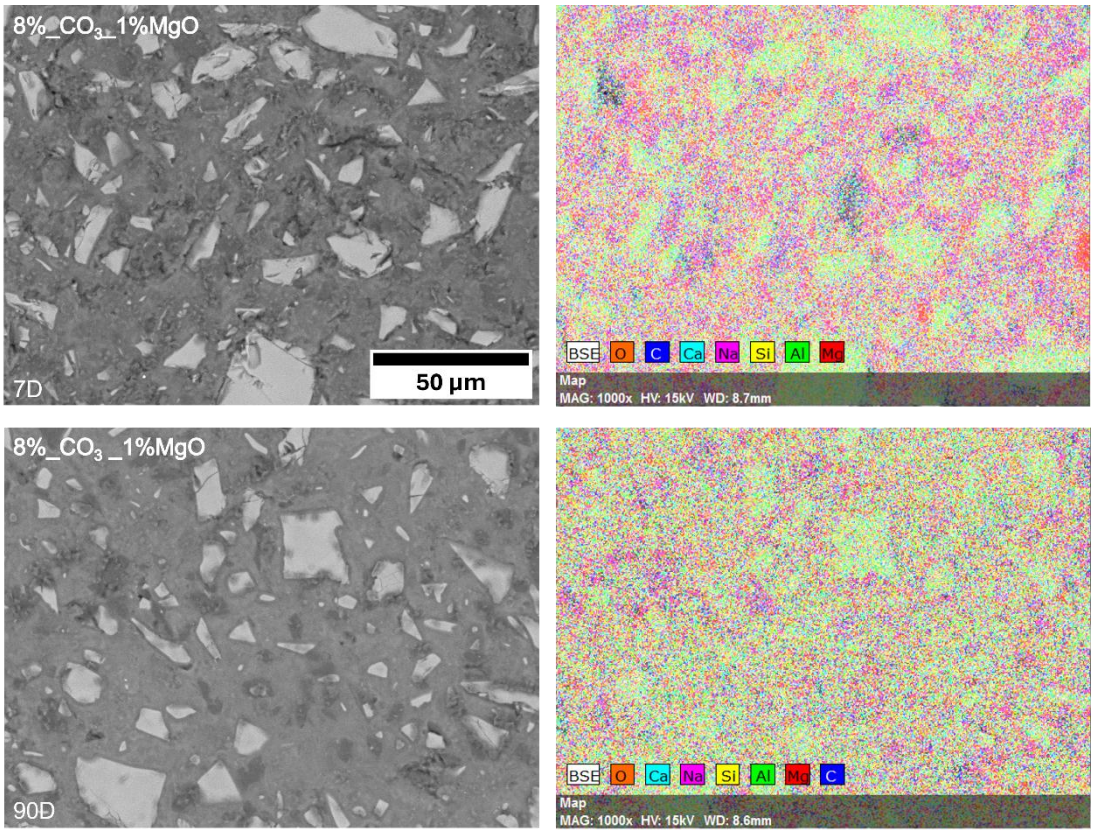

Figure 6-29 *Elemental mapping for carbonate-activated BFS with 1 % MgO, cured at 7 and 90 days, as labelled.*

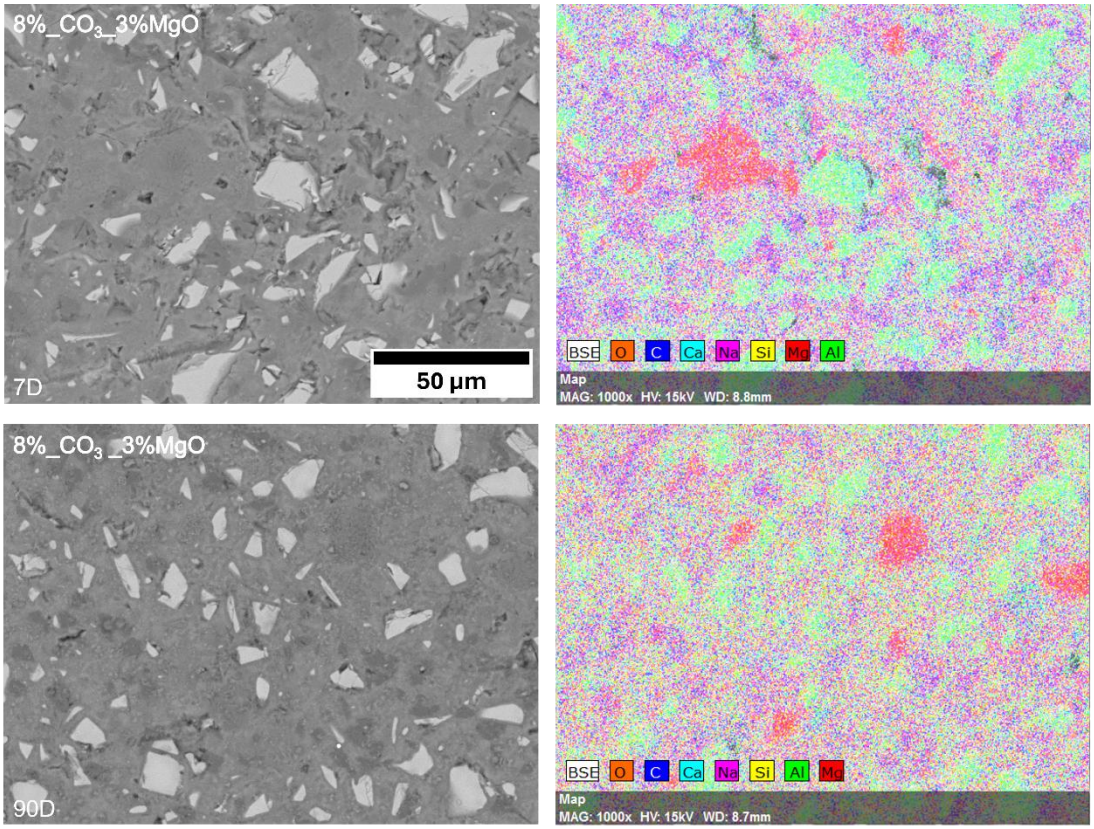

Figure 6-30 *Elemental mapping for carbonate-activated BFS with 3 % MgO, cured at 7 and 90 days, as labelled.*

From the elemental composition data acquired by EDX, ternary systems were developed for these samples to help understand the structural evolution with curing time. These systems are shown in **Figure 6-31** and **Figure 6-32** for the 1 and 3 wt.% replacement of slag with magnesium oxide in carbonate-activated binders respectively. For both dosages of magnesium oxide, the ternary CaO-Al_2O_3-SiO_2 system varies marginally between curing times and also shows little variation between wt.% dosages, with the occupied area aligning with past studies on alkali-activated slags [53], [211], [212], as well as studies into synthetic C-(A)-S-H and N-A-S-H gels [213]. The specific region where all points sit corresponds to the C-(N)-A-S-H gel phase [53], [161], [214], as seen in the carbonate-activated sample without additives.

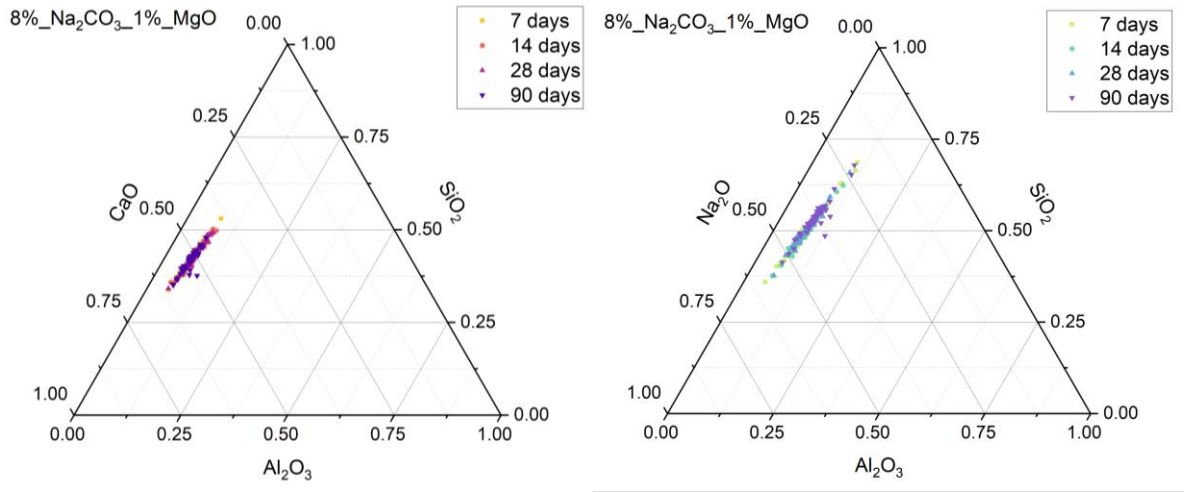

Figure 6-31 *Ternary systems of carbonate-activated slag with 1 % MgO cured for 7, 14, 28, and 90 days, as determined by SEM-EDX analysis. (L) Ternary CaO – Al_2O_3 – SiO_2 system (neglecting Na_2O content), and (R) Ternary Na_2O – Al_2O_3 – SiO_2 system (neglecting CaO) content, showing elemental composition.*

On the other hand, the ternary Na_2O-Al_2O_3-SiO_2 system shows more variation over time for both dosages of magnesium oxide, with a slight negative shift in Na_2O as curing time progresses, as well as a small increase in Al/Si, however there is little change between dosages, indicative of a similar reaction rate and mechanism, further suggesting the lack of impact from the inclusion of magnesium oxide.

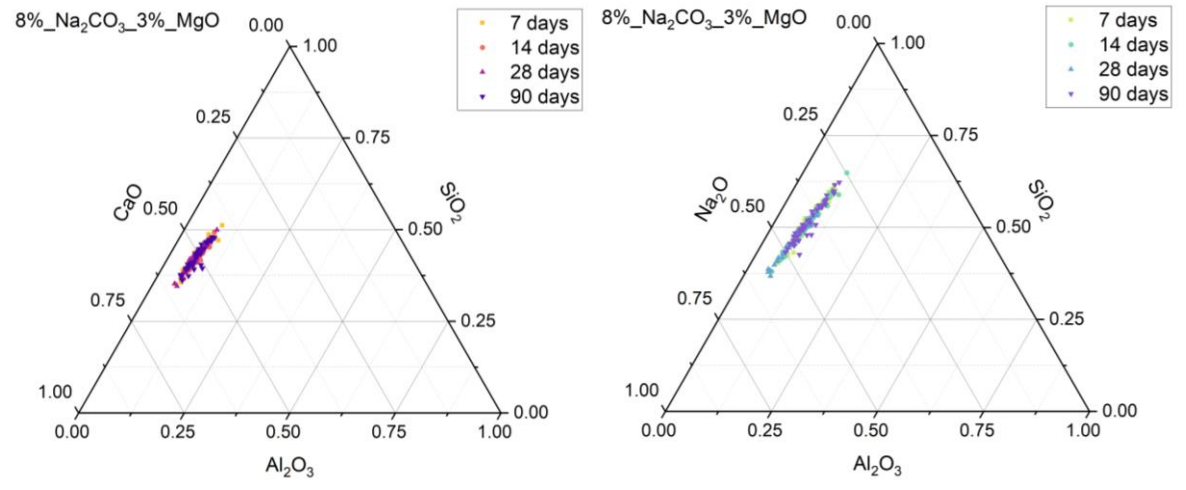

Figure 6-32 *Ternary systems of carbonate-activated slag with 3 % MgO cured for 7, 14, 28, and 90 days, as determined by SEM-EDX analysis. (L) Ternary CaO – Al_2O_3 – SiO_2 system (neglecting Na_2O content), and (R) Ternary Na_2O – Al_2O_3 – SiO_2 system (neglecting CaO) content, showing elemental composition.*

6.3.3 Physical Properties

Physical and mechanical properties of cements are typically influenced by the initial chemical composition, which in turn effects the phase evolution and thus the physical properties of the material. Understanding these structural phases and the subsequent physical behaviour is key to determine its appropriate application. Therefore, the physicomechanical properties of the carbonate-activated slag binders doped with 1 and 3 wt.% calcium and magnesium oxide are assessed hereafter, and these properties are discussed in relation to their reactionary chemistry and structural evolution determined thus far.

6.3.3.1 Workability and Setting Time

Average mini-slump diameters for the additive-containing sodium carbonate-activated slag samples are shown in **Figure 6-33** to illustrate how a replacement of slag with 1 or 3 wt.% of either calcium or magnesium oxide impacts the fluidity of binders. Firstly, for the samples containing calcium oxide, a generally negative effect on fluidity is observed, compared to an increase in fluidity when magnesium oxide is incorporated. The decrease in workability for carbonate-activated slag with the calcium oxide is likely due to the increased rate of formation of calcium carbonates. Where this increased rate of formation increased the overall rate of reaction discussed previously in *Section 6.3.1*, here the rapid formation of calcium carbonate polymorphs means an increased water demand as these phases adsorb water, leading to a reduced fluidity and workability retention, which is made only worse with increasing CaO content, as observed in previous studies on the influence of CaO on alkali-activated slag cements [122], [239], [240].

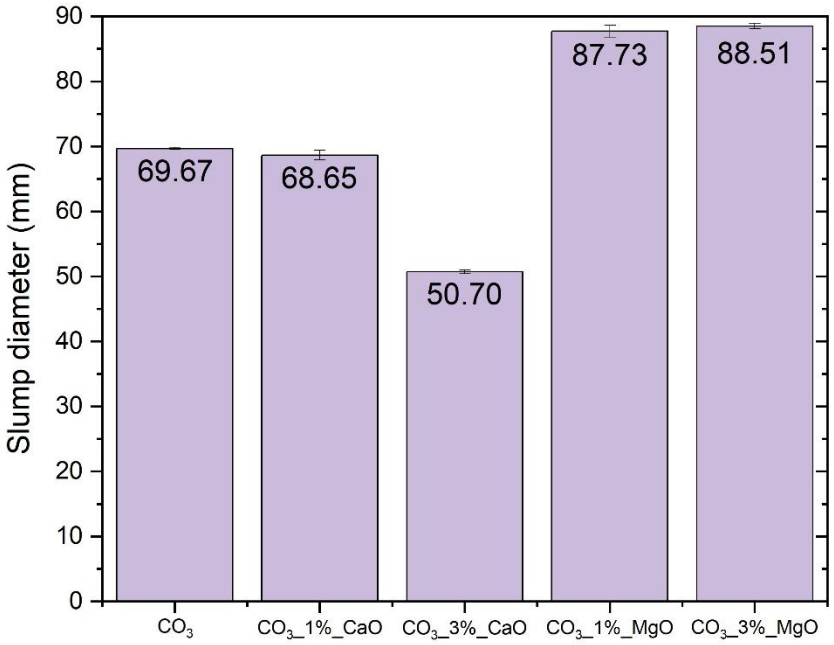

Figure 6-33 *Mini slump diameter values for carbonate-activated BFS with additives, in comparison to carbonate-activated BFS, as labelled.*

On the other hand, the increased fluidity observed with both 1 and 3 wt.% replacement of slag with magnesium oxide is not necessarily what is expected; typically, MgO generally decreased the workability of cements, similarly to the CaO inclusion, by consuming free water and increasing water demand of the mixture, due to it accelerating the hydration process and promoting the rapid formation of hydrates, which in turn lead to a thicker and less fluid mixture [123], [125]. However, as observed previously in this study, the inclusion magnesium oxide had minimal effect on the rate of reaction of the carbonate-activated slag binders, likely due to the limited reactivity (and low surface area) of the magnesia used in this study, but this reduced reactivity is likely favourable for fluidity here. The low surface area due to the large particle size of the MgO and its limited reactivity likely mean that it is causing a filler effect between calcium carbonates forming, preventing the consumption of water associated with such phases, and thus increasing the fluidity of the sodium carbonate-activated slag cement. This aligns with previous studies observing that a finer magnesia accelerates the formation of expansive phases,

like hydrotalcite, as well as increasing the general rate of reaction, resulting in a denser and less workable material [123], [241].

Table 6-5 *Setting times for carbonate-activated BFS with additives, as determined by Vicat apparatus.*

Sample	Setting Time	
	Initial	**Final**
8%_Na_2CO_3	3 h 10 m	4 h 40 m
8%_Na_2CO_3_1%_CaO	2 h 40 m	4 h 50 m
8%_Na_2CO_3_3%_CaO	2 h 20 m	4 h 00 m
8%_Na_2CO_3_1%_MgO	1 h 30 m	2 h 20 m
8%_Na_2CO_3_3%_MgO	1 h 20 m	2 h 00 m

Additionally, setting times were determined for the additive-including carbonate-activated samples using an automatic Vicat apparatus (**Table 6-5**). The inclusion of either additive at either wt.% replacement reduces the initial setting time, as well as mostly reducing the final setting time, for sodium carbonate-activated slag, which is often noted for its longer setting time [71], [73], [74], [77], [227]. The reduced setting times for the samples containing additional calcium oxide align with the increased rate of reaction due to an increase in alkalinity due to calcium hydroxide forming, as well as the formation of calcium carbonate polymorphs more quickly, thus creating a denser and less workable material more quickly. On the other hand, considering the lack of reactivity noted for the magnesium oxide used in this study, it has greatly reduced the setting time for the slag activated with sodium carbonate, possibly due to the MgO particles creating a filler effect within the sample matrix, between slag particles and any reaction products, resulting in a reduced setting time.

6.3.3.2 Viscometry

The flow curves (stress vs strain) for the carbonate-activated slag cements with replacements of slag with calcium or magnesium oxide are illustrated in **Figure 6-34** and the corresponding

Herschel-Bulkley parameters are outlined in **Table 6-6**, to aid in the understanding of the rheological behaviour of these binder systems. Akin to the solely carbonate-activated sample, all additive-containing carbonate-activated samples are shear-thinning fluids, i.e. they have a flow index (n) of less than 1, meaning that its viscosity reduces as shear rate increases, consistent with studies on carbonate-activated slag binders [117], [119], [231]. Further to this, although all samples have a yield stress similar or less than that of the carbonate-activated sample without additives, the consistency index (k) increases significantly with increasing replacements of slag with calcium oxide, indicating a greater resistance to flow. Essentially, a higher consistency index means a more viscous fluid overall, requiring more force to achieve a given shear rate. Conversely, the samples containing magnesium oxide have the opposite effect on consistency index, suggesting an increased fluidity. These observations corroborate the mini-slump data.

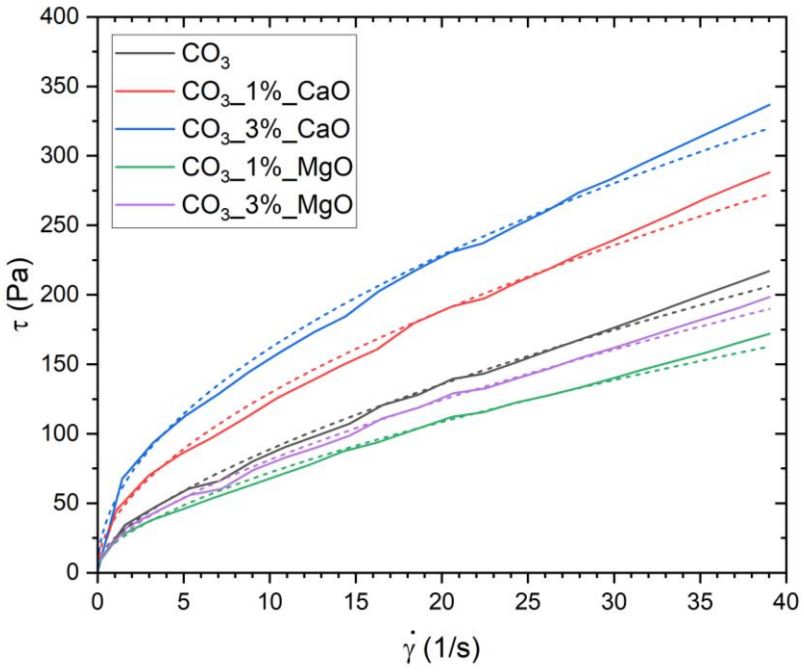

Figure 6-34 *Rheology of carbonate-activated BFS with additives, in comparison with silicate-activated BFS. Experimental data are the solid lines, and the model fits are the dotted lines.*

Table 6-6 *Herschel-Bulkley parameters for carbonate-activated BFS with additives, fitted to the curve in* ***Figure 6-34****.*

Sample	**τ_0**	**k**	**n**
8%_Na_2CO_3	6.77	18.22	0.65
8%_Na_2CO_3_1%_CaO	5.08	33.90	0.56
8%_Na_2CO_3_3%_CaO	1.12	50.22	0.50
8%_Na_2CO_3_1%_MgO	6.20	15.19	0.64
8%_Na_2CO_3_3%_MgO	7.33	16.00	0.66

6.3.3.3 Compressive Strength

Measurements of 7- and 28-day compressive strength for the carbonate-activated slag pastes including calcium or magnesium oxide are reported in **Figure 6-35**, with the solely carbonate-activated slag sample data also reported for comparison.

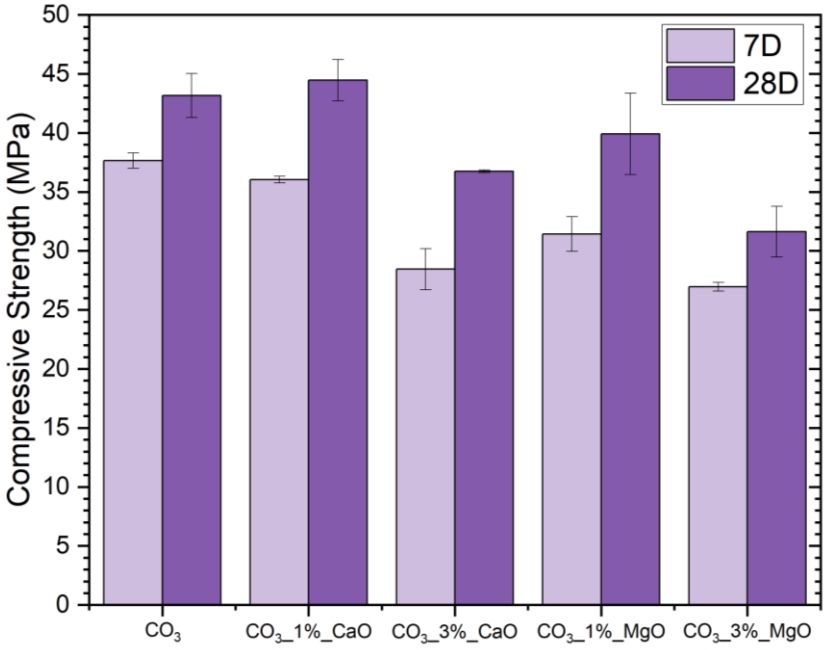

Figure 6-35 *Compressive strength values of carbonate-activated BFS with additives at 7 and 28 days, in comparison to carbonate-activated BFS, as labelled.*

The measured values for compressive strength at 7 and 28 days of curing for all of the carbonate-activated samples are higher than those reported in literature for carbonate-activated samples with similar experimental formulation parameters – water/binder ratio and activator dosage [69], [71], [84], [230], [232]. However, the trend for sodium carbonate-activated samples is that they have a lower strength development compared to slag binders utilising sodium silicate or hydroxide, due to the low initial pH and formation of calcium carbonate polymorphs inhibiting the reaction process, including the formation of the main strength-giving phase, C-A-S-H.

For the carbonate-activated sample containing 1 wt.% replacement of slag with calcium oxide, the strength values at both 7 and 28 days curing are very similar to the sample not containing additives, suggesting that although the incorporation of such a small amount of CaO increases the rate of reaction by ~16 hours, it has little influence on the strength development, which aligns with the similar structural evolution between these sample sets. Conversely, the inclusion of 3 wt.% of CaO negatively impacts compressive strength values at both 7 and 28 days. The reduced strength at 7 days is likely due to the increased rate of formation of calcium carbonate polymorphs, particularly the likes of calcite, and the sodium calcium carbonate hydrate, gaylussite, at early reaction meaning that high amounts of calcium are consumed in these phases preventing the formation of well-polymerised C-A-S-H, which is known to give AACs their strength. Although the strength increases at a similar rate between 7 and 28 days as the carbonate-activated sample without additives and with 1 wt.% CaO replacement, the 28-day strength value remains low for the 3 wt.% CaO addition, likely due to the lack of well-polymerised C-A-S-H described by the previous mechanism or other. It is also possible that the observed formation of the AFm-type calcium monocarboaluminates may be a result of the decalcification of any established C-A-S-H phases, akin to carbonation, or that their formation is occurring at a greater rate compared to C-A-S-H, meaning the C-A-S-H phase is not

polymerising to the degree needed for desirable strength development. Previous studies investigating the incorporation of CaO on the mechanical strength of alkali-activated slag cements tend to show an increase in performance with increased inclusion of calcium oxide up to some threshold, where it then appears to have a negative effect on compressive strength [124], [126], [239], [240].

On the other hand, the replacement of slag with magnesium oxide at both 1 and 3 wt.% in the sodium carbonate-activated slag pastes has a negative impact on compressive strength at both 7- and 28-days curing. Despite the observation of this additive having little to no impact on the early age reaction kinetics and mechanisms, its inclusion has revealed interesting effects on the physical properties of the carbonate-activated slag cements. The noted lack of reactivity of magnesia used in this study has likely led to particles behaving as a filler in the sample matrix, which has conveniently improved workability (by preventing consumption of free water by calcium carbonates) and then reduced setting time thereafter by filling gaps in the bulk structure, causing fluidity to decrease and the material to harden. This continued filler effect from the limited reactivity of the MgO has likely reduced the ability of sufficient C-A-S-H formation, therefore preventing successful strength development of these samples.

The American Concrete Institute [221] states that concrete, made with PC, requires a 28-day compressive strength value of between 17 and 28 MPa for use in “low-strength” applications like foundations, slabs, and footings or at least 34.5 MPa for high-strength applications like beams and girders. As such, even with the differing effects of CaO and MgO on compressive strength in the sodium carbonate-activated slag pastes, the 28-day values suggest that all of these samples are suitable in applications where Portland cement systems are currently used.

6.4 Conclusions

Due to the less than desirable properties of sodium carbonate-activated slag determined in the previous chapter, the inclusion of small amounts of the additives, calcium oxide and magnesium oxide, was investigated with the aim of improving the performance of the carbonate-activated slag formulation while maintaining a lower carbon footprint compared to when the likes of sodium silicate is utilised for alkali activation.

The findings show that the inclusion of magnesium oxide, in either 1 or 3 wt.% replacement of BFS in the system, had little to no effect on the reaction rate and mechanisms for the carbonate-activated slag binder, with the calorimetry data revealing almost identical shaped curves for both inclusions of MgO and the non-additive-containing carbonate-activated samples, but with the small reduction in the time point of the onset of the main reaction heat output when MgO was incorporated. Moreover, the DRIFTS data for the initial hours of reaction revealed no significant differences between the MgO-including carbonate-activated sample and the solely carbonate-activated sample.

On the other hand, the early rate of reaction for the sodium carbonate-activated slag binder was greatly improved by the incorporation of calcium oxide, in both 1 and 3 wt.% replacements of slag, due to the increased alkalinity occurring in the pore solution as a result of calcium hydroxide precipitation. Calorimetry data revealed that 1 and 3 wt.% inclusion of calcium oxide resulted in the achievement of the main reaction peak ~17 and ~33 hours sooner, respectively, than the solely carbonate-activated sample, with the heat evolution for the main reaction forming a taller and narrower curve with increasing inclusion of CaO. Additionally, DRIFTS and XRD data corroborated the increased rate of reaction, determining that the initial preferential reaction between CO_3^{2-} (from the activator) and Ca^{2+} (from the slag and/or additive) still occurs but at a much quicker rate, and that for the 3 wt.% incorporation of CaO,

C-A-S-H begins to form in the first 2 hours after mixing at the same time as the formation of the calcium carbonate polymorphs.

Despite the increased early reaction observed with the inclusion of calcium oxide, the extent of reaction of these systems at 7 days, determined by TGA, XRD, FTIR, and NMR spectroscopy, was very similar to the solely carbonate-activated sample at this same point, however, with a greater formation of AFm-type monocarboaluminates. Beyond this age, the C-A-S-H that formed in the CaO-containing samples does not appear to polymerise to the same extent as the solely carbonate-activated sample, indicating that the further continual reaction is limited, possibly by the formation of secondary species, monocarbonates; it is possible that, similarly to observations made by Ahmed *et al.* [242], the simultaneous precipitation of C-A-S-H and calcium-containing carbonate phases (AFm and calcite) during the initial days of reaction results in a lack of transportable cations between the solid surface and solution, preventing further sufficient reaction.

Conversely, although the incorporation of magnesium oxide had little to no effect on the early reaction of the slag binder utilising sodium carbonate as an alkali activator, the structural evolution differs slightly between the binder when MgO is included and when it is not. Solid state analysis of the microstructure revealed an increased quantity of hydrotalcite phases in the MgO-containing samples, suggesting that the increased magnesium content means a greater incorporation in and thus formation of the AFm-type hydrotalcite phase. Besides this, the formation of C-A-S-H and calcium carbonate polymorphs appeared similar for the carbonate-activated system whether magnesium oxide was included in the system or not.

In terms of physical properties, including fresh-state workability and 7- and 28-day compressive strength measurements, the inclusion of both additives appeared to have an

influence on the performance. Despite having a limited effect on reaction rate and structural evolution beyond hydrotalcite formation for the sodium carbonate-activated slag binder, the inclusion of magnesium oxide does indeed impact the mechanical properties; regardless of wt.% inclusion, the slump diameter increased and the yield stress decreased, resulting in a less-viscous paste at early age, however, the compressive strength of the carbonate-activated binder reduced with increasing wt.% inclusion of MgO at both 7 and 28 days curing. In contrast, the inclusion of calcium oxide reduced the workability and flow of the fresh carbonate-activated slag paste, and although 1 wt.% inclusion of CaO maintained similar strength values to the solely carbonate-activated binder, the 3 wt.% inclusion greatly reduced the mechanical properties at both time points, likely due to the lack of polymerised C-A-S-H (the main strength-giving phase) and the preferred formation of monocarbonates.

Due to its use in previous studies to a similar extent, it was expected that magnesium oxide would improve both the reaction and physical properties of the sodium carbonate-activated slag binder. However, it is likely that the MgO used within this study did not possess the reactivity desired to garner such improvements; “light-burned”, caustic-calcined magnesia is highly reactive, having high surface area and rapid hydration in water, while “hard-burned” MgO results in a lower surface area and thus is less reactive in nature. In this study, it is likely that the magnesium oxide was “hard-burned” due to its lack of reactivity and rather than integrating in the system as desired, instead filled voids in the bulk of the material and inhibited the long-term reaction.

Overall, the inclusion of magnesium oxide had limited influence on the early reaction of the sodium carbonate-activated slag binder, however, it greatly improved the fresh state properties. Conversely, the addition of calcium oxide improved the early rate of reaction and at 3 wt.% led to the simultaneous formation of calcium carbonates and C-A-S-H in the early hours of

reaction, but at the cost of the workability. However, beyond the initial 7 days, the extent of reaction levelled with the solely carbonate-activated sample while the C-A-S-H phases were less polymerised than the carbonate-activated sample, which in turn reduced the compressive strength. It is possible that the combination of both calcium and magnesium oxide may lead to both the increased rate of reaction and the improved fresh state properties, however, this would be unlikely to improve the strength development. On the whole, the inclusion of additives in small amounts does influence the performance of sodium carbonate-activated slag, and depending on the application and its requirements, the knowledge from this study can allow the tailoring of formulations with further study.

Chapter 7: Sodium Sulphate-activated Slag Binders

7.1 Introduction

Chemical activation of slags with near-neutral salts can eradicate concerns associated with highly alkaline activators – silicates and hydroxides – where handling of viscous corrosive and hazardous solutions pose safety risks for on-site production of AACs. Such activators have also been revealed to be the major contributors to the environmental impacts of AACs, due to being produced via energy intensive manufacturing processes and not being industrial wastes or natural resources.

Sodium sulphate is widely available and has a lower pH value (~7) compared to the likes of hydroxides and silicates (>13). It exists in huge volumes worldwide, as it can be obtained from mined mirabilite or as a by-product during HCl production or silica pigments, and thus its price is very competitive compared to sodium silicate and hydroxide [81], [114]. With its availability, low-cost, and near-neutral pH, there is potential for utilising sodium sulphate for activation of slags in the hopes of reducing minimising challenges associated with the more commonly used activators [48], [81], [87].

Unfortunately, similarly to where sodium carbonate is used for activation of AACs, sodium sulphate-activated binders are known to have delays in initial reaction, longer setting times, and lower strength development, credited to the near-neutral pH of the activator [67], [88], [89], [112], [113]. However, there is room for further understanding of how the fundamental chemistry governs the reaction and subsequent structural evolution and property development.

As such, this chapter explores the viability of sodium sulphate for the activation of slag, maintaining the formulation parameters outlined for previous samples for the sake of comparison. The initial reaction mechanisms and kinetics are investigated, as well as the

subsequent microstructure at different curing ages. The knowledge gained through this analysis will ultimately facilitate the optimisation of alkali-activated binders to reduce cement-associated emissions.

7.2 Methodology

Sample pastes used throughout this chapter were made from the mixture of blast furnace slag with either sodium sulphate solution or a 50:50 wt.% blend of sodium silicate and sodium sulphate in solution, and these samples were compared to the solely sodium silicate-activated sample detailed in *Chapter 4*. The formulations used herein *Chapter 7* are described in **Table 7-1**.

Table 7-1 *Sample formulations used in Chapter 7.*

No.	Sample Name	Activator	BFS (g)	Activator Na_2O (g)	Additive	Additive mass (g)
1	**BFS_8%_SiO_3**	Na_2SiO_3	100	8	--	--
4	**BFS_8%_SO_4**	Na_2SO_4	100	8	--	--
5	**BFS_8%_SiO_3_SO_4**	Na_2SiO_3 + Na_2SO_4 (50:50 wt.%)	100	8	--	--

Time-resolved data from isothermal conduction calorimetry and IR spectra measured *in situ* during the initial hours of reaction aid in the understanding of the early reaction rate and mechanism. While the microstructure and phase assemblage was probed using ATR-FTIR spectra, thermogravimetric analysis, X-ray patterns, and SEM-EDX analysis at various curing ages.

7.3 Results and Discussion

7.3.1 Reaction Mechanisms and Kinetics

7.3.1.1 ICC

As with the hydration reaction of Portland cement, the heat evolution of these slag binders (see **Figure 7-1**) follows distinct stages of reaction consistent with previous studies on alkali-activated slag systems [62], [100], [102], [106], including where sodium sulphate is used as the activator [88], [243]. A pre-induction period, where wetting and dissolution of anhydrous slag occurs, is observed followed by a dormant period where a very low rate of heat is released, which could last a few hours or days, depending on the type of activator used. This is then followed by periods of high-intensity acceleration and deceleration periods, which correspond to the formation of reaction products [62], [100].

The solely sodium sulphate-activated slag sample has a significantly longer induction period than that for the silicate- and mixed silicate-sulphate-activated samples, which both have minimal dormant periods. There is ~75 hours between initial mixing and the onset of the acceleration period of the sulphate-activated slag, which is nearly 70 hours later than the onset of such period for the silicate-activated sample, consistent with the slower reaction and setting times associated with sulphate-activated slag cements [243], [244]. The mixed silicate-sulphate-activated sample reacts significantly quicker than the sulphate-activated sample at a comparable rate to the solely silicate-activated sample, indicating that the inclusion of sodium silicate, even at a 50:50 wt.% replacement, massively influences and thus severely improves the rate of reaction for sulphate-activated slag. Moreover, the sulphate-activated slag sample not only takes a long time to begin its acceleration stage, but this stage itself takes ~30 hours to reach its peak and more than 50 hours to reach completion, unlike the samples containing

sodium silicate, whose acceleration periods are completed in less than 20 hours from their onset.

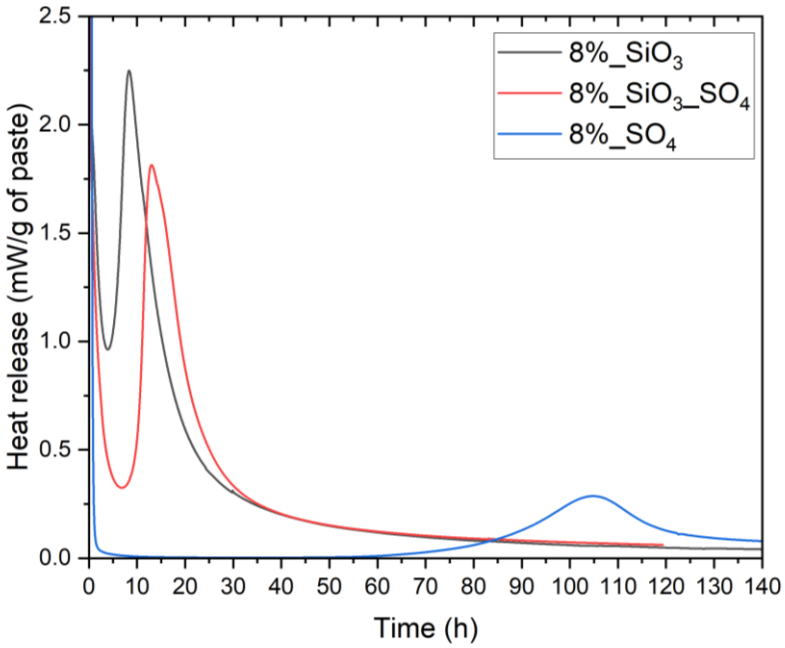

Figure 7-1 *Heat release rate of alkali silicate- and sulphate-activated slag binders, as labelled.*

Additionally, the heat output from the main reaction for the sulphate-activated sample is notably lower at ~0.3 mW/g at its peak than that for the silicate- and mixed silicate-sulphate-activated samples, measuring ~2.3 and ~1.8 mW/g at their peaks, respectively. Moreover, the cumulative heat release, shown in **Figure 7-2**, is about half of that for the blended silicate/sulphate-activated sample and even less compared to the silicate-activated binder. The significantly lower heat release suggests that although some reaction products are forming, it is unlikely to be substantial quantities required for subsequent desirable properties. This massive delay in the main reaction occurring is likely due to the near-neutral nature of the sulphate activator preventing the necessary rate of dissolution of slag particles and the subsequent environmental conditions for the precipitation and formation of key reaction products. Conversely, the mixed activator sample clearly favours both the reaction rate and

mechanism of the solely silicate-activated binder, suggesting that combining activators allows a compromise between rate of reaction, performance, and carbon footprint of the material.

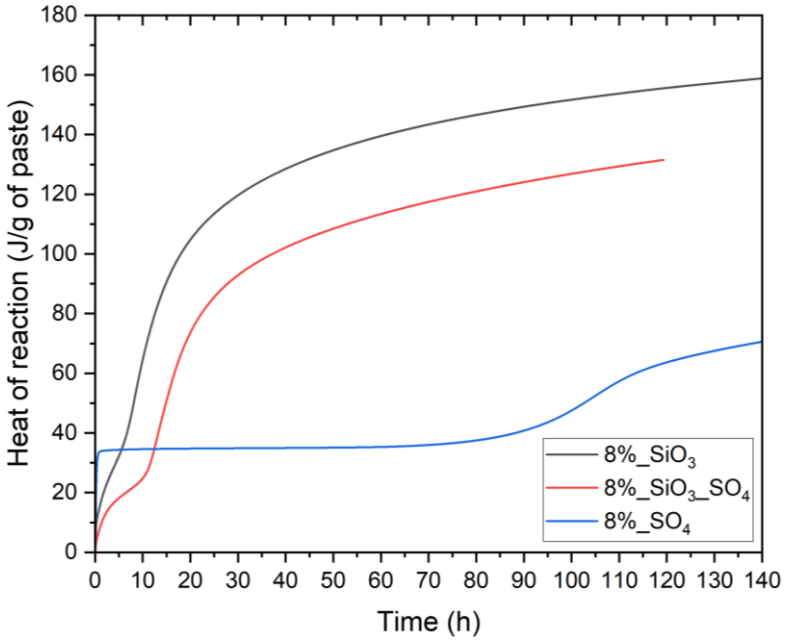

Figure 7-2 *Heat of reaction for BFS activated with sodium silicate and sulphate, as labelled.*

7.3.1.2 DRIFTS

To aid in the understanding of the early reaction rate and mechanisms, diffuse reflectance infrared Fourier transform spectroscopy (DRIFTS) was carried out specifically to observe changes in bond environments *in situ* of the sodium sulphate-activated slag binders during the initial hours of reaction. As such, IR spectra were measured every 2 minutes after mixing for the first 2 hours.

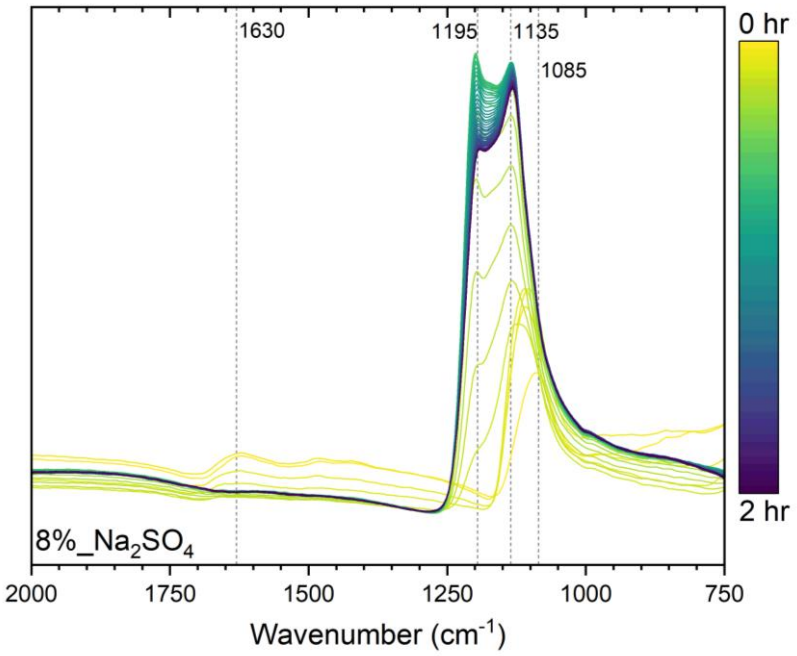

Figure 7-3 *DRIFTS spectra of sulphate-activated BFS over the first 2 hours of reaction.*

In **Figure 7-3**, peaks are observed at ~1630 and ~1085 cm^{-1} immediately after mixing, attributed to the bending of O-H bonds in water [135], [183] and the asymmetric stretching of S-O bonds within sulphate ions [143], [144], respectively, indicative of the presence of the sodium sulphate activating solution, highlighted earlier in **Figure 3-4**. Quite quickly after mixing, the peak at 1630 cm^{-1} reduces completely, while the peak at ~1085 cm^{-1} shifts leftward, and then two clear peaks at 1135 and 1195 cm^{-1} form within an hour and grow significantly by 2 hours. These peaks are both attributed to the asymmetric stretching of S-O within SO_4-containing species [245]–[247]. This likely suggests the presence of a calcium sulphate phase, possibly gypsum [248], whose asymmetric stretching of sulphate tetrahedron typically appears as a doublet around approximately 1120 and 1145 cm^{-1}, where the higher-wavenumber component can sometimes appear at ~1190 cm^{-1} due to the split nature of this mode [249], the AFt-type ettringite [250], [251], or the AFm-type calcium aluminate monosulphate [251], [252]. As the formation of monosulphates is a result of ettringite reacting with calcium ions,

and ettringite formation requires a high pH [253], it is more likely that the band in this region of the IR spectra is a result of gypsum formation from high sulphate levels.

It is noted that there is no presence of Si-O-T bonds (where T represents tetrahedral Si or Al) observed for the solely sulphate-activated slag sample, indicating a lack of aluminosilicate reaction products, i.e. C-A-S-H, aligning with the absence of heat release in the initial hours of reaction for the sample in the calorimetry data.

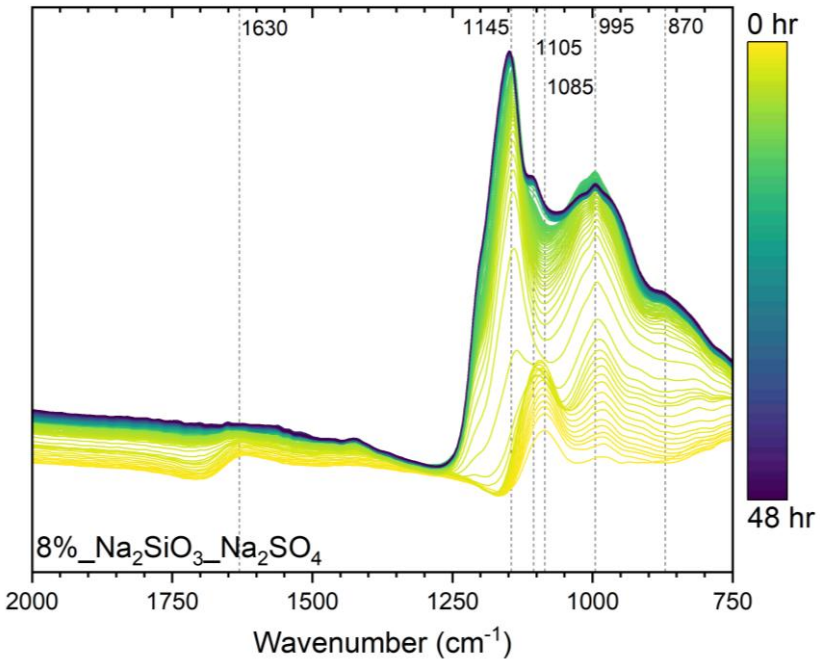

Figure 7-4 *DRIFTS spectra of BFS activated with both sodium silicate and sulphate over the first 2 hours of reaction.*

Similarly, DRIFTS was undertaken *in situ* for the sample activated with a combination of sodium silicate and sodium sulphate over the initial 2 hours after mixing, illustrated in **Figure 7-4**.

Due to the dual components of the activating solution – both silicate and sulphate in solution – there are initial peaks at ~1630, ~1085, and ~985 cm^{-1}, associated with the bending of O-H bonds in water [135], [183], the asymmetric stretching of S-O bonds within sulphate ions [143],

[144], and the Si-O stretching vibrations of silicate [53], [133], [140], respectively. As with the solely sulphate-activated sample, the peak at ~1630 cm^{-1} reduces entirely within 30 minutes, while the sulphate peak at ~1085 cm^{-1} shifts upward in wavenumber and grows in intensity into a peak at 1145 cm^{-1} with a shoulder at ~1105 cm^{-1}, suggesting the formation of calcium sulphate species, gypsum [247], [248], [254] and/or ettringite [250], [251], [255].

Simultaneously, the peak at ~985 cm^{-1} shifts slightly to a higher wavenumber and increases in intensity, centring at ~995 cm^{-1} as a clearly defined peak assigned to a more crystalline Si-O-Si bond, likely within C-A-S-H species[53], [133]. Additionally, a rounded shoulder forms to the right of the aforementioned peak at ~870 cm^{-1}, which is assigned to the asymmetric bending of C-O within calcium carbonate [135], [136], [141], [183], likely due to some atmospheric carbonation as a result of the open setup of the DRIFTS apparatus, as there are no carbonate ions provided in the sample formulation..

7.3.1.3 Summary

The calorimetry data coupled with the time-resolved IR spectra detail the early reaction kinetics and mechanisms of slag binders activated with the near-neutral sodium sulphate solution. It is evident that solely using sodium sulphate as an activator for BFS initiates a long delay of more than a couple of days before the main reaction occurs, and even when such reaction occurs, its extent is limited as a result of the low pH of the system preventing sufficient dissolution of slag particles and subsequent precipitation of reaction products. Instead, intermediary gypsum phases are formed as the calcium and alumina ions from the slag reacts with the activator's sulphate anions. Conversely, using a blended activator of both sodium sulphate and the more commonly used sodium silicate at 50:50 wt.% greatly improves the rate and extent of reaction for the sulphate-activated system, with the blended activator system favouring the high pH supplied by the sodium silicate and facilitating the main reaction within a day.

7.3.2 Structural Evolution

7.3.2.1 ATR-FTIR

ATR-FTIR spectroscopy was conducted at various curing times for the sulphate- and mixed silicate-sulphate-activated slag samples to identify bond environments present and their evolution with time. For the sulphate-activated sample in **Figure 7-5**, the spectra at 3 and 7 days are almost identical, indicative of a time period pre-existing the main reaction stage, while the spectra from 14 through to 90 days vary from the early age samples but have similar features, suggesting a more established structure following the main reaction. On the other hand, the spectra for the blended silicate-sulphate-activated slag sample in **Figure 7-6** shows very little variation over time, indicative of a great extent of reaction achieved in the first few days of curing.

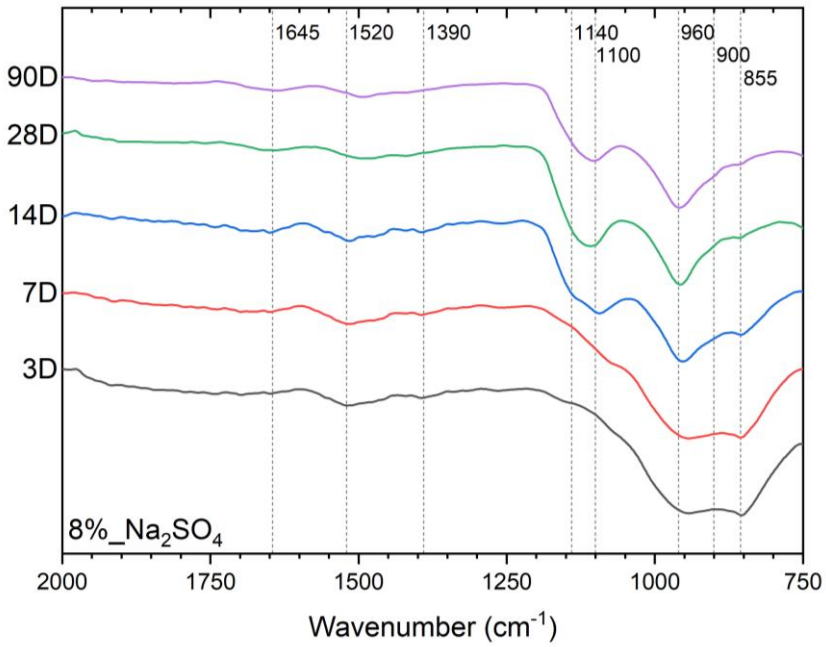

Figure 7-5 *FTIR spectra of sodium sulphate-activated BFS at various time points.*

Most bands identified appear in both sample sets, but with some minor variation in wavenumber and variations in intensity. The presence of a shallow peak at ~1640/1645 cm^{-1} is

attributed to the bending of O-H bonds in water [135], [183], likely from weakly bound water molecules trapped on the surface of the material. Additionally, peaks in the region of ~1390 to ~1520 cm^{-1} that appear in both sample sets, but possibly more prominent in the sulphate-activated slag sample, are characteristic of C-O within carbonates, likely calcium carbonate polymorphs including vaterite and aragonite [141], [142], [184], present due to atmospheric carbonation during curing. Similarly, a peak at ~850 cm^{-1} is observed for both samples, appearing very shallow in the blended activator sample and quite prominent in the sulphate-activated sample, particularly in the earlier ages, which is attributed to the asymmetric bending of C-O in calcium carbonate [135], [136], [141], [183]. Again, the presence of these calcium carbonates is likely due to atmospheric carbonation, and the higher intensity observed for the early age sulphate-activated sample is probably due to the existence of the material in the fresh state facilitating increased infiltration of atmospheric carbon dioxide into the sample. Another signal corresponding to the out-of-plane bending of C-O in calcite at 900 cm^{-1} [135], [136], [185] signifies the existence of calcium carbonate polymorphs as the effect of atmospheric carbonation increases with curing time.

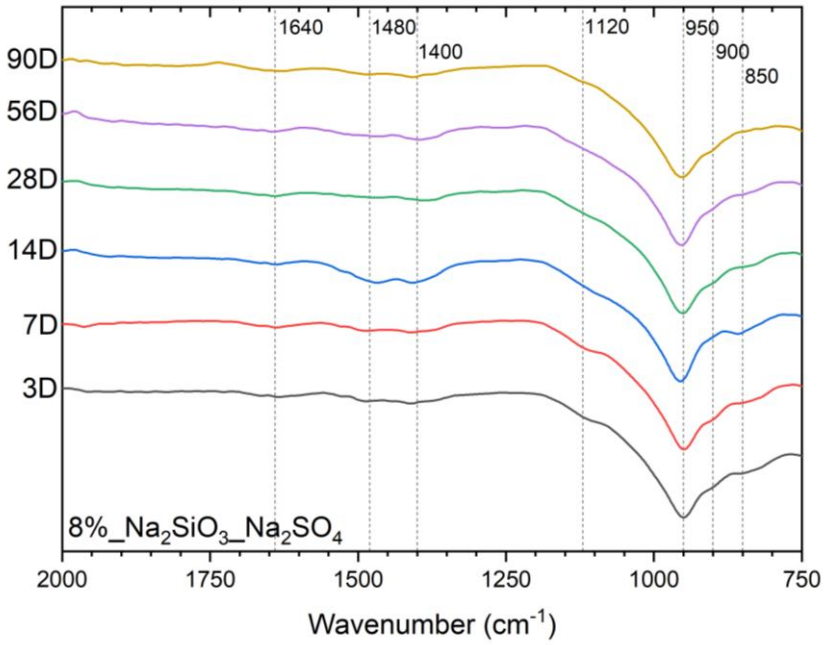

Figure 7-6 *FTIR spectra of BFS activated with both sodium silicate and sulphate, at various time points.*

The most prominent band in all spectra for both samples is observed at ~950 cm^{-1} and is attributed to the asymmetric stretching of Si-O-T bonds either within the unreacted aluminosilicate precursor or within the C-A-S-H structure [53], [133], [134]. This peak in the spectra at 3 and 7 days for the sulphate-activated slag sample is less pronounced than at later curing ages or than all curing ages for the sample activated with the blended silicate/sulphate solution, indicating the lack of reaction within the first week for the solely sulphate-activated sample. The general sharpening of the peak at ~950 cm^{-1} over time aligns with increasing structural ordering of C-(A)-S-H as the reaction continues [53], [183]. Similarly, there is a shallow band at 1120 cm^{-1} for the mixed silicate-sulphate-activated sample at all curing ages, attributed to the asymmetric stretching of S-O within SO_4-containing phases [245]–[247], likely the AFt-type phase, ettringite [250], [251] or a monosulphate [251]. A SO_4-containing phase also appears in the solely sulphate-activated slag with peaks existing at 1100 and 1140 cm^{-1}, which increase in intensity beyond 7 days of curing. The early doublet nature of these phases indicates the possible existence of the weakly bound hydrated calcium sulphate,

gypsum [248], [249], which then forms either just the AFt phase, ettringite, or ettringite and then its subsequent transformation into the AFm phase, calcium aluminate monosulphate, as the extent of reaction increases with time.

7.3.2.2 TGA

Thermogravimetric analysis was used to further probe the material structure and phase evolution as curing progresses by identifying and quantifying reaction products present in both the sulphate- and silicate-sulphate-activated samples at various time points. A general increase in the overall mass loss as curing time increases is observed for both sample sets, suggesting the expected increased extent of reaction with time: 11.5, 12.1, 17.8, 25.2, and 25.9 wt.% at 3, 7, 14, 28, and 90 days, respectively, for the sulphate-activated sample (**Figure 7-7**); and 25.6, 25.7, 28.7, 28.1, and 31.8 wt.% at the same time points respectively, for the silicate-sulphate-activated sample (**Figure 7-8**).

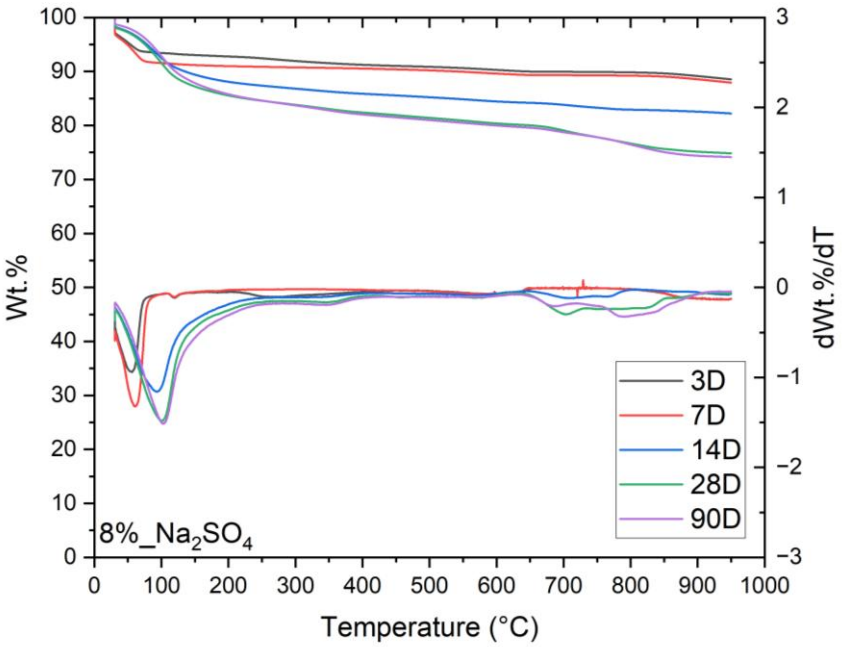

Figure 7-7 *TG/dTG trends of sodium sulphate-activated BFS, cured for various lengths of time, as labelled.*

A mass loss in the region between 60 and 200 °C is associated with the loss of water from the sample, typically free water from the calcium aluminosilicate hydrate (C-A-S-H) [186], [187]. For the sample activated with the blended silicate/sulphate activator, this mass loss centres just above 100 °C at all curing ages and increases slightly in magnitude as time progresses (from ~15 wt.% at 3 days to ~22 wt.% at 90 days), indicating an established C-A-S-H phase from early age which increases in quantity over time as the reaction proceeds with curing. On the contrary, for the sulphate-activated sample, the mass loss in this region is centred at ~70 °C up to and including 7 days of curing, before shifting to ~100 °C for the later curing ages, indicating the presence of free water, very loosely bound in the structure at early age, aligning with the lack of setting observed at this point for the binder. Where a mass loss centring at ~100 °C exists in both sample sets, a shoulder to this can be observed at ~170 °C, increasing in prominence as curing time progresses, which is attributed to the initial thermal dehydration of hydrotalcite [188], [189] and/or ettringite [256].

Further mass loss is observed between 300 and 500 °C for both sample sets, associated with additional loss of chemically bound water in hydrotalcite phases [186], [188], [190]. For the sulphate-activated sample, this mass loss appears as a small continuous loss at later curing ages, indicating the later formation of small amounts of hydrotalcite, while the silicate-sulphate-activated sample shows an equal minor loss for all curing ages at ~350 °C and a second more prominent mass loss at ~450 °C that increases in magnitude with curing age, indicating the existence of hydrotalcite phases at early age, which increase in quantity and bond strength as the reaction progresses.

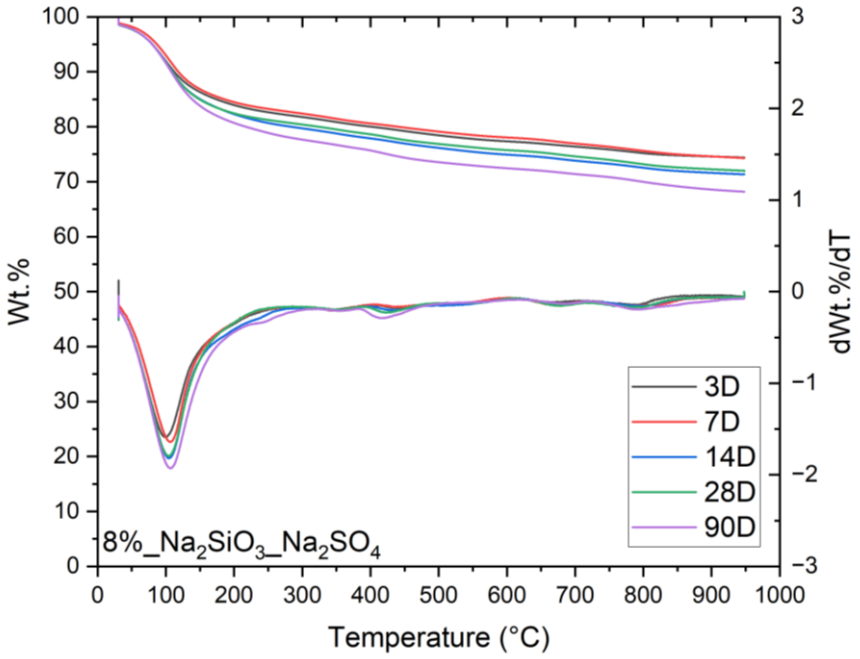

Figure 7-8 *TG/dTG trends of BFS activated with both sodium silicate and sulphate, cured for various lengths of time, as labelled.*

A final region of mass loss is observed in the region of 600-900 °C for both sample sets, but significantly more so for the sulphate-activated sample. This region likely encompasses two overlapping regions: a loss in the region of 600 to 800 °C is due to the decomposition of sulphate phases in calcium sulphoaluminate hydrates, like ettringite [257] or monosulphates [251], while in the region of 700-900 °C the decomposition of calcium hydrates [186] and decarbonation of calcium carbonates occurs [188], [192], [193]. For the mixed activator sample, it is likely that both ettringite and calcium carbonate phases are present in small amounts, while these phases exist in higher quantities for the sulphate-activated sample, the former as a result of the increased sulphate content and the latter due to the late hardening of the sample allowing CO_2 to penetrate into the sample and form calcium carbonates [95], [258], [259]. Both of these observations corroborate the observations from the IR spectra in *Section 7.3.2.1*.

7.3.2.3 XRD

Diffractograms were taken for the sulphate- and silicate-sulphate-activated slag samples at different curing times, illustrated in **Figure 7-9** and **Figure 7-10**, respectively. For the mixed activator sample, there is very little change in structure over time in XRD patterns, similar to the ATR-FTIR spectra and TGA curves, suggesting a stable and structurally ordered phase development from early age. In comparison, the sulphate-activated structure shows more noticeable changes in structure over time and contains more crystalline structures than the silicate-containing sample, in line with TGA and FTIR data.

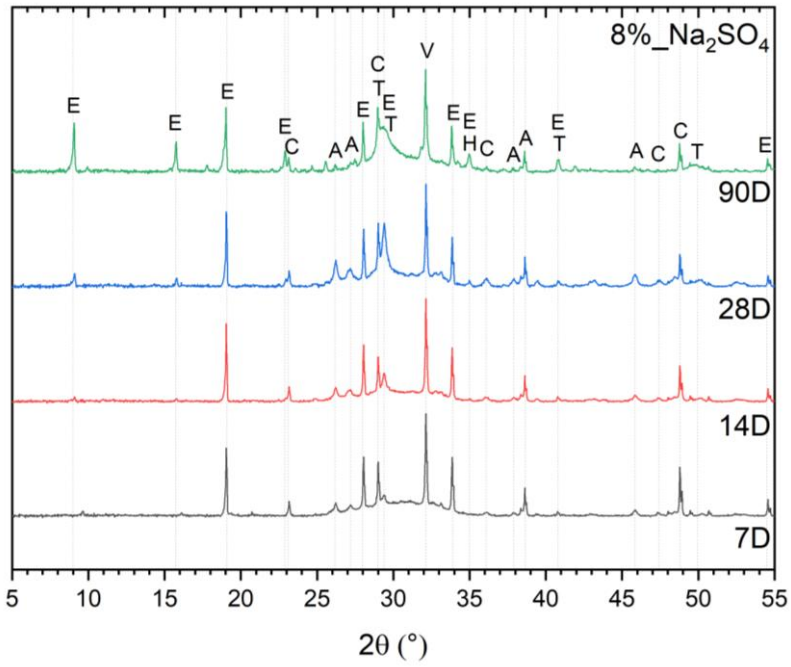

Figure 7-9 *XRD patterns of sulphate-activated BFS, at various curing times, as labelled. Phases identified have been labelled: A – Aragonite (PDF 04-008-5421), C – Calcite (PDF 00-066-0867), E –Ettringite (PDF 00-013-0350), H – Hydrotalcite (PDF 01-088-9171), T – Tobermorite (PDF 04-014-8455, and V – Vaterite (PDF 00-060-0483).*

A broad amorphous hump centred at ~30° 2Θ can be observed in all samples, characteristic of alumina-silica phases, most likely a C-A-S-H phase with a similar structure to tobermorite, which supports the observations from FTIR and TGA data. Moreover, where the mixed silicate-sulphate-activated sample is primarily amorphous in nature featuring very little crystalline

phases, the sulphate-activated slag exhibits moderate amounts of crystalline features. The existence of crystalline phases, specifically ettringite, for the sulphate-activated sample aligns with literature studies also using sodium sulphate as the activator [88], [115], [243], while the mixed activator sample apparently favours the nature of silicate-activated slag binders [101], [188], [216]. Additionally, tobermorite and hydrotalcite peaks can be observed in the diffractograms for both sample sets at various time points, as well as some amounts of calcium carbonate polymorphs – aragonite, calcite, and vaterite – aligning with the findings from FTIR and TGA.

The diffraction patterns for the sulphate-activated slag binder in **Figure 7-9** shows the aforementioned primary amorphous mound associated with C-A-S-H existing slightly from 7 days and the peak at ~29° 2Θ growing sharper over time before settling as a broad peak at 90 days, indicating its increase in quantity as well as stability with curing age. Additionally, the most featured phase in this sample set appears to be ettringite, some of which forms by 7 days and some forming as the reaction continues at later curing ages. The existence and/or growth of this phase is due to the sulphate content supplied by the activator reacting with the calcium and aluminium from the anhydrous slag, while the near-neutral pH impedes sufficient dissolution of slag, particularly the release of silicate tetrahedra, for subsequent formation of C-A-S-H. Furthermore, notable calcium carbonate phases are present in the sulphate-activated sample at all curing ages with some increase with curing time. The early existence of these phases is likely due to CO_2 infiltrating the pores of the sample in its fresh state, where it exists for ~7 days, and reacting with free calcium ions, while later formation is limited by the hardened state of the sample. There is a distinct lack of hydrotalcite in this sample set, likely due to a preferential formation of both ettringite and calcium carbonates, preventing the sufficient inclusion of alumina and carbonate ions into a hydrotalcite-type structure, as well as the lower, near-neutral pH limiting its formation.

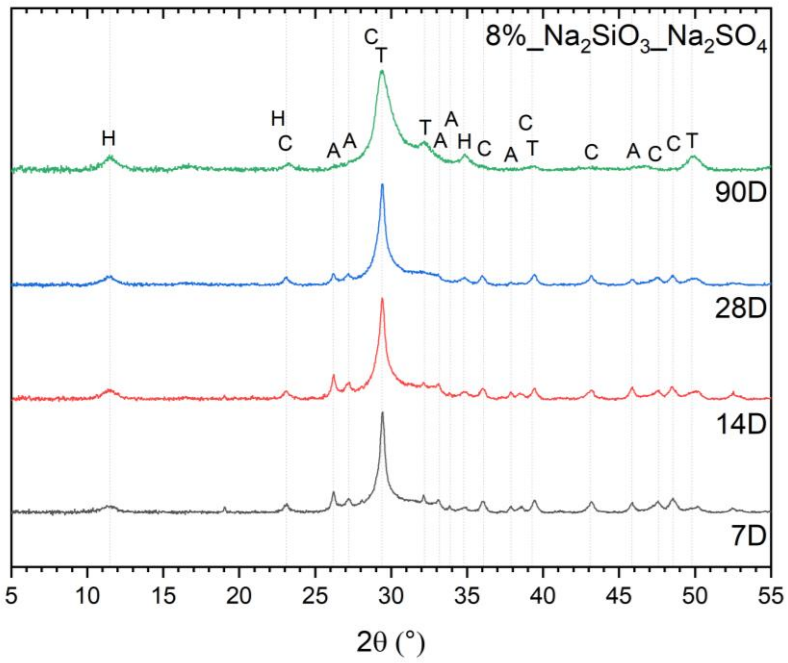

Figure 7-10 *XRD patterns of silicate/sulphate-activated BFS, at various curing times, as labelled. Phases identified have been labelled: A – Aragonite (PDF 04-008-5421), C – Calcite (PDF 00-066-0867), H – Hydrotalcite (PDF 01-088-9171), and T – Tobermorite (PDF 04-014-8455).*

On the other hand, the diffractograms for the blended silicate-sulphate-activated slag sample, as seen in **Figure 7-10**, are almost identical for all curing ages, with the presence of the tobermorite-like C-A-S-H and hydrotalcite phases noted for all ages but increasing with time, indicative of an increased extent of reaction. Additionally, small amounts of aragonite and calcite exist in this sample set, again suggesting atmospheric carbonation occurring during sample preparation and curing. It is noted that the diffractograms for the silicate-sulphate-activated sample are very similar to the solely silicate-activated slag sample (**Figure 4-6**), further suggesting that the inclusion of sodium silicate alongside sodium sulphate heavily influences the reaction and structure of the mixed activator sample, with the main difference being the level of atmospheric carbonation occurring where sulphate is used in the activator.

7.3.2.4 SEM-EDX

Scanning electron microscopy is used to understand the surface structure of cements, and coupled with energy dispersive x-ray analysis, its elemental composition can be determined, which allows the study of the structural evolution here at different curing times. As expected for alkali-activated slag binders, both the sulphate- and silicate-sulphate-activated samples in **Figure 7-11** and **Figure 7-12** respectively, show light grey remnant slag particles surrounded by a darker grey bulk structure, containing reaction phases such as C-A-S-H, hydrotalcite, ettringite, and calcium carbonates. Additional features like cracks or striations may be observed as a result of fracture samples being used instead of cut samples in this study, as well as some visible pores at this magnification, however, it is noted that most pores in cementitious binders exist on the nanoscale and therefore will not be observed in these images.

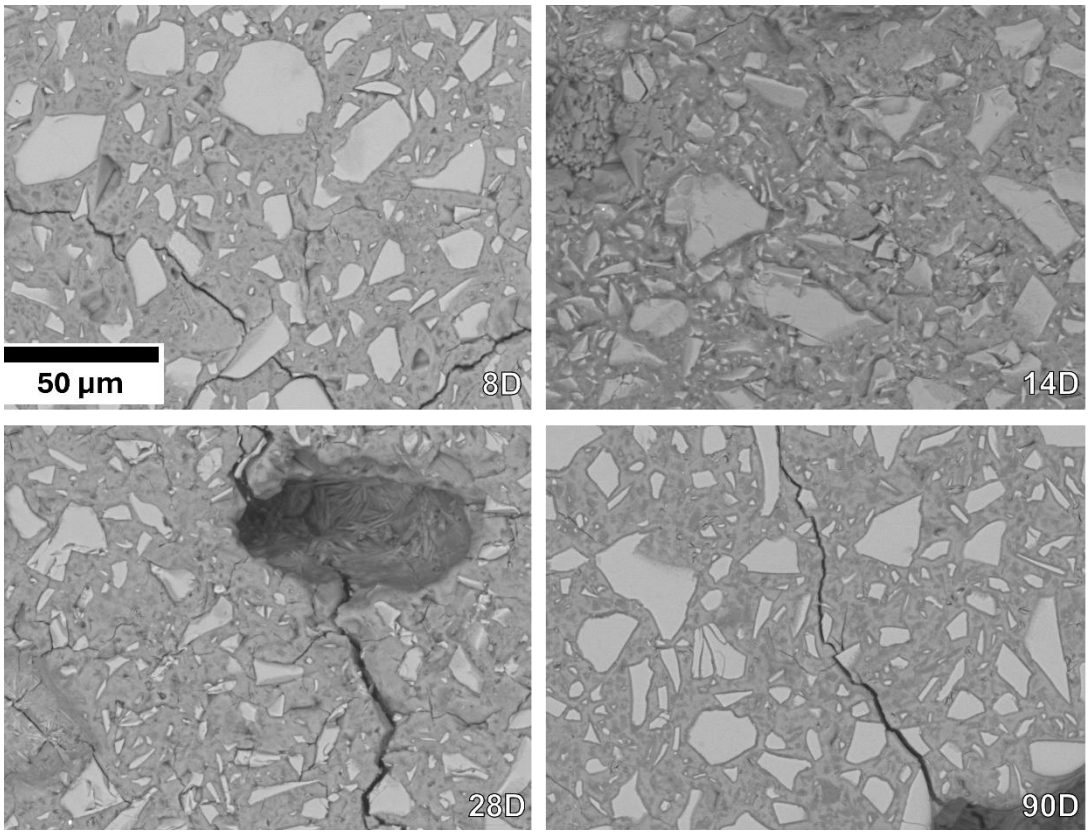

Figure 7-11 *SEM images for sulphate-activated BFS, at 1000x magnification, for various curing times, as labelled.*

Compared to all previous sample sets, the SEM images for the sulphate-activated samples (**Figure 7-11**) contain significantly more unreacted slag particles and the change in structure over time appears to occur at a slower rate, aligning with the moderate pH of the activator incurring a slow rate and extent of reaction. Additionally, the bulk structure is far less smooth-looking, i.e. cohesive, containing different distinct phases represented by the various shades of grey observed surrounding the slag particles. The different phases here may be ettringite or calcium carbonate polymorphs as a result of carbonation, which have been observed in previous data. Moreover, significant amounts of pores were observed, particularly at lower magnifications, for all curing ages, similar to the one observed at 28 days in the above figure. This increased porosity is likely allowing easier infiltration of carbon dioxide into the sample and promoting the formation of the observed calcium carbonate polymorphs, as well as likely negatively influencing the compressive strength of the samples, as it is known that porosity and compressive strength have an inverse relationship [223].

In comparison, the mixed silicate-sulphate-activated sample, in **Figure 7-12**, contains significantly less remnant slag particles and a much more cohesive bulk structure from early curing age, indicating the positive influence that the inclusion of sodium silicate has on the reaction extent and general structure over time. Furthermore, it is noted that like the sulphate-activated sample, the blended silicate-sulphate-activated sample also contains areas of dark grey within the bulk structure, which may possibly be free sulphate or sulphate-containing phases, like ettringite.

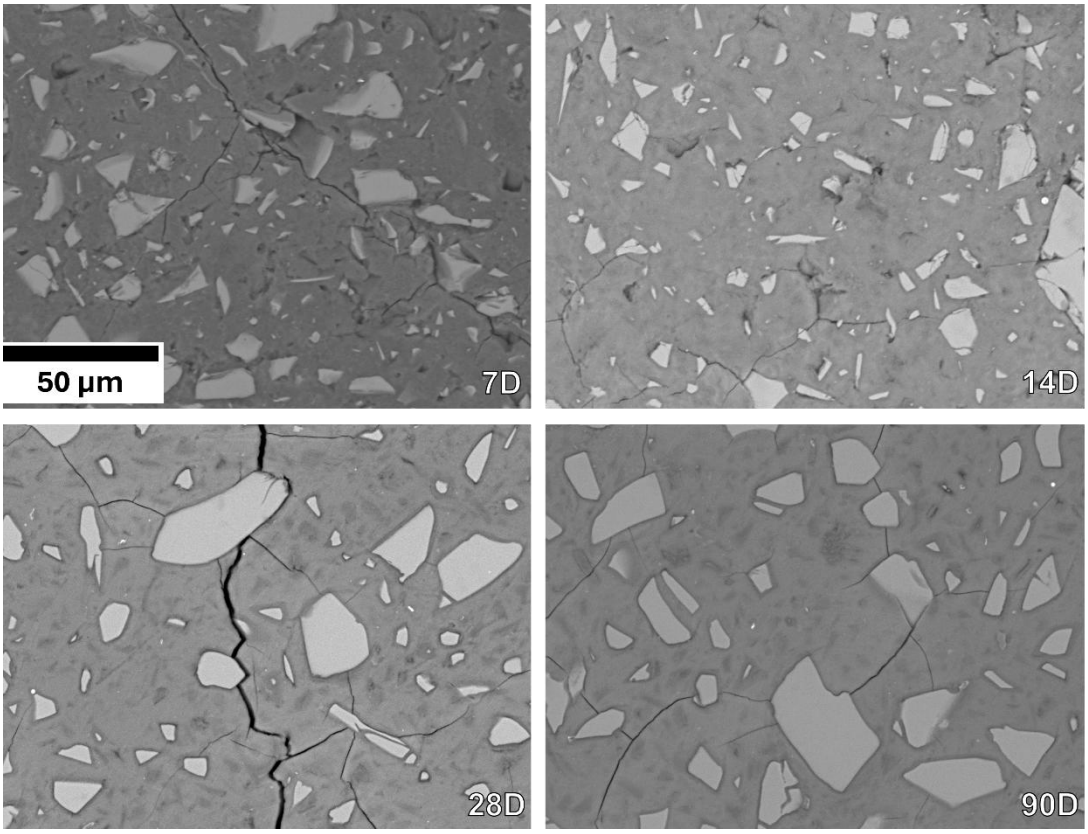

Figure 7-12 *SEM images for silicate/sulphate-activated BFS, at 1000x magnification, for various curing times, as labelled.*

EDX scans provide elemental maps of samples to aid in understanding the chemical composition of the samples at different time points. For the sulphate-activated sample (**Figure 7-13**) at 8 days, there is some distinction between the slag particles, which primarily consist of silicon and aluminium, and the surrounding bulk structure, and by 90 days, this structure remains similar, with distinct slag particles rich in silicon, aluminium, and calcium, surrounded by a sodium-rich bulk structure with some magnesium, calcium, carbon, and sulphate integrated. There is a more distinct change over time for the mixed silicate-sulphate-activated sample (**Figure 7-14**), where the bulk structure appears to contain more elements distributed evenly around some unreacted slag particles. Rather than being sodium-rich like the sulphate-activated sample, the bulk structure appears to contain similar amounts of sodium and magnesium, with some areas of carbon as well as sulphur, indicative of the lack of integration of the latter into the reaction phases. Moreover, there appears to be more calcium in the phase

structure for the sulphate-activated sample, aligning with previous observations of calcium sulphates in the FTIR, TGA, and XRD data, akin to ettringite or monosulphates.

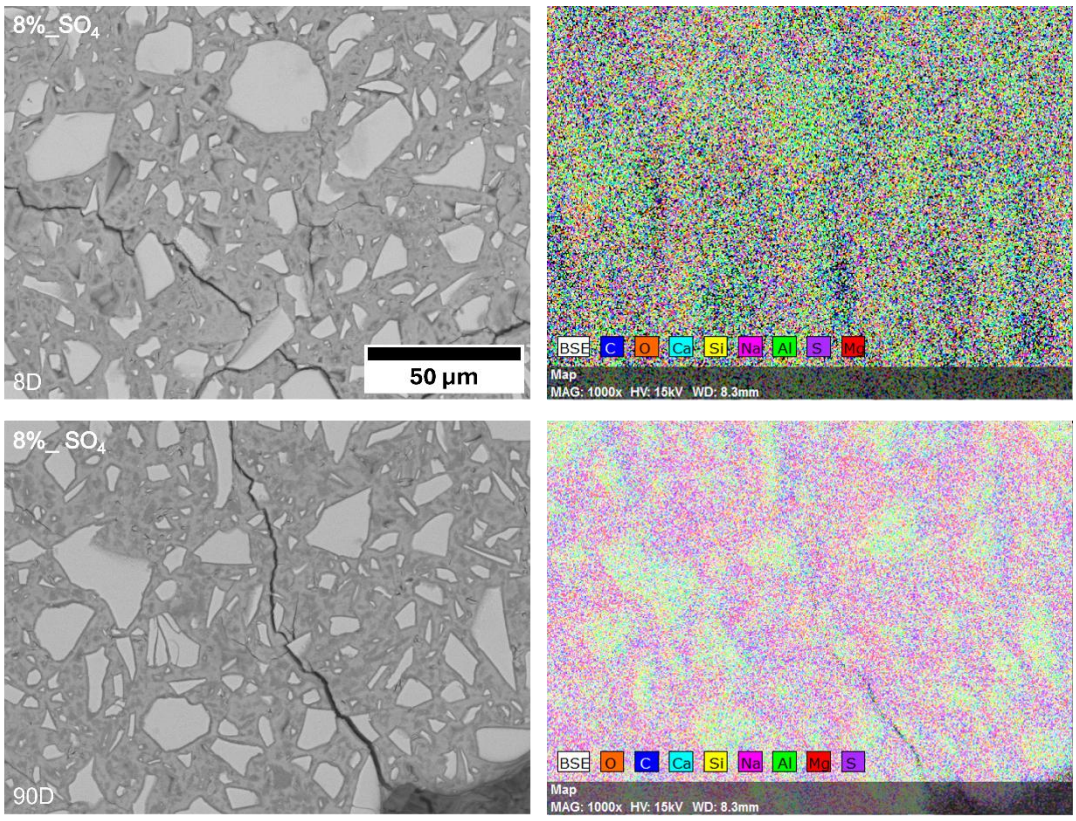

Figure 7-13 *Elemental mapping for sulphate-activated BFS, cured at 8 and 90 days, as labelled.*

The elemental composition data from EDX scans were used to develop ternary systems for the sulphate- and silicate-sulphate-activated samples, as shown in **Figure 7-15** and **Figure 7-16** respectively. The ternary CaO-Al_2O_3-SiO_2 system for both samples stays relatively consistent as curing time increases, and its structure aligns with previous studies of alkali-activated slag cements [53], [211], [212] and synthetic C-(A)-S-H and N-A-S-H gels [213]. The area occupied on the ternary diagram is associated with the composition of the C-(N)-A-S-H gel [53], [161], [214], as expected for alkali-activated slags. Additionally, the Al/Si ratio also remains consistent over time, suggesting a stable C-A-S-H structure with little change in crosslinking and chain length.

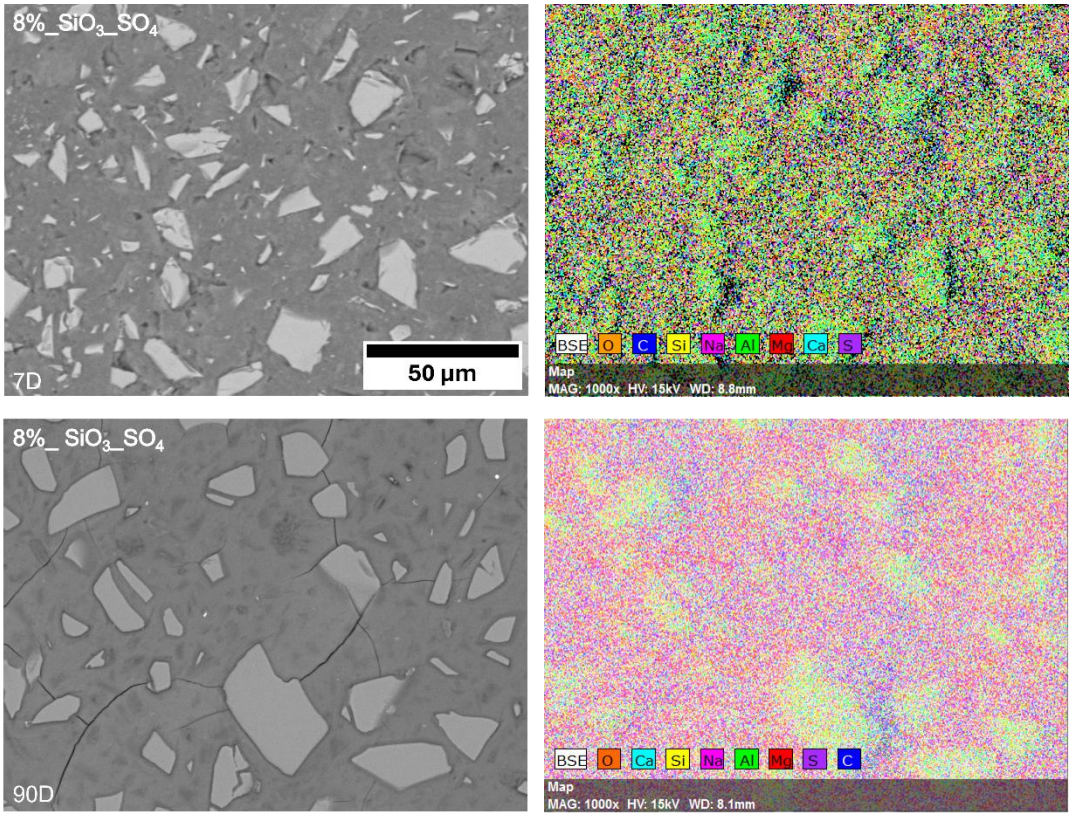

Figure 7-14 *Elemental mapping for silicate/sulphate-activated BFS, cured at 7 and 90 days, as labelled.*

Conversely, the ternary Na_2O-Al_2O_3-SiO_2 systems for the different sample sets differ; for the sulphate-activated sample, the structure remains in the same region over time, while for the mixed activator sample, there is a distinct decrease in sodium content over time.

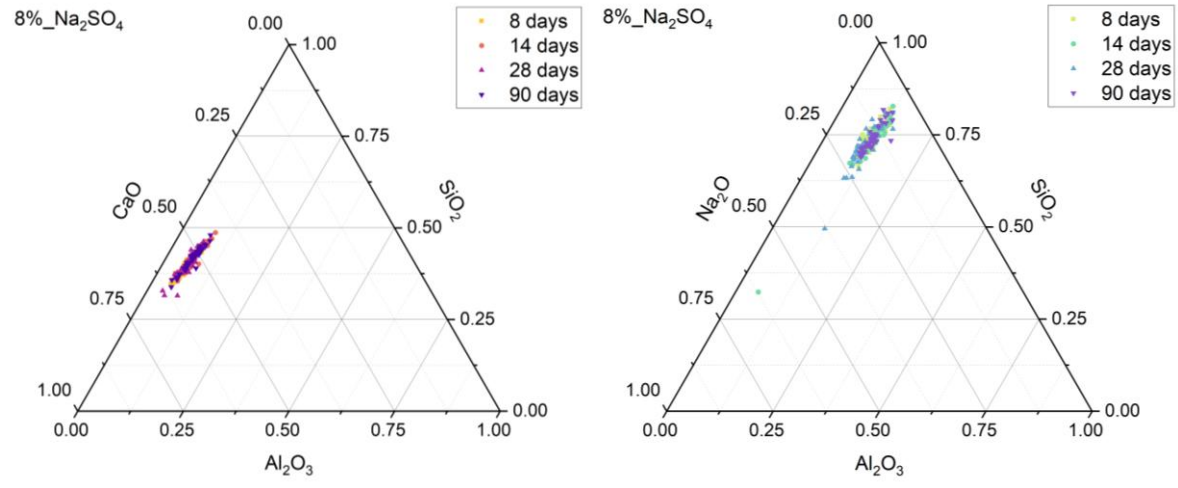

Figure 7-15 *Ternary systems of sulphate-activated slag cured for 7, 14, 28, and 90 days, as determined by SEM-EDX analysis. (L) Ternary $CaO – Al_2O_3 – SiO_2$ system (neglecting Na_2O content), and (R) Ternary $Na_2O – Al_2O_3 – SiO_2$ system (neglecting CaO) content, showing elemental composition.*

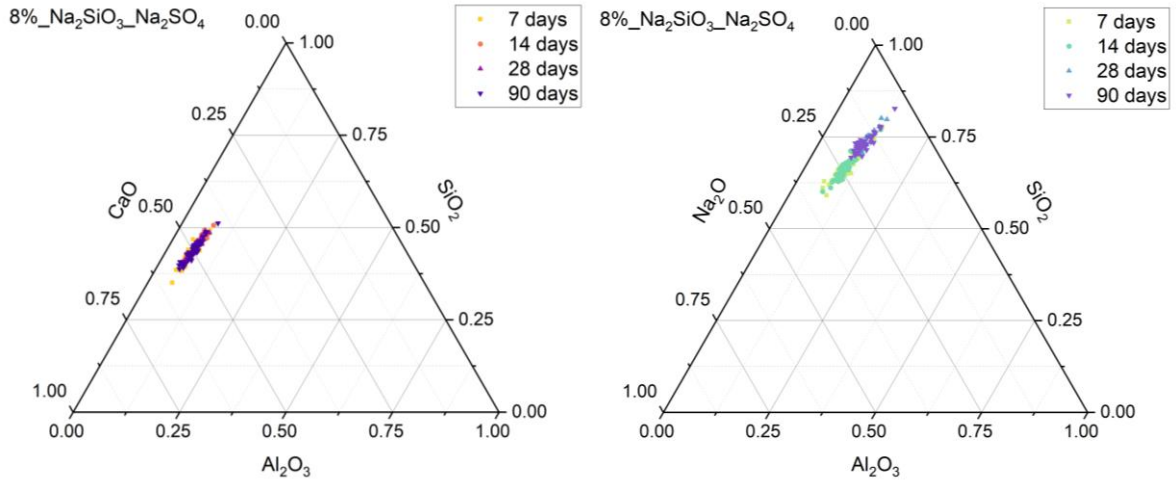

Figure 7-16 *Ternary systems of silicate/sulphate-activated slag cured for 7, 14, 28, and 90 days, as determined by SEM-EDX analysis. (L) Ternary CaO – Al_2O_3 – SiO_2 system (neglecting Na_2O content), and (R) Ternary Na_2O – Al_2O_3 – SiO_2 system (neglecting CaO) content, showing elemental composition.*

7.4 Conclusions

This chapter explored the use of sodium sulphate for a low-carbon alternative for the activation of blast furnace slag to form a cementitious binder. Sodium sulphate not only has a lower carbon footprint than the more commonly used alkali silicates and hydroxides, but it is also near-neutral in nature and thus would mitigate some of the challenges with handling highly caustic solutions for the production of AACs. The reaction rate and mechanisms were explored as was the development of structural phases with curing age of the sodium sulphate-activated slag binder, as well as comparing this material's performance to a slag binder utilising a 50:50 wt.% blend of sodium silicate and sodium sulphate as its alkaline activator, and also the control sample, sodium silicate-activated slag, detailed in *Chapter 4*.

Calorimetry data revealed that the sodium sulphate-activated slag reacts much slower than the silicate-activated sample, with the onset of the main reaction peak being nearly 72 hours after mixing, the main reaction itself lasting more than 50 hours, and the heat output being heavily reduced in comparison to all previous samples in this body of work. For comparison, after 100 hours, the cumulative heat release for the sodium sulphate-activated slag sample is ~26 %

and ~40 % of that for the silicate- and carbonate-activated slag samples, respectively, at the same time point. This long dormant period and significantly low heat release reveal that the lack of strong alkalinity supplied by the activator is inhibiting the main reaction from occurring and also hindering its extent, i.e. the lower heat release means lower quantities of and/or less thermodynamically stable phases forming. DRIFTS spectra measured during the initial hours of reaction after mixing show that very little is occurring, other than a slight dissolution and rearrangement of species in the sample, possibly forming calcium sulphate species, like gypsum or ettringite.

Further to this, the structural evolution was probed using TGA, FTIR, XRD, and SEM-EDX, which revealed a lack of reaction at 3 days and minimal reaction by 7 days, where C-A-S-H structures were beginning to form in addition to existing calcium aluminosulphates. However, it is noted that the C-A-S-H does not appear to polymerise over time, meaning that a stable enough structure forms and maintains, but does not further develop, which likely means a limited strength and resistance to attack for this material. Additionally, some quantities of calcium carbonate polymorphs were determined, forming as a result of atmospheric carbonation, likely due to the material's prolonged existence as a paste and its greatly porous nature upon eventual setting allowing easy infiltration of CO_2 into the pore structure. Moreover, due to the poor reaction rate and extent of reaction, the physical properties were not investigated.

In contrast, similar to what was observed for the silicate/carbonate blend, the use of sodium silicate in combination with sodium sulphate at a 50:50 wt.% blend to activate the slag proved very positive, favouring the performance of the solely silicate-activated sample instead of the sulphate-activated one. The increased pH of the mixed activator sample meant that the reaction rate was far more comparable to that of the sodium silicate-activated sample, where the main

reaction occurred and completed within ~24 hours after mixing. Likewise, the reaction products formed are very similar to the silicate-activated sample: C-A-S-H and hydrotalcite form from early age with small amounts of calcium carbonates precipitating due to atmospheric carbonation.

Overall, sodium sulphate can be used as an activator for blast furnace slag, however, the formulation used here is not best suited for a sufficient rate and extent of reaction – an increased dosage or combination with a more alkaline species would likely improve the performance. The use of a 50:50 wt.% blend of sodium silicate and sodium sulphate as the activating solution greatly improved the performance of the slag binder, with a reaction rate and structural phase development quite comparable to the solely silicate-activated slag binder.

Chapter 8: Sodium Sulphate-activated Slag Binders – Incorporation of Additives

8.1 Introduction

Using sodium sulphate for the activation of blast furnace slag for the production of a cementitious binder has the potential to reduce embodied carbon of alkali-activated cements and thus the carbon footprint of the construction industry, as well as mitigating issues with handling caustic solutions like alkali silicates and hydroxides. However, as suggested in literature and confirmed in the previous chapter, sodium sulphate-activated slags induce a very slow reaction where limited heat is released, and give slow setting and hardening times, due to the near-neutral pH of sulphate salts impeding sufficient dissolution of slag for subsequent formation of binding phases.

As with the sodium carbonate-activated slag binder, different strategies were explored to improve the reaction kinetics, structural evolution and physical property development, and the incorporation of small amounts of calcium and magnesium oxide was chosen as a viable approach, which has been performed and assessed for alkali-activated slag binders previously [123]–[127]. Both CaO and MgO possess significant carbon footprints due to their production processes being energy-intensive and/or directly CO_2-emitting via calcination [29], [260]–[262], which may seem counterintuitive when the overarching theme of this project is to minimise cement-associated carbon emissions. However, studies have shown that even small quantities of these chemical compounds can be used to tailor performance properties of cementitious slag binders [123], [125], [126], [239], and therefore, if the replacement of BFS with minor amounts of CaO or MgO within the sulphate-activated slag binder does improve its performance, then there can be a compromise between carbon footprint and material performance to prove the material efficacy for use in industry.

Therefore, this chapter focuses on the replacement of 1 and 3 wt.% of slag with calcium oxide and also magnesium oxide in slag binders utilising sodium sulphate for activation, with the aim of improving the rate of reaction and the subsequent phase development. Once more, the information gained in this chapter can be used to enhance chemical formulation of alkali-activated cements with the intention of driving implementation in industry and reduce the cement sector's CO_2 emissions.

8.2 Methodology

For the samples in this chapter, BFS was mixed with sodium sulphate solution of dosage 8 wt.% of Na_2O with respect to the anhydrous precursor, as well as including calcium and magnesium oxide in 1 and 3 wt.% replacements of BFS, with the aim of improving the rate of reaction. These formulations are detailed in **Table 8-1**.

Table 8-1 *Sample formulations used in Chapter 8.*

No.	Sample Name	Activator	BFS (g)	Activator Na_2O (g)	Additive	Additive mass (g)
4	**BFS_8%_SO_4**	Na_2SO_4	100	8	--	--
10	**BFS_8%_SO_4_1%_CaO**	Na_2SO_4	99	8	CaO	1
11	**BFS_8%_SO_4_3%_CaO**	Na_2SO_4	97	8	CaO	3
12	**BFS_8%_SO_4_1%_MgO**	Na_2SO_4	99	8	MgO	1
13	**BFS_8%_SO_4_3%_MgO**	Na_2SO_4	97	8	MgO	3

The reaction rate and mechanisms were explored using isothermal calorimetry and well as DRIFTS measurements taken *in situ* during the initial hours of reaction. Additionally, at set curing times, the microstructure and phase assemblage was probed using ATR-FTIR spectroscopy, TGA, XRD, and SEM-EDX analysis.

8.3 Results and Discussion

8.3.1 Reaction Mechanisms and Kinetics

8.3.1.1 ICC

The heat evolutions of slag binder samples activated with sodium sulphate and incorporating 1 or 3 wt.% of either calcium or magnesium oxide are depicted in **Figure 8-1** with the corresponding data for the sulphate-activated slag binder included for comparison. As with all the previous slag binder sample sets, the heat evolution of these additive-containing sulphate-activated slag cements follows a similar process as the hydration reaction of Portland cement, where distinct stages of reaction are observed, consistent with previous studies of alkali-activated slag systems [62], [100], [102], [106], including those utilising sodium sulphate as the activator [88], [243]. A pre-induction period occurs first, where the anhydrous slag particles are wetted and initial dissolution occurs, however, as this period occurs during and immediately after mixing, and the mixing was conducted outside of the calorimeter, the heat evolution does not properly display pre-induction. This is then typically followed by a dormant (or induction) period where very low heat is released, before periods of high-intensity acceleration, corresponding to the precipitation and formation of reaction products, and subsequent deceleration, where the reaction reduces [62], [100].

According to **Figure 8-1**, the inclusion of either additive at both 1 and 3 wt.% replacement of BFS improves the rate of reaction of the sulphate-activated slag binder, and the calcium oxide has a greater influence than the magnesium oxide. Interestingly, the inclusion of the 1 wt.% of calcium oxide has a greater effect than 3 wt.%, while for the inclusion of magnesium oxide, the higher replacement performs better than the lower. Based on the peak heat release, the reaction rate increased by ~83 and ~77 hours for 1 and 3 wt.%, respectively, of calcium oxide, and by ~31 and ~52 hours for 1 and 3 wt.%, respectively, of magnesium oxide.

The inclusion of calcium oxide is expected to have a greater impact on the reaction rate compared to magnesium oxide, as, although both should increase the pH of the bulk solution when hydrated, calcium hydroxide typically has a higher pH at ~12.5 compared to magnesium oxide's ~10. This does appear to be the case when comparing the performance of calcium oxide to magnesium oxide, but it is also reasonable to assume that a greater quantity would have more of an influence than a lesser quantity, which is the case for the magnesium oxide. The shape of the heat output curve for the magnesium oxide-containing samples is very similar to the solely sulphate-activated sample, indicating that the MgO only increases the reaction rate and not the mechanism, suggesting that its sole purpose is to increase the pH.

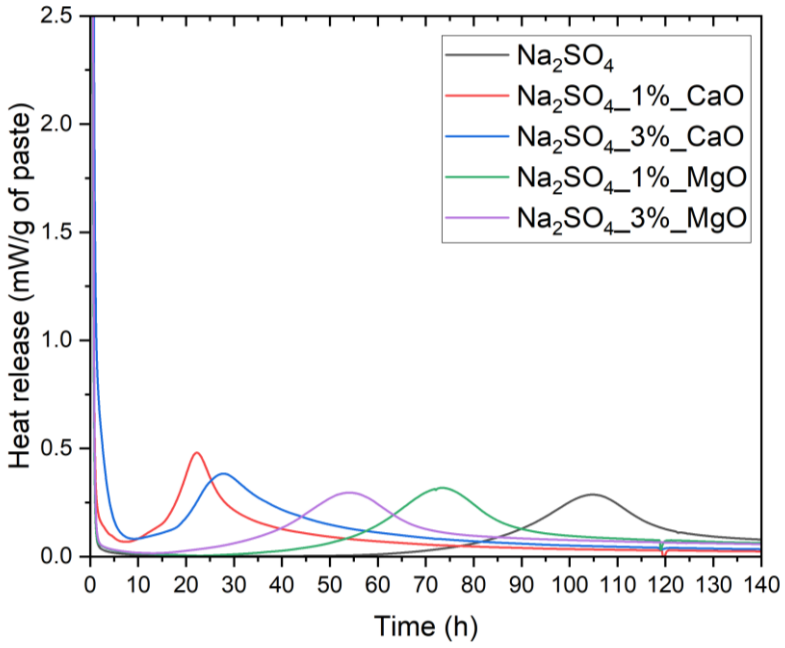

Figure 8-1 *Heat release rate of sulphate-activated BFS with additives, as labelled.*

However, the inclusion of 1 wt.% of CaO performing better than the 3 wt.% is unexpected. Both quantities appear to alter the shape of the heat output curve of the sulphate-activated sample, with a small shoulder noticeable to the left of the primary heat output and a generally left-heavy shape to the curve, compared to the more symmetrical curve shape for the sulphate-

activated sample as well as those containing magnesium oxide. This leftward shoulder suggests an initial reaction preceding, and possibly occurring simultaneously to, the main reaction, where the likes of C-A-S-H structures form. The initial reaction is likely to be between the calcium ions, from both the additive and the slag particles, and the sulphate ions from the activator, forming ettringite, and possibly then transforming into monosulphate as the pH decreases with calcium consumption. It is noted that the onset of this shoulder occurs at almost the same point, however, this initial reaction as well as the subsequent main reaction, depicted by the bell-shaped curve, occur for longer with the 3 wt.% of calcium oxide addition.

As such, it is possible that the lower quantity of calcium oxide means the limit of ettringite formation and its subsequent transformation into its more stable phase, monosulphate, is achieved more quickly as the pH is reduced, which then enables the primary reaction to occur. Whereas the 3 wt.% of calcium oxide leads to the sole formation of ettringite as the increased calcium ions maintain a higher pH for longer, leading to the formation of C-A-S-H simultaneously to ettringite and its subsequent conversion into monosulphate.

Furthermore, the overall heat output over 140 hours, shown in **Figure 8-2**, is very similar for all sulphate-activated samples, except for the one containing 3 wt.% of calcium oxide. In terms of the magnesium oxide-including samples, this supports the previous statement that this additive only improves the reaction rate and does not alter the reaction mechanism, and as such the same extent of reaction is eventually gained whether or not MgO is incorporated into the sulphate-activated slag binder. On the other hand, considering the 1 wt.% inclusion of calcium oxide resulted in a slightly quicker rate of reaction than the 3 wt.% inclusion, the latter has a greater overall heat output, aligning with a greater extent of reaction, i.e. higher quantities of more stable reaction products are forming. This aligns with the main reaction peaking to a

similar level for both calcium oxide quantities but the greater quantity resulting in a longer main reaction period.

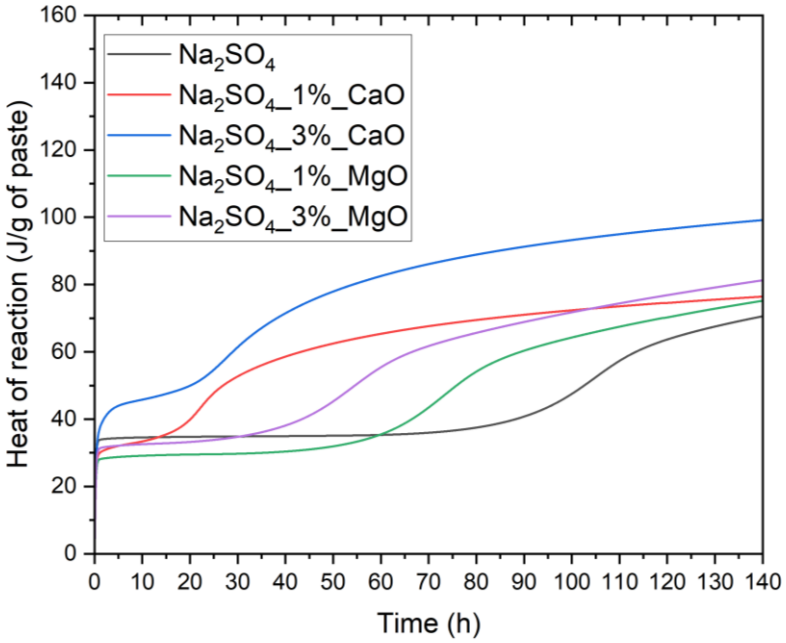

Figure 8-2 *Heat of reaction for sulphate-activated slag with additives, as labelled.*

8.3.1.2 DRIFTS

Time-resolved IR data were used to further investigate the reaction rate and mechanisms during the initial hours following mixing. Diffuse reflectance infrared Fourier transform spectroscopy (DRIFTS) was conducted to observe changes in bond environments *in situ* of the additive-containing sulphate-activated slag samples, where spectra were measured every 2 minutes for the first 2 hours after mixing.

For all the additive-containing samples, as seen in **Figure 8-3** and **Figure 8-4**, there are peaks at ~1630 and ~1085 cm^{-1} present from 0 minutes, which are attributed to the bending of O-H bonds in water [135], [183] and the asymmetric stretching of S-O bonds within sulphate ions [143], [144], respectively, indicative of the presence of the sodium sulphate solution. Soon after mixing, the peak at 1630 cm^{-1} reduces completely, and the peak at ~1085 cm^{-1} reduces slightly,

shifts to a higher wavenumber and increases in intensity. From the spectra for the calcium oxide-containing samples, it is clear that the peak to the left of the aforementioned sulphate ion peak begins as a shoulder before growing in intensity into its own peak at ~1200 cm^{-1}. The two clear peaks at ~1135 and ~1200 cm^{-1} are both also attributed to the asymmetric stretching of S-O within sulphate-containing phases [245]–[247]; these peaks suggest the presence of either gypsum [248], ettringite [250], [251], or monosulphate [251], [252]. Additionally, all samples display a peak in the region of 1340-1400 cm^{-1}, which is attributed to asymmetric stretching of C-O bonds of carbonate ions [141], [142], while the peak at ~1590 cm^{-1} is in the region associated with O-H bonds in water.

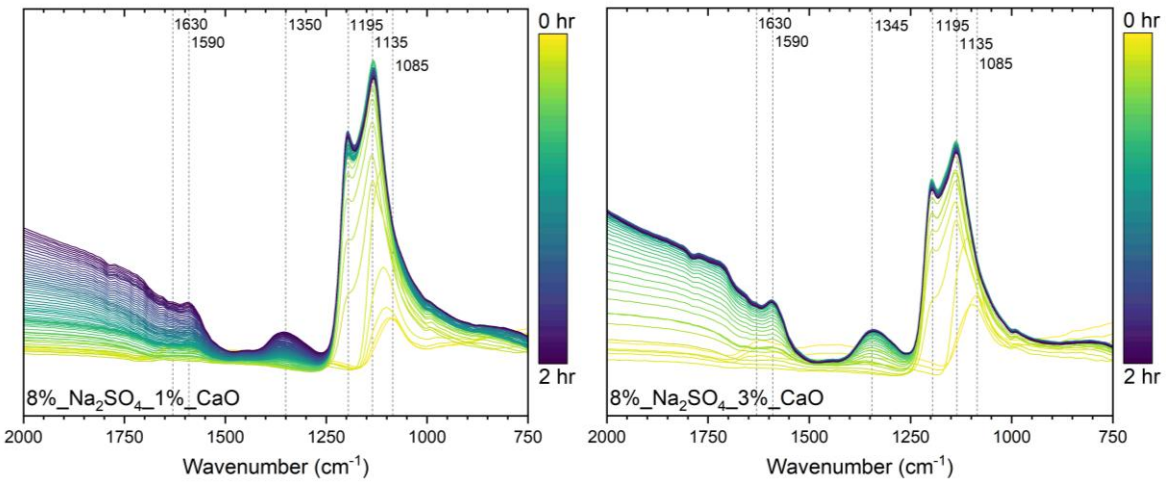

Figure 8-3 *DRIFTS spectra for sulphate-activated BFS with calcium oxide, as marked, over the first 2 hours.*

Although all of the sample sets contain each of these signals beyond the initial dissolution of the activating solution, they exist in different intensities and occur at different rates. For both calcium oxide-doped samples, the presence of the sulphate-associated bands is significantly greater than for the samples incorporating magnesium oxide, indicating that the calcium sulphate phase – be it gypsum, ettringite, or monosulphate – is forming for all samples, but at a much quicker rate and to a higher degree for those containing calcium oxide, likely due to both a higher alkalinity and a greater presence of calcium ions. In contrast, the band in the

region attributed to carbonate ions is more pronounced for the samples containing magnesium oxide (compared to those containing calcium oxide), meaning a greater presence of carbonate-containing phases. This is likely due to atmospheric carbonation occurring, but rather than forming the typical calcium carbonates, as is likely in the calcium oxide-containing samples, it is possible that the increased concentration of magnesium in conjunction with the atmospheric carbonation is leading to the formation of the AFm-type phase, hydrotalcite, with the carbonate ions integrating into its interlayer.

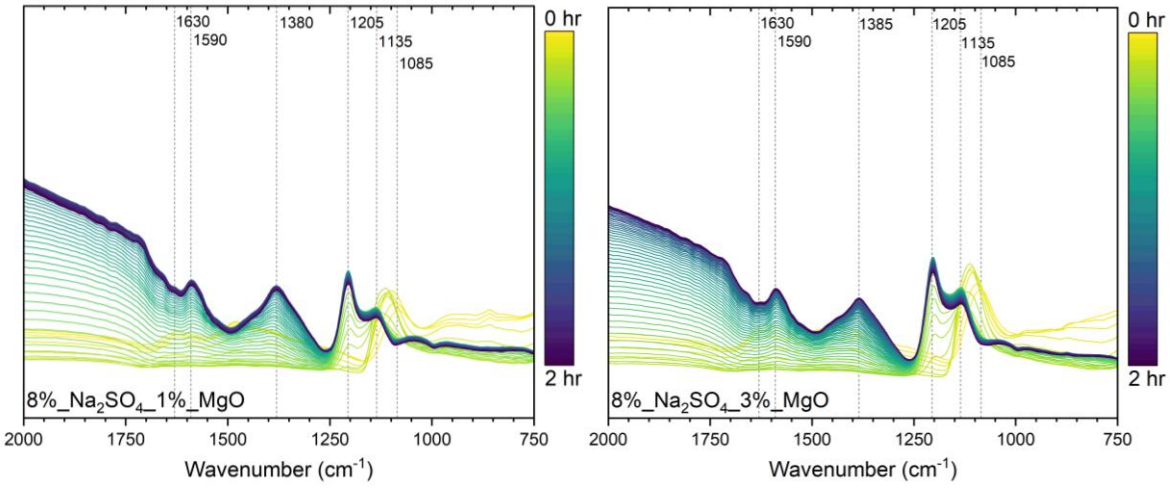

Figure 8-4 *DRIFTS spectra for sulphate-activated BFS with magnesium oxide, as marked, over the first 2 hours.*

As with the solely sulphate-activated sample (**Figure 7-3**), there is no presence of Si-O-T bonds in any of the samples containing either calcium or magnesium, suggesting a lack of aluminosilicate reaction phases, i.e. C-A-S-H, which aligns with the lack of heat output in the early hours of reaction in the calorimetry data.

8.3.1.3 Summary

Coupling the data from calorimetry with that of *in-situ* DRIFTS, it is evident that the incorporation of small amounts of the additives, calcium oxide and magnesium oxide, does have a positive impact on the rate of reaction for sulphate-activated slag binders. It was

observed that calcium oxide had a greater influence on the reaction rate than magnesium oxide, likely due to the respective formation of calcium hydroxide and magnesium oxide in the bulk solution, with the former having a higher pH than the latter. Moreover, the calcium oxide-containing samples favoured the formation of calcium sulphate-containing phases – likely ettringite and possibly its subsequent dissolution into monosulphate – while the magnesium oxide-including samples may prefer the formation of hydrotalcite, at early age.

8.3.2 Structural Evolution

8.3.2.1 ATR-FTIR

FTIR spectroscopy was undertaken to identify bond environments present at various curing times for the sulphate-activated samples incorporating either calcium or magnesium oxide at 1 and 3 wt.% replacement of slag in order to determine how the formulation chemistry influences the structural evolution. All sample sets appear to have mostly similar spectra at all time points with the exception of the sample containing 1 wt.% of magnesium oxide at 3 days of curing, indicating a lack of sufficient reaction, which aligns with the calorimetry data for such sample.

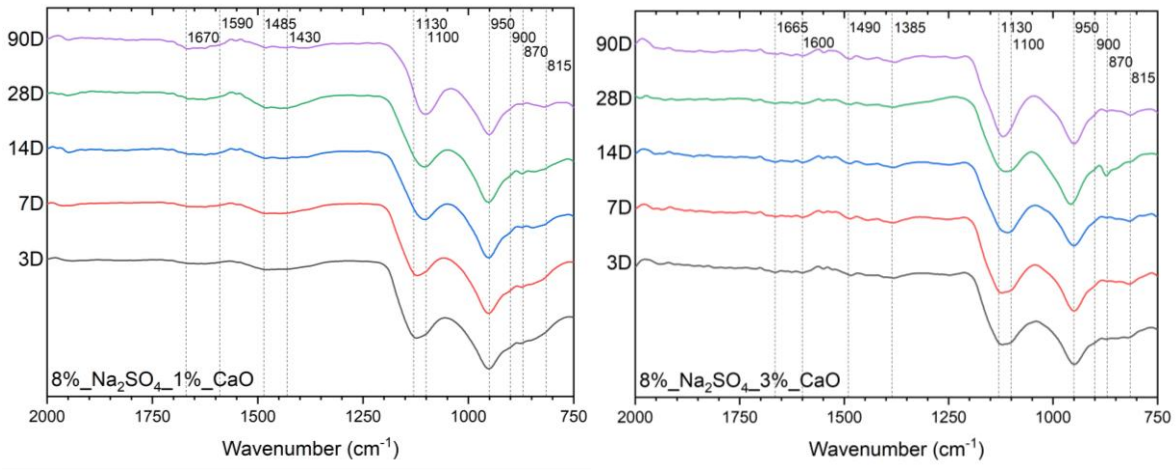

Figure 8-5 *FTIR spectra of sodium sulphate-activated BFS with calcium oxide, at various time points.*

The peaks in the region of 1590 to 1670 cm^{-1} are attributed to the bending of O-H bonds in water [135], [183], from weakly bound water molecules un the materials, while peaks in the region of ~1385 to ~1490 cm^{-1} are characteristic of C-O bonds within carbonates, likely calcium carbonate polymorphs, including vaterite and aragonite [141], [142], [184], indicative of atmospheric carbonation during curing and preparation. Furthermore, peaks at ~850, 875 and 900 cm^{-1} are all also associated with the asymmetric bending of C-O in calcium carbonate [135], [136], [141], [183], with the latter band specifically attributed to calcite [135], [136], [185].

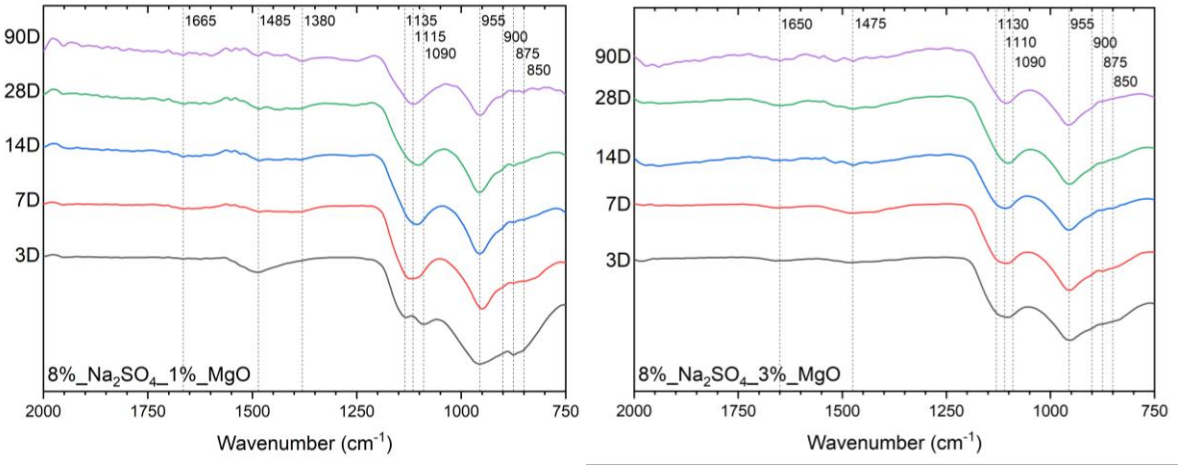

Figure 8-6 *FTIR spectra of sodium sulphate-activated BFS with magnesium oxide, at various time points.*

Additionally, peaks from 1085 to 1140 cm^{-1} are attributed to the asymmetric stretching of S-O within SO_4-containing phases [245]–[247], likely either the AFt-type phase, ettringite [250], [251] or a AFm-type monosulphate [251]. The doublet nature of these peaks at an early age, most notable in **Figure 8-6** at 3 days curing for the sample containing 1 wt.% of magnesium oxide, suggests the initial formation of the weakly bound calcium sulphate hydrate, gypsum [248], [249], which will then proceed to form ettringite, and likely its subsequent transformation into monosulphate as the extent of reaction progresses with time. Finally, the sharp peak at 950 cm^{-1} and the more shallow peak at ~815 cm^{-1} are both attributed to the

asymmetric stretching of Si-O-T bonds (where T represents tetrahedral Si or Al) within a C-A-S-H structure, more specifically Q^2 and Q^1 Si sites, respectively [53], [133], [134]. The sharper nature of the band at 950 cm^{-1} represents a greater structural ordering of the C-(A)-S-H as the reaction proceeds [53], [183].

For both sample sets, the main peak associated with C-A-S-H at ~950 cm^{-1} is present and sharp in nature from 3 days except for the sample containing 1 wt.% of magnesium oxide, where the band is broad, indicative of a limited reaction at this time point, similar to observations from the calorimetry data. Additionally, sulphate-containing phases are present in all samples from early age suggests the initial formation of gypsum, which then forms ettringite, which subsequently converts to the more stable monosulphate. The calcium oxide-containing samples (**Figure 8-5**) display a greater intensity for these calcium sulphate phases, indicating that the increased quantity of calcium ions from the additive leads to the formation of larger quantities of these phases.

8.3.2.2 TGA

TGA was conducted to further the understanding of the structural evolution of the sodium sulphate-activated slag binders incorporating additives, calcium or magnesium oxide, at 1 and 3 wt.% by identifying and quantifying reaction products at different curing times. Generally, an increase in the overall mass loss with time is observed, with some exceptions due to experimental variation, for all samples, indicating the expected increased extent of reaction as time progresses. These values of overall mass losses are summarised in **Table 8-2**. The values for overall mass loss at 3 days highlight the influence of additives on the early reaction, specifically how both the additive and quantity of such additive impact the reaction products: both 3 wt.% inclusions of additives result in a greater formation of reaction phases than their 1 wt.% counterparts. However, beyond 7 days and definitely by 90 days, the mass losses are

very similar regardless of type and quantity of additive incorporated in the sulphate-activated samples, suggesting that structural development plateaus at a similar point for all samples.

Table 8-2 *Overall mass loss values for additive-containing sulphate-activated slags, as determined from TGA data characterised in* ***Figure 8-7*** *and* ***Figure 8-8****.*

	Curing Age				
Sample	**3 days**	**7 days**	**14 days**	**28 days**	**90 days**
Na_2SO_4_1%_CaO	10.8	11.4	20.9	16.0	22.3
Na_2SO_4_3%_CaO	15.6	15.0	21.6	18.5	21.6
Na_2SO_4_1%_MgO	5.4	13.0	25.8	18.9	21.5
Na_2SO_4_3%_MgO	13.5	16.7	21.2	17.8	20.7

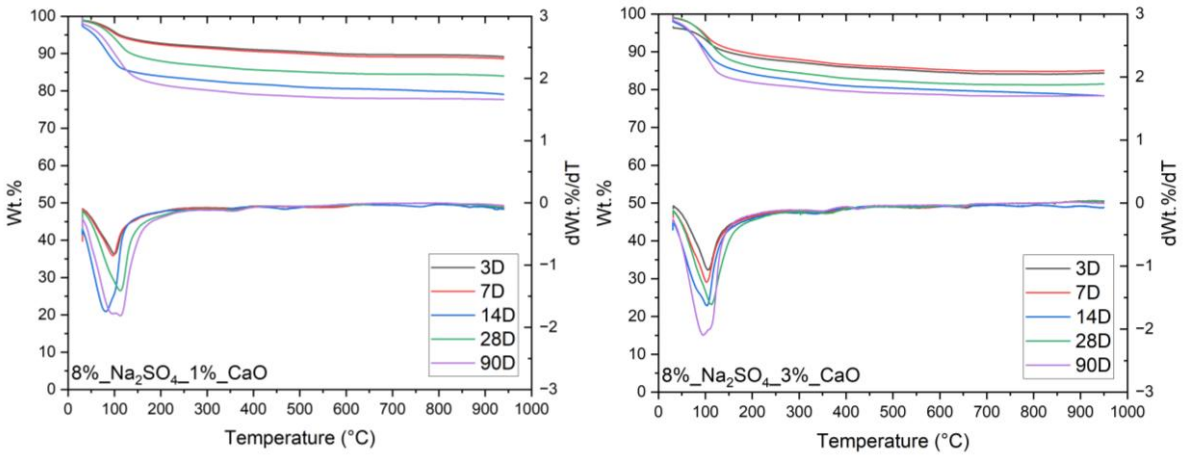

Figure 8-7 *TG/dTG trends of sodium sulphate-activated BFS with calcium oxide, cured for various lengths of time, as labelled.*

Mass losses in the region between 60 and 200 °C are attributed to the loss of water from C-A-S-H [186], [187]. For all samples, this mass loss increases in size and slightly shifts to a higher temperature over time, indicative of a more strongly bound C-A-S-H structure developing as the reaction progresses. There is a notable lack of such mass loss for the sample containing 1 wt.% of magnesium oxide after only 3 days of curing, aligning with previous observations from ICC and FTIR that the main reaction has not commenced by this point for such sample. Furthermore, a shoulder to the initial mass loss at ~170 °C may be observed, particularly at

later time points, associated with the initial thermal degradation of hydrotalcite [188], [189]. Moreover, a mass loss in the region of 300 to 500 °C is also associated with the presence of hydrotalcite phases, more specifically the additional dehydroxylation of chemically bound water within the structure [186], [188], [190]. All sample sets display some mass loss associated with the presence of hydrotalcite, but more so for the samples doped with magnesium oxide, understandably as the increased magnesium content allows for greater formation of the magnesium-aluminium-based structure.

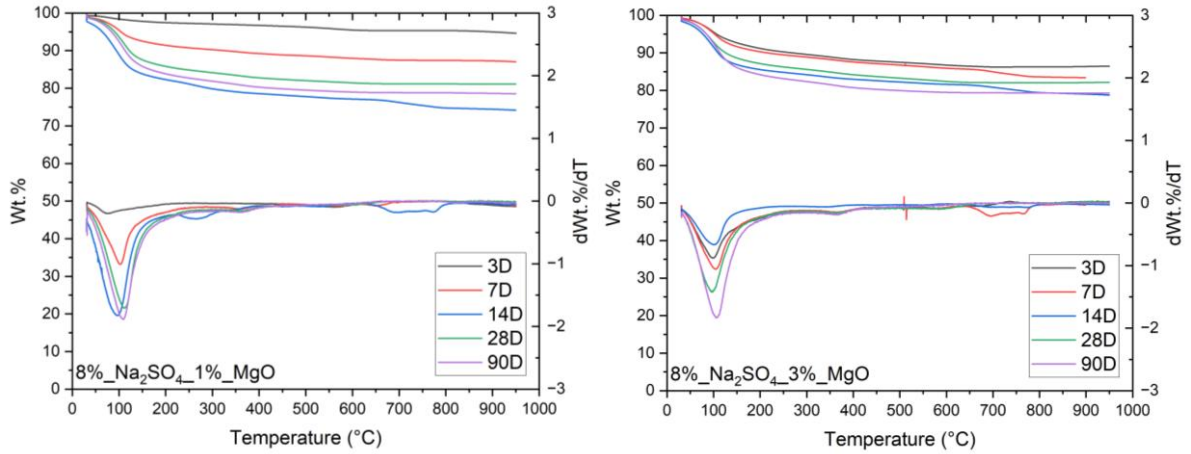

Figure 8-8 *TG/dTG trends of sodium sulphate-activated BFS, cured for various lengths of time, as labelled.*

Typically, additional mass losses associated with the progressive dehydration of the C-A-S-H phase would be expected in the region of 500 to 700 °C [186], [188], however, there is very limited mass loss in this region for any sample at any time point, suggesting that the C-A-S-H structure within the sulphate-activated samples is not very strongly bound or polymerised, which aligns with the low overall heat release of reaction illustrated in **Figure 8-2**.

Furthermore, mass losses in the region of 600 to 900 °C are associated to the decomposition of calcium hydrates [186], including the sulphate-containing phases, ettringite and monosulphate [186], [251], [257], as well as the decarbonation of carbonates, including calcium carbonate polymorphs – calcite, vaterite, and aragonite [188], [192], [193]. Despite observations from IR

spectroscopy, there is very little indication of the presence of sulphate- or carbonate-containing phases in the TGA curves for most of the samples.

8.3.2.3 XRD

Diffraction patterns were measured for the additive-containing sulphate-activated samples at various curing ages, shown in **Figure 8-9** and **Figure 8-10** for the calcium oxide- and magnesium oxide-doped samples, respectively. Generally, there is very little change observed in the XRD patterns over time and between samples sets, suggesting that by 7 days, a stable structure is formed and does not develop much further beyond this curing age.

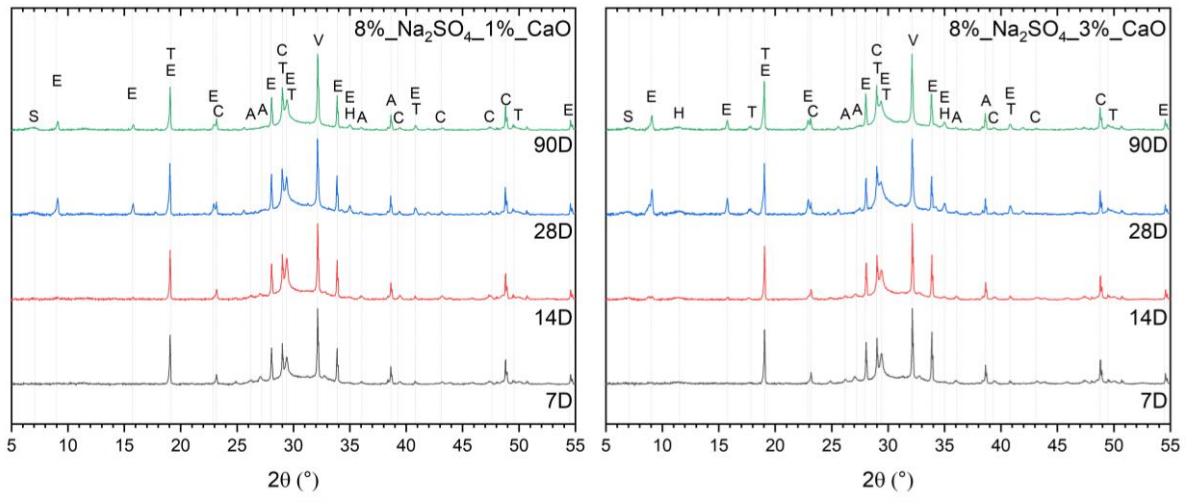

Figure 8-9 *XRD patterns of sulphate-activated BFS with calcium oxide, at various curing times, as labelled. Phases identified have been labelled: A – Aragonite (PDF 04-008-5421), C – Calcite (PDF 00-066-0867), E –Ettringite (PDF 00-013-0350), H – Hydrotalcite (PDF 01-088-9171), Strätlingite (PDF 04-012-1915), T – Tobermorite (PDF 04-014-8455), and V – Vaterite (PDF 00-060-0483).*

As expected with alkali-activated slag samples, there is a generally broad and amorphous hump centred at ~30° 2Θ observed in all samples, characteristic of the tobermorite-like C-A-S-H structure, aligning with observations from FTIR and TGA data. Small quantities of peaks associated with tobermorite and hydrotalcite are present at most time points, as well as some amounts of calcium carbonate polymorphs – aragonite, calcite, and vaterite – from early age,

in all samples, aligning with the previous findings in this study. The existence of such calcium carbonates is due to atmospheric carbonation, which appears to occur at an undesirable rate due to the porous nature of the material as well as its longer setting time, allowing infiltration of CO_2 into the pore solution more easily.

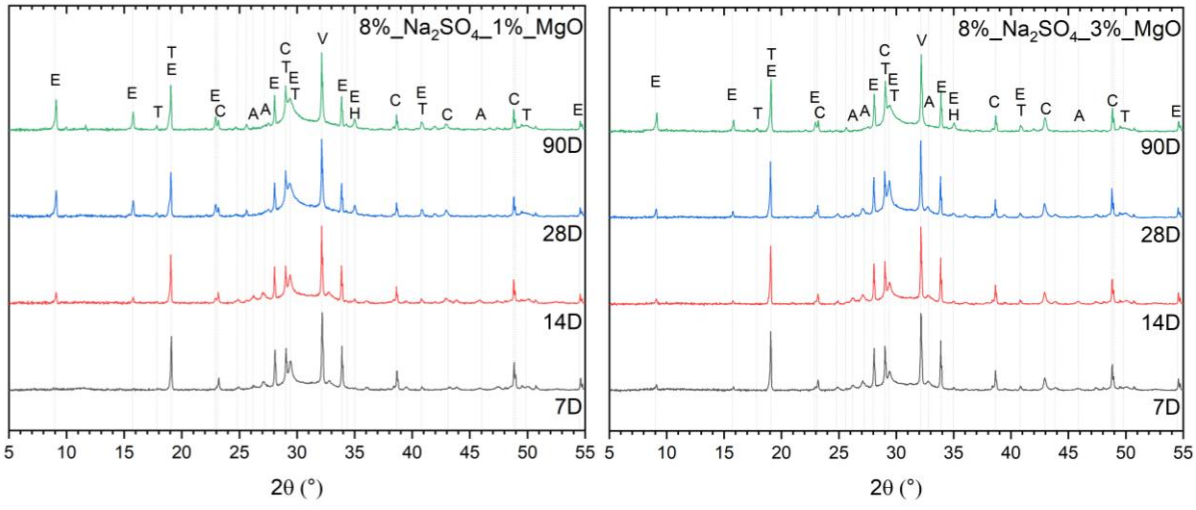

Figure 8-10 *XRD patterns of sulphate-activated BFS with magnesium oxide, at various curing times, as labelled. Phases identified have been labelled: A – Aragonite (PDF 04-008-5421), C – Calcite (PDF 00-066-0867), E –Ettringite (PDF 00-013-0350), H – Hydrotalcite (PDF 01-088-9171), T – Tobermorite (PDF 04-014-8455), and V – Vaterite (PDF 00-060-0483).*

In addition to this structure, there are notable crystalline phases present, including calcium sulphate hydrate, ettringite, which is often found in alkali-activated slag binders where sodium sulphate is used as the activator component [88], [115], [243]. Peaks for ettringite often overlap with monosulphate due to their similar structure, so it is possible that the formation of some of the peaks labelled ettringite, beyond the initial 7 days of curing, may in fact be monosulphates formed once the sulphate from the activator is used up and when the pH reduces, limiting ettringite formation [251], [253]. It is likely that the formation of such phases from the calcium and aluminium supplied by the slag with the sulphate species in the activator, as well as the lower pH hindering sufficient slag dissolution and the release of silicate tetrahedra, is delaying the formation of strongly bound and polymerised C-A-S-H.

8.3.2.4 SEM-EDX

Scanning electron microscopy coupled with energy dispersive x-ray analysis was undertaken to image the surface structure and determine its elemental composition, in order to further probe the structural evolution of the sodium sulphate-activated slag binders with the incorporation of additives.

8.3.2.4.1 SEM Images

SEM images at 7, 14, 28, and 90 days curing for the additive-containing sulphate-activated samples are shown in **Figure 8-11** and **Figure 8-12** for the 1 and 3 wt.% inclusion of calcium oxide, respectively, and **Figure 8-13** and **Figure 8-14** for the 1 and 3 wt.% inclusion of magnesium oxide.

As for all the alkali-activated slag binders in this study, these sulphate-activated slag samples show lighter grey slag particles within a darker grey bulk structure, which contains the reaction products, like C-A-S-H, hydrotalcite, ettringite, and calcium carbonate polymorphs. As with the non-additive-containing sulphate-activated sample (**Figure 7-11**), these sulphate-activated samples contain significantly more unreacted slag particles and the bulk structure evolves slower over time, compared to the binders in this study using other activators. This supports the observed lesser extent of reaction, i.e. a stable structure forms by 7 days and changes very little beyond this curing age, as seen in FTIR, TGA, and XRD. It is noted that the samples containing calcium oxide appear to have much greater quantities of unreacted slag particles compared to the magnesium oxide-containing samples at all time points, which is contrary to observations of greater rate and extent of reaction. However, it may be that the additive and activator are preferentially reacting more than the slag particles at the early ages. Additionally, the samples containing magnesium oxide have dark areas within the bulk structure, most notable for the 28 and 90-day samples for 1 wt.% of magnesium addition.

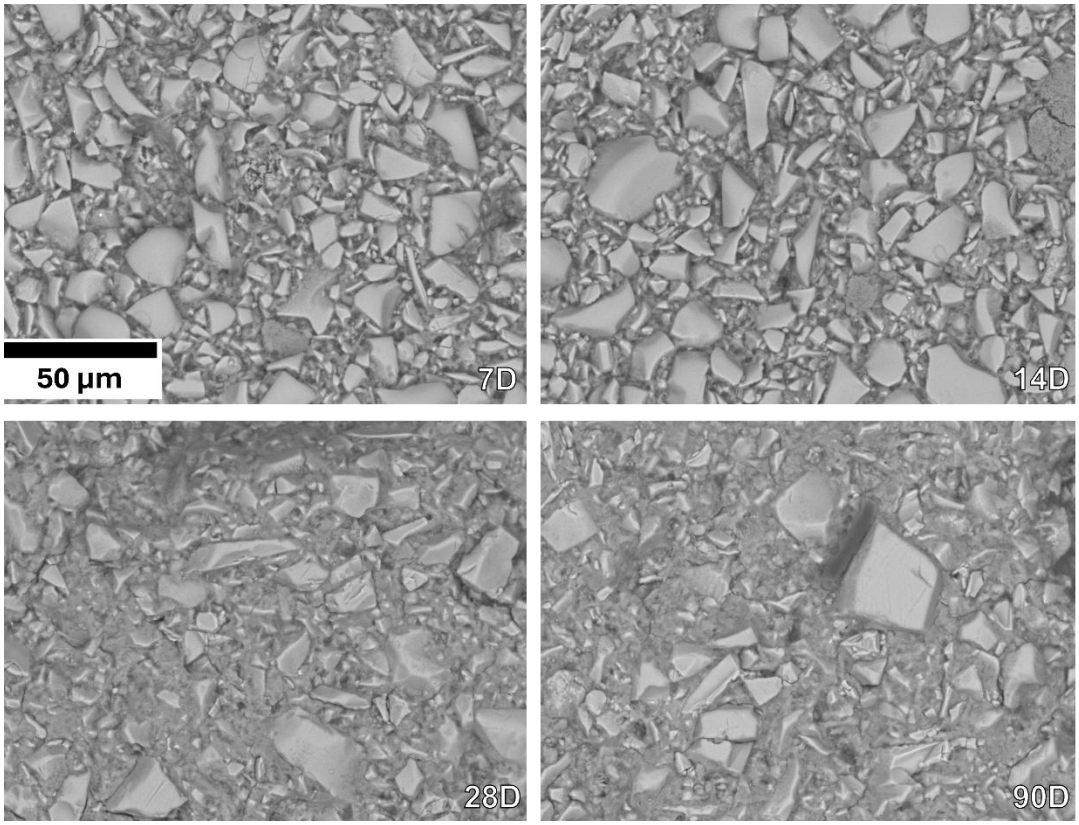

Figure 8-11 *SEM images for sulphate-activated BFS with 1 % CaO, at 1000x magnification, for various curing times, as labelled.*

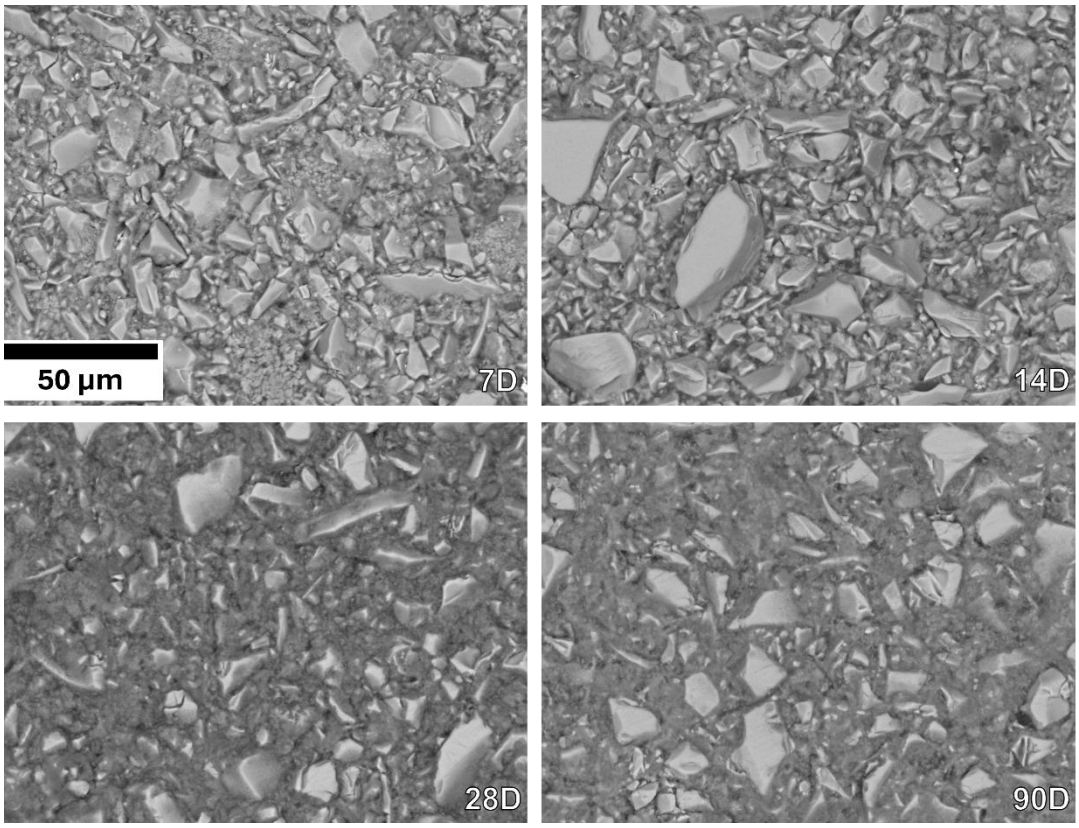

Figure 8-12 *SEM images for sulphate-activated BFS with 3 % CaO, at 1000x magnification, for various curing times, as labelled.*

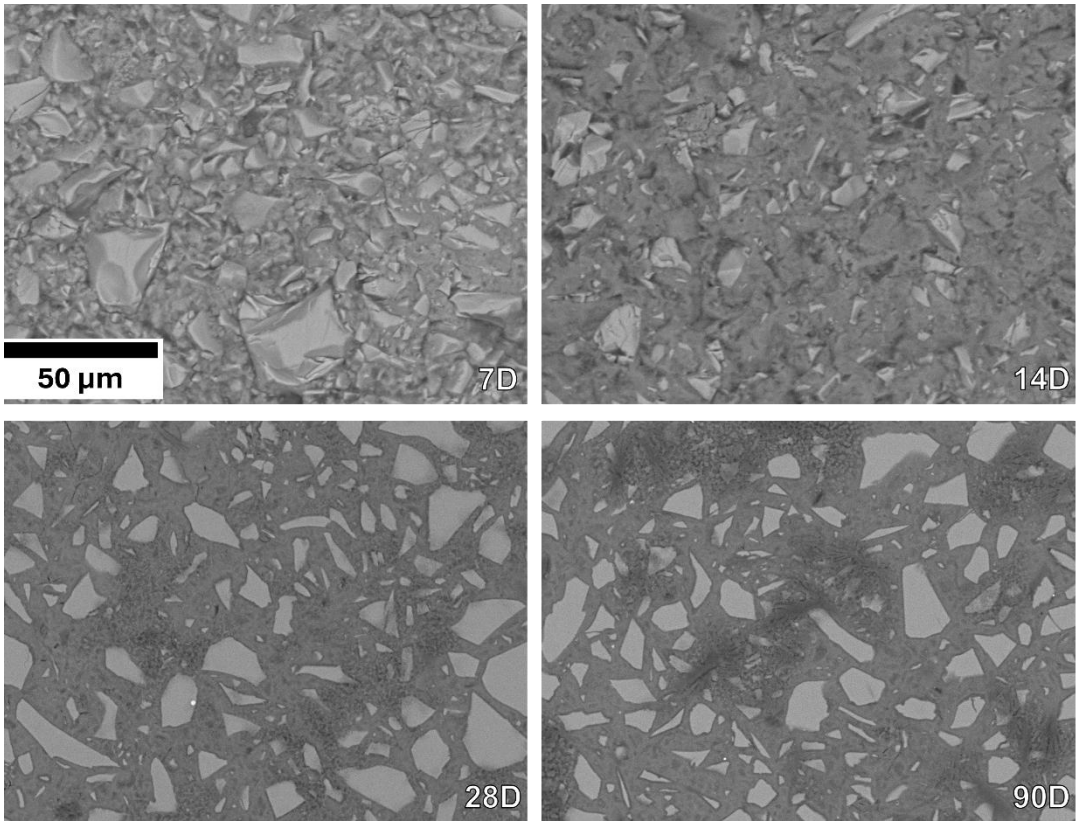

Figure 8-13 *SEM images for sulphate-activated BFS with 1 % MgO, at 1000x magnification, for various curing times, as labelled.*

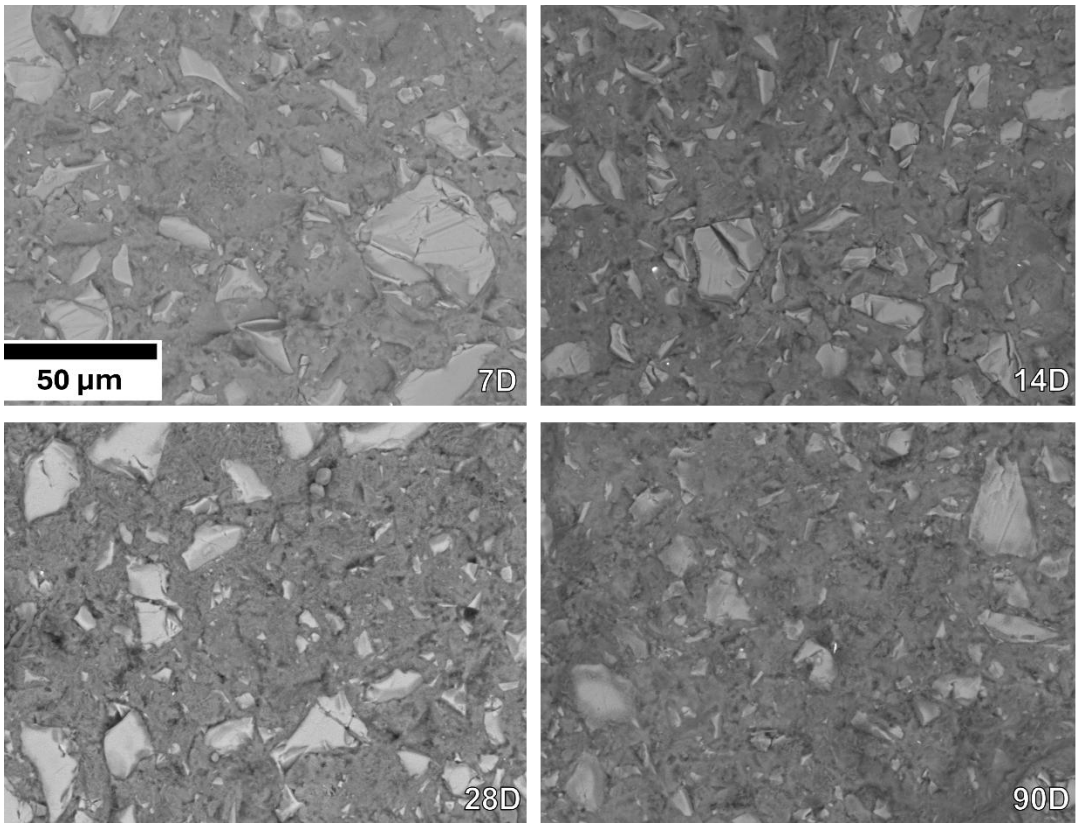

Figure 8-14 *SEM images for sulphate-activated BFS with 3 % MgO, at 1000x magnification, for various curing times, as labelled.*

8.3.2.4.2 EDX Elemental Maps

Elemental maps of each sample was formed with the data from EDX scanning, which can provide further insight into the chemical composition of the samples at various time points, and thus the structural phase evolution.

For the calcium oxide-containing samples (**Figure 8-15** and **Figure 8-16**), the bulk structure becoming more sodium-rich over time with some contributions from magnesium, calcium, and silicate, while the slag particles remain aluminium- and silicon-concentrated with some areas rich in calcium nearby. This evolution indicates a sodium-rich C-A-S-H phase forming the bulk of the reaction product as well as continual dissolution of slag particles.

On the other hand, over time for the magnesium oxide-containing samples (**Figure 8-17** and **Figure 8-18**), the bulk structure also becomes sodium-rich but also rich in magnesium with strong contributions of aluminium and lesser contributions from calcium and silicate. This implies a greater formation of hydrotalcite, which is rich in both magnesium and aluminium. Moreover, the slag particles become less silicon-rich over time, suggesting the incorporation of this element in the bulk structure. Additionally, there are distinct areas of concentrated magnesium, possibly due to the lower reactive nature of the magnesium oxide resulting in a limited incorporation into reaction products.

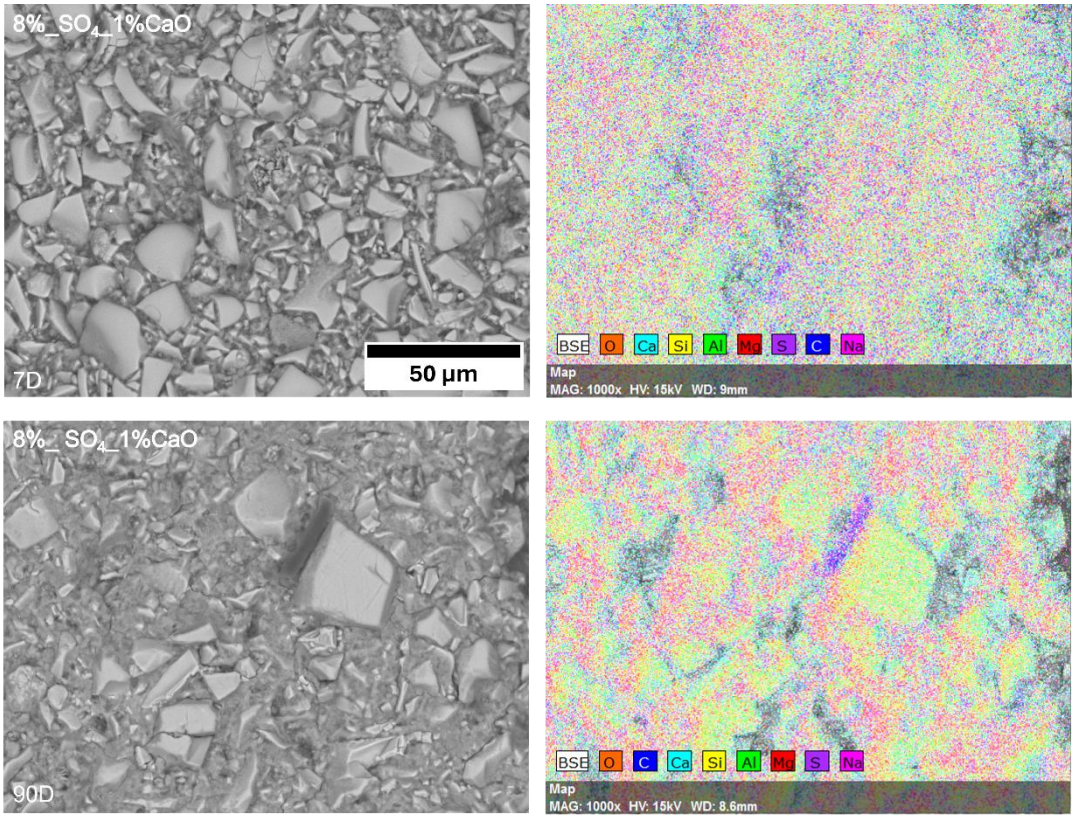

Figure 8-15 *Elemental mapping for sulphate-activated BFS with 1 % CaO, cured at 7 and 90 days, as labelled.*

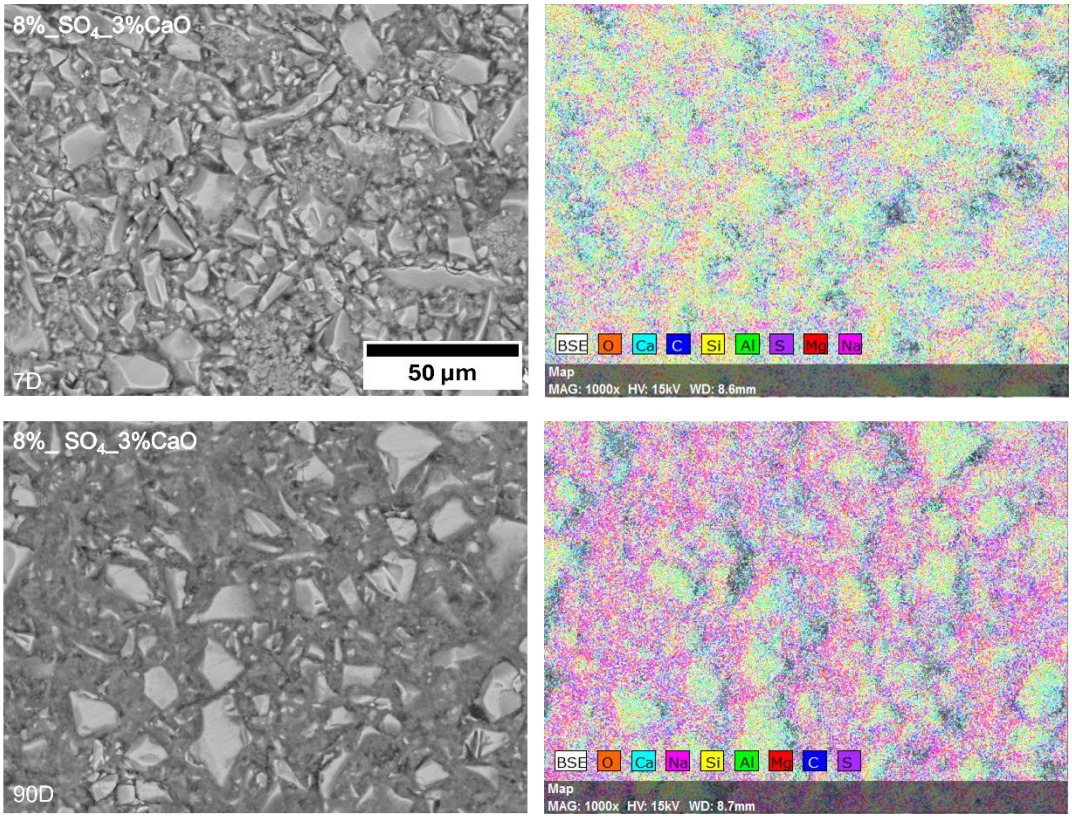

Figure 8-16 *Elemental mapping for sulphate-activated BFS with 3 % CaO, cured at 7 and 90 days, as labelled.*

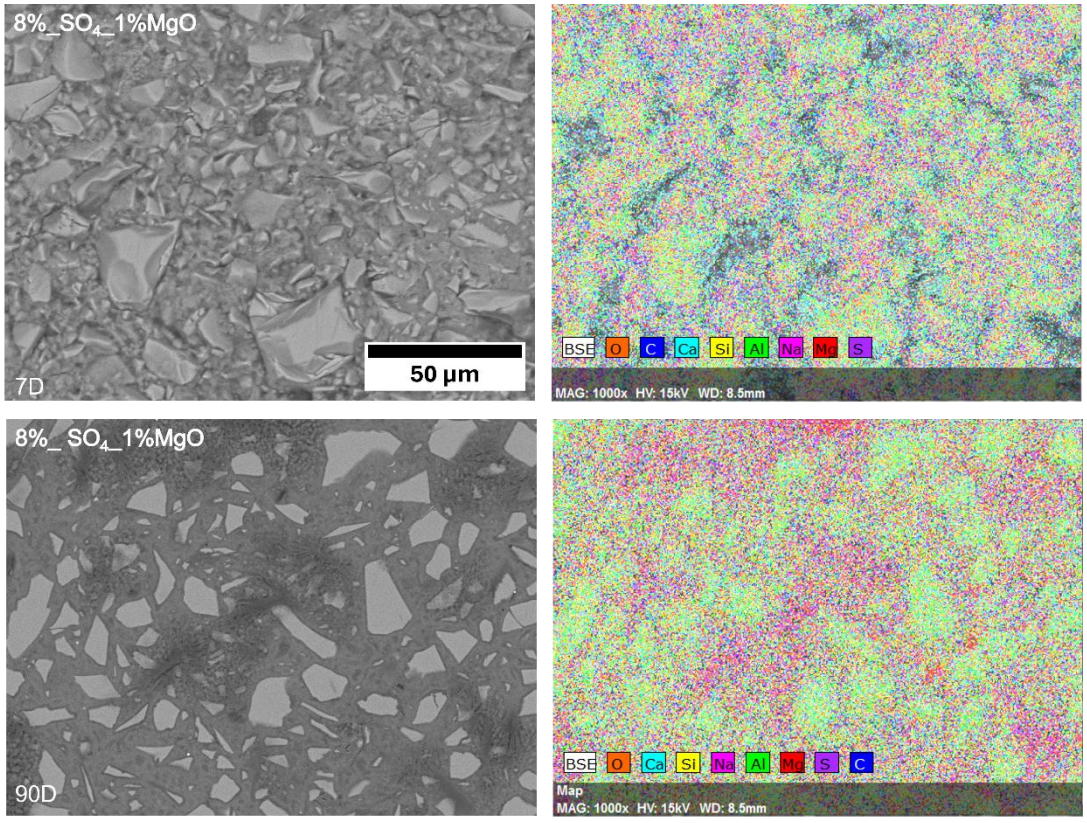

Figure 8-17 *Elemental mapping for sulphate-activated BFS with 1 % MgO, cured at 7 and 90 days, as labelled.*

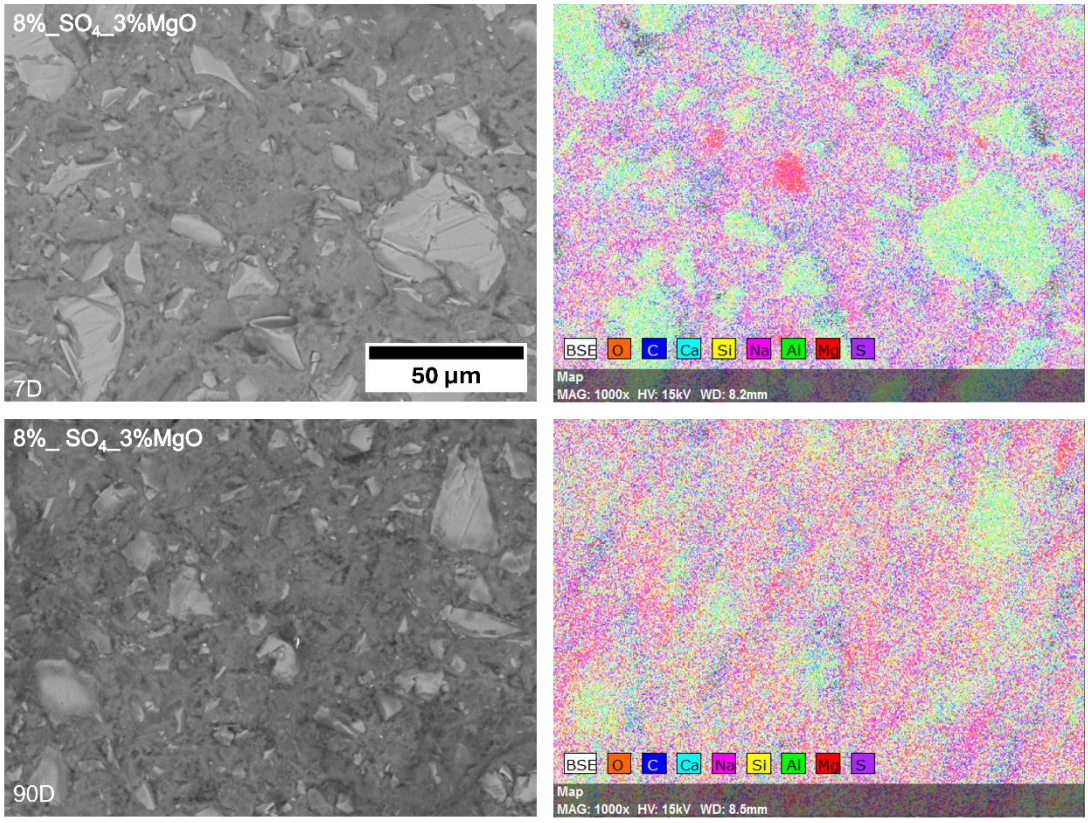

Figure 8-18 *Elemental mapping for sulphate-activated BFS with 3 % MgO, cured at 7 and 90 days, as labelled.*

8.3.2.4.3 Ternary Systems

Ternary systems were developed from the elemental composition data acquired by EDX scans for the sulphate-activated samples incorporating calcium oxide at 1 and 3 wt.% (**Figure 8-19** and **Figure 8-20**, respectively), and magnesium oxide at 1 and 3 wt.% (**Figure 8-21** and **Figure 8-22**, respectively).

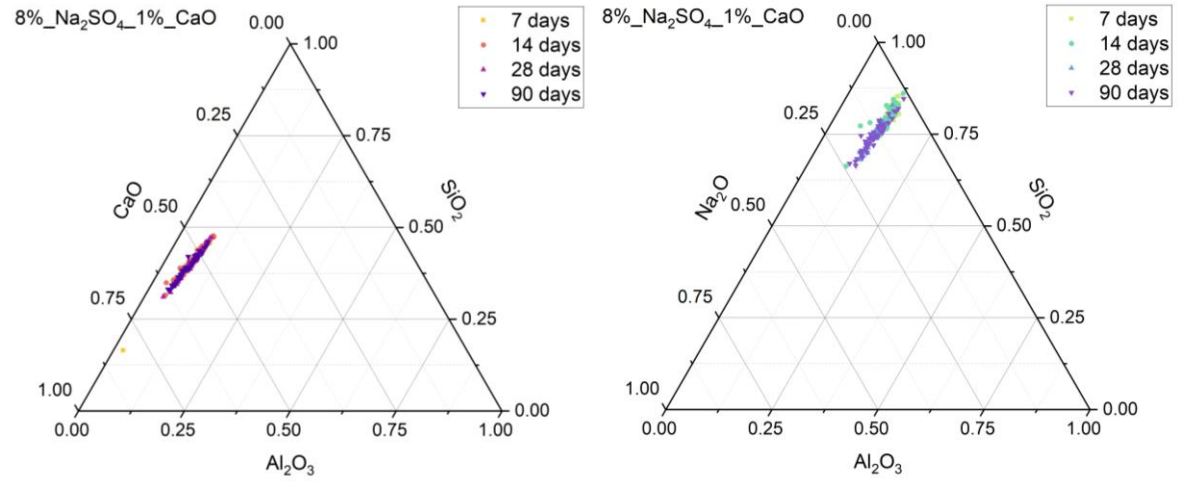

Figure 8-19 *Ternary systems of sulphate-activated slag with 1 % CaO cured for 7, 14, 28, and 90 days, as determined by SEM-EDX analysis. (L) Ternary CaO – Al_2O_3 – SiO_2 system (neglecting Na_2O content), and (R) Ternary Na_2O – Al_2O_3 – SiO_2 system (neglecting CaO) content, showing elemental composition.*

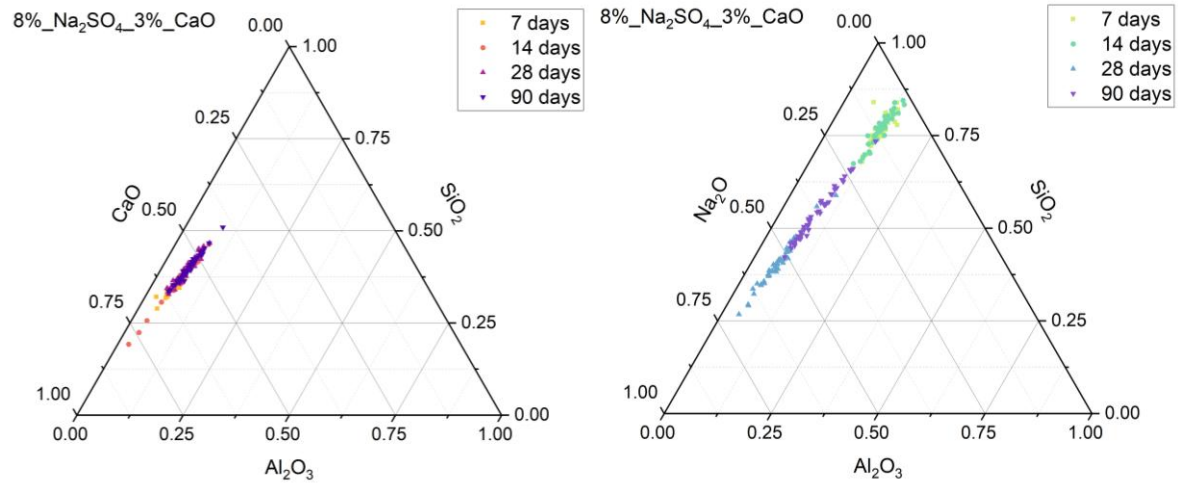

Figure 8-20 *Ternary systems of sulphate-activated slag with 3 % CaO cured for 7, 14, 28, and 90 days, as determined by SEM-EDX analysis. (L) Ternary CaO – Al_2O_3 – SiO_2 system (neglecting Na_2O content), and (R) Ternary Na_2O – Al_2O_3 – SiO_2 system (neglecting CaO) content, showing elemental composition.*

The ternary CaO-Al_2O_3-SiO_2 system for all sample sets remains relatively consistent with some points of higher CaO content noted for early time points for the samples with the addition of CaO. The general structure for all samples lines up with previous studies of alkali-activated slag binder as well as synthetic C-(A)-S-H and N-A-S-H gels [53], [211]–[213]; the region occupied on the ternary diagrams is associated with the composition of the sodium-rich aluminosilicate hydrate, C-(N)-A-S-H [53], [161], [214], which aligns with the sodium rich bulk structure observed in the EDX mapping. Moreover, the Al/Si ratio remains relatively constant over time, indicative of a stable C-A-S-H structure, with little to no change in crosslinking and chain length, which supports earlier observations of an established structure by 7 days, which varies very little beyond this time point.

In contrast, the ternary Na_2O-Al_2O_3-SiO_2 systems for the sample sets do differ from the non-additive-containing sulphate-activated sample and somewhat from each other, as there is a general decrease in sodium content over time, particularly noticeable in the 3 wt.% additive-containing samples. Additionally, there is a slight decrease in the Al/Si ratio over time for each of the sample sets.

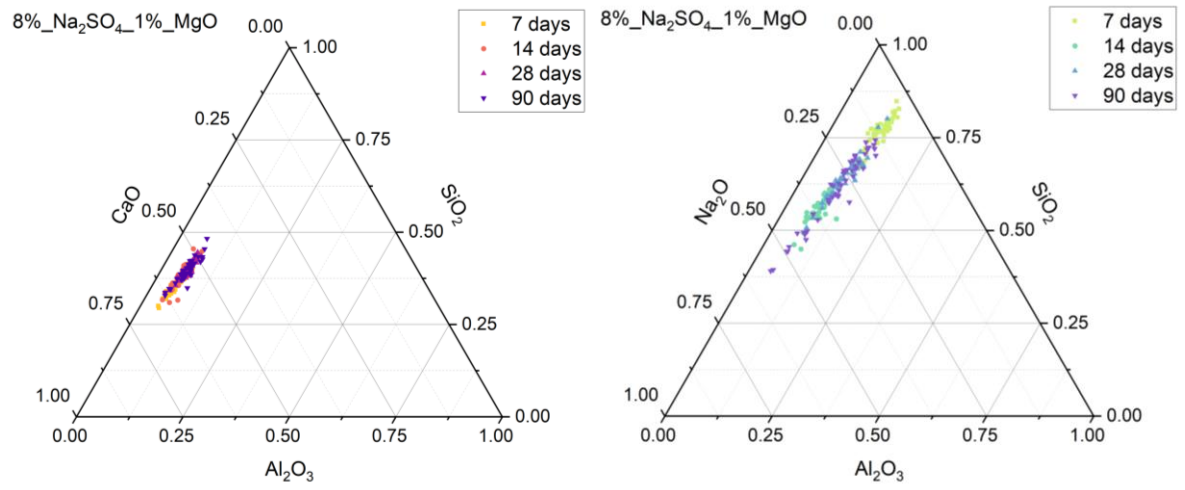

Figure 8-21 *Ternary systems of sulphate-activated slag with 1 % MgO cured for 7, 14, 28, and 90 days, as determined by SEM-EDX analysis. (L) Ternary CaO – Al_2O_3 – SiO_2 system (neglecting Na_2O content), and (R) Ternary Na_2O – Al_2O_3 – SiO_2 system (neglecting CaO) content, showing elemental composition.*

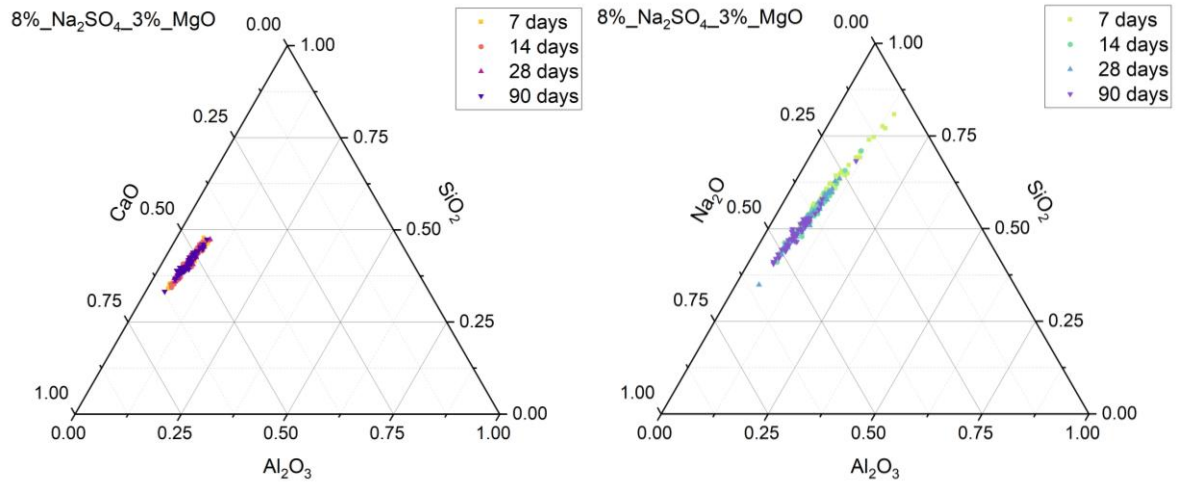

Figure 8-22 *Ternary systems of sulphate-activated slag with 3 % MgO cured for 7, 14, 28, and 90 days, as determined by SEM-EDX analysis. (L) Ternary CaO – Al_2O_3 – SiO_2 system (neglecting Na_2O content), and (R) Ternary Na_2O – Al_2O_3 – SiO_2 system (neglecting CaO) content, showing elemental composition.*

8.4 Conclusions

The use of small amounts of additives – calcium oxide and magnesium oxide – to improve the performance of sodium sulphate-activated slag binders was explored in this chapter, with specific focus on the early reaction and subsequent phase evolution.

Findings show that for both additives at both 1 and 3 wt.% replacement of BFS in the system, the rate of reaction is improved for the sodium sulphate-activated slag binder, with the calcium oxide increasing the rate of reaction more than the magnesium oxide inclusion. This is due to the increased pH associated with the precipitation of calcium hydroxide compared to magnesium hydroxide. Despite increasing the rate of reaction, it appears that the reaction mechanism remains the same regardless of additive type or quantity included, and that the overall cumulative heat output is not greatly improved, with the exception of 3 wt.% of CaO, suggesting that a similar extent of reaction is achieved whether an additive is incorporated in the formulation or not. Further to this, according to data from TGA, FTIR, XRD, and SEM-EDX, the general structure of the additive-containing sulphate-activated sample is very similar

to the sulphate-activated sample without any additives. Beyond 7 days, regardless of additive type or quantity, the reaction products are very similar to one another suggesting that a stable structure forms and does not change much with time, however, the C-A-S-H that does form does not appear to be very strongly bound according to TGA, which validates the observations of low heat of reaction from calorimetry data.

Overall, the inclusion of small amounts of calcium and magnesium oxide can improve the rate of reaction for slag binders utilising sodium sulphate as an activator, however, the general reaction mechanism and subsequent phase formation remains the same. Moreover, the limited quantity of phases present and the lack of polymerisation of C-A-S-H suggests the limited physical performance of these sodium sulphate-activated slag cements and as such, their use in industry does not appear feasible without further formulation optimisation.

Chapter 9: Comparative Analysis, Conclusions & Future Work Recommendations

9.1 Introduction

Throughout this body of work, multiple alkali-activated slag binder formulations have been made using low-carbon alkaline solutions, sodium carbonate and sulphate, with an overarching aim of underpinning the fundamental chemistry that governs the performance of alkali-activated slag cements, while minimising the carbon footprint where possible. They have been characterised and analysed in terms of reaction kinetics and mechanisms and structural evolution (on both the micro and nano scale), and where a sufficient binder has formed, physicomechanical properties have also been analysed in comparison to a sodium silicate-activated slag as a control. Understanding these composition-structure-property relationships is paramount for optimising formulations of such binders in order to drive rapid industrial implementation and thus, reduce the anthropogenic carbon output associated with the cement industry. As such, this chapter will briefly explore and compare some of the key performance properties relevant to industrial use, as well as the carbon footprint, of the alkali-activated slag samples.

9.2 Performance Comparison

9.2.1 Reaction

Key performance measures for reaction based on calorimetry data are provided in **Table 9-1**, which include the time at which the main reaction peaks, the corresponding heat release at said time, and the cumulative heat of reaction at 72 hours. The first two parameters are a measure of when the main reaction – where C-A-S-H phases tend to form – occurs and the extent to which this occurs, respectively, while the third parameter can be used as a comparison of the extent of reaction at 3 days.

Table 9-1 *Key reaction parameters for each formulation taken from calorimetry data.*

Sample Formulation	Peak Reaction Time (hr)	Heat release at Peak Reaction (mW/g)	Cumulative Heat at 72 hr (J/g)
BFS_8%_Na_2SiO_3	8.1	2.3	144.1
BFS_8%_Na_2CO_3	57.2	0.9	97.8
BFS_8%_ Na_2SiO_3_ Na_2CO_3	11.1	1.7	121.7
BFS_8%_Na_2CO_3_1%_CaO	40.9	1.2	101.3
BFS_8%_Na_2CO_3_3%_CaO	23.8	1.5	111.7
BFS_8%_Na_2CO_3_1%_MgO	56.7	0.9	90.4
BFS_8%_Na_2CO_3_3%_MgO	54.0	0.9	95.1
BFS_8%_Na_2SO_4	104.5	0.3	36.2
BFS_8%_ Na_2SiO_3_Na_2SO_4	13.0	1.7	118.1
BFS_8%_Na_2SO_4_1%_CaO	22.2	0.5	67.9
BFS_8%_Na_2SO_4_3%_CaO	27.8	0.4	86.9
BFS_8%_Na_2SO_4_1%_MgO	73.3	0.3	45.5
BFS_8%_Na_2SO_4_3%_MgO	54.0	0.3	62.8

Silicate-activated sample reacts the quickest and its peak has the greatest heat release. Its cumulative heat of reaction at 72 hours is the greatest for all samples, corresponding to a significant degree of reaction, i.e. a significant amount of reaction products have formed, which are also likely to be well-bound. Similarly, those samples activated with a combination of sodium silicate and a low-carbon activator (either sodium carbonate or sulphate) show the next best performance in these categories, with the sodium carbonate blend having slightly improved indicators than the sodium sulphate blend, likely due to the differences in pH. This observation reinforces that the use 50:50 blend of sodium silicate with a low-carbon activator tends toward the behaviour of the silicate activator.

Along those lines, the solely sodium carbonate-activated sample's reaction parameters are greatly improved by the incorporation of calcium oxide, while the inclusion of magnesium oxide in this sample only slightly improves the onset of the main reaction but has no effect on the heat release at this time point and actually slightly reduces the cumulative heat of reaction at 72 hours. As previously discussed, the addition of CaO likely leads to an increase in pH in the pore solution with the formation of calcium hydroxide, which in turn speeds up the onset of the main reaction, while the inclusion of MgO in this study does not appear to alter the early reaction environment much or at all, supporting the lack of effect on the carbonate-activated slag.

Similarly, for the sodium sulphate-activated slag binder, the inclusion of calcium oxide has a greater improvement on the reaction compared to magnesium oxide, however, magnesium oxide does indeed improve the rate of reaction, unlike its inertness on the carbonate-activated system. Despite the change in reaction kinetics, the heat release at the peak of the main reaction remains very similar with or without additives in the sulphate-activated system, reinforcing that the sodium sulphate is not providing sufficient conditions for the precipitation of key reaction products. As the initial formulation parameters – w/b ratio and dosage – were selected with respect to previous studies on sodium carbonate-activated slags, it is noted that optimising these parameters may allow for a sufficient binder utilising sodium sulphate as an activator.

Additionally, DRIFTS spectra at 2 hours after mixing for each of the sodium carbonate- and sodium sulphate-activated binders, in comparison to the control sample, are displayed in **Figure 9-1** and **Figure 9-2** respectively.

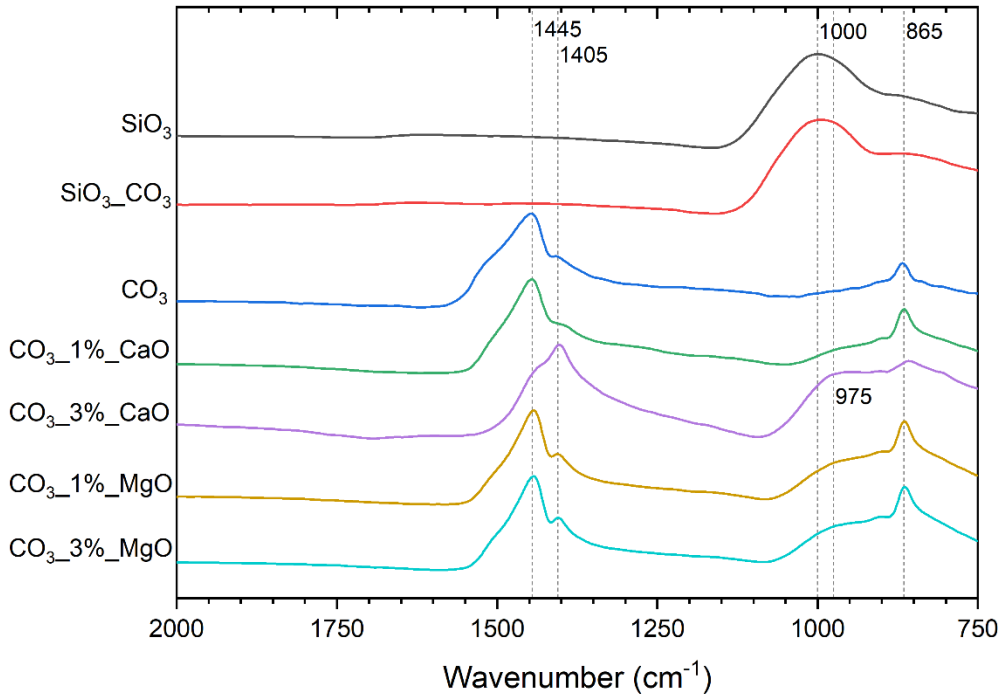

Figure 9-1 *DRIFTS spectra for the carbonate-activated samples at 2 hr after mixing, in comparison with the silicate-activated control sample.*

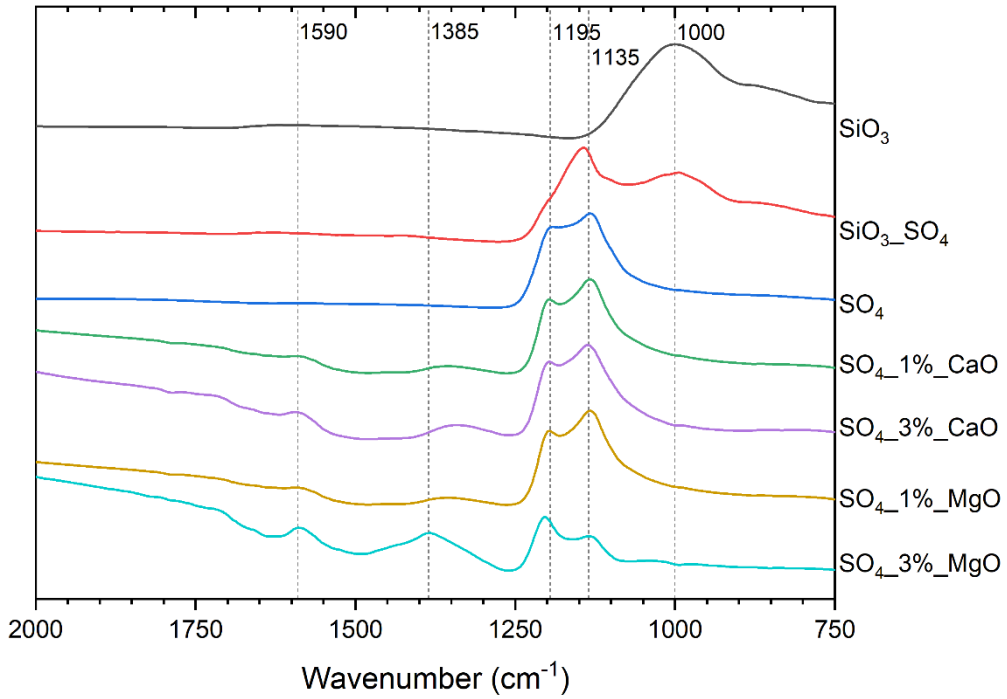

Figure 9-2 *DRIFTS spectra of each sulphate-activated binder at 2 hr after mixing, compared to the silicate-activated control sample.*

The general trend of the DRIFTS spectra aligns with the trend observed from the calorimetry data, with the silicate blends being most similar to the solely silicate-activated sample. However, where the silicate-carbonate-activated slag has an almost identical spectrum to the silicate-activated sample, the silicate-sulphate blend has features of both the solely silicate- and solely sulphate-activated binders. This suggests that sodium sulphate is in fact hindering the very early dissolution, but sodium carbonate does not have this effect.

Beyond this, the inclusion of either calcium oxide or magnesium oxide show little changes in key features of the spectra compared to the non-additive-containing samples, with the exception of the sodium carbonate-activated slag including an addition of 3 wt.% of CaO. This is primarily due to the likely formation of calcium hydroxide increasing the rate of reaction and the initial preferential reaction previously identified as well as starting to induce the formation of some C-A-S-H at 2 hours.

9.2.2 Phase Evolution

The FTIR spectra at 7 days of curing for each sample formulation are displayed in **Figure 9-3** in order to showcase the bond environments present after the initial reaction.

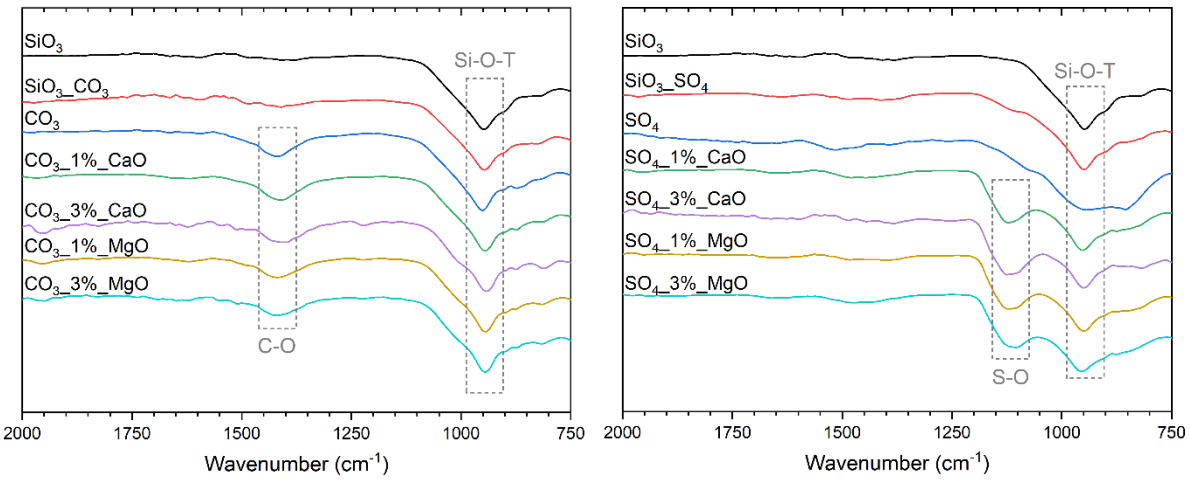

Figure 9-3 *FTIR spectra for each formulation at 7 days curing.*

As expected, the carbonate-activated samples display a C-O bond associated with carbonate polymorphs formed during the early reaction, while most of the sulphate-activated samples have an S-O bond corresponding to the likes of ettringite forming. It is noted that this bond is not present in the non-additive-containing sulphate-activated binder, showcasing a lack of extent of reaction.

All samples' FTIR spectra contain an Si-O-T bond, where T is either tetrahedral Si or Al, by 7 days, although this is more pronounced in some samples compared to others. Notably this peak is not very defined for the sodium sulphate-activated sample, meaning that the signal here is more likely in reference to the aluminosilicate bonding within the precursor slag, rather than a formed C-A-S-H structure. The existence of C-A-S-H suggests a sufficient binder forming, and thus, for the sulphate-activated slag, it is fair to say that a sufficient binder has not formed by 7 days. Although this bond is present in the additive-containing samples, when combined with the limited cumulative heat of reaction observed in calorimetry data, it is likely that the quantity and polymerisation of C-A-S-H in these samples is also not enough for a sufficient binder to form. This observation, in combination with the lack of secondary product, ettringite in the solely sulphate-activated sample, suggests a lack of a sufficient binder forming, and therefore further characterisation was halted, in particular a choice was made not to conduct solid-state MAS NMR spectroscopy on any sulphate-activated samples.

Furthermore, ^{29}Si MAS NMR spectroscopy was conducted on the carbonate-activated samples, as well as the silicate-activated control sample, to probe the structure of the C-A-S-H phases formed. The quantification of the tetrahedral Si sites based on deconvolutions of these spectra are summarised in **Table 9-2** and **Table 9-3**.

Table 9-2 *NMR parameters for alkali-activated slag samples, extracted from the deconvoluted 29Si MAS NMR spectra.*

Sample	Parameter	Assignment								
		Unreacted slag	**Q^0**	**Q^1(I)**	**Q^1(II)**	**Q^2**	**Q^2(1Al)**	**Q^3 or Q^4(3 Al)**	**Q^3(1 Al)**	**Q^4(4 Al)**
	δ_{iso} (ppm)	***-75***	***-72***	***-76***	***-78.6***	***-84.4***	***-81.4***	***-92***	***-87***	***-87***
	FWHM (ppm)	***13***	***5***	***6***	***3***	***3.8***	***3***	***8***	***9***	***9***
SiO_3_3D	Relative integral area (%)	31.8	0.0	7.6	16.0	17.0	16.7	2.8	7.0	1.2
SiO_3_7D	Relative integral area (%)	33.1	0.0	7.1	17.2	16.3	17.9	2.0	5.2	1.2
SiO_3_28D	Relative integral area (%)	29.2	0.0	6.7	15.1	17.8	18.0	2.7	7.6	2.9
SiO_3_90D	Relative integral area (%)	15.9	0.0	9.2	14.9	22.6	21.1	4.7	8.5	3.2
CO_3_3D	Relative integral area (%)	38.3	2.6	9.4	12.0	13.2	15.6	2.8	5.8	0.4
CO_3_7D	Relative integral area (%)	34.9	2.6	8.8	13.8	13.8	16.4	2.8	6.2	0.9
CO_3_28D	Relative integral area (%)	34.8	1.8	9.7	14.5	14.3	17.2	1.4	5.5	1.0
CO_3_90D	Relative integral area (%)	32.7	0.8	8.1	14.4	16.9	15.9	2.2	7.1	2.0
SiO_3_CO_3_3D	Relative integral area (%)	29.4	2.3	8.4	16.4	15.3	16.8	6.1	5.0	0.3
SiO_3_CO_3_7D	Relative integral area (%)	29.6	1.5	8.7	19.2	15.6	17.7	2.4	4.8	0.5
SiO_3_CO_3_28D	Relative integral area (%)	23.5	1.5	9.0	17.8	18.3	18.5	3.0	7.6	0.8
SiO_3_CO_3_90D	Relative integral area (%)	18.4	1.6	7.8	17.6	20.7	19.6	4.4	7.9	2.1

Based on the quantifications of these Q sites, a continual dissolution of slag over time can be observed for all of the activated slag binders, and an increased reaction for the two silicate-activated samples is observed due to the uptake of silica into the solid binder. Additionally, all samples appear to have a sodium and aluminium substituted calcium silicate hydrate (C-(N)-

A-S-H) with significant crosslinking, which continues to polymerise over time due to increased incorporation of calcium ions in the interlayer as curing progresses.

Furthermore, the existence of Q^4 sites in the non-additive-containing samples indicates the precipitation of N-A-S-H in addition to C-A-S-H, specifically from an early age for the silicate-activated binder, and a bit slower but at a similar rate for the carbonate- and silicate-carbonate-activated slag binders. However, the quantifications of such Q^4 sites suggest very small amounts of N-A-S-H is forming in the carbonate-activated slag cements, likely not sufficient enough to affect the crosslinking of the main reaction product. Additionally, for the CaO-containing samples, it was concluded that no Q^4 Si environments exist at any curing age for either dosage, and therefore the aluminium-rich N-A-S-H phase does not form in carbonate-activated samples incorporating calcium oxide. Moreover, the C-A-S-H that formed in the CaO-containing samples does not appear to polymerise to the same extent as the solely carbonate-activated sample and definitely nowhere near the extent of the control sample, indicating that the further continual reaction is limited, possibly by the formation of secondary species, monocarbonates.

Table 9-3 *NMR parameters for the carbonate-activated slag samples with additives, extracted from the deconvoluted 29Si MAS NMR spectra.*

Sample	**Parameter**	**Assignment**							
		Unreacted slag	**Q^0**	**Q^1(I)**	**Q^1(II)**	**Q^2**	**Q^2(1Al)**	**Q^3**	**Q^3(1Al)**
	δ_{iso} (ppm)	*-75*	*-72*	*-76*	*-78.6*	*-84.4*	*-81.4*	*-92*	*-87*
	FWHM (ppm)	*13*	*5*	*6*	*3*	*3.8*	*3*	*8*	*9*
CO_3_1%CaO_3D	Relative integral area (%)	49.4	1.9	7.9	14.9	9.4	15.1	1.3	0.0
CO_3_1%CaO_7D	Relative integral area (%)	39.0	1.5	7.9	13.5	14.8	15.9	4.2	3.1
CO_3_1%CaO_28D	Relative integral area (%)	38.7	1.2	9.7	13.0	17.9	13.0	3.0	3.5

CO_3_1%CaO_90D	Relative integral area (%)	36.3	1.5	8.6	18.3	15.4	16.0	1.7	2.3
CO_3_3%CaO_3D	Relative integral area (%)	43.9	1.9	7.9	19.5	9.4	15.1	1.3	1.2
CO_3_3%CaO_7D	Relative integral area (%)	38.1	1.2	7.8	20.5	10.8	16.6	2.6	2.3
CO_3_3%CaO_28D	Relative integral area (%)	38.1	1.0	6.4	21.6	12.1	16.0	1.1	3.7
CO_3_3%CaO_90D	Relative integral area (%)	33.5	1.3	8.3	23.2	12.4	16.5	0.0	4.8

9.2.3 Physical Properties

Physical properties were characterised for only those samples deemed sufficient binders from reaction and structural evolution data analysis. As such, no physicomechanical data exists for the slag binders activated with sodium sulphate. Measures of workability include mini slump diameter (**Error! Reference source not found.**) and viscometry data shown as a stress vs strain plot (**Figure 9-5**) and the Herschel-Bulkley model parameters (**Table 9-4**); these data are used to determine how long and how well a cementitious material is workable in site. Additionally, compressive strength measurements provide an idea of the application of the binder, i.e. how the material can perform once set and in use.

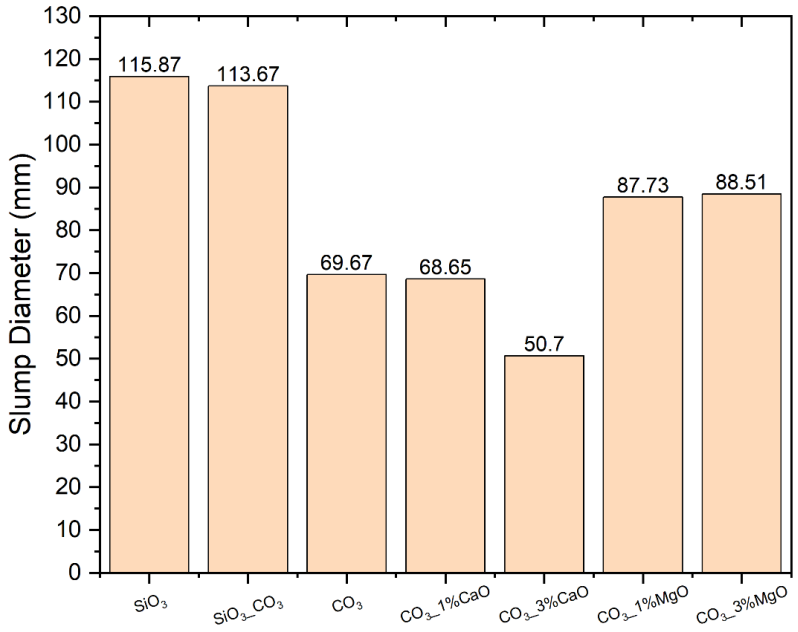

Figure 9-4 *Summary of slump diameter for each carbonate-activated slag binder in comparison to the silicate-activated control.*

Typically, the silicate-activated control sample flows far better than the carbonate-activated binders, likely due to the nature of sodium silicate to act as a dispersant in a particle suspension, having a wider spread in the mini slump test (**Figure 9-4**). Furthermore, the mixed activator sample tends towards the nature of the silicate activator in terms of flowability, as it has with reaction and phase evolution, suggesting that sodium silicate has a greater influence on the system than just its pH. This trend continues with the viscometry data, showing that both silicate-activated samples behave as Bingham-type fluids, while the carbonate-activated slag binder exhibits shear thinning behaviour, meaning that its viscosity decreases with increasing stress (**Figure 9-5** and **Table 9-4**).

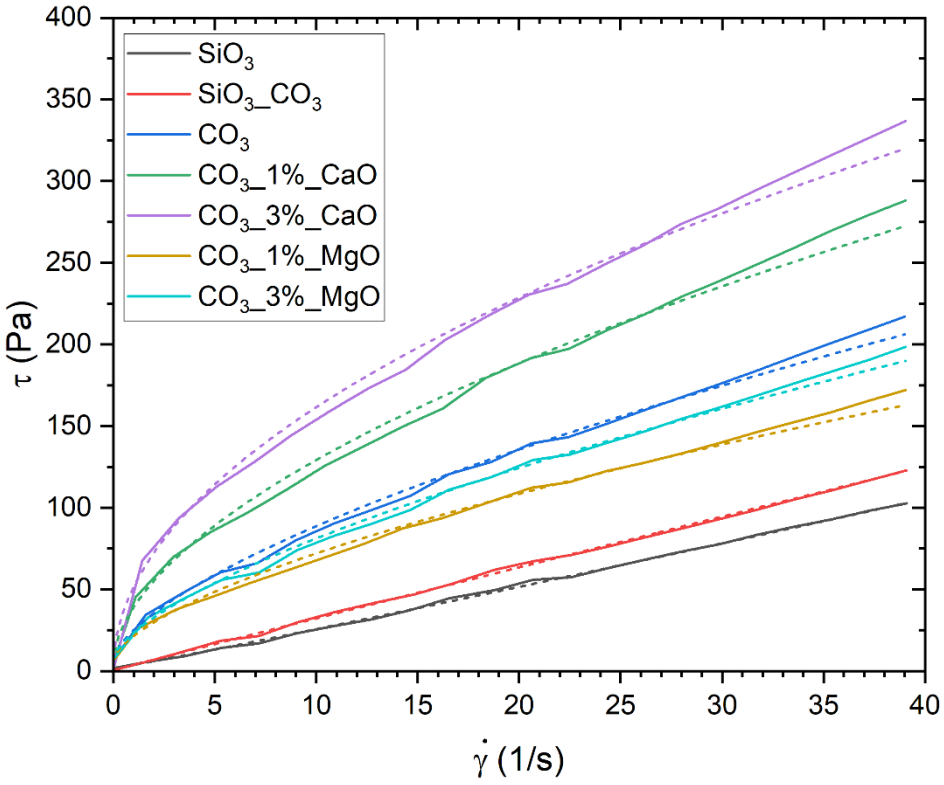

Figure 9-5 *Comparison of viscometry data for all carbonate-activated samples and the silicate-activated control sample.*

Table 9-4 *Summary of Herschel-Bulkley parameters for all carbonate-activated BFS and the silicate-activated control, as per the curve fitting of the model.*

Sample	**τ_0**	**k**	**n**
BFS_8%_Na_2SiO_3	1.69	2.11	1.06
BFS_8%_Na_2SiO_3_Na_2CO_3	1.56	3.25	0.99
BFS_8%_Na_2CO_3	6.77	18.22	0.65
BFS_8%_Na_2CO_3_1%_CaO	5.08	33.90	0.56
BFS_8%_Na_2CO_3_3%_CaO	1.12	50.22	0.50
BFS_8%_Na_2CO_3_1%_MgO	6.20	15.19	0.64
BFS_8%_Na_2CO_3_3%_MgO	7.33	16.00	0.66

Although the inclusion of MgO had little effect on the rate of reaction of the sodium carbonate-activated binder, it improved the workability as evident by slump diameter and viscometry data, however led to reduced compressive strength measurements at both 7 and 28 days. On the other hand, while the addition of CaO in the sodium carbonate-activated slag system improved the initial rate of reaction, it has had a negative effect on the workability and compressive strength of the material, with the 3 wt.% inclusion leading to a significant reduction in strength.

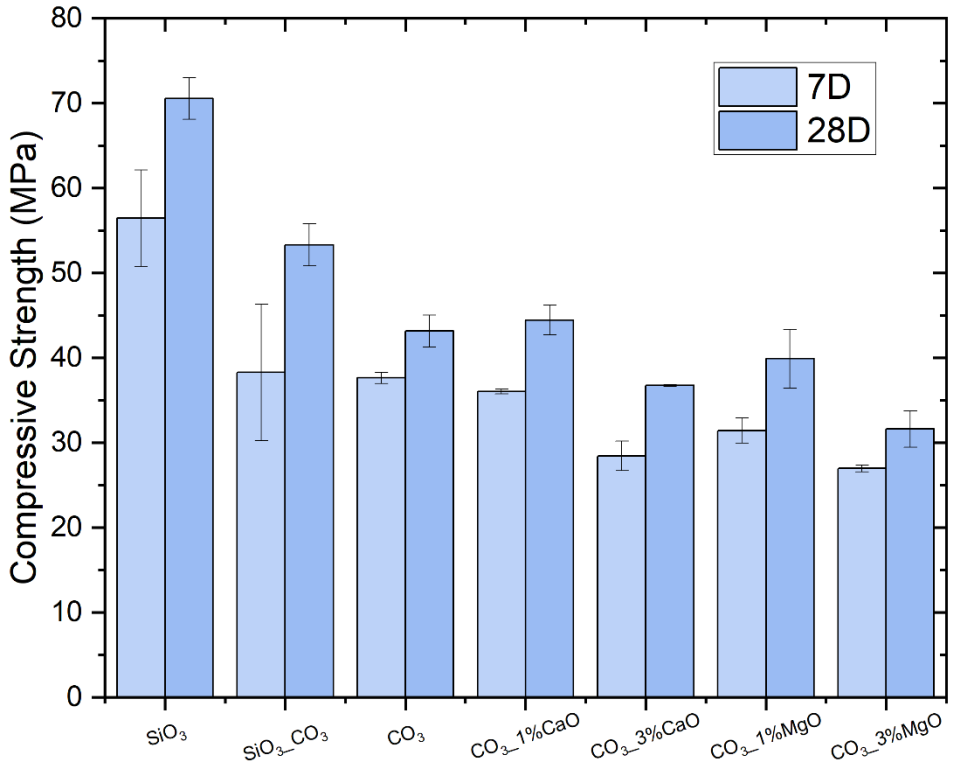

Figure 9-6 *Comparison of compressive strength for all carbonate-activated samples and the silicate-activated control sample.*

9.2.4 Carbon Footprint

With one of the overarching principles of this project being environmental sustainability, a measure of carbon footprint has been calculated for each of the samples. Taking a unit of 1 kg of cementitious binder, a preliminary value of the carbon footprint of each sample was calculated using the formulation recipe and the carbon intensity value of each of the material components listed in **Table 9-5**. Values for carbon intensity were taken from literature or

sourced from Ecoinvent 3.1 [263], where sourced values followed a cradle-to-gate methodology for consistency. This is a measure of a product's environmental impact from the extraction of raw materials (the cradle) up to the point it leaves the production facility (the factory gate) and thus excludes the use and disposal phases. As such, it is emphasised that this is not an LCA, but a complimentary calculation to capture the general environmental footprint associated with alkali-activated slag binders, particularly when incorporating the less commonly used – and typically more sustainable – activating solutions. Calculated carbon footprints (**Table 9-6**) herein should be taken as indicative trends and not absolute values.

Table 9-5 *Carbon intensity values for the components of samples used in this study, using a cradle-to-gate boundary where possible.*

Material	Carbon Intensity Value ($kgCO_2e/kg$)	Notes	Reference(s)
Portland Cement	0.84	CEM I	[264]
Blast Furnace Slag	0.155	GGBS to BS EN 15167-1 for use in concrete mortar and grout	[264]
Water	0.000407	Deionised water (Europe without Switzerland)	[263]
Sodium Silicate	0.71	48 % solution	[263]
Sodium Hydroxide	1.12	>99% solids	[265]
Sodium Carbonate	0.46		[266]
Sodium Sulphate	0.46		[267]
Calcium Oxide	2.71		[260]
Magnesium Oxide	2.70	Caustic calcined magnesia	[261], [262]

Table 9-6 *Calculated carbon footprints of sample formulations in this study.*

Sample	Calculated Carbon Intensity Value ($kgCO_2e/kg$)
BFS_8%_SiO_3	0.238
BFS_8%_CO_3	0.137
BFS_8%_SiO_3_CO_3	0.187
BFS_8%_CO_3_1%_CaO	0.152

BFS_8%_CO_3_3%_CaO	0.186
BFS_8%_CO_3_1%_MgO	0.152
BFS_8%_CO_3_3%_MgO	0.185
BFS_8%_SO_4	0.145
BFS_8%_SiO_3_SO_4	0.190
BFS_8%_SO_4_1%_CaO	0.160
BFS_8%_SO_4_3%_CaO	0.191
BFS_8%_SO_4_1%_MgO	0.160
BFS_8%_SO_4_3%_MgO	0.191

As expected, the sodium silicate-activated slag binder has the highest carbon footprint of the samples used in this study, while the lowest intensity value is associated with the slag binders activated solely with sodium carbonate, followed by the sodium sulphate-activated sample, with the low-carbon activated samples having more than 10 % more CO_2 savings than the silicate-activated sample compared to the carbon intensity value of Portland cement (0.84 kgCO_2e/kg). Furthermore, the inclusion of either calcium oxide or magnesium oxide, which are both known to be produced in carbon-intensive ways, in small quantities in either of the low-carbon alkali-activated systems maintains a lower carbon footprint than the silicate-activated sample, however, the 3 wt.% additive incorporation have very similar carbon intensity values to the silicate-modified carbonate- or sulphate-activated samples. This would suggest that if an improved rate of reaction is desired for the likes of the carbonate-activated slag sample, with the aim of a compromise between performance and carbon footprint, then the blended silicate-carbonate-activator system is a better choice than the 3 wt.% inclusion of calcium oxide.

9.3 Key Property Comparison

In addition to the carbon footprint of the binder, additional highly desirable property types were selected based on industrial use and general applications: workability, setting time, peak

reaction time, and 7-day compressive strength. The workability of cement encompasses how well the material flows and for how long it can be sufficiently poured and moulded before it cannot be reworked without weakening the structure. Subsequently, the point when the material can no longer be shaped is known as its setting time. Moreover, the peak reaction time is a measure of when the primary reaction, where the key strength-giving phases are formed, has sufficiently proceeded, before the rate of reaction reduces to a very low but continual level. And finally, a 7-day compressive strength value is typically a good indicator of the overall strength potential of the material, with its value expected to be at least 65 % of the material's ultimate compressive strength. The 7-day value was selected here rather than the 28-day value as early strength development is key for the progress of construction projects, as well as being an indicator for what will likely be the 28-day strength value.

All of these additional properties have been determined for the carbonate-activated samples, with and without additives, as well as the silicate-activated slag sample. However, due to the lack of influence on the reaction rate of the carbonate-activated system, the magnesium oxide-doped samples were not included in the property comparison. Moreover, the physical properties of the sulphate-activated samples were not tested due to the poor reaction and structural evolution observed during analysis, and as such these samples are also excluded from the property comparison.

The aforementioned five properties, relevant to industry implementation, have been plotted for the best performing carbonate-activated samples as well as the silicate-activated sample for comparison, as shown in **Figure 9-7**, to more easily identify strengths and weaknesses of each of said formulations.

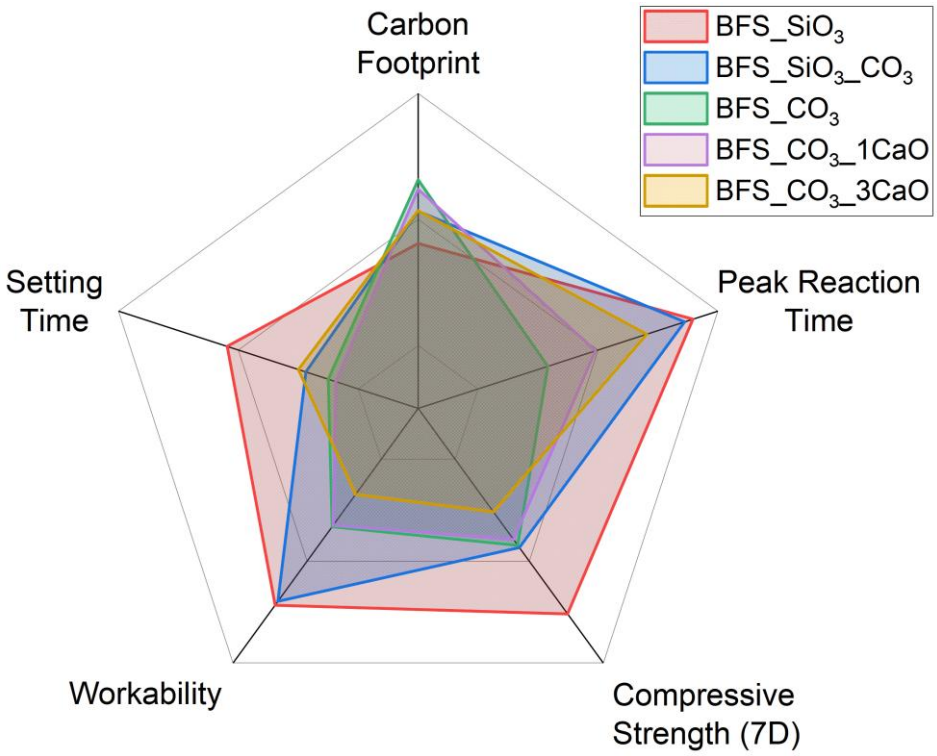

Figure 9-7 *Property-benefit analysis of alkali-activated binders. Property scales are as such: 0.5 – 0.0 kgCO_2e/kg of binder (Carbon footprint); 100 – 0 hr (Peak reaction time); 0 – 70 MPa (7D Compressive strength); 0 – 150 mm slump diameter (Workability); and 400 – 0 min (Setting time).*

As expected, the silicate-activated sample outperforms all other samples in terms of reaction rate and physical properties, however, it also incurs the highest carbon footprint of the selected samples. On the other hand, the sodium carbonate-activated sample has the least typically desirable property values but has the greatest carbon savings compared to PC. Moreover, the carbonate-samples either modified with sodium silicate in the activator or where small amounts of calcium oxide replaced slag, improve some of the reaction and physical properties, while having a carbon footprint somewhere between that of the silicate- and the carbonate-activated samples.

As the overarching aim of this project is to optimise formulations for enhanced performance as well as reducing the CO_2 emissions associated with the cement industry, an appropriate comparison of key parameters is necessary. This chapter identified key performance properties

of cements relevant for general industry applications – workability, setting time, peak reaction time, 7-day compressive strength, and carbon footprint – in order to compare and contrast the top cement formulations in this body of work.

As expected, the silicate-activated slag binder displayed the best performance while the carbonate-activated sample performed worst, however, the former has the greatest carbon footprint, and the latter has the highest carbon savings compared to Portland cement. The performance of the carbonate-activated binder is improved by the inclusion of the small amounts of calcium oxide or the 50:50 wt. blend of the activator with sodium silicate, which also increased the carbon intensity value but not as high as the solely silicate-activated sample.

Overall, there is likely a balance to be found between performance and carbon savings, depending on the properties required for the desired application of the binder. For example, if high compressive strength is required, then the carbon footprint is likely to be greater, whereas if a slower reaction and strength development can be afforded, the carbon savings are greater.

9.4 Conclusions of the Study

The implementation of alkali-activated cements in industry has the potential to significantly reduce the carbon emissions associated with the construction industry, due to their incorporation of industrial waste and/or by-products as well as naturally occurring minerals. Despite this, the more commonly used activators – hydroxides and silicates – contribute a greater carbon footprint than their less widely used counterparts, alkali carbonates and

sulphates. However, the use of these low-carbon activators in current AAC production is hindered by their poor initial reaction and early property development.

With the aim of optimising the design of such materials to prioritise both performance and environmental impact, this study focuses on the use of sodium carbonate and sodium sulphate as potential activators for alkali-activated slag binders, and how the fundamental chemistry of the system influences the reaction, phase evolution, and physical properties of the material. Additionally, the inclusion of additives, calcium oxide and magnesium oxide, into these low-carbon alkali-activated systems was investigated, as was the blending of the low-carbon activators with the more commonly used sodium silicate, both with the aim to improve binder performance. All samples were compared to a sodium silicate-activated slag sample of similar formulation. Additionally, novel lab-scale systems have been designed and successfully used for the *in-situ* investigation of reaction kinetics and mechanisms of alkali-activated cement, which can be extended to characterise other cement systems. The findings of this study provide insight to enable optimisation of formulations for enhanced performance and sustainability in order to drive rapid industrial implementation of AACs. Key outcomes from this study are outlined below.

Both sodium carbonate and sodium sulphate proved successful for the activation of blast furnace slag when used in a dosage of 8 wt.% of Na_2O with respect to the precursor, however, the time for the onset and subsequent completion of the early reaction was particularly long, as expected; the main reaction started ~54 hours after mixing for the sodium carbonate-activated sample and nearly 72 hours for the sodium sulphate-activated sample. These slow reaction kinetics are attributed to the low alkalinity of these low-carbon activators hindering the dissolution of the slag particles, specifically the amount of soluble silica released from the slag which will form the eventual main binding phase, C-A-S-H.

For the slag binder where sodium carbonate was used for activation, an initial reaction peaking within the first 2 hours post-mixing was confirmed through *in-situ* characterisation, where calcium ions from the precursor and sodium ions from either the precursor or the activator preferentially react with carbonate ions from the activator to form (sodium) calcium carbonate polymorphs, which in turn results in the observed long dormant period before the main reaction ensues. However, once this preferential reaction concluded when all CO_3^{2-} ions are consumed, the pH in the pore solution can increase, and the main reaction proceeds after a few days. This was confirmed by solid-state characterisation, showing clear formation of a calcium aluminosilicate phase by 3 days, which continued to form and polymerise over time, as well as hydrotalcite, and eventual formation of a N-A-S-H-type structure in addition to the existing C-N-A-S-H. The fresh-state properties of the sodium carbonate-activated slag were less than desirable, where a higher yield stress was determined compared to the silicate-activated sample, and the shear-thinning nature resulted in a limited flowability. Compressive strength values at 7 and 28 days were also measured to be lower than that of silicate-activated slag cements, due to the reduced polymerisation of C-A-S-H in the carbonate-activated binders, but higher than those reported in the literature for similar slag binders.

On the other hand, the sodium sulphate-activated slag binder revealed early formation of calcium sulphates, a propensity for increased carbonation, and C-A-S-H formed only after 7 days. The low cumulative heat measured by ICC for these binders highlights the limited degree of reaction, which was further observed by the reduced formation of reaction products, and more specifically the lack of change in C-A-S-H phase assemblage and nanostructure over time, in TGA, XRD, and FTIR data. Essentially, where sodium sulphate was used for the activation of slag, the limited formation and further polymerisation of key binding phases coupled with the precipitation of secondary reaction products results in a material that will be limited in strength and resistance to external stresses.

The combination of the low-carbon activators with sodium silicate in 50:50 wt.% blends saw great improvement in performance for both sample sets, where the binders tended towards the behaviour of the sodium silicate-activated slag sample. Moreover, the incorporation of additives influenced the reaction of the slag binders differently depending on the activator used; calcium oxide improved the rate of reaction when either activator was used, while the magnesium oxide had little to no effect on the carbonate-activated slag but did indeed increase the reaction kinetics for the sulphate-activated binder. It is likely that the reduced reactivity of the magnesium oxide meant that it reacted in the pore solution at almost the same time as the main reaction of the sodium carbonate-activated sample, but the slower reactivity of the sodium sulphate-activated binder enabled an improved rate of reaction when used in this system. The use of calcium oxide at 3 wt.% replacement of slag when activated with sodium carbonate resulted in the completion of the main reaction within 24 hours and an expedited initial preferential reaction, which also saw the simultaneous early precipitation of C-A-S-H. Despite the improved early rate of reaction, beyond 7 days, the extent of reaction of this carbonate-activated slag had levelled to that of its non-additive-containing counterpart, with the developed C-A-S-H structure even showing less polymerisation due to less transportable cations from the early simultaneous formation of calcium carbonate polymorphs and C-A-S-H. Overall, the inclusion of additives in small amounts, for the most part, led to the improved early rate of reaction for both sodium carbonate- and sodium sulphate-activated slags due to an increased pH in the pore solution. For the carbonate-activated samples, additional secondary reaction products were observed, limiting its later age mechanical properties, while for the sulphate-activate slags, beyond the improved kinetics, the general reaction mechanism and subsequent structural evolution did not change.

Altogether, the use of low-carbon activators, alkali carbonates and sulphates, have proved successful for the activation of BFS, however, their reaction rate, structural evolution and

physical properties are limited compared to silicate-activated slag binders. The use of either a combination of the activator with sodium silicate or the addition of CaO and MgO resulted in improved reaction kinetics and saw both positive and negative responses in phase assemblage, fresh-state properties, and strength measurements. Further understanding is required to tailor these low-carbon alkali-activated binders for improved kinetics while not compromising on fresh-state and strength properties.

On the whole, identifying the efficacy of chemical formulation of AACs is integral for the design of novel low-carbon binders with enhanced performance to drive implementation in industry and reduce cement-associated carbon emissions. The mechanistic understanding determined in this study that the activator controls the not just the rate of reaction but also the reaction pathway can be applied to optimise systems. Further lab-scale studies must then be done to assess viability, which can then lead to scale-up studies as well as long-term stability and durability testing to validate such materials. This in turn can hopefully lead to the eventual uptake of low-carbon alkali-activated cement binders in industry, legislation-permitting.

9.5 Future Work Recommendations

This study has revealed a comprehensive analysis of the relationship between chemical formulation of alkali-activated slag binders and their reaction, structural evolution, and physical property development. Nonetheless, there are various aspects to further investigate, both more in the immediate and broader senses, to enhance the understanding of these materials for their potential use within the construction industry.

In the immediate future following this project, it would be useful to more extensively determine how the inclusion of additives or combination of activating solutions improves the performance of these low-carbon alkali-activated binders with particular focus on balancing enhanced

properties and carbon savings. Assessing the performance of slag binders with varying the mass ratios of sodium silicate to either sodium carbonate or sulphate will shed light on the influence of sodium silicate in the system to determine its minimum requirement to strike a balance between reducing the carbon footprint of AACs while sustaining boosted performance. Further to this, additional replacements of slag with calcium oxide – e.g. 5, 7, and 9 wt.% – in the carbonate-activated system should be explored to fully understand the effect and the limit of additive inclusion. Along the same lines, although the addition of MgO had limited effect on the activation of slag with sodium carbonate, it was observed to improve the fresh-state properties, which were hindered by CaO incorporation, so a combination of these additives should be investigated to determine binder performance in order to optimise both reaction and physical properties. Additionally, varying the formulation parameters of the sodium sulphate-activated binder is pertinent to determine the viability of this low-carbon activator; different dosages and water-to-binder ratios may improve the general performance of sulphate-activated slags.

For the broader future, research should focus on underpinning the key properties of these alkali-activated systems for long-term use, including durability and late-age performance – the ability to resist chemical attack and carbonation. Additional studies into upscaling formulations would be useful to understand the effects of scalability and the practicality of these systems beyond a laboratory setting for real-world applications. Along the same lines, the incorporation of sand and aggregates should be studied to determine the performance of alkali-activated binders within concrete structures.

References

[1] ‘Concrete needs to lose its colossal carbon footprint’, *Nature*, vol. 597, no. 7878, pp. 593–594, Sep. 2021, doi: 10.1038/d41586-021-02612-5.

[2] J. L. Provis and S. A. Bernal, ‘Geopolymers and related alkali-activated materials’, *Annu. Rev. Mater. Res.*, vol. 44, pp. 299–327, 2014, doi: 10.1146/annurev-matsci-070813-113515.

[3] P. C. Hewlett and M. Liska, ‘Lea’s Chemistry of Cement and Concrete’, *Leas Chem. Cem. Concr.*, vol. 5, pp. 1–858, 2019, doi: 10.1016/C2013-0-19325-7.

[4] K. L. Scrivener and R. J. Kirkpatrick, ‘Innovation in use and research on cementitious material’, *Cem. Concr. Res.*, vol. 38, no. 2, pp. 128–136, 2008, doi: 10.1016/j.cemconres.2007.09.025.

[5] J. G. J. Olivier, G. Janssens-Maenhout, M. Muntean, and J. Peters, ‘Trends in Global CO_2 Emissions: 2016 Report;PBL Netherlands Environmental Assessment Agency: The Hague’, *PBL Neth. Environ. Assess. Agency Eur. Comm. Jt. Res. Cent. JRC*, p. 86, 2016.

[6] R. M. Andrew, ‘Global CO_2 emissions from cement production’, *Earth Syst. Sci. Data*, vol. 10, pp. 2213–2239, 2018, doi: 10.5281/ZENODO.831454.

[7] United Nations, ‘World Population Prospects: 2017 Revision’. 2017.

[8] Global Infrastructure Hub, ‘The Role of Infrastructure in the Circular Economy’. 2021.

[9] J. L. Provis, ‘Green concrete or red herring? - Future of alkali-activated materials’, *Adv. Appl. Ceram.*, vol. 113, no. 8, pp. 472–477, Nov. 2014, doi: 10.1179/1743676114Y.0000000177.

[10] P. Duxson and J. S. J. Van Deventer, ‘Commercialization of geopolymers for construction – opportunities and obstacles’, in *Geopolymers: Structures, Processing, Properties and Industrial Applications*, 2009, pp. 379–400.

[11] G. Habert and C. Ouellet-Plamondon, ‘Recent update on the environmental impact of geopolymers’, *RILEM Tech. Lett.*, vol. 1, p. 17, 2016, doi: 10.21809/rilemtechlett.v1.6.

[12] F. Pacheco-Torgal, Z. Abdollahnejad, S. Miraldo, and M. Kheradmand, ‘Alkali-Activated Cement-Based Binders (AACBs) as Durable and Cost-Competitive Low-CO_2 Binder Materials: Some Shortcomings That Need to be Addressed’, in *Handbook of Low Carbon Concrete*, Elsevier Inc., 2017, pp. 195–216. doi: 10.1016/B978-0-12-804524-4.00009-9.

[13] P. Duxson, A. Fernández-Jiménez, J. L. Provis, G. C. Lukey, A. Palomo, and J. S. J. Van Deventer, ‘Geopolymer technology: The current state of the art’, *J. Mater. Sci.*, vol. 42, no. 9, pp. 2917–2933, May 2007, doi: 10.1007/s10853-006-0637-z.

[14] J. Davidovits and S. France, ‘Geopolymeric concretes for environmental protection’, *ACI Concr. Int.*, vol. 12, no. 7, pp. 30–41, 1990.

[15] P. Duxson, J. L. Provis, G. C. Lukey, and J. S. J. V. Deventer, ‘The role of inorganic polymer technology in the development of “ green concrete ”’, vol. 37, pp. 1590–1597, 2007, doi: 10.1016/j.cemconres.2007.08.018.

[16] S. D. Wang and K. L. Scrivener, ‘Hydration products of alkali activated slag cement’, *Cem. Concr. Res.*, vol. 25, no. 3, pp. 561–571, 1995, doi: 10.1016/0008-8846(95)00045-E.

[17] International Energy Agency, ‘Global Status Report 2017’.

[18] International Energy Agency, ‘2019 Global Status Report for Buildings and Construction’, 2019.

[19] P.-C. Aitcin, ‘Cements of yesterday and today: Concrete of tomorrow’, *Cem. Concr. Res.*, vol. 30, pp. 1349–1359, 2000.

[20] C. R. Gagg, ‘Cement and concrete as an engineering material: An historic appraisal and case study analysis’, *Eng. Fail. Anal.*, vol. 40, pp. 114–140, 2014, doi: 10.1016/j.engfailanal.2014.02.004.

[21] The World Commission on Environment and Development, ‘The Brundtland Report: “Our Common Future”’, 1987.

[22] L. Coppola *et al.*, ‘Binders alternative to Portland cement and waste management for sustainable construction—part 1’, *J. Appl. Biomater. Funct. Mater.*, vol. 16, no. 3, pp. 186–202, 2018.

[23] E. Gartner and H. Hirao, ‘A review of alternative approaches to the reduction of CO_2 emissions associated with the manufacture of the binder phase in concrete’, *Cem. Concr. Res.*, vol. 78, pp. 126–142, 2015, doi: 10.1016/j.cemconres.2015.04.012.

[24] J. Xiao, S. Zou, and C. S. Poon, ‘How to make concrete sustainable’, *Nature*, vol. 638, pp. 888–890, 2025.

[25] E. Gartner, ‘Industrially interesting approaches to “low-CO_2” cements’, *Cem. Concr. Res.*, vol. 34, no. 9, pp. 1489–1498, 2004, doi: 10.1016/j.cemconres.2004.01.021.

[26] E. A. R. Trout, ‘The History of Calcareous Cements’, in *Lea’s Chemistry of Cement and Concrete*, P. C. Hewlett and M. Liska, Eds, Butterworth-Heinemann, 2019, pp. 1–30.

[27] F. Glasser, *Application of inorganic cements to the conditioning and immobilisation of radioactive wastes*. Woodhead Publishing Limited, 2011. doi: 10.1533/9780857090959.1.67.

[28] C. Costa, ‘Hydraulic binders’, in *Materials for Construction and Civil Engineering: Science, Processing, and Design*, Springer International Publishing, 2015, pp. 1–52. doi: 10.1007/978-3-319-08236-3_1.

[29] M. B. Ali, R. Saidur, and M. S. Hossain, ‘A review on emission analysis in cement industries’, *Renew. Sustain. Energy Rev.*, vol. 15, no. 5, pp. 2252–2261, 2011, doi: 10.1016/j.rser.2011.02.014.

[30] J. Deja, A. Uliasz-Bochenczyk, and E. Mokrzycki, ‘CO_2 emissions from Polish cement industry’, *Int. J. Greenh. Gas Control*, vol. 4, no. 4, pp. 583–588, 2010, doi: 10.1016/j.ijggc.2010.02.002.

[31] P. Strother, ‘Manufacture of Portland Cement’, in *Lea’s Chemistry of Cement and Concrete*, P. Hewlett and M. Liska, Eds, Elsevier Science and Technology Ltd., 2019.

[32] A. M. Harrisson, ‘Constitution and Specification of Portland Cement’, in *Lea’s Chemistry of Cement and Concrete*, P. Hewlett and M. Liska, Eds, Elsevier Science and Technology Ltd., 2019, pp. 87–156.

[33] J. Beaudoin and I. Odler, ‘Hydration, Setting and Hardening of Portland Cement’, in *Lea’s Chemistry of Cement and Concrete*, P. C. Hewlett and M. Liska, Eds, Elsevier Science and Technology Ltd., 2019, pp. 157–250.

[34] K. Scrivener, R. Snellings, and B. Lothenbach, *A Practical Guide to Microstructural Analysis of Cementitious Materials*. 2018. doi: 10.1201/b19074.

[35] J. W. Bullard *et al.*, 'Mechanisms of cement hydration', *Cem. Concr. Res.*, vol. 41, no. 12, pp. 1208–1223, 2011, doi: 10.1016/j.cemconres.2010.09.011.

[36] K. Scrivener, A. Ouzia, P. Juilland, and A. Kunhi Mohamed, 'Advances in understanding cement hydration mechanisms', *Cem. Concr. Res.*, vol. 124, no. July, p. 105823, 2019, doi: 10.1016/j.cemconres.2019.105823.

[37] S. Kearney *et al.*, 'Cement-based stabilization/solidification of radioactive waste', *Low Carbon Stab. Solidif. Hazard. Wastes*, pp. 407–431, Jan. 2021, doi: 10.1016/B978-0-12-824004-5.00005-0.

[38] J. J. Chen, J. J. Thomas, H. F. W. Taylor, and H. M. Jennings, 'Solubility and structure of calcium silicate hydrate', *Cem. Concr. Res.*, vol. 34, pp. 1499–1519, 2004, doi: 10.1016/j.cemconres.2004.04.034.

[39] A. Madadi and J. Wei, 'Characterization of Calcium Silicate Hydrate Gels with Different Calcium to Silica Ratios and Polymer Modifications', *Gels*, vol. 8, no. 75, Jan. 2022, doi: 10.3390/GELS8020075.

[40] A. Nonat, 'The structure and stoichiometry of C-S-H', *Cem. Concr. Res.*, vol. 34, pp. 1521–1528, 2004, doi: 10.1016/j.cemconres.2004.04.035.

[41] I. G. Richardson, 'The calcium silicate hydrates', *Cem. Concr. Res.*, vol. 38, no. 2, pp. 137–158, 2008, doi: 10.1016/j.cemconres.2007.11.005.

[42] B. Walkley and J. L. Provis, 'Solid-state nuclear magnetic resonance spectroscopy of cements', *Mater. Today Adv.*, 2019, doi: 10.1016/j.mtadv.2019.100007.

[43] P.-C. Aïtcin, 'Portland Cement', in *Science and Technology of Concrete Admixtures*, Elsevier, 2016, pp. 27–51. doi: 10.1016/B978-0-08-100693-1.00003-5.

[44] C. Shi, P. V. Krivenko, and D. Roy, *Alkali-Activated Cements and Concretes*. Oxford: Taylor & F., 2005. doi: 10.4324/9780203390672.

[45] A. V. Saetta, B. A. Schrefler, and R. V. Vitaliani, 'The carbonation of concrete and the mechanism of moisture, heat and carbon dioxide flow through porous materials', *Cem. Concr. Res.*, vol. 23, no. 4, pp. 761–772, 1993, doi: 10.1016/0008-8846(93)90030-D.

[46] Q. Yuan, Z. Liu, K. Zheng, and C. Ma, 'Inorganic cementing materials', *Civ. Eng. Mater.*, pp. 17–57, Jan. 2021, doi: 10.1016/B978-0-12-822865-4.00002-7.

[47] M. J. McCarthy and T. D. Dyer, 'Pozzolanas and Pozzolanic Materials', *Leas Chem. Cem. Concr.*, pp. 363–467, Jan. 2019, doi: 10.1016/B978-0-08-100773-0.00009-5.

[48] J. L. Provis and J. S. J. Van Deventer, *Alkali activated materials: State-of-the-Art Report*. Springer, 2014.

[49] J. De Brito and F. Agrela, *New trends in eco-efficient and recycled concrete*. 2018. doi: 10.1016/C2017-0-01898-0.

[50] M. C. G. Juenger, F. Winnefeld, J. L. Provis, and J. H. Ideker, 'Advances in alternative cementitious binders', *Cem. Concr. Res.*, vol. 41, no. 12, pp. 1232–1243, 2011, doi: 10.1016/j.cemconres.2010.11.012.

[51] P. Duxson and J. L. Provis, 'Designing precursors for geopolymer cements', *J. Am. Ceram. Soc.*, vol. 91, no. 12, pp. 3864–3869, Dec. 2008, doi: 10.1111/j.1551-2916.2008.02787.x.

[52] B. Lothenbach, K. Scrivener, and R. D. Hooton, 'Supplementary cementitious materials', *Cem. Concr. Res.*, vol. 41, no. 12, pp. 1244–1256, Dec. 2011, doi: 10.1016/j.cemconres.2010.12.001.

[53] B. Walkley *et al.*, 'Phase evolution of C-(N)-A-S-H/N-A-S-H gel blends investigated via alkali-activation of synthetic calcium aluminosilicate precursors', *Cem. Concr. Res.*, vol. 89, pp. 120–135, Nov. 2016, doi: 10.1016/j.cemconres.2016.08.010.

[54] J. L. Provis and J. S. J. Van Deventer, *Geopolymers: Structures, processing, properties and industrial applications*. 2009. doi: 10.1533/9781845696382.

[55] B. Walkley, R. San Nicolas, M. A. Sani, J. D. Gehman, J. S. J. Van Deventer, and J. L. Provis, 'Phase evolution of Na_2O-Al_2O_3-SiO_2-H_2O gels in synthetic aluminosilicate binders', *Dalton Trans.*, vol. 45, no. 13, pp. 5521–5535, 2016, doi: 10.1039/c5dt04878h.

[56] I. Garcia-Lodeiro, A. Palomo, and A. Fernández-Jiménez, 'An overview of the chemistry of alkali-activated cement-based binders', in *Handbook of Alkali-Activated Cements, Mortars and Concretes*, Elsevier Inc., 2015, pp. 19–47. doi: 10.1533/9781782422884.1.19.

[57] D. L. Wang, M. L. Chen, and D. D. C. W. Tsang, 'Green remediation by using low-carbon cement-based stabilization/solidification approaches', in *Sustainable Remediation of Contaminated Soil and Groundwater*, Elsevier, 2020, pp. 93–118. doi: 10.1016/b978-0-12-817982-6.00005-7.

[58] B. Walkley, X. Ke, J. L. Provis, and S. A. Bernal, 'Activator Anion Influences the Nanostructure of Alkali-Activated Slag Cements', *J. Phys. Chem. C*, pp. 20727–20739, 2021, doi: 10.1021/acs.jpcc.1c07328.

[59] S. Song, D. Sohn, H. M. Jennings, and T. O. Mason, 'Hydration of alkali-activated ground granulated blast furnace slag', *J. Mater. Sci.*, vol. 35, no. 1, pp. 249–257, 2000, doi: 10.1023/A:1004742027117.

[60] J. L. Provis and J. S. J. Van Deventer, 'Introduction to geopolymers', *Geopolymers Struct. Process. Prop. Ind. Appl.*, pp. 1–11, 2009, doi: 10.1533/9781845696382.1.

[61] A. Fernández-Jiménez, J. G. Palomo, and F. Puertas, 'Alkali-activated slag mortars: Mechanical strength behaviour', *Cem. Concr. Res.*, vol. 29, no. 8, pp. 1313–1321, 1999, doi: 10.1016/S0008-8846(99)00154-4.

[62] X. Ke, S. A. Bernal, and J. L. Provis, 'Controlling the reaction kinetics of sodium carbonate-activated slag cements using calcined layered double hydroxides', *Cem. Concr. Res.*, vol. 81, pp. 24–37, 2016, doi: 10.1016/j.cemconres.2015.11.012.

[63] G. Habert, J. B. Espinose, D. Lacaillerie, and N. Roussel, 'An environmental evaluation of geopolymer based concrete production : reviewing current research trends', *J. Clean. Prod.*, vol. 19, no. 11, pp. 1229–1238, 2011, doi: 10.1016/j.jclepro.2011.03.012.

[64] M. L. Nehdi and A. Yassine, 'Mitigating portland cement CO_2 emissions using alkali-activated materials: System dynamics model', *Materials*, vol. 13, no. 20, pp. 1–23, 2020, doi: 10.3390/ma13204685.

[65] A. Adesina, 'Effect of Green Activators on the Properties of Alkali Activated Materials : a Review', in *SynerCrete'18 International Conference on Interdisciplinary Approaches for Cement-based Materials and Structural Concrete*, Funchal, Madeira Island, 2018.

[66] L. Valentini, S. Contessi, M. C. Dalconi, F. Zorzi, and E. Garbin, 'Alkali-activated calcined smectite clay blended with waste calcium carbonate as a low-carbon binder', *J. Clean. Prod.*, vol. 184, pp. 41–49, May 2018, doi: 10.1016/j.jclepro.2018.02.249.

[67] N. Mobasher, S. A. Bernal, and J. L. Provis, 'Structural evolution of an alkali sulfate activated slag cement', *J. Nucl. Mater.*, vol. 468, pp. 97–104, 2016, doi: 10.1016/j.jnucmat.2015.11.016.

[68] A. J. Moseson, D. E. Moseson, and M. W. Barsoum, 'High volume limestone alkali-activated cement developed by design of experiment', *Cem. Concr. Compos.*, vol. 34, no. 3, pp. 328–336, Mar. 2012, doi: 10.1016/j.cemconcomp.2011.11.004.

[69] S. A. Bernal, R. San Nicolas, J. S. J. Van Deventer, and J. L. Provis, 'Alkali-activated slag cements produced with a blended sodium carbonate/sodium silicate activator', *Adv. Cem. Res.*, vol. 28, no. 4, pp. 262–273, 2016.

[70] A. Sakulich, S. Miller, and M. Barsoum, 'Chemical and Microstructural Characterization of 20-Month-Old Alkali-Activated Slag Cements', *J. Am. Ceram. Soc.*, vol. 93, pp. 1741–1748, Feb. 2010, doi: 10.1111/j.1551-2916.2010.03611.x.

[71] S. A. Bernal, J. L. Provis, R. J. Myers, R. San Nicolas, and J. S. J. Van Deventer, 'Role of carbonates in the chemical evolution of sodium carbonate-activated slag binders', *Mater. Struct.*, vol. 48, pp. 517–529, 2015, doi: 10.1617/s11527-014-0412-6.

[72] J. L. Provis, 'Alkali-activated materials', *Cem. Concr. Res.*, vol. 114, pp. 40–48, Dec. 2018, doi: 10.1016/j.cemconres.2017.02.009.

[73] C. Shi and R. L. Day, 'Some Factors Affecting Early Hydration of Alkali-Slag Cements', *Cem. Concr. Res.*, vol. 26, no. 3, 1995.

[74] A. Fernández-Jiménez and F. Puertas, 'Effect of activator mix on the hydration and strength behaviour of alkali-activated slag cements', *Adv. Cem. Res.*, vol. 15, no. 3, pp. 129–136, Jul. 2003, doi: 10.1680/adcr.2003.15.3.129.

[75] J. R. MacGregor, 'Mineral Commodity Summaries: Soda Ash'. U.S. Geological Survey, Jan. 2025.

[76] B. Yuan, Q. L. Yu, and H. J. H. Brouwers, 'Evaluation of slag characteristics on the reaction kinetics and mechanical properties of Na_2CO_3 activated slag', *Constr. Build. Mater.*, vol. 131, pp. 334–346, Jan. 2017, doi: 10.1016/j.conbuildmat.2016.11.074.

[77] A. Fernández-Jiménez and F. Puertas, 'Setting of alkali-activated slag cement. Influence of activator nature', *Adv. Cem. Res.*, vol. 13, no. 3, pp. 115–121, 2001, doi: 10.1680/adcr.2001.13.3.115.

[78] A. F. Abdalqader, F. Jin, and A. Al-Tabbaa, 'Development of greener alkali-activated cement: utilisation of sodium carbonate for activating slag and fly ash mixtures', *J. Clean. Prod.*, vol. 113, pp. 66–75, Feb. 2016, doi: 10.1016/j.jclepro.2015.12.010.

[79] M. Kovtun, E. P. Kearsley, and J. Shekhovtsova, 'Chemical acceleration of a neutral granulated blast-furnace slag activated by sodium carbonate', *Cem. Concr. Res.*, vol. 72, pp. 1–9, Jun. 2015, doi: 10.1016/j.cemconres.2015.02.014.

[80] P. Perumal, J. Kiventer, and M. Illikainen, ‘Influence of alkali source on properties of alkali activated silicate tailings’, *Mater. Chem. Phys.*, vol. 271, 2021, doi: 10.1016/j.matchemphys.2021.124932.

[81] S. A. Bernal, ‘Advances in near-neutral salts activation of blast furnace slags’, *RILEM Tech. Lett.*, vol. 1, pp. 39–44, 2016, doi: 10.21809/rilemtechlett.2016.8.

[82] H. Xu, J. L. Provis, J. S. J. V. Deventer, and P. V. Krivenko, ‘Characterization of Aged Slag Concretes’, *ACI Mater. J.*, vol. 105, no. 2, pp. 131–140, 2008.

[83] A. Fernandez-Jimenez and F. Puertas, ‘Structure of Calcium Silicate Hydrates Formed in Alkaline-Activated Slag: Influence of the Type of Alkaline Activator’, *J. Am. Ceram. Soc.*, vol. 86, no. 8, pp. 1389–1394, 2003.

[84] C. Duran Atiş, C. Bilim, Ö. Çelik, and O. Karahan, ‘Influence of activator on the strength and drying shrinkage of alkali-activated slag mortar’, *Constr. Build. Mater.*, vol. 23, no. 1, pp. 548–555, Jan. 2009, doi: 10.1016/j.conbuildmat.2007.10.011.

[85] B. Akturk, S. Nayak, S. Das, and A. B. Kizilkanat, ‘Microstructure and Strength Development of Sodium Carbonate–Activated Blast Furnace Slags’, *J. Mater. Civ. Eng.*, vol. 31, no. 11, p. 04019283, Nov. 2019, doi: 10.1061/(ASCE)MT.1943-5533.0002944.

[86] ‘Mineral Commodity Summaries: Sodium Sulfate’. U.S. Geological Survey, 2013.

[87] J. M. Etcheverry *et al.*, ‘Phase Evolution of Hybrid Alkali Sulfate-Activated Ground-Granulated Blast Furnace Slag Cements’, *ACS Sustain. Chem. Eng.*, vol. 11, no. 49, pp. 17519–17531, Dec. 2023, doi: 10.1021/acssuschemeng.3c05937.

[88] A. T. M. Marsh, Z. Yue, Y. Dhandapani, K. Button, S. Adu-Amankwah, and S. A. Bernal, ‘Influence of limestone addition on sodium sulphate activated blast furnace slag cements’, *Constr. Build. Mater.*, vol. 360, p. 129527, Dec. 2022, doi: 10.1016/j.conbuildmat.2022.129527.

[89] H. Tan *et al.*, ‘Compressive strength and hydration process of wet-grinded granulated blast-furnace slag activated by sodium sulfate and sodium carbonate’, *Cem. Concr. Compos.*, vol. 97, pp. 387–398, 2019, doi: 10.1016/j.cemconcomp.2019.01.012.

[90] A. M. Rashad, Y. Bai, P. A. M. Basheer, N. C. Collier, and N. B. Milestone, ‘Chemical and mechanical stability of sodium sulfate activated slag after exposure to elevated temperature’, *Cem. Concr. Res.*, vol. 42, no. 2, pp. 333–343, Feb. 2012, doi: 10.1016/j.cemconres.2011.10.007.

[91] Y. Bai, N. B. Milestone, and C. Yang, ‘Sodium Sulphate Activated GGBS/PFA and Its Potential as a Nuclear Waste Immobilisation Matrix’, *MRS Online Proc. Libr.*, vol. 932, no. 1, p. 381, Sep. 2006, doi: 10.1557/PROC-932-38.1.

[92] A. R. Brough and A. Atkinson, ‘Sodium silicate-based, alkali-activated slag mortars - Part I. Strength, hydration and microstructure’, *Cem. Concr. Res.*, vol. 32, no. 6, pp. 865–879, 2002, doi: 10.1016/S0008-8846(02)00717-2.

[93] F. Puertas, R. De Gutierrez, A. Fernández-Jiménez, S. Delvasto, and J. Maldonado, ‘Alkaline cement mortars. Chemical resistance to sulfate and seawater attack’, *Mater. Construccion*, vol. 2002, no. 267, pp. 55–71, 2002, doi: 10.3989/mc.2002.v52.i267.326.

[94] T. Bakharev, J. G. Sanjayan, and Y. B. Cheng, ‘Resistance of alkali-activated slag concrete to acid attack’, *Cem. Concr. Res.*, vol. 33, no. 10, pp. 1607–1611, 2003, doi: 10.1016/S0008-8846(03)00125-X.

[95] F. Puertas, M. Palacios, and T. Vázquez, 'Carbonation process of alkali-activated slag mortars', *J. Mater. Sci.*, vol. 41, no. 10, pp. 3071–3082, 2006, doi: 10.1007/s10853-005-1821-2.

[96] F. Puertas, M. Palacios, H. Manzano, J. S. Dolado, A. Rico, and J. Rodríguez, 'A model for the C-A-S-H gel formed in alkali-activated slag cements', *J. Eur. Ceram. Soc.*, vol. 31, pp. 2043–2056, 2011, doi: 10.1016/J.JEURCERAMSOC.2011.04.036.

[97] I. Lecomte, C. Henrist, M. Liégeois, F. Maseri, A. Rulmont, and R. Cloots, '(Micro)-structural comparison between geopolymers, alkali-activated slag cement and Portland cement', *J. Eur. Ceram. Soc.*, vol. 26, no. 16, pp. 3789–3797, 2006, doi: 10.1016/j.jeurceramsoc.2005.12.021.

[98] S. D. Wang and K. L. Scrivener, '^{29}Si and ^{27}Al NMR study of alkali-activated slag', *Cem. Concr. Res.*, vol. 33, no. 5, pp. 769–774, 2003, doi: 10.1016/S0008-8846(02)01044-X.

[99] E. Bernard, W. J. Zucha, B. Lothenbach, and U. Mäder, 'Stability of hydrotalcite (Mg-Al layered double hydroxide) in presence of different anions', *Cem. Concr. Res.*, vol. 152, no. October 2021, 2022, doi: 10.1016/j.cemconres.2021.106674.

[100] M. Criado, B. Walkley, X. Ke, J. L. Provis, and S. A. Bernal, 'Slag and Activator Chemistry Control the Reaction Kinetics of Sodium Metasilicate-Activated Slag Cements', *Sustainability*, vol. 10, no. 4709, 2018, doi: 10.3390/su10124709.

[101] X. Ke, S. A. Bernal, and J. L. Provis, 'Layered double hydroxides modify the reaction of sodium silicate-activated slag cements', *Green Mater.*, vol. 7, no. 2, pp. 52–60, 2019.

[102] A. Fernandez-Jimenez and F. Puertas, 'Alkali-activated Slag Cements: Kinetic Studies', *Cem. Concr. Res.*, vol. 27, no. 3, pp. 359–368, 1997.

[103] S. D. Wang, K. L. Scrivener, and P. L. Pratt, 'Factors affecting the strength of alkali-activated slag', *Cem. Concr. Res.*, vol. 24, no. 6, pp. 1033–1043, 1994, doi: 10.1016/0008-8846(94)90026-4.

[104] M. Chi and R. Huang, 'Effects of dosage and modulus ratio of alkali-activated solution on the properties of slag mortars', *Adv. Sci. Lett.*, vol. 16, no. 1, pp. 7–12, 2012, doi: 10.1166/asl.2012.3313.

[105] V. Zivica, 'Effects of type and dosage of alkaline activator and temperature on the properties of alkali-activated slag mixtures', *Constr. Build. Mater.*, vol. 21, pp. 1463–1469, 2007, doi: 10.1016/j.conbuildmat.2006.07.002.

[106] S. A. Bernal *et al.*, 'MgO content of slag controls phase evolution and structural changes induced by accelerated carbonation in alkali-activated binders', *Cem. Concr. Res.*, vol. 57, pp. 33–43, 2014, doi: 10.1016/j.cemconres.2013.12.003.

[107] M. B. Haha, B. Lothenbach, G. Le Saout, and F. Winnefeld, 'Influence of slag chemistry on the hydration of alkali-activated blast-furnace slag - Part I: Effect of MgO', *Cem. Concr. Res.*, vol. 41, pp. 955–963, Sep. 2011, doi: 10.1016/j.cemconres.2011.05.002.

[108] M. Ben Haha, B. Lothenbach, G. Le Saout, and F. Winnefeld, 'Influence of slag chemistry on the hydration of alkali-activated blast-furnace slag - Part II: Effect of Al2O3', *Cem. Concr. Res.*, vol. 42, no. 1, pp. 74–83, Jan. 2012, doi: 10.1016/j.cemconres.2011.08.005.

[109] D. Krizan and B. Zivanovic, ‘Effects of dosage and modulus of water glass on early hydration of alkali-slag cements’, *Cem. Concr. Res.*, vol. 32, no. 8, pp. 1181–1188, 2002, doi: 10.1016/S0008-8846(01)00717-7.

[110] R. Tänzer, A. Buchwald, and D. Stephan, ‘Effect of slag chemistry on the hydration of alkali-activated blast-furnace slag’, *Mater. Struct.*, vol. 48, no. 3, pp. 629–641, Mar. 2015, doi: 10.1617/s11527-014-0461-x.

[111] C. Shi and R. L. Day, ‘A calorimetric study of early hydration of alkali-slag cements’, *Cem. Concr. Res.*, vol. 25, no. 6, pp. 1333–1346, Aug. 1995, doi: 10.1016/0008-8846(95)00126-w.

[112] I. Garcia-Lodeiro, A. Palomo, and A. Fernández-Jiménez, ‘Crucial insights on the mix design of alkali-activated cement-based binders’, in *Handbook of Alkali-Activated Cements, Mortars and Concretes*, Elsevier Inc., 2015, pp. 49–73. doi: 10.1533/9781782422884.1.49.

[113] A. M. Fernandez-Jimenez, ‘Cementos de escorias activadas alcalinamante: influencia de las variables y modelización del proceso’, Universidad Autónoma de Madrid, Spain, 2000.

[114] A. M. Rashad, Y. Bai, P. A. M. Basheer, N. B. Milestone, and N. C. Collier, ‘Hydration and properties of sodium sulfate activated slag’, *Cem. Concr. Compos.*, vol. 37, pp. 20–29, Mar. 2013, doi: 10.1016/j.cemconcomp.2012.12.010.

[115] Z. Yue, Y. Dhandapani, and S. A. Bernal, ‘Structural alterations in alkali-sulfate-activated slag cement pastes induced by natural and accelerated carbonation’, *Cem. Concr. Res.*, vol. 187, p. 107713, Jan. 2025, doi: 10.1016/j.cemconres.2024.107713.

[116] T. Luukkonen, Z. Abdollahnejad, K. Ohenoja, P. Kinnunen, and M. Illikainen, ‘Suitability of commercial superplasticizers for one-part alkali-activated blast-furnace slag mortar’, *J. Sustain. Cem.-Based Mater.*, vol. 8, no. 4, pp. 244–257, 2019, doi: 10.1080/21650373.2019.1625827.

[117] C. Lu, Z. Zhang, C. Shi, N. Li, D. Jiao, and Q. Yuan, ‘Rheology of alkali-activated materials: A review’, *Cem. Concr. Compos.*, vol. 121, no. April, p. 104061, 2021, doi: 10.1016/j.cemconcomp.2021.104061.

[118] A. Habbaba and J. Plank, ‘Surface chemistry of ground granulated blast furnace slag in cement pore solution and its impact on the effectiveness of polycarboxylate superplasticizers’, *J. Am. Ceram. Soc.*, vol. 95, no. 2, pp. 768–775, Feb. 2012, doi: 10.1111/J.1551-2916.2011.04968.X.

[119] X. Dai, Q. Ren, S. Aydin, M. Y. Yardimci, and G. De Schutter, ‘Accelerating the reaction process of sodium carbonate-activated slag mixtures with the incorporation of a small addition of sodium hydroxide/sodium silicate’, *Cem. Concr. Compos.*, vol. 141, p. 105118, Aug. 2023, doi: 10.1016/j.cemconcomp.2023.105118.

[120] Yong Zheng *et al.*, ‘Effect of composite activator on hydration kinetics and micromechanical properties of alkali-activated slag’, *Cem. Concr. Compos.*, vol. 160, Jul. 2025, Accessed: Sep. 22, 2025. [Online]. Available: https://find.shef.ac.uk

[121] F. Winnefeld, M. Ben Haha, G. Le Saout, M. Costoya, S.-C. Ko, and B. Lothenbach, ‘Influence of slag composition on the hydration of alkali-activated slags’, *J. Sustain. Cem.-Based Mater.*, vol. 4, no. 2, pp. 85–100, Apr. 2015, doi: 10.1080/21650373.2014.955550.

[122] A. M. Rashad, ‘A Concise on the Effect of Calcium Oxide on the Properties of Alkali-Activated Materials: A Manual for Civil Engineers’, *Int. J. Concr. Struct. Mater.*, vol. 17, no. 1, p. 72, Dec. 2023, doi: 10.1186/s40069-023-00635-y.

[123] H. A. Abdel-Gawwad, ‘Effect of Reactive Magnesium Oxide on Properties of Alkali Activated Slag Geopolymer Cement Pastes’, in *Advances in Civil, Environmental, and Materials Research*, Busan, Korea, 2014.

[124] S. Feng, J. Zhu, R. Wang, Z. Qu, L. Song, and H. Wang, ‘The Influence of CaO and MgO on the Mechanical Properties of Alkali-Activated Blast Furnace Slag Powder’, *Materials*, vol. 15, no. 17, p. 6128, Sep. 2022, doi: 10.3390/ma15176128.

[125] J. He, W. Zheng, W. Bai, T. Hu, J. He, and X. Song, ‘Effect of reactive MgO on hydration and properties of alkali-activated slag pastes with different activators’, *Constr. Build. Mater.*, vol. 271, p. 121608, Feb. 2021, doi: 10.1016/J.CONBUILDMAT.2020.121608.

[126] J. Wang, X. Lyu, L. Wang, X. Cao, Q. Liu, and H. Zang, ‘Influence of the combination of calcium oxide and sodium carbonate on the hydration reactivity of alkali-activated slag binders’, *J. Clean. Prod.*, vol. 171, pp. 622–629, Jan. 2018, doi: 10.1016/j.jclepro.2017.10.077.

[127] M. J. De Hita and M. Criado, ‘Influence of admixtures on the workability and strength of sodium carbonate-activated slag/fly ash cement’, *Mater. Lett.*, vol. 312, p. 131695, Apr. 2022, doi: 10.1016/j.matlet.2022.131695.

[128] C. Ju, Y. Liu, M. Jia, K. Yu, Z. Yu, and Y. Yang, ‘Effect of calcium oxide on mechanical properties and microstructure of alkali-activated slag composites at sub-zero temperature’, *J. Build. Eng.*, vol. 32, p. 101561, Nov. 2020, doi: 10.1016/j.jobe.2020.101561.

[129] S.-D. Wang, X.-C. Pu, K. L. Scrivener, and P. L. Pratt, ‘Alkali-activated slag cement and concrete: a review of properties and problems’, *Adv. Cem. Res.*, vol. 7, no. 27, pp. 93–102, Jul. 1995, doi: 10.1680/adcr.1995.7.27.93.

[130] D. M. Roy, ‘Alkali-activated cements Opportunities and challenges’, *Cem. Concr. Res.*, vol. 29, pp. 249–254, 1999.

[131] S. Wang, ‘Review of recent research on alkali-activated concrete in China’, *Mag. Concr. Res.*, vol. 43, no. 154, pp. 29–35, Mar. 1991, doi: 10.1680/macr.1991.43.154.29.

[132] S. Ghorbani *et al.*, ‘Characterisation of alkali-activated stainless steel slag and blast-furnace slag cements’, *Cem. Concr. Compos.*, vol. 143, p. 105230, Oct. 2023, doi: 10.1016/J.CEMCONCOMP.2023.105230.

[133] I. Garcia-Lodeiro, A. Fernandez-Jimenez, M. T. Blanco, and A. Palomo, ‘FTIR study of the sol-gel synthesis of cementitious gels: C-S-H and N-A-S-H’, pp. 63–72, 2008, doi: 10.1007/s10971-007-1643-6.

[134] P. Yu, R. J. Kirkpatrick, B. Poe, P. F. McMillan, and X. Cong, ‘Structure of Calcium Silicate Hydrate (C-S-H): Near-, Mid-, and Far-Infrared Spectroscopy’, *J. Am. Ceram. Soc.*, vol. 82, no. 3, pp. 742–748, Mar. 1999, doi: 10.1111/j.1151-2916.1999.tb01826.x.

[135] W. K. W. Lee and J. S. J. Van Deventer, ‘The effects of inorganic salt contamination on the strength and durability of geopolymers’, *Colloids Surf. Physicochem. Eng. Asp.*, vol. 211, no. 2–3, pp. 115–126, Dec. 2002, doi: 10.1016/S0927-7757(02)00239-X.

[136] M. A. Trezza and A. E. Lavat, ‘Analysis of the system $3CaO{\cdot}Al_2O_3$–$CaSO_4{\cdot}2H_2O$–$CaCO_3$–H_2O by FT-IR spectroscopy’, *Cem. Concr. Res.*, 2001.

[137] F. Gervais, A. Blin, D. Massiot, J. P. Coutures, M. H. Chopinet, and F. Naudin, 'Infrared reflectivity spectroscopy of silicate glasses', *J. Non-Cryst. Solids*, vol. 89, no. 3, pp. 384–401, Mar. 1987, doi: 10.1016/S0022-3093(87)80280-6.

[138] B. S. Krumgalz, 'Temperature Dependence of Mineral Solubility in Water. Part 3. Alkaline and Alkaline Earth Sulfates', *J. Phys. Chem. Ref. Data*, vol. 47, no. 2, p. 023101, Jun. 2018, doi: 10.1063/1.5031951.

[139] Y. Xu, P. Liu, and Y. Zhang, 'Mid-infrared spectroscopy of hemispherical water droplets', *Spectrochim. Acta*, vol. 264, p. 120256, 2022, doi: 10.1016/j.saa.2021.120256.

[140] J. S. Jr. Falcone, J. L. Bass, M. Angelella, E. R. Schenk, and K. A. Brensinger, 'The Determination of Sodium Silicate Composition Using ATR FT-IR', *Ind. Eng. Chem. Res.*, vol. 49, no. 14, pp. 6287–6290, Jul. 2010, doi: 10.1021/ie1002747.

[141] M. O. Yusuf, 'Bond Characterization in Cementitious Material Binders Using Fourier-Transform Infrared Spectroscopy', *Appl. Sci.*, vol. 13, no. 5, p. 3353, Mar. 2023, doi: 10.3390/app13053353.

[142] V. H. J. M. D. Santos *et al.*, 'Application of Fourier Transform infrared spectroscopy (FTIR) coupled with multivariate regression for calcium carbonate ($CaCO_3$) quantification in cement', *Constr. Build. Mater.*, vol. 313, p. 125413, Dec. 2021, doi: 10.1016/j.conbuildmat.2021.125413.

[143] E. A. Secco, 'Spectroscopic properties of SO_4 (and OH) in different molecular and crystalline environments. I. Infrared spectra of $Cu_4(OH)_6SO4$, $Cu4(OH)_4OSO_4$, and $Cu_3(OH)_4SO_4$', *Can. J. Chem.*, vol. 66, no. 2, pp. 329–336, Feb. 1988, doi: 10.1139/v88-057.

[144] D. Peak, R. Ford, and D. L. Sparks, 'An in Situ ATR-FTIR Investigation of Sulfate Bonding Mechanisms on Goethite', *J. Colloid Interface Sci.*, vol. 218, no. 1, pp. 289–299, 1999.

[145] N. C. Collier, J. H. Sharp, N. B. Milestone, J. Hill, and I. H. Godfrey, 'The influence of water removal techniques on the composition and microstructure of hardened cement pastes', *Cem. Concr. Res.*, vol. 38, no. 6, pp. 737–744, Jun. 2008, doi: 10.1016/j.cemconres.2008.02.012.

[146] R. Snellings *et al.*, 'Report of TC 238-SCM: hydration stoppage methods for phase assemblage studies of blended cements—results of a round robin test', *Mater. Struct.*, vol. 51, no. 4, p. 111, Aug. 2018, doi: 10.1617/s11527-018-1237-5.

[147] J. Zhang and G. W. Scherer, 'Comparison of methods for arresting hydration of cement', *Cem. Concr. Res.*, vol. 41, no. 10, pp. 1024–1036, 2011, doi: 10.1016/j.cemconres.2011.06.003.

[148] H. F. W. Taylor and A. B. Turner, 'Reactions of tricalcium silicate paste with organic liquids', *Cem. Concr. Res.*, vol. 17, no. 4, pp. 613–623, Jul. 1987, doi: 10.1016/0008-8846(87)90134-7.

[149] L. D. Mitchell and J. C. Margeson, 'The effects of solvents on C–S–H as determined by thermal analysis', *J. Therm. Anal. Calorim.*, vol. 86, no. 3, pp. 591–594, Dec. 2006, doi: 10.1007/s10973-006-7712-1.

[150] Z. Zhou, M. Sofi, E. Lumantarna, R. S. Nicolas, G. H. Kusuma, and P. Mendis, 'Strength Development and Thermogravimetric Investigation of High-Volume Fly Ash Binders', *Materials*, vol. 12, no. 20, 2019.

[151] B. C. Smith, *Fundamentals of Fourier transform infrared spectroscopy*. CRC Press, 2011.

[152] B. D. Cullity, *Elements of x-ray diffraction*, 2. ed. in Addison-Wesley series in metallurgy and materials. Reading, Mass.: Addison-Wesley, 1978.

[153] D. D. B. Nergis, M. M. A. B. Abdullah, A. V. Sandu, and P. Vizureanu, 'XRD and TG-DTA Study of New Alkali Activated Materials Based on Fly Ash with Sand and Glass Powder', *Materials*, vol. 13, 2020.

[154] R. Snellings, A. Salze, and K. L. Scrivener, 'Use of X-ray diffraction to quantify amorphous supplementary cementitious materials in anhydrous and hydrated blended cements', *Cem. Concr. Res.*, vol. 64, pp. 89–98, Oct. 2014, doi: 10.1016/j.cemconres.2014.06.011.

[155] T. Bakharev, J. G. Sanjayan, and Y. B. Cheng, 'Resistance of alkali-activated slag concrete to carbonation', *Cem. Concr. Res.*, vol. 31, no. 9, pp. 1277–1283, 2001, doi: 10.1016/S0008-8846(01)00574-9.

[156] W. A. Hunnicutt, 'Characterization of Calcium-Silicate-Hydrate and Calcium-Alumino-Silicate-Hydrate', University of Illinois, 2013.

[157] O. Burciaga-Diaz, R. X. Magallanes-Rivera, and J. I. Escalante-garcia, 'Alkali-activated slag-metakaolin pastes : strength, structural, and microstructural characterization', *J. Sustain. Cem.-Based Mater.*, 2013, doi: 10.1080/21650373.2013.801799.

[158] K. Mackenzie, 'Multinuclear solid-state NMR of inorganic materials', Jan. 2002, doi: 10.1016/S1470-1804(02)X8001-8.

[159] G. Engelhardt and D. Michel, 'High-resolution solid-state NMR of silicates and zeolites', 1987. Accessed: Mar. 26, 2026. [Online]. Available: https://www.semanticscholar.org/paper/High-resolution-solid-state-NMR-of-silicates-and-Engelhardt-Michel/ca028b95f3c08f03af81c63e55f045d434935e27

[160] B. Walkley and J. L. Provis, 'Solid-state nuclear magnetic resonance spectroscopy of cements', *Mater. Today Adv.*, vol. 1, p. 100007, 2019, doi: 10.1016/j.mtadv.2019.100007.

[161] R. J. Myers, S. A. Bernal, R. San Nicolas, and J. L. Provis, 'Generalized Structural Description of Calcium–Sodium Aluminosilicate Hydrate Gels: The Cross-Linked Substituted Tobermorite Model', *Langmuir*, vol. 29, no. 17, pp. 5294–5306, Apr. 2013, doi: 10.1021/la4000473.

[162] J. Akhila and N. V. Rao, 'Experimental Investigation on Carbonation of Concrete Using SEM–EDX (Scanning Electron Microscopy (SEM) with Energy Dispersive X-Ray Analysis (EDX) & Environmental Scanning Electron Microscope (ESEM) Analysis', in *IOP Conference Series: Earth and Environmental Science*, 2023. doi: 10.1088/1755-1315/1130/1/012022.

[163] L. Dodds, 'Microstructure Characterisation of Ordinary Portland Cement Composites for the Immobilisation of Nuclear Waste', University of Manchester, 2012.

[164] W. Franus, R. Panek, and M. Wdowin, 'SEM Investigation of Microstructures in Hydration Products of Portland Cement', in *2nd International Multidisciplinary Microscopy and Microanalysis Congress*, 2015, pp. 105–112.

[165] ASTM International, ‘C 109/C 109M - 07: Standard Test Method for Compressive Strength of Hydraulic Cement Mortars (Using 2-in. or [50-mm] Cube Specimens)’, 2008. doi: 10.1201/9781420091175-c5.

[166] TAM-Air, ‘TAM Air Isothermal Calorimetry’, 2020.

[167] D. Treichel, L. Wadsö, A. L. Smith, H. Shirazi, and S. R. Mulligan, ‘The Isothermal Heat Conduction Calorimeter : A Versatile Instrument for Studying Processes in Physics , Chemistry , and Biology’, *J. Chem. Educ.*, vol. 78, no. 8, 2001.

[168] PIKE Technologies, Inc., ‘EasyDiff Manual’. Jan. 2014.

[169] R. Snellings, G. Mertens, Ö. Cizer, and J. Elsen, ‘Early age hydration and pozzolanic reaction in natural zeolite blended cements: Reaction kinetics and products by in situ synchrotron X-ray powder diffraction’, *Cem. Concr. Res.*, vol. 40, no. 12, pp. 1704–1713, Dec. 2010, doi: 10.1016/j.cemconres.2010.08.012.

[170] A. Cuesta *et al.*, ‘Multiscale understanding of tricalcium silicate hydration reactions’, *Sci. Rep.*, vol. 8, no. 1, Jun. 2018, doi: 10.1038/s41598-018-26943-y.

[171] G. Álvarez-Pinazo *et al.*, ‘In-situ early-age hydration study of sulfobelite cements by synchrotron powder diffraction’, *Cem. Concr. Res.*, vol. 56, pp. 12–19, Feb. 2014, doi: 10.1016/j.cemconres.2013.10.009.

[172] Z. Tan, S. A. Bernal, and J. L. Provis, ‘Reproducible mini-slump test procedure for measuring the yield stress of cementitious pastes’, *Mater. Struct.*, vol. 50, no. 6, pp. 1–12, 2017, doi: 10.1617/s11527-017-1103-x.

[173] P. R. de Matos, R. Pilar, C. A. Casagrande, P. J. P. Gleize, and F. Pelisser, ‘Comparison between methods for determining the yield stress of cement pastes’, *J. Braz. Soc. Mech. Sci. Eng.*, vol. 42, 2020.

[174] K. Walters and W. M. Jones, ‘Measurement of Viscosity’, in *Instrumentation Reference Book*, 3rd edn, Butterworth-Heinemann, 2003, pp. 45–52.

[175] M. Palacios, P. F. G. Banfill, and F. Puertas, ‘Rheology and Setting of Alkali-Activated Slag Pastes and Mortars: Effect of Organic Admixture’, *ACI Mater. J.*, 2008.

[176] H. Ramli, N. F. A. Zainal, M. Hess, and C. H. Chan, ‘Basic principle and good practices of rheology for polymers for teachers and beginners’, *Chem. Teach. Int.*, vol. 4, no. 4, pp. 307–326, Dec. 2022, doi: 10.1515/cti-2022-0010.

[177] British Standards Institution, ‘BS EN 196-10:2006 Methods of testing cement’, 2005.

[178] E. Yusslee, ‘The potential of one-part alkali-activated materials (AAMs) as a concrete patch mortar’, *Sci. Rep.*, pp. 1–10, 2022, doi: 10.1038/s41598-022-19830-0.

[179] A. B. E. Douglas and V. M. Malhotra, ‘Properties and Durability of Alkali-Activated Slag Concrete’, *ACI Mater. J.*, vol. 89, no. 5, Sep. 1992, doi: 10.14359/1832.

[180] A. Komkova and G. Habert, ‘Environmental impact assessment of alkali-activated materials: Examining impacts of variability in constituent production processes and transportation’, *Constr. Build. Mater.*, vol. 363, p. 129032, Jan. 2023, doi: 10.1016/j.conbuildmat.2022.129032.

[181] F. Lolli and K. E. Kurtis, ‘Life Cycle Assessment of alkali activated materials: preliminary investigation for pavement applications’, *RILEM Tech. Lett.*, vol. 6, pp. 124–130, Dec. 2021, doi: 10.21809/rilemtechlett.2021.120.

[182] A. Fernandez-Jimenez and F. Puertas, ‘Setting of alkali-activated slag cement. Influence of activator nature’, *Adv. Cem. Res.*, vol. 13, no. 3, pp. 115–121, Jul. 2001, doi: 10.1680/adcr.13.3.115.39288.

[183] I. García Lodeiro, D. E. Macphee, A. Palomo, and A. Fernández-Jiménez, ‘Effect of alkalis on fresh C–S–H gels. FTIR analysis’, *Cem. Concr. Res.*, vol. 39, no. 3, pp. 147–153, Mar. 2009, doi: 10.1016/j.cemconres.2009.01.003.

[184] R. Ylmén and U. Jäglid, ‘Carbonation of Portland Cement Studied by Diffuse Reflection Fourier Transform Infrared Spectroscopy’, *Int. J. Concr. Struct. Mater.*, vol. 7, no. 2, pp. 119–125, 2013, doi: 10.1007/s40069-013-0039-y.

[185] H. Niu *et al.*, ‘Recycling mica and carbonate-rich mine tailings in alkali-activated composites: A synergy with metakaolin’, *Miner. Eng.*, vol. 157, 2020.

[186] I. P. Segura *et al.*, ‘Comparison of One-Part and Two-Part Alkali-Activated Metakaolin and Blast Furnace Slag’, *J. Sustain. Metall.*, vol. 8, no. 4, pp. 1816–1830, Dec. 2022, doi: 10.1007/s40831-022-00606-9.

[187] S. O. Sore, A. Messan, E. Prud’Homme, G. Escadeillas, and F. Tsobnang, ‘Comparative Study on Geopolymer Binders Based on Two Alkaline Solutions (NaOH and KOH)’, *J. Miner. Mater. Charact. Eng.*, vol. 08, no. 06, pp. 407–420, 2020, doi: 10.4236/jmmce.2020.86026.

[188] S. A. Bernal *et al.*, ‘Gel nanostructure in alkali-activated binders based on slag and fly ash, and effects of accelerated carbonation’, *Cem. Concr. Res.*, vol. 53, pp. 127–144, 2013, doi: 10.1016/j.cemconres.2013.06.007.

[189] F. Rey, V. Fornes, and J. M. Rojo, ‘Thermal decomposition of hydrotalcites. An infrared and nuclear magnetic resonance spectroscopic study’, *J Chem Soc Faraday Trans*, vol. 88, no. 15, pp. 2233–2238, 1992, doi: 10.1039/ft9928802233.

[190] J. Ren *et al.*, ‘Experimental comparisons between one-part and normal (two-part) alkali-activated slag binders’, *Constr. Build. Mater.*, vol. 309, p. 125177, Nov. 2021, doi: 10.1016/j.conbuildmat.2021.125177.

[191] J. M. Rivas-Mercury, P. Pena, A. H. De Aza, and X. Turrillas, ‘Dehydration of $Ca_3Al_2(SiO_4)_y(OH)_{4(3-y)}$ ($0<y<0.176$) studied by neutron thermodiffractometry’, *J. Eur. Ceram. Soc.*, vol. 28, no. 9, pp. 1737–1748, Jan. 2008, doi: 10.1016/j.jeurceramsoc.2007.12.038.

[192] S. A. Bernal, J. L. Provis, D. G. Brice, A. Kilcullen, P. Duxson, and J. S. J. Van Deventer, ‘Accelerated carbonation testing of alkali-activated binders significantly underestimates service life: The role of pore solution chemistry’, *Cem. Concr. Res.*, vol. 42, no. 10, pp. 1317–1326, 2012, doi: 10.1016/j.cemconres.2012.07.002.

[193] S. A. Bernal, R. M. De Gutierrez, J. L. Provis, and V. Rose, ‘Effect of silicate modulus and metakaolin incorporation on the carbonation of alkali silicate-activated slags’, *Cem. Concr. Res.*, vol. 40, no. 6, pp. 898–907, Jun. 2010, doi: 10.1016/j.cemconres.2010.02.003.

[194] R. J. Myers, S. A. Bernal, J. D. Gehman, J. S. J. Van Deventer, and J. L. Provis, ‘The Role of Al in Cross-Linking of Alkali-Activated Slag Cements.pdf’, *J. Am. Ceram. Soc.*, vol. 98, no. 3, pp. 996–1004, 2015.

[195] P. J. Sideris, F. Blanc, Z. Gan, and C. P. Grey, ‘Identification of Cation Clustering in Mg−Al Layered Double Hydroxides Using Multinuclear Solid State Nuclear Magnetic Resonance Spectroscopy’, *Chem. Mater.*, vol. 24, pp. 2449–2461, 2012.

[196] M. D. Andersen, H. J. Jakobsen, and J. Skibsted, 'A new aluminium-hydrate species in hydrated Portland cements characterized by ^{27}Al and ^{29}Si MAS NMR spectroscopy', *Cem. Concr. Res.*, vol. 36, no. 1, pp. 3–17, 2006.

[197] A. Kunhi Mohamed *et al.*, 'The Atomic-Level Structure of Cementitious Calcium Aluminate Silicate Hydrate', *J. Am. Chem. Soc.*, vol. 142, no. 25, pp. 11060–11071, Jun. 2020, doi: 10.1021/jacs.0c02988.

[198] P. Faucon, A. Delagrave, J C Petit, C. Richet, J. M. Marchand, and H. Zanni, 'Aluminum Incorporation in Calcium Silicate Hydrates (C−S−H) Depending on Their Ca/Si Ratio', *J. Phys. Chem.*, vol. 103, no. 37, pp. 7796–7802, 1999, doi: 10.1021/jp990609q.

[199] G. K. Sun, J. F. Young, and R. J. Kirkpatrick, 'The role of Al in C–S–H: NMR, XRD, and compositional results for precipitated samples', *Cem. Concr. Res.*, vol. 36, no. 1, pp. 18–29, Jan. 2006, doi: 10.1016/j.cemconres.2005.03.002.

[200] I. G. Richardson, A. R. Brough, G. W. Groves, and C. M. Dobson, 'The characterization of hardened alkali-activated blast-furnace slag pastes and the nature of the calcium silicate hydrate (C-S-H) phase', *Cem. Concr. Res.*, vol. 24, no. 5, pp. 813–829, 1994, doi: 10.1016/0008-8846(94)90002-7.

[201] F. Bonk, J. Schneider, M. A. Cincotto, and H. Panepucci, 'Characterization by Multinuclear High-Resolution NMR of Hydration Products in Activated Blast-Furnace Slag Pastes', *J. Am. Ceram. Soc.*, vol. 86, no. 10, pp. 1712–1719, 2003.

[202] C. A. Love, I. G. Richardson, and A. R. Brough, 'Composition and structure of C–S–H in white Portland cement–20% metakaolin pastes hydrated at 25 °C', *Cem. Concr. Res.*, vol. 37, no. 2, pp. 109–117, Feb. 2007, doi: 10.1016/j.cemconres.2006.11.012.

[203] R. Taylor, I. G. Richardson, and R. M. D. Brydson, 'Composition and microstructure of 20-year-old ordinary Portland cement–ground granulated blast-furnace slag blends containing 0 to 100% slag', *Cem. Concr. Res.*, vol. 40, no. 7, pp. 971–983, Jul. 2010, doi: 10.1016/j.cemconres.2010.02.012.

[204] B. Walkley, S. J. Page, G. J. Rees, J. L. Provis, and J. V. Hanna, 'Nanostructure of CaO-(Na_2O)-Al_2O_3-SiO_2-H_2O Gels Revealed by Multinuclear Solid-State Magic Angle Spinning and Multiple Quantum Magic Angle Spinning Nuclear Magnetic Resonance Spectroscopy', *J. Phys. Chem. C*, vol. 124, no. 2, pp. 1681–1694, Jan. 2020, doi: 10.1021/acs.jpcc.9b10133.

[205] I. G. Richardson, A. R. Brough, R. Brydson, G. W. Groves, and C. M. Dobson, 'Location of Aluminum in Substituted Calcium Silicate Hydrate (C-S-H) Gels as Determined by 29Si and 27AI NMR and EELS', *J. Am. Ceram. Soc.*, vol. 76, no. 9, Sep. 1993.

[206] P. Rejmak, J. S. Dolado, M. J. Stott, and A. Ayuela, '^{29}Si NMR in Cement: A Theoretical Study on Calcium Silicate Hydrates', *J. Phys. Chem. C*, vol. 116, no. 17, pp. 9755–9761, May 2012, doi: 10.1021/jp302218j.

[207] G. Engelhardt and D. Michel, *High Resolution Solid State NMR of Silicates and Zeolites*. Chichester: Wiley, 1988.

[208] M. Palacios and F. Puertas, 'Effect of carbonation on alkali-activated slag paste', *J. Am. Ceram. Soc.*, vol. 89, no. 10, pp. 3211–3221, 2006, doi: 10.1111/j.1551-2916.2006.01214.x.

[209] J. L. Provis, P. Duxson, G. C. Lukey, and J. S. J. Van Deventer, 'Statistical Thermodynamic Model for Si/Al Ordering in Amorphous Aluminosilicates', *Chem. Mater.*, vol. 17, no. 11, pp. 2976–2986, May 2005, doi: 10.1021/cm050219i.

[210] B. Walkley, X. Ke, O. H. Hussein, S. A. Bernal, and J. L. Provis, 'Incorporation of strontium and calcium in geopolymer gels', *J. Hazard. Mater.*, vol. 382, 2020, doi: 10.1016/j.jhazmat.2019.121015.

[211] I. Ismail, S. A. Bernal, J. L. Provis, R. San Nicolas, S. Hamdan, and J. S. van Deventer, 'Modification of phase evolution in alkali-activated blast furnace slag by the incorporation of fly ash', *Cem. Concr. Compos.*, vol. 45, pp. 125–135, 2014, doi: 10.1016/j.cemconcomp.2013.09.006.

[212] J. S. J. Van Deventer, R. San Nicolas, I. Ismail, S. A. Bernal, D. G. Brice, and J. L. Provis, 'Microstructure and durability of alkali-activated materials as key parameters for standardization', *J. Sustain. Cem.-Based Mater.*, vol. 4, no. 2, pp. 116–128, Apr. 2015, doi: 10.1080/21650373.2014.979265.

[213] I. Garcia-Lodeiro, A. Palomo, A. Fernández-Jiménez, and D. E. Macphee, 'Compatibility studies between N-A-S-H and C-A-S-H gels. Study in the ternary diagram Na_2O–CaO–Al_3O_2–SiO_2–H_2O', *Cem. Concr. Res.*, vol. 41, no. 9, pp. 923–931, Sep. 2011, doi: 10.1016/j.cemconres.2011.05.006.

[214] R. R. Lloyd, J. L. Provis, and J. S. J. Van Deventer, 'Microscopy and microanalysis of inorganic polymer cements. 1: remnant fly ash particles', *J. Mater. Sci.*, vol. 44, no. 2, pp. 608–619, Jan. 2009, doi: 10.1007/s10853-008-3077-0.

[215] K. Vance, A. Dakhane, G. Sant, and N. Neithalath, 'Observations on the rheological response of alkali activated fly ash suspensions: the role of activator type and concentration', *Rheol. Acta*, vol. 53, no. 10–11, pp. 843–855, Nov. 2014, doi: 10.1007/s00397-014-0793-z.

[216] X. Dai, S. Aydin, M. Y. Yardimci, and G. De Schutter, 'Rheology and structural build-up of sodium silicate- and sodium hydroxide-activated GGBFS mixtures', *Cem. Concr. Compos.*, vol. 131, p. 104570, Aug. 2022, doi: 10.1016/j.cemconcomp.2022.104570.

[217] M. Palacios *et al.*, 'Early reactivity of sodium silicate-activated slag pastes and its impact on rheological properties', *Cem. Concr. Res.*, vol. 140, p. 106302, Feb. 2021, doi: 10.1016/j.cemconres.2020.106302.

[218] J. J. Chang, 'A study on the setting characteristics of sodium silicate-activated slag pastes', vol. 33, pp. 1005–1011, 2003, doi: 10.1016/S0008-8846(02)01096-7.

[219] F. Puertas, C. Varga, and M. Alonso, 'Rheology of alkali-activated slag pastes. Effect of the nature and concentration of the activating solution', *Cem. Concr. Compos.*, vol. 53, pp. 279–288, 2014, doi: 10.1016/j.cemconcomp.2014.07.012.

[220] L. Stefanini, B. Walkley, and J. L. Provis, 'Investigating the retarding effect of CAC in alkali-activated cements', *Front. Mater.*, vol. 10, Jun. 2023, doi: 10.3389/fmats.2023.1212177.

[221] *ACI SPEC-301-20: Specifications for Concrete Construction*, Farmington Hills, Michigan.

[222] O. A. Mohamed, 'A review of durability and strength characteristics of alkali-activated slag concrete', *Materials*, vol. 12, no. 8, pp. 1198–1216, 2019, doi: 10.3390/ma12081198.

[223] C. Lian, Y. Zhuge, and S. Beecham, 'The relationship between porosity and strength for porous concrete', *Constr. Build. Mater.*, vol. 25, no. 11, pp. 4294–4298, Nov. 2011, doi: 10.1016/j.conbuildmat.2011.05.005.

[224] M. Fawer, M. Concannon, and W. Rieber, 'Life cycle inventories for the production of sodium silicates', *Int. J. Life Cycle Assess.*, vol. 4, no. 4, p. 207, Jul. 1999, doi: 10.1007/BF02979498.

[225] A. Heath, K. Paine, and M. McManus, 'Minimising the global warming potential of clay based geopolymers', *J. Clean. Prod.*, vol. 78, pp. 75–83, Sep. 2014, doi: 10.1016/j.jclepro.2014.04.046.

[226] L. K. Turner and F. G. Collins, 'Carbon dioxide equivalent (CO_2-e) emissions: A comparison between geopolymer and OPC cement concrete', *Constr. Build. Mater.*, vol. 43, pp. 125–130, Jun. 2013, doi: 10.1016/j.conbuildmat.2013.01.023.

[227] L. Stefanini, B. Walkley, and J. L. Provis, 'Basic oxygen furnace (BOF) slag as an additive in sodium carbonate-activated slag cements', *Mater. Struct.*, vol. 57, no. 7, p. 153, Sep. 2024, doi: 10.1617/s11527-024-02425-8.

[228] A. Kiiashko, M. Chaouche, and L. Frouin, 'Effect of phosphonate addition on sodium carbonate activated slag properties', *Cem. Concr. Compos.*, vol. 119, p. 103986, May 2021, doi: 10.1016/j.cemconcomp.2021.103986.

[229] B. Akturk, A. B. Kizilkanat, and N. Kabay, 'Effect of calcium hydroxide on fresh state behavior of sodium carbonate activated blast furnace slag pastes', *Constr. Build. Mater.*, vol. 212, pp. 388–399, Jul. 2019, doi: 10.1016/j.conbuildmat.2019.03.328.

[230] A. Adesina, 'Performance and sustainability overview of sodium carbonate activated slag materials cured at ambient temperature', *Resour. Environ. Sustain.*, vol. 3, p. 100016, Mar. 2021, doi: 10.1016/j.resenv.2021.100016.

[231] Artur Kiiashko, 'Improving the rheological and early age properties of sodium carbonated alkali-activated GGBS', l'Université Paris-Saclay, 2019.

[232] X. Ke, S. A. Bernal, O. H. Hussein, and J. L. Provis, 'Chloride binding and mobility in sodium carbonate-activated slag pastes and mortars', *Mater. Struct.*, vol. 50, no. 6, p. 252, Dec. 2017, doi: 10.1617/s11527-017-1121-8.

[233] F. Jin and A. Al-Tabbaa, 'Strength and drying shrinkage of slag paste activated by sodium carbonate and reactive MgO', *Constr. Build. Mater.*, vol. 81, pp. 58–65, Apr. 2015, doi: 10.1016/j.conbuildmat.2015.01.082.

[234] S. Rossignol, 'Alkali-Activated Materials Based on Callovo-Oxfordian Argillite: Formation, Structure and Mechanical Properties', *J. Ceram. Sci. Technol.*, no. 02, 2018, doi: 10.4416/JCST2017-00086.

[235] C. K. Huang and Paul F. Kerr, 'Infrared Study of the Carbonate Minerals', *Am. Mineral.*, vol. 45, no. March-April, 1960.

[236] S. M. Holmes, V. L. Zholobenko, A. Thursfield, R. J. Plaisted, C. S. Cundy, and J. Dwyer, 'In situ FTIR study of the formation of MCM-41', *J. Chem. Soc. Faraday Trans.*, vol. 94, no. 14, pp. 2025–2032, 1998, doi: 10.1039/a801898g.

[237] F. Georget, B. Lothenbach, W. Wilson, F. Zunino, and K. L. Scrivener, 'Stability of hemicarbonate under cement paste-like conditions', *Cem. Concr. Res.*, vol. 153, p. 106692, Mar. 2022, doi: 10.1016/J.CEMCONRES.2021.106692.

[238] M. R. Jones *et al.*, 'Studies using ^{27}Al MAS NMR of AFm and AFt phases and the formation of Friedel's salt', *Cem. Concr. Res.*, vol. 33, no. 2, pp. 177–182, Feb. 2003, doi: 10.1016/S0008-8846(02)00901-8.

[239] Z. Chen and H. Ye, 'The role of CaO and MgO incorporation in chloride resistance of sodium carbonate-activated slag', *Cem. Concr. Compos.*, vol. 132, p. 104625, 2022, doi: 10.1016/j.cemconcomp.2022.104625.

[240] Mahmoud Gharieb and Alaa M. Rashad, 'Impact of Sugar Beet Waste on Strength and Durability of Alkali-Activated Slag Cement', *ACI Mater. J.*, vol. 119, no. 2, Mar. 2022, doi: 10.14359/51734354.

[241] C.-L. Hwang, D.-H. Vo, V.-A. Tran, and M. D. Yehualaw, 'Effect of high MgO content on the performance of alkali-activated fine slag under water and air curing conditions', *Constr. Build. Mater.*, vol. 186, pp. 503–513, Oct. 2018, doi: 10.1016/j.conbuildmat.2018.07.129.

[242] M. J. Ahmed, K. Lambrechts, X. Ling, K. Schollbach, and H. J. H. Brouwers, 'Effect of hydroxide, carbonate, and sulphate anions on the β-dicalcium silicate hydration rate', *Cem. Concr. Res.*, vol. 173, p. 107302, Nov. 2023, doi: 10.1016/j.cemconres.2023.107302.

[243] Z. Yue, Y. Dhandapani, S. Adu-Amankwah, and S. A. Bernal, 'Phase evolution and performance of sodium sulfate-activated slag cement pastes', *CEMENT*, vol. 18, p. 100117, Dec. 2024, doi: 10.1016/j.cement.2024.100117.

[244] T. Matschei, F. Bellmann, and J. Stark, 'Hydration behaviour of sulphate-activated slag cements', *Adv. Cem. Res.*, vol. 17, no. 4, pp. 167–178, Oct. 2005, doi: 10.1680/adcr.2005.17.4.167.

[245] G. Das, N. Kakati, S. H. Lee, N. Karak, and Y. S. Yoon, 'Water Soluble Sodium Sulfate Nanorods as a Versatile Template for the Designing of Copper Sulfide Nanotubes', *J. Nanosci. Nanotechnol.*, vol. 14, no. 6, pp. 4455–4461, Jun. 2014, doi: 10.1166/jnn.2014.8282.

[246] Z. Sun *et al.*, 'Steel slag for carbon fixation and synthesis of alkali-activated material', *Constr. Build. Mater.*, vol. 351, p. 128959, Oct. 2022, doi: 10.1016/j.conbuildmat.2022.128959.

[247] T. Li and B. Wang, 'Effect and mechanism of nano-alumina on early hydration properties and heavy metals solidification/stabilization of alkali-activated MSWI fly ash solidified body', *J. Hazard. Mater.*, vol. 452, p. 131327, Jun. 2023, doi: 10.1016/j.jhazmat.2023.131327.

[248] Yang Liu, Alian Wang, and John J. Freeman, 'Raman, MIR, and NIR spectroscopic study of calcium sulfates: Gypsum, Bassanite, and Anhydrite', in *40th Lunar and Planetary Science Conference*, 2009.

[249] G. Anbalagan, S. Mukundakumari, K. S. Murugesan, and S. Gunasekaran, 'Infrared, optical absorption, and EPR spectroscopic studies on natural gypsum', *Vib. Spectrosc.*, vol. 50, no. 2, pp. 226–230, Jul. 2009, doi: 10.1016/j.vibspec.2008.12.004.

[250] T. Missana, O. Almendros-Ginestà, F. Colmenero, A. M. Fernández, and M. García-Gutiérrez, 'Investigation of the surface charge behaviour of ettringite: Influence of pH, calcium, and sulphate ions', *Heliyon*, vol. 10, no. 16, p. e36117, Aug. 2024, doi: 10.1016/j.heliyon.2024.e36117.

[251] W. Szudek, J. Szydłowski, I. Buchała, and E. Kapeluszna, ‘Synthesis and Characterization of Calcium Sulfoaluminate Hydrates—Ettringite (AFt) and Monosulfate (AFm)’, *Materials*, vol. 17, no. 21, p. 5216, Oct. 2024, doi: 10.3390/ma17215216.

[252] L. G. Baquerizo, T. Matschei, K. L. Scrivener, M. Saeidpour, and L. Wadsö, ‘Hydration states of AFm cement phases’, *Cem. Concr. Res.*, vol. 73, pp. 143–157, Jul. 2015, doi: 10.1016/j.cemconres.2015.02.011.

[253] J. Havlica and S. Sahu, ‘Mechanism of ettringite and monosulphate formation’, *Cem. Concr. Res.*, vol. 22, pp. 671–677, Jul. 1992, doi: 10.1016/0008-8846(92)90019-R.

[254] B. A. Akinyemi, B. Orogbade, J. Kayode, and P. A. Alaba, ‘Physico-mechanical and thermal properties of chemical admixture modified bamboo reinforced gypsum-cement composite’, *Eur. J. Environ. Civ. Eng.*, vol. 27, no. 4, pp. 1730–1746, Mar. 2023, doi: 10.1080/19648189.2022.2094468.

[255] E. Scholtzová, L. Kucková, J. Kožíšek, and D. Tunega, ‘Structural and spectroscopic characterization of ettringite mineral –combined DFT and experimental study’, *J. Mol. Struct.*, vol. 1100, pp. 215–224, Nov. 2015, doi: 10.1016/j.molstruc.2015.06.075.

[256] E. Qoku, T. A. Bier, and T. Westphal, ‘Phase assemblage in ettringite-forming cement pastes: A X-ray diffraction and thermal analysis characterization’, *J. Build. Eng.*, vol. 12, pp. 37–50, Jul. 2017, doi: 10.1016/j.jobe.2017.05.005.

[257] S. M. Antao, M. J. Duane, and I. Hassan, ‘DTA, TG, AND XRD STUDIES OF STURMANITE AND ETTRINGITE’, *Can. Mineral.*, vol. 40, no. 5, pp. 1403–1409, Oct. 2002, doi: 10.2113/gscanmin.40.5.1403.

[258] K. Mei *et al.*, ‘Effectiveness and microstructure change of alkali-activated materials during accelerated carbonation curing’, *Constr. Build. Mater.*, vol. 274, p. 122063, 2021, doi: 10.1016/j.conbuildmat.2020.122063.

[259] M. Nedeljković, ‘Carbonation mechanism of alkali-activated fly ash and slag materials’, TU Delft, 2019.

[260] CarbonCloud, ‘Technical Report - Climate Footprint of Calcium Oxide (CaO). E529’, 2025.

[261] V.-T. Luong, R. Amal, J. A. Scott, S. Ehrenberger, and T. Tran, ‘A comparison of carbon footprints of magnesium oxide and magnesium hydroxide produced from conventional processes’, *J. Clean. Prod.*, vol. 202, pp. 1035–1044, Nov. 2018, doi: 10.1016/j.jclepro.2018.08.225.

[262] W. Ren, B. Xue, C. Lu, Z. Zhang, Y. Zhang, and L. Jiang, ‘Evaluation of GHG emissions from the production of magnesia refractory raw materials in Dashiqiao, China’, *J. Clean. Prod.*, vol. 135, pp. 214–222, Nov. 2016, doi: 10.1016/j.jclepro.2016.06.118.

[263] G. Wernet, C. Bauer, B. Steubing, J. Reinhard, E. Moreno-Ruiz, and B. Weidema, ‘The ecoinvent database version 3 (part I): overview and methodology’, *Int. J. Life Cycle Assess.*, vol. 21, no. 9, pp. 1218–1230, Sep. 2016, doi: 10.1007/s11367-016-1087-8.

[264] Mineral Products Association, ‘Fact Sheet 18 - Embodied CO2e of UK Cements’. 2025.

[265] CarbonCloud, ‘Technical Report - Climate Footprint of Sodium Hydroxide (NaOH). E524’, 2025.

[266] CarbonCloud, ‘Technical Report - Climate Footprint of Sodium Carbonate (Na_2CO_3). E500’, 2025.

[267] Minera Santa Marta, ‘Climate Declaration for Sodium Sulphate’. 2025.